

# **Material and mesostructural design guidelines for high performing photoelectrodes**

**Thèse N° 7408**

Présentée le 13 septembre 2019

à la Faculté des sciences et techniques de l'ingénieur

Laboratoire de la science et de l'ingénierie de l'énergie renouvelable

Programme doctoral en énergie

pour l'obtention du grade de Docteur ès Sciences

par

**Yannick Kenneth GAUDY**

Acceptée sur proposition du jury

Dr J. Van Herle, président du jury

Prof. S. Haussener, directrice de thèse

Prof. R. van de Krol, rapporteur

Prof. J. Ager, rapporteur

Prof. K. Sivula, rapporteur

2019

À ma famille grandissante

# Acknowledgements

First and foremost, I would like to deeply thank Prof. Sophia Haussener for her continuous support throughout these years of research at her laboratory. A special thank for teaching me scientific rigor in all of my research and publications. Thank you for all your advices, discussions, and for the trust you have always placed in me.

A special thanks go to my colleagues at the Laboratory of Renewable Energy Science and Engineering for all the fun we had together. It is definitely a massive plus to work in environment with a lot of fun and definitely balanced out all the hard work. Many thanks go especially to my colleague Mikael Dumortier for early help in my research and to Silvan Suter for all the nice moments at conferences we had during these shared years of PhD. I would like to thank also Marc Schiffler for all the nice tennis matches we had together that helped to refresh the brain. Many thanks to Sarah van Rooij for a great motivation and to create the first PhD association at EPFL.

Individual thanks go to Simone Pokrant, Stefan Dilger and Steve Landsman for their support on experimental work and in-depth discussions concerning particle-based  $\text{LaTiO}_2\text{N}$  photoelectrodes, a very complex system that remains partially mysterious. A big thank to Robin Humphry-Baker for helping me out to control our solar simulator and for friendly discussions. I would like to thank also Pavel Aseev for interesting discussion on  $\text{In}_x\text{Ga}_{1-x}\text{N}$  photoelectrodes, Carlos Morales-Guio and Thomas Moehl for helpful discussions on electrochemical impedance spectroscopy, Jean-François Carlin for the deposition of GaN on sapphire substrate, Néstor Guijarro and Liang Yao for IPCE measurements on  $\text{In}_x\text{Ga}_{1-x}\text{N}$  photoelectrodes.

J'aimerais également remercier ma famille, mon père qui aurait eu le torse plus que bombé de fierté pour son fils, un homme pour qui ses enfants et sa femme comptait plus que lui. Ma mère pour son soutien indéfectible et pour avoir été le pilier de notre famille durant de nombreuses années, une tâche parfois ingrate. Mon frère, un

modèle de remise en question, de motivation à inventer des activités et à faire du sport, même si parfois l'effort devient trop grand et le corps lâche comme mon tendon d'Achille en dernière année de thèse. Vous trois, vous m'avez placé à une proximité palpable du bonheur ce qui est un cadeau inestimable. Il me reste donc peu de chemin pour atteindre ce bonheur, un chemin que j'effectue désormais avec ma propre famille. Cela m'amène à remercier la femme de ma vie. Ça y est je suis docteur ;-). Merci pour ton énorme soutien psychologique et tes conseils sur les relations humaines qui font une grande partie de la thèse. Il y a eu beaucoup de hauts et parfois des bas et tu as toujours su être là pour moi, à me conseiller avec ta grande sensibilité et ce durant tout un chapitre de ma vie, de notre vie. Tu m'as tellement apporté durant cette période et quel chemin parcouru ensemble durant ma thèse. On s'est marié, on a déménagé chaque année ☺ et finalement on a matérialisé notre amour avec notre enfant, Solal, si beau et si chou. Ma gratitude envers toi est énorme et je ne l'oublierai jamais. Dis que tu m'appartiens...parce que moi je suis bien avec toi ;-).

Nyon, à un moment en 2019

Yannick Gaudy



# Abstract

The fabrication of particle-based photoelectrodes by coating or dipping procedures—similar to the scaled fabrication of battery electrodes—can be a route to overcome the efficiency-cost tradeoff of photoelectrochemical (PEC) water splitting devices. Additional strategies for practical and economically competitive PEC approaches include the use of stable ternary metal oxides with complex mesostructures and/or the use of tunable bandgap material. Identifying and quantifying the key parameters limiting the efficiency of the photoelectrodes is fundamental to providing material and mesostructural design guidelines. This quantification is experimentally not accessible given by the multi-physical nature of the processes taking place in the photoelectrodes. Computational modeling can provide the necessary insights but requires the detailed knowledge of material parameters that are often unknown for new photoelectrode materials and requires to account for the complex mesostructure of the photoelectrode. In this thesis, the development of versatile and validated computational models that allow for the material characterization, material parameters optimization, and mesostructural optimization of photoelectrodes is presented.

In order to develop a reliable, predictive, and validated multi-physics model of morphologically complex photoelectrodes, a numerical model of a well-known photoelectrode with well-defined morphology, a thin film GaN photoanode, was first developed. This numerical model simulating photocurrent-voltage ( $I$ - $V$ ) curves combines electromagnetic wave propagation, charge generation and transport in the semiconductor, and charge transfer across the catalytically active semiconductor-electrolyte interface. This model was subsequently validated by reproducing  $I$ - $V$  curves of a flat n-type GaN photoelectrode. The model was then used in combination of a fractional factorial design and a statistical analysis using analysis of

variance to highlight the significant impact of surface recombination at the semiconductor-electrolyte interface.

The developed model was then applied to morphologically complex LaTiO<sub>2</sub>N particle-based photoelectrodes. Numerous dedicated experiments such as UV-VIS-NIR spectrophotometry, nano-tomography, open-circuit voltage measurements, Mott-Schottky analysis, and conductivity measurements along with density functional theory calculations were used to determine all the required material parameters for the numerical model to be able to reproduce experimental  $I-V$  curves of particle-based LaTiO<sub>2</sub>N photoelectrodes. The impact of key parameters on the photoelectrode performance was then investigated in order to deduce material design guidelines. As a second step, the inter-particle charge transfer mechanism of these photoelectrode was investigated. Different theoretical inter-particle charge transfer mechanisms that could potentially occur in particle-based photoelectrode were introduced and their related equations were implemented in the model. The numerical  $I-V$  curves provided by the model were subsequently compared to experimental  $I-V$  curves and proved that charges transferred through inter-particle contacts were negligible. Only the particles in direct contact with the fluorine doped tin oxide glass substrate were significantly contributing to the photocurrent and thus indicating that inter-connecting particles is not an efficient approach for particle-based photoelectrodes with multiple layers of particles.

In contrast to the highly complex modeling framework developed for flat GaN photoelectrode and particle-based LaTiO<sub>2</sub>N photoelectrode, a rapid method was developed for performance optimization of photoelectrodes. This method, based on an incident photon-to-current efficiency model, provides the diffusion length, the optical, bulk, and surface losses of photoelectrodes. Furthermore, a novel dimensionless parameter that can objectively quantify the performance of photoelectrode materials, the diffusion optical number—defined as the product of the absorption coefficient and the diffusion length at 500 nm—was introduced and extracted for numerous photoelectrodes with varying materials and morphologies: flat Cu<sub>2</sub>O, Si, Fe<sub>2</sub>O<sub>3</sub>, Fe<sub>2</sub>O<sub>3</sub>, BiVO<sub>4</sub>, Cu<sub>2</sub>V<sub>8</sub>O<sub>3</sub>, CuFeO<sub>2</sub> photoelectrodes, nanostructured Fe<sub>2</sub>O<sub>3</sub>, and particle-based LaTiO<sub>2</sub>N photoelectrodes. By comparing the diffusion optical number of flat Fe<sub>2</sub>O<sub>3</sub> photoelectrodes and state-of-the-art nanostructured Fe<sub>2</sub>O<sub>3</sub> photoelectrodes, a benchmark to determine if a photoelectrode should be nanostructured or if its synthesis method should be modified was defined. Using this benchmark, Si was found to be a high performing material without nanostructuring and Cu<sub>2</sub>O and LaTiO<sub>2</sub>N were found to be potentially high performing photoelectrode materials if nanostructured. In contrast,

$\text{Fe}_2\text{O}_3$ ,  $\text{BiVO}_4$ ,  $\text{Cu}_2\text{V}_8\text{O}_3$ , and  $\text{CuFeO}_2$  were concluded not being high performing photoelectrode materials even if nanostructured. Their synthesis method should be rather modified. In order to support and guide material research and development, an easy to use and free software of the method, called POPE, was developed.

Finally, the impact on the performance of the indium content in  $\text{In}_x\text{Ga}_{1-x}\text{N}/\text{Si}$  tandem photoelectrodes was investigated by numerical simulations of electromagnetic wave propagation. A maximum theoretical photogeneration efficiency of 27 % was determined for  $\text{In}_x\text{Ga}_{1-x}\text{N}/\text{Si}$  tandem photoelectrodes with an indium content between 0.5 and 0.6. Then, Mott-Schottky analysis were performed to determine the doping concentration and the flatband potential of  $\text{In}_x\text{Ga}_{1-x}\text{N}$  photoanodes with varying indium content of 0.095, 0.165, 23.5, 33.3, and 41.4.  $I-V$  curves and IPCE spectra of these  $\text{In}_x\text{Ga}_{1-x}\text{N}$  photoanodes were measured and used with the software POPE to determine the diffusion optical number. The surface morphology has been shown to play a key role in the performance of these photoelectrodes. Finally,  $\text{In}_x\text{Ga}_{1-x}\text{N}$  photoanodes was found to be not highly performing even if nanostructured because of the high doping concentration, an issue that must be addressed in priority to improve its performance.

In conclusion, the methods developed in this work provide potential improvements of flat and structured photoelectrodes focused on charge generation, recombination, and transport, exemplified by flat GaN and  $\text{In}_x\text{Ga}_{1-x}\text{N}$  photoelectrodes and particle-based  $\text{LaTiO}_2\text{N}$  photoelectrodes. All the material parameters determined for these materials can be further used to investigate numerically the impact on the photoelectrode performance of novel mesostructures and particle arrangements. Furthermore, mesostructural guidelines and charge transport mechanism of particle-based  $\text{LaTiO}_2\text{N}$  photoelectrodes were provided and indicate that the design of efficient particle-based photoelectrodes should aim at densely packed single particle layers with internal nano-pores, or particles externally connected to the conductive substrate. Finally, the developed rapid method will help to identify if emerging photoelectrode materials should be nanostructured or if the synthesis method should be rather modified. This method can also be used to investigate degradation and explore charge transport mechanism under different concentrated solar irradiation.

**Keywords:** Photoelectrochemical water splitting, particles-based photoelectrodes, performance optimization, tunable bandgap, semiconductor-electrolyte interface, numerical and analytical model, coupled multi-physics model.

# Résumé

La fabrication de photoélectrodes à base de poudre par des procédés de revêtement ou de trempage, semblables à la fabrication à grande échelle d'électrodes pour batteries, est potentiellement un moyen de s'affranchir du piètre rapport coût-efficacité des dispositifs actuels de l'électrolyse de l'eau par photoélectrochimie. De nouvelles approches pour ce procédé de conversion photoélectrochimique telles que l'utilisation de photoélectrodes avec des mésostructures complexes à base d'oxydes de métaux stables dans l'eau, ou l'utilisation de semi-conducteurs avec une bande interdite variable pour permettre de hauts rendements, peuvent être économiquement plus compétitives. Cependant, il est fondamental de pouvoir identifier et quantifier les propriétés clés limitant l'efficacité de ces photoélectrodes afin de fournir des recommandations pour l'amélioration de ces dernières. Cette quantification étant expérimentalement limitée de par la nature multi-physique des processus qui se déroulent dans les photoélectrodes, une modélisation numérique est nécessaire. Néanmoins, la modélisation numérique des photoélectrodes nécessite la connaissance des différentes propriétés du matériau photoélectrochimique étudié, des propriétés souvent inconnues pour de nouveaux matériaux. De plus, cette modélisation nécessite de prendre en considération la mésostructure complexe de la photoélectrode, une tâche difficile à effectuer. Cette thèse propose divers modèles numériques qui permettent la caractérisation et l'optimisation de matériaux photoélectrochimiques. Ce travail de modélisation est accompagné d'un travail expérimental pour la détermination des propriétés physiques des matériaux étudiés et pour la validation des modèles. De plus, la grande diversité des modèles proposés dans cette thèse permet d'étudier une vaste catégorie de photoélectrodes allant des photoélectrodes nanostructurées à des photoélectrodes à base de poudres.

Afin de développer un modèle multi-physique fiable, prédictif et validé de photoélectrodes morphologiquement complexes, un modèle numérique d'une photoélectrode avec un matériau connu et une morphologie bien définie, une couche mince de GaN, a d'abord été développé. Ce modèle numérique, simulant des courbes de photocourant-tension ( $I-V$ ), combine la physique de propagation des ondes électromagnétiques, de génération et transport de porteurs de charges dans le semi-conducteur, et de transfert de charges à travers l'interface semi-conducteur-électrolyte. Ce modèle, validé en reproduisant les courbes  $I-V$  d'une photoélectrode plate à base de GaN, a ensuite été utilisé avec un plan factoriel fractionnaire afin de détecter l'élément principal limitant la performance de la photoélectrode. Cet élément s'avère être la recombinaison de surface à l'interface semi-conducteur-électrolyte pour des photoélectrodes plates à base de GaN.

Ce modèle a ensuite été appliqué à des photoélectrodes morphologiquement complexes à base de poudre d'oxynitride  $\text{LaTiO}_2\text{N}$ . Des mesures de spectrophotométrie UV-VIS-NIR, de nano-tomographie, de tension en circuit ouvert, de conductivité, ainsi que des analyses Mott-Schottky et des calculs par la théorie de la fonctionnelle de la densité ont permis de déterminer toutes les propriétés nécessaires à l'utilisation de ce modèle numérique reproduisant les courbes  $I-V$  expérimentales desdites photoélectrodes. L'impact des propriétés clés sur la performance a ensuite été étudié afin d'améliorer les performances de ces photoélectrodes. Puis, dans un deuxième temps, le mécanisme de transfert de charge entre les particules de ces photoélectrodes a été étudié. Différents mécanismes théoriques de transfert de charges interparticulaire potentiellement présents dans ces photoélectrodes ont été développés et inclus dans le modèle numérique. Les courbes  $I-V$  numériques fournies par le modèle ont ensuite été comparées aux courbes  $I-V$  expérimentales. Cette comparaison a permis de mettre en exergue le fait que les charges transférées par contact entre particules étaient négligeables. De plus, elle a permis de prouver que seules les particules en contact direct avec le substrat en oxyde d'étain hautement dopé au fluor contribuaient de façon significative au photocourant. Il est donc apparu évident qu'interconnecter les particules ne constitue pas une approche efficace pour les photoélectrodes à base de poudre.

Contrairement au cadre de modélisation très complexe mis au point pour les photoélectrodes plates de GaN et les photoélectrodes à base de poudre de  $\text{LaTiO}_2\text{N}$ , une méthode rapide et facile a été développée afin d'optimiser les performances de photoélectrodes. Cette méthode, capable de reproduire l'efficacité quantique d'une photoélectrode, fournit la longueur de diffusion des porteurs de charges minoritaires, les pertes liées à la réflexion de la lumière, ainsi que les pertes de

recombinaisons internes et surfaciques des photoélectrodes. De plus, un nouveau paramètre adimensionnel permettant de quantifier objectivement la performance des photoélectrodes, a été introduit et déterminé pour de nombreuses photoélectrodes avec des matériaux différents et des morphologies variables: des photoélectrodes plates d'oxyde de cuivre (I) ( $\text{Cu}_2\text{O}$ ), de silicium (Si), d'hématite ( $\text{Fe}_2\text{O}_3$ ), de vanadate de bismuth ( $\text{BiVO}_4$ ), d'oxyde de vanadium et de cuivre ( $\text{Cu}_2\text{V}_8\text{O}_3$ ), de delafossite ( $\text{CuFeO}_2$ ), des photoélectrodes nanostructurées de  $\text{Fe}_2\text{O}_3$  et des photoélectrode à base de poudre de  $\text{LaTiO}_2\text{N}$ . Ce paramètre, nommé à cet effet le nombre optique de diffusion, est le produit du coefficient d'absorption à 500 nm et de la longueur de diffusion. En comparant le nombre optique de diffusion des photoélectrodes plates et nanostructurées de  $\text{Fe}_2\text{O}_3$ , une valeur de référence a été définie pour déterminer si un matériau photoélectrochimique devrait être nanostructuré ou si sa méthode de synthèse devrait être modifiée. D'après cette valeur, seul Si est à haute performance sans être nanostructuré.  $\text{Cu}_2\text{O}$  et  $\text{LaTiO}_2\text{N}$  sont des matériaux photoélectrochimiques qui peuvent potentiellement être à haute performance s'ils sont nanostructurés. En revanche,  $\text{Fe}_2\text{O}_3$ ,  $\text{BiVO}_4$ ,  $\text{Cu}_2\text{V}_8\text{O}_3$ , et  $\text{CuFeO}_2$  ne sont pas des matériaux pouvant atteindre de haut rendement même si nanostructurés. Une modification de la méthode de synthèse est à privilégier pour ces derniers. Cette recherche a finalement abouti à un logiciel accessible gratuitement et facile d'utilisation, appelé POPE, afin de déterminer rapidement quels types de modification doivent être entrepris en priorité afin d'augmenter la performance de nouveaux matériaux photoélectrochimiques.

Finalement, l'impact de la teneur en indium sur la performance des photoélectrodes en tandem de  $\text{In}_x\text{Ga}_{1-x}\text{N}/\text{Si}$  a été étudié en simulant la propagation des ondes électromagnétiques. Une efficacité de photogénération maximale de 27 % a été théoriquement établie pour les photoélectrodes ayant une teneur en indium comprise entre 50 % et 60 %. Ensuite, une analyse Mott-Schottky a été effectuée afin de déterminer le potentiel de bande plate et la concentration en impuretés des photoanodes de  $\text{In}_x\text{Ga}_{1-x}\text{N}$  à teneur variable en indium, spécifiquement 9.5 %, 16.5 %, 23.5 %, 33.3 %, et 41.4 %. L'efficacité quantique de ces photoanodes a été mesurée et avec l'aide du logiciel POPE, le nombre optique de diffusion de ce matériau photoélectrochimique a été établie. Cette étude a permis de mettre en avant l'importance de l'état de surface dans la performance de ces photoélectrodes. De plus, elle a démontré que la méthode de synthèse du  $\text{In}_x\text{Ga}_{1-x}\text{N}$  doit être modifiée afin de diminuer la trop haute concentration d'impuretés qui affecte grandement la performance de ces photoélectrodes.

En conclusion, les méthodes développées dans ce travail fournissent des recommandations, basées sur la photogénération, la recombinaison et le transport de porteurs de charges, pour l'amélioration des performances de photoélectrodes plates et à morphologies complexes. Les photoélectrodes à base de poudre de  $\text{LaTiO}_2\text{N}$  sont caractérisées et optimisées en particulier.

En outre, les recommandations mésostructurelles et de transport de porteurs de charges majoritaires des photoélectrodes à base de poudre de  $\text{LaTiO}_2\text{N}$  permettent d'orienter la conception de photoélectrodes à haut rendement vers des photoélectrodes avec une seule couche de particules denses comportant des nanopores internes, et vers des particules reliées au substrat conducteur par un réseau à haute conductivité électrique. Enfin, la méthode basée sur l'efficacité quantique permet de rapidement évaluer les meilleures modifications à effectuer afin d'augmenter la performance de nouvelles photoélectrodes. De plus, cette méthode peut être utilisée pour étudier la dégradation et le mécanisme de transport de charge dans des photoélectrodes exposées à des intensités lumineuses variables.

**Mots clés :** Photosynthèse artificielle, électrolyse de l'eau par photoélectrochimie, photoélectrode à base de poudre, optimisation de la performance, bande interdite variable, interface semi-conducteur-électrolyte, modèle numérique et analytique, modèle multi-physique couplé.

# Table of contents

ACKNOWLEDGEMENTS.....	III
ABSTRACT .....	V
RÉSUMÉ .....	VIII
TABLE OF CONTENTS.....	XII
LIST OF FIGURES .....	XVI
LIST OF TABLES .....	XXIX
LIST OF SYMBOLS.....	XXX
INTRODUCTION.....	1
<b>1. UTILIZING MODELING, EXPERIMENTS, AND STATISTICS FOR THE ANALYSIS OF WATER-SPLITTING PHOTOELECTRODES .....</b>	<b>15</b>
1.1. INTRODUCTION.....	15
1.2. GOVERNING EQUATIONS AND METHODOLOGY .....	16
1.2.1. <i>Model domain and assumption</i> .....	16
1.2.2. <i>Governing equations</i> .....	18
1.2.3. <i>Boundary conditions</i> .....	22
1.2.4. <i>Numerical design of experiment</i> .....	27
1.3. APPLICATION TO GALLIUM NITRIDE.....	28
1.3.1. <i>Computational details</i> .....	28
1.3.2. <i>Material properties</i> .....	29
1.3.3. <i>Experimental details</i> .....	31
1.3.4. <i>Experimental parameter value estimation</i> .....	33
1.3.5. <i>Numerical model validation</i> .....	35
1.3.6. <i>Numerical design of experiment</i> .....	38
1.3.7. <i>Parametric analysis on key factors</i> .....	40
1.4. SUMMARY AND CONCLUSION.....	45
<b>2. DETERMINATION AND OPTIMIZATION OF MATERIAL PARAMETERS OF PARTICLE-BASED LATIO<sub>2</sub>N PHOTOELECTRODES.....</b>	<b>48</b>



2.1.	INTRODUCTION.....	48
2.2.	NUMERICAL <i>I-V</i> CURVE MODEL.....	51
2.2.1.	<i>Model domain and general assumptions .....</i>	51
2.2.2.	<i>Radiation absorption .....</i>	52
2.2.3.	<i>Charge transport and conservation .....</i>	54
2.3.	DETERMINATION OF MATERIAL PARAMETERS.....	56
2.3.1.	<i>Complex refractive index .....</i>	56
2.3.2.	<i>Density of states of the valence and conduction bands, and relative permittivity .....</i>	57
2.3.3.	<i>Flatband potential and doping concentration .....</i>	58
2.3.4.	<i>Electron and hole mobilities .....</i>	59
2.3.5.	<i>Electron and hole effective lifetimes and interfacial hole transfer velocity .....</i>	60
2.4.	EXPERIMENTAL SECTION .....	61
2.4.1.	<i>Photoelectrode preparation and characterization .....</i>	61
2.4.2.	<i>Photoelectrochemical measurements.....</i>	61
2.5.	RESULTS AND DISCUSSION .....	62
2.5.1.	<i>Determination of material parameters.....</i>	62
2.5.2.	<i>Identifying key material parameters .....</i>	71
2.5.3.	<i>Pathways to improved performance.....</i>	74
2.6.	CONCLUSION .....	76
<b>3.</b>	<b>MAJORITY CHARGE CARRIER TRANSPORT IN PARTICLE-BASED PHOTOELECTRODES.....</b>	<b>78</b>
3.1.	INTRODUCTION.....	78
3.2.	METHODOLOGY.....	81
3.2.1.	<i>Estimated thickness contributing to the photocurrent.....</i>	81
3.2.2.	<i>Theoretical inter-particle charge transfer mechanisms .....</i>	83
3.2.3.	<i>Expected impact of particle size on the photocurrent.....</i>	89
3.2.4.	<i>Photoelectrode preparation and characterization .....</i>	90
3.3.	RESULTS AND DISCUSSION .....	90
3.3.1.	<i>Thickness dependency of the front and back photocurrent .....</i>	90
3.3.2.	<i>Numerical inter-particle charge transfer mechanisms .....</i>	95
3.3.3.	<i>Impact of particle size on the photocurrent.....</i>	99
3.3.4.	<i>Design guidelines for particle-based photoelectrodes .....</i>	101
3.4.	CONCLUSION .....	104
<b>4.</b>	<b>RAPID PERFORMANCE OPTIMIZATION METHOD FOR PHOTOELECTRODES.....</b>	<b>106</b>
4.1.	INTRODUCTION.....	106
4.2.	METHODOLOGY.....	109
4.2.1.	<i>Definition of metrics .....</i>	109
4.2.2.	<i>Numerical determination of the IPCE .....</i>	111
4.2.3.	<i>Determination of the diffusion optical number and the ratio of currents .....</i>	113
4.2.4.	<i>Required material parameters .....</i>	117
4.2.5.	<i>Investigated photoelectrode materials.....</i>	118
4.2.6.	<i>Model limitations .....</i>	121
4.3.	RESULTS AND DISCUSSIONS.....	122

4.3.1.	<i>Model validation</i> .....	122
4.3.2.	<i>Diffusion lengths and diffusion optical numbers</i> .....	124
4.3.3.	<i>Pathways to photoelectrode improvements</i> .....	128
4.4.	CONCLUSION .....	136
<b>5.</b>	<b>THEORETICAL MAXIMUM EFFICIENCY AND PERFORMANCE CHARACTERIZATION OF <math>\text{In}_x\text{Ga}_{1-x}\text{N}/\text{Si}</math> TANDEM WATER-SPLITTING PHOTOELECTRODES</b> .....	<b>139</b>
5.1.	INTRODUCTION .....	139
5.2.	METHODOLOGY .....	140
5.2.1.	<i>Theoretical photogeneration efficiency of <math>\text{In}_x\text{Ga}_{1-x}\text{N}/\text{Si}</math> photoelectrodes</i> .....	140
5.2.2.	<i>Performance and characteristics of <math>\text{In}_x\text{Ga}_{1-x}\text{N}</math> photoelectrodes</i> .....	144
5.2.3.	<i>Experimental details</i> .....	145
5.3.	RESULTS AND DISCUSSION .....	147
5.3.1.	<i>Photogeneration efficiency of <math>\text{In}_x\text{Ga}_{1-x}\text{N}/\text{Si}</math> tandem photoelectrodes</i> .....	147
5.3.2.	<i>Performance characteristics of <math>\text{In}_x\text{Ga}_{1-x}\text{N}</math> photoelectrodes</i> .....	149
5.4.	CONCLUSION .....	154
	CONCLUSION .....	156
<b>A1.</b>	<b>APPENDIX OF CHAPTER 1</b> .....	<b>164</b>
A1.1.	NUMERICAL MODEL BOUNDARY CONDITIONS .....	164
A1.1.1.	<i>Majority current</i> .....	164
A1.2.	EXPERIMENTAL DETAILS .....	166
A1.3.	NUMERICAL MODEL – DETAILED RESULTS .....	168
A1.4.	PARAMETRIC ANALYSIS ON KEY FACTORS .....	171
<b>A2.</b>	<b>APPENDIX OF CHAPTER 2</b> .....	<b>172</b>
A2.1.	QUANTITATIVE STRUCTURAL ANALYSIS OF LTON PARTICLE-BASED PEs .....	172
A2.2.	SOLAR SIMULATOR CHARACTERISTICS .....	174
A2.3.	SOLAR OPEN-CIRCUIT VOLTAGE .....	175
A2.4.	ELECTROCHEMICAL IMPEDANCE SPECTROSCOPY .....	176
A2.5.	OPTICAL PARAMETERS .....	178
A2.6.	OPTICAL SIMULATIONS .....	179
A2.6.1.	<i>Computational details for photoabsorption model</i> .....	179
A2.6.2.	<i>Model validation by transmittance</i> .....	179
A2.7.	DFT CALCULATIONS .....	182
A2.7.1.	<i>DFT computational details</i> .....	182
A2.7.2.	<i>Electronic band structure</i> .....	182
A2.7.3.	<i>Full dielectric tensor</i> .....	183
A2.8.	SEMICONDUCTOR PHYSICS SIMULATIONS .....	184
A2.8.1.	<i>Computational details for charge transport and conservation</i> .....	184
A2.8.2.	<i>I-V curves for varying light intensity</i> .....	184
A2.8.3.	<i>Photoelectrode with the entire thickness being active</i> .....	185
A2.8.4.	<i>Electron mobility</i> .....	185
A2.8.5.	<i>Doping concentration</i> .....	186

A2.8.6.	Numerical I-V curves for bare-LTON .....	187
<b>A3.</b>	<b>APPENDIX OF CHAPTER 3 .....</b>	<b>189</b>
A3.1.	NUMERICAL INTER-PARTICLE CHARGE TRANSFER MECHANISMS .....	189
A3.2.	BEST-LTON PHOTOELECTRODES WITH 50 NM $\text{IrO}_x$ .....	189
<b>A4.</b>	<b>APPENDIX OF CHAPTER 4 .....</b>	<b>192</b>
A4.1.	DEVELOPMENT OF THE INTERNAL QUANTUM EFFICIENCY EQUATION .....	192
A4.2.	SENSITIVITY ANALYSIS .....	196
A4.2.1.	Complex refractive index.....	197
A4.2.2.	Flatband potential .....	198
A4.2.3.	Doping concentration.....	199
A4.2.4.	Relative permittivity.....	200
A4.2.5.	Photoelectrode thickness.....	201
A4.2.6.	Minority charge carrier mobility .....	202
A4.2.7.	Surface states distribution factor.....	203
A4.2.8.	Applied potential of the IPCE .....	204
A4.3.	PARTICLE-BASED $\text{LaTiO}_2\text{N}$ PHOTOELECTRODE.....	205
A4.3.1.	IPCE measurements.....	205
A4.3.2.	Complex refractive index.....	207
A4.4.	IPCE AT 500 NM AS A FUNCTION OF DOPING CONCENTRATION FOR Si .....	208
<b>A5.</b>	<b>APPENDIX OF CHAPTER 5 .....</b>	<b>210</b>
A5.1.	INDIUM CONTENT MEASUREMENTS OF $\text{In}_x\text{Ga}_{1-x}\text{N}$ .....	210
A5.2.	CONDUCTIVITY AND PHOTOCORROSION MEASUREMENTS OF THE PREPARED $\text{In}_x\text{Ga}_{1-x}\text{N}$ PHOTOELECTRODES.....	211
A5.3.	PHOTOGENERATION EFFICIENCY OF $\text{In}_x\text{Ga}_{1-x}\text{N}/\text{Si}$ TANDEM PHOTOELECTRODES. ....	213
A5.4.	MOTT-SCHOTTKY ANALYSIS .....	215
A5.5.	NUMERICAL AND EXPERIMENTAL IPCE .....	216
<b>A6.</b>	<b>APPENDIX: POPE MANUAL.....</b>	<b>218</b>
A6.1.	INSTRUCTIONS .....	218
A6.2.	DESCRIPTION OF THE RESULTS .....	219
	<b>BIBLIOGRAPHY.....</b>	<b>221</b>
	<b>CURRICULUM VITAE .....</b>	<b>244</b>

# List of figures

- Fig. I1. Schematic of a particle-based tandem PEC water splitting system in an acidic electrolyte. A zoom of the semiconductor-electrolyte interface with an energy band diagram for the n-type semiconductor is included..... 3
- Fig. I2. Schematic of the energy band diagrams of a n-type semiconductor-electrolyte interface under dark a) before the semiconductor and the electrolyte are in contact, b) at thermodynamic equilibrium without any interface states or Helmholtz layer formation (ideal case), c) at thermodynamic equilibrium with p-type interface states and a Helmholtz layer (real case), and d) under illumination with p-type interface states and a Helmholtz layer. The thicknesses of the band bending related to the interface states and the Helmholtz layer are exaggerated for clarity. The subscript “dark” stands for dark condition and “ill” for illuminated condition. .... 8
- Fig. I3. Qualitative spider chart example of key properties for photoelectrode materials: a) Si and b)  $\text{Fe}_2\text{O}_3$ . A value of 1 means an excellent property and 0 a poor property..... 11
- Fig. 1.1. Scheme of the model domain (not to scale) of the photoanode (GaN) immersed in electrolyte including the 2D EMW propagation model domain (dotted) and boundary conditions, and the 1D semiconductor model domain (red line). b) Detailed 1D semiconductor model domain and boundary conditions. .... 17
- Fig. 1.2. Illustration of a n-type semiconductor-electrolyte interface under dark (a) and illumination (b). The applied potential  $V_a$  is between the ohmic contact at the back of the photoelectrode and the reference electrode vs RHE. The subscript “dark” stands for dark condition and “ill” for illuminated condition. The applied potential in this illustration is the same

in the dark and illuminated conditions although it does not result in the same SCR. This situation is possible due to different flatband potentials in the dark and under illumination.....	24
Fig. 1.3. Photo of the GaN photoelectrode.....	31
Fig. 1.4. Scheme of the experimental PEC water-splitting test cell connected to the potentiostat. The UV LED illuminates the working electrode through air, quartz glass, and electrolyte.....	33
Fig. 1.5. a) Mott-Schottky plot for four frequencies (500 Hz, 1 kHz, 5 kHz, 10 kHz) of a 1 $\mu\text{m}$ -thick n-d-GaN sample immersed in 1M $\text{H}_2\text{SO}_4$ electrolyte under dark. b) Experimental dark current density (dashed line) and photocurrent density (solid line) vs RHE. ....	34
Fig. 1.6. Dark current densities (dashed lines) and photocurrent densities (solid lines) vs RHE, and comparison between experimentally measured values and numerically calculated values. ....	36
Fig. 1.7. Pareto plots indicating the significance of the photocurrent response at a potential of 1.23 $V_{\text{RHE}}$ (a) and 0.3 $V_{\text{RHE}}$ (b) vs RHE calculated utilizing the FFD of experiment. White bars indicate an increase and black bars a decrease, respectively, of the photocurrent when increasing the corresponding parameter. $\tau_{\text{eff},n}$ and $\tau_{\text{eff},p}$ are effective electron and hole lifetimes, $N_{\text{D}}^+$ is the doping concentration, and $\mu_p$ is the hole mobility, $V_{\text{FB}}$ , is the flatband potential, and $v_{s,p}$ is the hole surface transfer kinetic velocity. ....	40
Fig. 1.8. Photocurrent-voltage curves for varying hole surface lifetimes for the reference case (parameters indicated in Table 1.1 and Table 1.2. For large hole surface lifetimes (above 0.1 to 1 ns), surface recombination is negligible at large applied potentials. For small hole surface lifetimes (around 1 ps), the photocurrent is still affected by surface recombination at large potentials. ....	41
Fig. 1.9. Photocurrent density at 1.23 $V_{\text{RHE}}$ as a function of the hole surface lifetime for various electron lifetimes ( $\tau_{s,n} = 10^{-9}, 10^{-10}, 10^{-11}, 10^{-12}, 10^{-13}$ s) and two doping concentrations ( $N_{\text{D}}^+ = 10^{16} \text{ cm}^{-3}$ and $N_{\text{D}}^+ = 10^{18} \text{ cm}^{-3}$ ).....	43
Fig. 1.10. Photocurrent-voltage curves for varying doping concentration for the reference case (parameters indicated in Table 1.1 and Table 1.2. For small doping concentrations (below $10^{14} \text{ cm}^{-3}$ ), the photocurrent-potential relation is linear. For intermediate doping concentrations (around $10^{16} \text{ cm}^{-3}$ ), the photocurrent shows an optimum at which the band bending is maximized and recombination is reasonable. At large doping concentrations (above $10^{18} \text{ cm}^{-3}$ ) recombination dominates. ....	44

## List of figures

---

- Fig. 1.11. Photocurrent density at 0.3 V<sub>RHE</sub> as a function of the hole surface lifetime for various electron lifetimes ( $\tau_{s,n} = 10^{-9}, 10^{-10}, 10^{-11}, 10^{-12}, 10^{-13}$  s) and two flatband potentials: a)  $V_{FB} = -0.5$  V<sub>RHE</sub>, and b)  $V_{FB} = -0.7$  V<sub>RHE</sub>. ..... 45
- Fig. 2.1. a) Scanning electron microscopy picture of a LTON particle-based PE and indication of the domain sizes used for the numerical model (yellow for the EMW simulations, blue for the semiconductor physics simulations), b) EMW propagation model domain and boundary conditions, and c) semiconductor physics model domain and boundary conditions. The generation rate calculated with model b) is used as an input in model c). ..... 54
- Fig. 2.2. Complex refractive index of LTON particle-based PE using reflectance and transmittance measurements with an integrating sphere. The refractive index (left y-axis) is calculated using Fresnel's equation (eqn (2.1)) in conjunction with total reflectance measurements. The extinction coefficient (right y-axis) is determined using reflectance and transmittance measurements in conjunction with eqn (2.5) derived by considering multiple internal reflections in a single, partially transmitting thick layer ( $D > \lambda$ ). ..... 63
- Fig. 2.3. Generation rate of LTON particle-based PEs under back- and front-side illumination with the AM1.5G solar simulator's spectral irradiance. The integrated photogenerated current density is indicated for PEs of thickness 1.42  $\mu\text{m}$  (dashed line) and 8.43  $\mu\text{m}$ . ..... 64
- Fig. 2.4. Frequency-independent Mott-Schottky plots for best-LTON photoelectrodes with the determined doping concentration. The equivalent circuit for the electrochemical impedance analysis is also indicated. ..... 66
- Fig. 2.5. Numerical and experimental photocurrent-voltage curves of best-LTON under a) back- and b) front-side illumination for varying effective electron lifetimes. The photocurrent density was reduced from 1.18 mA cm<sup>-2</sup> to 0.63 mA cm<sup>-2</sup> at 1.23 V<sub>RHE</sub> when reducing the effective electron lifetime by four orders of magnitude under back-side illumination (from 10 ns to 1 ps). Under front-side illumination, the photocurrent density was reduced from 0.55 mA cm<sup>-2</sup> to 0.34 mA cm<sup>-2</sup> at 1.23 V<sub>RHE</sub> when reducing the effective electron lifetime by four orders of magnitude. ..... 67
- Fig. 2.6. Numerical and experimental photocurrent-voltage curves of best-LTON under a) back- and b) front-side illumination for varying effective hole lifetimes. The photocurrent density was reduced from 1.01 mA cm<sup>-2</sup> to 0.37 mA cm<sup>-2</sup> at 1.23 V<sub>RHE</sub> when reducing the effective hole lifetime by four orders of magnitude under back-side illumination (from 10 ns to 1

- ps). Under front-side illumination, the photocurrent density was reduced from  $0.68 \text{ mA cm}^{-2}$  to  $0.11 \text{ mA cm}^{-2}$  at  $1.23 \text{ V}_{\text{RHE}}$  when reducing the effective hole lifetime by four orders of magnitude. .... 69
- Fig. 2.7. Numerical and experimental photocurrent-voltage curves of best-LTON PEs under a) back- and b) front-side illumination for varying interfacial hole transfer velocities. The hole transfer velocity was significantly affecting the photocurrent under back-side illumination: a photocurrent of  $3.48 \text{ mA cm}^{-2}$  at  $1.23 \text{ V}_{\text{RHE}}$  with  $\nu_{s,p}=1\cdot 10^{-4} \text{ cm s}^{-1}$  and of  $1.01 \text{ mA cm}^{-2}$  with  $\nu_{s,p}=3.5\cdot 10^{-6} \text{ cm s}^{-1}$ . Under front-side illumination, the hole transfer velocity was less affecting the photocurrent since the photocurrent reached almost saturation at  $1.23 \text{ V}_{\text{RHE}}$  with  $\nu_{s,p}=3.5\cdot 10^{-6} \text{ cm s}^{-1}$ , a photocurrent density of  $0.61 \text{ mA cm}^{-2}$  at  $1.23 \text{ V}_{\text{RHE}}$  with  $\nu_{s,p}=1\cdot 10^{-4} \text{ cm s}^{-1}$  and of  $0.54 \text{ mA cm}^{-2}$  for  $\nu_{s,p}=3.5\cdot 10^{-6} \text{ cm s}^{-1}$ . .... 70
- Fig. 2.8. Numerical and experimental photocurrent-voltage curves of best-LTON under a) back- and b) front-side illumination for varying hole mobilities. The photocurrent density was reduced from  $1.02 \text{ mA cm}^{-2}$  to  $0.37 \text{ mA cm}^{-2}$  at  $1.23 \text{ V}_{\text{RHE}}$  when reducing the hole mobility from  $500 \text{ cm}^2 \text{ V}^{-1} \text{ s}^{-1}$  to  $0.01 \text{ cm}^2 \text{ V}^{-1} \text{ s}^{-1}$ . Under front-side illumination, the photocurrent density was reduced from  $0.59 \text{ mA cm}^{-2}$  to  $0.07 \text{ mA cm}^{-2}$  at  $1.23 \text{ V}_{\text{RHE}}$  when reducing the hole mobility from  $500 \text{ cm}^2 \text{ V}^{-1} \text{ s}^{-1}$  to  $0.01 \text{ cm}^2 \text{ V}^{-1} \text{ s}^{-1}$ . .... 73
- Fig. 2.9. Numerical and experimental photocurrent-voltage curves of best-LTON under back-side illumination for effective lifetime and interfacial hole transfer velocity optimization (blue line) and for additionally doping concentration optimization (red line). The current IPCE is 3 % (black or green line) and is improved to 9 % (blue line) by only improving the effective lifetimes of hole and electron from 0.5 ns to 1 ns and the interfacial hole transfer velocity from  $3.5\cdot 10^{-6} \text{ cm s}^{-1}$  to  $1\cdot 10^{-4} \text{ cm s}^{-1}$ . The IPCE can be further improved to an IPCE of 10 % by reducing the doping concentration from  $7.43\cdot 10^{17} \text{ cm}^{-3}$  to  $1\cdot 10^{16} \text{ cm}^{-3}$ . The onset potential can be reduced to  $0.1 \text{ V}_{\text{RHE}}$  by increasing the interfacial hole transfer velocity to  $100 \text{ cm s}^{-1}$  (red dashed line). .... 76
- Fig. 3.1. a) SEM of LTON PBPEs, b) schematic of electron and hole generation and transport in LTON particles, c) simplified morphology model considering case 1: only the first layer of particles contributes to the photocurrent, case 2: quasi-Fermi level continuity between the particles, and case 3: particles in “pseudo-series” with computational domain dimensions. d) Details about each case with a scheme of the corresponding energy band diagram. .... 88

## List of figures

---

- Fig. 3.2. Experimental front- and back-side illumination photocurrent densities at 1.23 V<sub>RHE</sub> and averaged thicknesses of the PBPE depending on the electrophoretic deposition time for bare-LTON PBPEs. Dashed curves indicate the numerical fit curves with their corresponding goodness of fit ( $R^2$ ). ..... 92
- Fig. 3.3. Thickness-dependent generation rate and photogenerated current of a LTON PBPE with a thickness of 5  $\mu\text{m}$ , calculated by eqns (3.2) and (3.3) (Beer-Lambert law). The opaque colors are for case 1 considering a single layer of particles (1.42  $\mu\text{m}$ ) contributing to the photogenerated current (Fig. 3.1). The semitransparent colors are for case 2 with the full thickness of the PBPE (5  $\mu\text{m}$ ) contributing to the photogenerated current (Fig. 3.1). Red color indicate front-side illumination and black colors back-side illumination. .... 93
- Fig. 3.4. Experimental photocurrent ratio 1.23 V<sub>RHE</sub> and numerical photogenerated current ratio ( $\hat{q}_{\text{front/back}} < 1$ ) depending on the total averaged thickness of bare-LTON PBPEs. The fitting exponential curves are depicted with dashed lines. The fitting curve for the experimental ratio is given by  $1.13 \cdot e^{0.352 \cdot d}$  ( $R^2=0.91$ ). Case 1, with a current-contributing thickness of 1.42  $\mu\text{m}$  out of the total averaged thickness, has a fitting curve given by  $1.97 \cdot e^{-0.405 \cdot d}$  ( $R^2=1$ ). Case 1, with only a current-contributing thickness of 0.45  $\mu\text{m}$ , has a fitting curve given by  $1.32 \cdot e^{-0.403 \cdot d}$  ( $R^2=1$ ). Case 2, with the full height contributing to the photogenerated current, has a constant fitting curve of 1.11 ( $R^2=1$ ). Case 3, with only a contributing thickness of 2.82  $\mu\text{m}$  (two times an averaged particle height), has a fitting curve given by  $2.67 \cdot e^{-0.338 \cdot d}$  ( $R^2=0.95$ ). ..... 95
- Fig. 3.5. Experimental  $I-V$  curves of best-LTON PBPEs with an average film thickness of 8.43  $\mu\text{m}$  taken from Gaudy et al.[160]. The corresponding numerical  $I-V$  curves obtained with the advanced 2D multi-physics PBPE model with assumed inter-particle charge transfer of a) case 1, b) case 2 with linear potential drop and infinite inter-particle mobility (situation  $i$ ), c) case 2 without potential drop and infinite inter-particle mobility (situation  $ii$ ), and d) case 2 without potential drop but mobility drops (type I and II). ..... 97
- Fig. 3.6. Experimental  $I-V$  curves of best-LTON PBPE with an average film thickness of 8.43  $\mu\text{m}$  taken from Gaudy et al.[160]. The corresponding numerical  $I-V$  curves of case 3) for varying inter-particle contact hole velocities under a) back-side illumination and c) front-side illumination, and the corresponding contribution of the 2<sup>nd</sup> particle on the right side in b) and d). ..... 99



Fig. 3.7. Generation rate and photogenerated current density under back-side illumination for small LTON (PC-LTON) and large LTON (SS-LTON) PBPEs. ....	101
Fig. 3.8. Schemes of particulate photoabsorber water-splitting systems: a) PBPE with inter-particle contacts and b) PBPE with a conductive network.....	103
Fig. 4.1. Flowchart of the numerical IPCE analysis used to determine the diffusion length and the surface recombination velocity from which reflection, bulk and surface recombination losses are determined. The ratio of currents, the diffusion optical numbers, the nanostructuring opportunity factor, and the doping concentration that maximize the IPCE are also determined. The inputs are the measured IPCE (at least at two wavelengths, for a given applied potential), the bandgap, the spectral complex refractive index, the flatband potential, the fully ionized acceptor/donor doping concentration, the permittivity, and the electrode thickness. The surface state distribution factor, the minority charge carrier mobility, and the surface charge transfer coefficient were assumed (section 4.2.4). ....	115
Fig. 4.2. Numerical IQE of a planar p-Si photoelectrode of 1 mm thickness at 1 $V_{RHE}$ for varying a) diffusion lengths and b) ratios of currents. In a), the surface recombination velocity is fixed to zero and in b) the diffusion length is fixed to infinite and the surface charge transfer to $10^{-2} \text{ cm s}^{-1}$ . The ratios of currents at 1 $V_{RHE}$ in b) were obtained by varying $S_{R,0}$ from 0, 10, 100, 1000, and $10^4 \text{ cm s}^{-1}$ .....	116
Fig. 4.3. $R^2$ of the numerical-experimental IPCE fitting at 0 $V_{RHE}$ depending on diffusion length and the ratio of currents for p-Cu <sub>2</sub> O photocathode covered by Ga <sub>2</sub> O <sub>3</sub> /TiO <sub>2</sub> /RuO <sub>x</sub> [168]. $L$ and $S_{R,0}$ were varied with 50 points per decade from $10^{-0.5}$ to $10^{1.5} \mu\text{m}$ for $L$ and $10^{-2}$ to $10^3 \text{ cm s}^{-1}$ for $S_{R,0}$ . ....	123
Fig. 4.4. Numerical and experimental IPCE at 0 $V_{RHE}$ for a planar p-Cu <sub>2</sub> O photocathode covered by a Ga <sub>2</sub> O <sub>3</sub> /TiO <sub>2</sub> /RuO <sub>x</sub> layer with the internal losses (grey), the reflection loss (blue), the surface recombination loss (red), and the numerical IPCE (green). The numerical IPCE was fitted to the experimental IPCE from Niu et al.[168] (black dots).....	124
Fig. 4.5. Diffusion lengths of all water-splitting photoelectrode materials investigated in this work. The black error bars are the variation in the diffusion length due to variations in the input material parameters (see Table 4.1) and the black dots are the nominal values. The red error bars are the variation in the diffusion lengths reported in literature. The green lines indicate the diffusion lengths for which the IQE without surface recombination is	

above 95 % at 500 nm,  $L_{0.95}$  (eqn (4.4)). The diffusion lengths of  $\text{Cu}_2\text{O}$  reported from literature vary from 1  $\mu\text{m}$  to 4  $\mu\text{m}$ [179]. The calculated diffusion length of Si varies from 7  $\mu\text{m}$  to 467  $\mu\text{m}$ [193] using a p-Si photoelectrode with a resistivity of 0.01-1  $\Omega\text{ cm}$ [184] and a doping concentration of  $8 \times 10^{18}$ - $1.5 \times 10^{16}\text{ cm}^{-3}$ [192]. The diffusion lengths of  $\text{Fe}_2\text{O}_3$  reported from literature are 2, 3, 4, 10 nm[177], and 20 nm[205]. The diffusion lengths of  $\text{BiVO}_4$  reported from literature are 20 nm[178]), 45 nm[206], 70 nm[207], and 100 nm[208]. The reported diffusion length of  $\text{CuFeO}_2$  is 225 nm[204]. The diffusion length of p-b.  $\text{LaTiO}_2\text{N}$  photoelectrode is 280 nm[160]. .....127

Fig. 4.6. Diffusion optical numbers,  $\alpha_{500}L$ , of various photoelectrode materials and nanostructures. The green lines indicate the  $\alpha_{500}L_{0.95}$  for which the IQE without surface recombination is above 95 % at 500 nm (eqn (4.4)). The red lines indicate the minimum  $\alpha_{500}L$  for which a photoelectrode can perform very well when nanostructured (eqn (4.5)), i.e. an  $\alpha_{500}L$  (black lines) below the red line indicates a photoelectrode with low performance even when nanostructured. The black dots are the determined nominal values, the error bars are due to the variations in the input parameters (according to Table 4.1). .....128

Fig. 4.7. Numerical and experimental IPCE for water splitting a) planar p-Si photocathode covered by a mesoporous layer of hematite[184], b) planar n- $\text{Fe}_2\text{O}_3$  photoanode[23], c) planar n- $\text{Fe}_2\text{O}_3$  photoanode[23], d) planar n- $\text{BiVO}_4$  photoanode[185], e) planar n- $\text{Cu}_3\text{V}_2\text{O}_8$  photoanode[173], f) planar n- $\text{CuFeO}_2$  photoanode[200], g) nanorods n- $\text{Fe}_2\text{O}_3$  photoanode without co-catalyst, h) nanorods n- $\text{Fe}_2\text{O}_3$  photoanode with  $\text{CoB}_i$  co-catalyst [187], and p-b.  $\text{LaTiO}_2\text{N}$  photoanodes using complex refractive index from i) DFT calculations (Fig. A4.6) and from j) Gaudy et al.[160]and our experimental IPCE measurements (Fig. A4.5). The applied potential of the IPCE,  $V_{\text{IPCE}}$ , and the  $R^2$  of the IPCE fitting are also indicated. ....133

Fig. 4.8. Calculated IPCE at 500 nm as a function of the doping concentration for the p- $\text{Cu}_2\text{O}$  photocathode covered by  $\text{Ga}_2\text{O}_3/\text{TiO}_2/\text{RuO}_x$ [168] with a fixed diffusion length of 1  $\mu\text{m}$  (Table 4.2). A maximum IPCE at 500 nm of 0.78 is obtained at an acceptor doping concentration of  $1.0 \times 10^{15}\text{ cm}^{-3}$ . .....135

Fig. 5.1. Scheme of the numerical 2D EMW propagation model domain for an  $\text{In}_x\text{Ga}_{1-x}\text{N}/\text{Si}$  tandem water-splitting photoelectrode (not to scale). ....141

Fig. 5.2. a) Spectral refractive index and b) extinction coefficient of  $\text{In}_x\text{Ga}_{1-x}\text{N}$  interpolated from the data of Hazari et al.[221]. .....143

Fig. 5.3. Image of the prepared $\text{In}_x\text{Ga}_{1-x}\text{N}$ photoelectrodes. The different copper wire colors corresponds to the different indium content: yellow for $x=9.5$ %, red for $x=16.5$ %, green for $x=23.5$ %, blue for $x=33.3$ %, and black for $x=41.4$ % as given in Table 5.1.....	146
Fig. 5.4. Top and cross-sectional view scanning electron microscopy images of: (a), b)) $\text{In}_x\text{Ga}_{1-x}\text{N}$ with $x=9.5$ %; (c), d)) $\text{In}_x\text{Ga}_{1-x}\text{N}$ with $x=16.5$ %; (e), f)) $\text{In}_x\text{Ga}_{1-x}\text{N}$ with $x=23.5$ %; (g), h)) $\text{In}_x\text{Ga}_{1-x}\text{N}$ with $x=33.3$ %; (e), f)) $\text{In}_x\text{Ga}_{1-x}\text{N}$ with $x=41.4$ %.....	146
Fig. 5.5. Photogeneration efficiency of $\text{In}_x\text{Ga}_{1-x}\text{N}/\text{Si}$ tandem water-splitting photoelectrode depending on film thickness and bandgap a) with and b) without reflection loss at the $\text{In}_x\text{Ga}_{1-x}\text{N}/\text{water}$ interface.....	148
Fig. 5.6. Photocurrent–voltage curves of $\text{In}_x\text{Ga}_{1-x}\text{N}$ photoelectrodes with chopped light in a) 1 M $\text{H}_2\text{SO}_4$ and b) 1 M $\text{Na}_2\text{SO}_4$ .....	150
Fig. 5.7. Flatband potential and doping concentration of $\text{In}_x\text{Ga}_{1-x}\text{N}$ water-splitting photoelectrodes determined by Mott–Schottky plots (A5.4). The equivalent circuit for the electrochemical impedance spectra fit is also indicated.....	151
Fig. 5.8. Diffusion optical number ( $y_1$ -axis) and the ratio of current ( $y_2$ -axis) of $\text{In}_x\text{Ga}_{1-x}\text{N}$ photoelectrodes in function of the bandgap (indium content). The dot colors corresponds to the indium content according to Table 5.1 and Fig. 5.3.....	154
Fig. C1. Energy band diagram of a n-type semiconductor with p-type surface states including the different current paths at the semiconductor-electrolyte interface: 1) direct hole transfer 2) direct electron transfer 3) surface state mediated hole transfer 4) surface state mediated electron transfer 5) space charge tunneling hole transfer 6) space charge tunneling electron transfer. $R_{\text{bulk}}$ stands for bulk recombination, $R_{\text{SC}}$ for SCR recombination, and $R_{\text{SS}}$ for surface states recombination. ....	160
Fig. A1.1. Spectral irradiance of the UV LED used for the experimental measurements. Only the part of the LED spectrum below 365.6 nm is actually absorbed by GaN (dashed line).....	167
Fig. A1.2. Current density versus time during linear sweep voltammetry. Potential sweep from 1.7 $V_{\text{RHE}}$ to -0.8 $V_{\text{RHE}}$ . The dashed line indicates the current density at $t = 0$ .....	167
Fig. A1.3. Numerical results of the electron-hole pair generation rate inside the semiconductor. The right side at 0 $\mu\text{m}$ is the illuminated side with the	

## List of figures

---

semiconductor-electrolyte interface and the left side at 1 $\mu\text{m}$ is the ohmic back contact (according to Fig. 1.1).	168
Fig. A1.4. Numerical results of the electron (blue line) and hole (red line) concentration at 0 $V_{\text{RHE}}$ inside the semiconductor. The right side at 0 $\mu\text{m}$ is the illuminated side with the semiconductor-electrolyte interface and the left side at 1 $\mu\text{m}$ is the back ohmic contact (according to Fig. 1.1).	169
Fig. A1.5. Numerical results of the band potential diagram at 0 $V_{\text{RHE}}$ with conduction band (red line), valence band (blue line), electron and hole quasi-Fermi potential (dashed and dotted lines respectively) inside the semiconductor. The right side at 0 $\mu\text{m}$ is the illuminated side with the semiconductor-electrolyte interface and the left side at 1 $\mu\text{m}$ is the back ohmic contact (according to Fig. 1.1).	170
Fig. A1.6. Photocurrent density at 1.23 $V_{\text{RHE}}$ as a function of the doping concentration for various hole surface lifetimes ( $\tau_{\text{sp}} = 10^{-9}, 10^{-10}, 10^{-11}, 10^{-12}, 10^{-13}$ s) and an electron surface lifetime of 1 ps. An optimum doping concentration appeared at $1 \cdot 10^{16} \text{ cm}^{-3}$ .	171
Fig. A1.7. Photocurrent-voltage curves for varying flatband potentials for the reference case (parameters indicated in Table 1.1 and Table 1.2).	171
Fig. A2.1. Size distribution of the three ellipsoid diameters based on lognormal distributions: $d_{\text{s,mean}}=272 \text{ nm}$ , $d_{\text{s,SD}}=88 \text{ nm}$ ; $d_{\text{t,mean}}=932 \text{ nm}$ , $d_{\text{t,SD}}=427 \text{ nm}$ ; $d_{\text{l,mean}}=1789 \text{ nm}$ , $d_{\text{l,SD}}=773 \text{ nm}$ .	173
Fig. A2.2. Particle orientation determined by the direction of the longest diameter. Elevation angle=90°: particle lies flat relative to the FTO, and elevation angle=0°: particle stands upright relative to the FTO. The scatter plot demonstrates no trend of particle orientation as a function of z-position; however, normal vectors of the particles were elevated most frequently by 10° or 45°, as shown in the frequency distribution.	173
Fig. A2.3. Normalized density profile of LTON photoelectrodes electrophoretically deposited on a FTO substrate.	174
Fig. A2.4. Spectral irradiance of the Verasol-2 LED class AAA solar simulator from Newport and the reference spectral irradiance AM1.5G.	175
Fig. A2.5. Variation of the open-circuit potential under periodic light chopping of 10s for a) bare-LTON and b) best-LTON photoelectrodes immersed in 0.1 M $\text{NaSO}_4$ and $\text{NaOH}$ (pH=13.2) under back- (blue) and front-side (red) illumination. The OCV increased by adding a co-catalyst, i.e. the	

OCV of bare-LTON was 0.01 V under back-side illumination while it was 0.25 V for best-LTON.....	176
Fig. A2.6. Mott-Schottky plot for three frequencies (100Hz, 500Hz, 1kHz) of best-LTON electrodes immersed in 0.1 M NaSO <sub>4</sub> and NaOH (pH=13.2) under dark conditions. ....	177
Fig. A2.7. Experimental and simulated impedance spectra of best-LTON photoelectrodes at 0.12 V <sub>RHE</sub> immersed in 0.1 M NaSO <sub>4</sub> and NaOH (pH=13.2) under dark conditions. The electrical impedances at 0.12 V <sub>RHE</sub> are R <sub>s</sub> =25.43 Ω, R <sub>sc</sub> =6.228 Ω, Y <sub>0,sc</sub> =2.221·10 <sup>-5</sup> F s <sup>α-1</sup> with α <sub>sc</sub> =0.96, R <sub>ss</sub> =347.7 Ω and Y <sub>0,ss</sub> =8.182·10 <sup>-4</sup> F s <sup>α-1</sup> with α <sub>ss</sub> =0.65.....	177
Fig. A2.8. Direct bandgap Tauc plot of LTON particle-based PEs based on the calculated absorption coefficient, eqn (2.5). The direct bandgap is found to be 1.9 eV according to the linear interpolation (dashed black line). If the plot is corrected for the constant absorption of light scattering, the estimated bandgap is 2.1 eV (crossing of red and black dashed lines).178	
Fig. A2.9. Direct bandgap Tauc plot of LTON particle-based PEs based on K-M transform. The direct bandgap is found to be 2.1 eV according to the linear interpolation (dashed black line).....	179
Fig. A2.10. Complex refractive index of bare glass of 2.2 μm for TCO22-15 transparent conductive layer of Solaronix.....	180
Fig. A2.11. Complex refractive index of SnO <sub>2</sub> layer of 360 nm for TCO22-15 transparent conductive layer of Solaronix.....	180
Fig. A2.12. Measured and calculated transmittance of LTON particle-based photoelectrode under a) back- and b) front-side illumination. Transmittance is calculated with an EMW propagation model each 10 nm and a cubic spline interpolation is used for smoothing. The numerical transmittance is below 2 % error compared to the measured transmittance from 400 nm to 590 nm (2.1 eV, band gap of LTON). The experimental variation is obtained by measuring four different LTON photoelectrodes.....	181
Fig. A2.13. Measured and calculated transmittance of LTON particle-based photoelectrodes under a) back- and b) front-side illumination. Transmittance is calculated using Beer-Lambert's law and is below 2% error compared to the measured transmittance in the spectral range of 400 nm to 590 nm (2.1 eV, band gap of LTON). The experimental variation is obtained by measuring four different LTON photoelectrodes. ....	182

## List of figures

---

Fig. A2.14. Electronic band structure of orthorhombic $\text{LaTiO}_2\text{N}$ along high-symmetry lines of the Brillouin zone. ....	183
Fig. A2.15. Numerical (dashed lines) and experimental (solid lines) photocurrent-voltage curves of best-LTON photoelectrode under back-side illumination for varying light intensities (1, 0.1, and 0.01 sun). ....	184
Fig. A2.16. Numerical and experimental photocurrent-voltage curves of best-LTON PEs with entire thickness (8.43 $\mu\text{m}$ ) being active (no potential loss along the thickness of the PE) and only the first single particle's layer (1.42 $\mu\text{m}$ ) being active under back- and front-side illumination. ....	185
Fig. A2.17. Numerical and experimental photocurrent-voltage curves of best-LTON PEs under a) back- and b) front-side illumination for varying electron mobilities. ....	186
Fig. A2.18. Numerical photocurrent-voltage curves of best-LTON PEs under a) back- and b) front-side illumination for varying doping concentration. ....	187
Fig. A2.19. Numerical and experimental photocurrent-voltage curves of bare-LTON under back- and front-side illumination. ....	188
Fig. A3.1. Experimental $I$ - $V$ curves of best-LTON PBPE with an average film thickness of 8.43 $\mu\text{m}$ taken from Gaudy et al.[160]. The corresponding numerical $I$ - $V$ curves of case 3) for varying inter-particle contact electron velocities under a) back-side illumination and c) front-side illumination, and the corresponding contribution of the 2 <sup>nd</sup> particle on the right side in b) and d). ....	190
Fig. A3.2. Experimental I-V curves of best-LTON PE with and without a 50 nm layer of $\text{IrO}_x$ in 0.1 M $\text{Na}_2\text{SO}_4$ at $\text{pH}=13.0\pm0.2$ by adding NaOH. ....	191
Fig. A4.1. Schematic of the band diagram for an n-type semiconductor photoanode in contact with an electrolyte. ....	192
Fig. A4.2. Experimental spectral IPCE at 1.46 VRHE (black dotted) and numerical IPCE (green), surface recombination loss (red), reflection loss (blue) and bulk loss (grey), for planar n- $\text{Fe}_2\text{O}_3$ photoanodes[23] with the complex refractive index from a) Query[183] and b) Longtin et al.[182]. The numerical IPCE was fitted to the experimental IPCE from Yan et al.[23] and the optimized fitting resulted in R2 of a) 0.567 and b) 0.964. The determined diffusion lengths are a) 8.3 nm and b) 9.1 nm. ....	198
Fig. A4.3. Normalized numerical $I$ - $V$ curves of p- $\text{Cu}_2\text{O}$ photocathode for varying surface states distribution factor (eqn (4.9)). The numerical normalization is the $I$ - $V$ curves under AM1.5G divided by the photocurrent at -0.2 $\text{V}_{\text{RHE}}$ .	

	The experimental $I-V$ curve of p-Cu <sub>2</sub> O photocathode was taken from Niu et al.[168] under AM1.5G and normalized by the photocurrent density of -6.63 mA cm <sup>-2</sup> obtained at -0.2 V <sub>RHE</sub> . ....	204
Fig. A4.4.	Numerical and experimental IPCE at a) 1.21 V <sub>RHE</sub> and b) 1.71 V <sub>RHE</sub> for a planar n- Cu <sub>2</sub> V <sub>8</sub> O <sub>3</sub> photoanode with the bulk loss (grey), the reflection loss (blue), the surface recombination loss (red), and the numerical IPCE (green). The numerical IPCE was fitted to the experimental IPCE from Segev et al.[173] (black dots).....	205
Fig. A4.5.	IPCE of p.-b. LaTiO <sub>2</sub> N photoanodes at 1.23 V <sub>RHE</sub> under back illumination in 0.1 M Na <sub>2</sub> SO <sub>4</sub> (pH 13 by adding NaOH). The dot points are the average IPCE of four fresh photoelectrodes and the error bars are the IPCE measurement variations. ....	206
Fig. A4.6.	Spectral a) real part of the complex refractive index and b) imaginary part of the complex refractive index of LaTiO <sub>2</sub> N in $x$ , $y$ and $z$ directions and the mean in all directions calculated by DFPT. ....	208
Fig. A4.7.	Calculated IPCE at 500 nm as a function of the doping concentration for a planar p-Si photocathode covered by a ~80nm mesoporous hematite layer[184] with a) a fixed diffusion length of 50 $\mu$ m and b) a diffusion length as a function of the doping concentration. The relation of the diffusion length as a function of the doping concentration is given on the right y-axis of figure b).....	209
Fig. A5.1.	X-ray diffraction spectra and indium contents in percentage of the fabricated In <sub>x</sub> Ga <sub>1-x</sub> N photoelectrodes. ....	210
Fig. A5.2.	Photocurrent density over 24 hours of pure GaN photoelectrodes at 1.23V <sub>RHE</sub> in 1 M, 0.1 M and 0.01 M H <sub>2</sub> SO <sub>4</sub> under UV light with a nominal wavelength at 368 nm and an irradiance of 9.9 mW cm <sup>-2</sup> .....	212
Fig. A5.3.	Cyclic voltammograms of GaN photoelectrode in 1 M, 0.1 M and 0.01 M H <sub>2</sub> SO <sub>4</sub> under UV light with a nominal wavelength at 368 nm and an irradiance of 9.9 mW cm <sup>-2</sup> . ....	212
Fig. A5.4.	Photogeneration efficiency of In <sub>x</sub> Ga <sub>1-x</sub> N/Si tandem water-splitting photoelectrode depending on film thickness and indium a) with and b) without reflection loss at the In <sub>x</sub> Ga <sub>1-x</sub> N/water interface.....	213
Fig. A5.5.	Generation rate along the In <sub>x</sub> Ga <sub>1-x</sub> N thickness of In <sub>x</sub> Ga <sub>1-x</sub> N/Si tandem water-splitting photoelectrode for varying bandgap and a thickness of a) 200 nm and b) 1000 nm.....	214

## List of figures

---

- Fig. A5.6. Photogeneration efficiency of ultrathin  $\text{In}_x\text{Ga}_{1-x}\text{N}$  film on  $350\text{ }\mu\text{m}$  Si layer as water-splitting photoelectrode depending on film thickness and bandgap with reflection loss at the  $\text{In}_x\text{Ga}_{1-x}\text{N}$ /water interface. ....214
- Fig. A5.7. Experimental and simulated impedance spectra of  $\text{In}_{0.414}\text{Ga}_{0.586}\text{N}$  photoelectrodes under dark conditions in  $1\text{ M H}_2\text{SO}_4$  at  $0.4\text{ V}_{\text{RHE}}$  and  $-0.6\text{ V}_{\text{RHE}}$ . The equivalent circuit for the electrochemical impedance spectra fit is also indicated. At  $0.4\text{ V}_{\text{RHE}}$ , the electrical components values are  $R_s=11.22\text{ }\Omega$ ,  $R_{sc}=338.7\text{ }\Omega$ ,  $R_{ss}=9.955\cdot 10^4\text{ }\Omega$ ,  $C_{sc}=1.362\cdot 10^{-6}\text{ F}$ ,  $C_{ss}=2.801\cdot 10^{-6}\text{ F}$ , and  $W=1.239\cdot 10^6\text{ }\Omega\text{ s}^{-0.5}$ . At  $-0.6\text{ V}_{\text{RHE}}$ , the electrical components values are  $R_s=11.06\text{ }\Omega$ ,  $R_{sc}=257.4\text{ }\Omega$ ,  $R_{ss}=304.8\text{ }\Omega$ ,  $C_{sc}=3.363\cdot 10^{-6}\text{ F}$ ,  $C_{ss}=8.713\cdot 10^{-6}\text{ F}$ , and  $W=152.8\text{ }\Omega\text{ s}^{-0.5}$ . ....215
- Fig. A5.8. Mott-Schottky plot of the space charge layer capacitance,  $C_{sc}$ , of  $\text{In}_{0.414}\text{Ga}_{0.586}\text{N}$  photoelectrodes under dark conditions in  $1\text{ M H}_2\text{SO}_4$ . The calculated doping concentration and flatband potential are also indicated. ....216
- Fig. A5.9. Numerical and experimental IPCE at  $1.23\text{ V}_{\text{RHE}}$  for  $\text{In}_x\text{Ga}_{1-x}\text{N}$  water-splitting photoanodes in  $1\text{ M Na}_2\text{SO}_4$  and indium content of a)  $x=0.095$ , b)  $x=0.165$ , c)  $x=0.235$ , d)  $x=0.333$ , e)  $x=0.414$ . The internal losses are in grey, the reflection loss in blue, the surface recombination loss in red, the numerical IPCE in green, and the experimental IPCEs are depicted with black dots. ....217
- Fig. A6.1. Print screen of the software POPe after running the calculation for nanostructured  $\text{Fe}_2\text{O}_3$  with  $\text{CoB}_i$  catalysts[187]. ....219



# List of tables

Table 1.1. Material parameters and numerical values used for the model system made of n-d-GaN .....	30
Table 1.2. Material parameters determined by fitting to the linear sweep voltammetry measurement. ....	35
Table 1.3. Minimum and maximum parameter values used in the FFD under illumination.....	38
Table 2.1. Material parameters of LTON particle-based PE determined by dedicated experiments (Mott-Schottky analysis and conductivity measurements), DFT calculations, and inverse analysis.....	71
Table 4.1. Material parameters used for the IPCE analysis with references in bracket. n/p-type, is a material doped negatively or positively. $\lambda_{\text{investigate}}$ is the investigated wavelength range, $R_{\lambda,m}$ , indicates if the reflection loss are experimentally measured ('yes') or numerically calculated according to eqn (4.12) ('no'). The first value of each parameter is the nominal value, the second or third values are estimated variations.....	120
Table 4.2. Summary of the determined material parameters and factors for all the photoelectrode materials investigated in this work. Only nominal values are depicted according to Table 4.1. ....	136
Table 5.1. Numerical values of the material parameters of $\text{In}_x\text{Ga}_{1-x}\text{N}$ water-splitting photoelectrodes used as inputs for POPe[212].....	152
Table 5.2. Calculated diffusion length, diffusion optical number, nanostructuring opportunity factor, and ratio of currents of $\text{In}_x\text{Ga}_{1-x}\text{N}$ photoelectrodes. ....	153
Table A5.1. Measured surface area and ohmic resistance between two ohmic contacts separated by a distance of 3 mm of the prepared $\text{In}_x\text{Ga}_{1-x}\text{N}$ photoelectrodes.....	211

# List of symbols

$f_{\text{viability}}$	Viability factor	[-]
$\Delta\phi_{\text{H}}$	Helmholtz layer potential difference	[V]
$\Delta\phi_{\text{sc}}$	Space charge region potential difference	[V]
$\hat{\mathbf{n}}$	Surface normal	[-]
$C_{\text{aug},n}$	Electron Auger recombination factor	[m <sup>6</sup> s <sup>-1</sup> ]
$C_{\text{aug},p}$	Hole Auger recombination factor	[m <sup>6</sup> s <sup>-1</sup> ]
$C_{\text{dir}}$	Direct recombination factor	[m <sup>3</sup> s <sup>-1</sup> ]
$C_{\text{sc}}$	Space charge region capacitance	[F]
$C_{\text{ss}}$	Capacitance of surface states	[F]
$D^*$	Effective depth	[m]
$E_{\text{Ag/AgCl}}$	Potential measured at the Ag/AgCl electrode	[V]
$E_{\text{Ag/AgCl}}^0$	Standard Ag/AgCl potential vs SHE	[V]
$E_{\text{C}}$	Conduction band energy level	[eV]
$E_{\text{F},n}$	Electron quasi-Fermi energy level	[eV]
$E_{\text{F},p}$	Hole quasi-Fermi energy level	[eV]
$E_{\text{F}}$	Fermi energy level	[eV]
$E_{\text{gap}}$	Bandgap	[eV]
$E_{\text{i}}$	Intrinsic energy Fermi level	[eV]
$E_{\text{RHE}}$	Reversible hydrogen electrode potential	[V]
$E_{\text{t}}$	Trap energy level	[eV]
$E_{\text{V}}$	Valence band energy level	[eV]

$E_{\text{vacuum}}$	Vacuum energy level	[eV]
$F_b$	Flux of holes at the bulk-SCR interface	[m <sup>-2</sup> s <sup>-1</sup> ]
$F_p$	Total flux of holes reaching the surface	[m <sup>-2</sup> s <sup>-1</sup> ]
$G_n$	Electron generation rate	[cm <sup>-3</sup> s <sup>-1</sup> ]
$G_p$	Hole generation rate	[cm <sup>-3</sup> s <sup>-1</sup> ]
$L_{0.95}$	Diffusion length that provides a IQE > 95 %	[m]
$N_A^-$	Ionized acceptor density	[m <sup>-3</sup> ]
$N_C$	Density of states of the conduction band	[m <sup>-3</sup> ]
$N_D^+$	Ionized donor density	[m <sup>-3</sup> ]
$N_{\text{opt}}$	Optimal doping concentration	[m <sup>-3</sup> ]
$N_V$	Density of states of the valence band	[m <sup>-3</sup> ]
$P_{\text{abs}}$	Optical power absorbed per unit volume	[W m <sup>-3</sup> ]
$Q_{\text{SC}}$	Total charge enclosed in space charge region	[C]
$R_{\text{back}}$	Spectral reflectance under back illumination	[-]
$R_{\text{front}}$	Spectral reflectance under front illumination	[-]
$R_{S,V_{\text{IPCE}}}$	Ratio of currents at the IPCE potential	[-]
$R_s$	Series resistance	[Ω]
$R_{ss}$	Surface states resistance	[Ω]
$R_n^{\text{Au}}$	Auger electron recombination rate	[cm <sup>-3</sup> s <sup>-1</sup> ]
$R_n^{\text{Au}}$	Auger hole recombination rate	[cm <sup>-3</sup> s <sup>-1</sup> ]
$R_n^{\text{SRH}}$	Shockley-Read-Hall electron recombination rate	[cm <sup>-3</sup> s <sup>-1</sup> ]
$R_n^{\text{SRH}}$	Shockley-Read-Hall hole recombination rate	[cm <sup>-3</sup> s <sup>-1</sup> ]
$R_\lambda$	Spectral reflection loss	[-]
$S_{R,0}$	Surface recombination velocity factor	[m s <sup>-1</sup> ]
$S_R$	Surface charge recombination velocity	[m s <sup>-1</sup> ]
$S_T$	Surface charge transfer velocity	[m s <sup>-1</sup> ]
$U^*$	Probability of charge to reach the surface	[-]
$U_n$	Net electron recombination rate	[cm <sup>-3</sup> s <sup>-1</sup> ]
$U_p$	Net hole recombination rate	[cm <sup>-3</sup> s <sup>-1</sup> ]
$V_{\text{FB,dark}}$	Flatband potential in dark condition	[V]

## List of symbols

---

$V_{\text{FB,ill}}$	Flatband potential under illumination	[V]
$V_{\text{FB}}$	Flatband potential	[V]
$V_{\text{IPC}}$	Potential drop at the inter-particle contact	[V]
$V_{\text{SCR}}$	Potential drop in the space charge region	[V]
$V_{\text{th}}$	Thermal voltage	[V]
$Y_0$	Admittance factor for constant phase element	[F s <sup>-1</sup> ]
$Y_{\text{CPE}}$	Admittance of constant phase element	[F]
$i_{\text{H}_2}^0$	Exchange current density for HER	[A m <sup>-2</sup> ]
$i_0$	Photon flux converted to photocurrent density	[A m <sup>-2</sup> ]
$i_{\text{H}}$	Current density in the Helmholtz layer	[A m <sup>-2</sup> ]
$i_{\text{rec}}$	Photocurrent density recombining in the SCR	[A m <sup>-2</sup> ]
$i_{\text{sc}}$	Current density in the semiconductor	[A m <sup>-2</sup> ]
$i_{\text{SCR}}$	Photocurrent density generated in the SCR	[A m <sup>-2</sup> ]
$i_{\text{l,back}}$	Back photogeneration current density	[A m <sup>-2</sup> ]
$i_{\text{l,back}}^*$	Effective back photogeneration current density	[A m <sup>-2</sup> ]
$i_{\text{l,front}}$	Front photogeneration current density	[A m <sup>-2</sup> ]
$i_{\text{l,front/back}}$	Front to back photogeneration current density ratio	[-]
$i_{\text{l,front/back}}^*$	Effective front to back generated current ratio	[-]
$i_{\text{l,front}}^*$	Effective front photogeneration current density	[A m <sup>-2</sup> ]
$i_{\text{l}}$	Photogeneration current	[A m <sup>-2</sup> ]
$i_{\text{n}}^0$	Electron dark current density	[A m <sup>-2</sup> ]
$i_{\text{p}}^0$	Hole dark current density	[A m <sup>-2</sup> ]
$k^*$	Effective extinction coefficient	[-]
$k_0$	Vacuum wavenumber	[m <sup>-1</sup> ]
$k_{\text{B}}$	Boltzmann constant	[J K <sup>-1</sup> ]
$m_{\text{cond}}^*$	Conduction effective mass	[-]
$m_{\text{e}}^*$	Effective mass of electron	[-]
$m_{\text{h}}^*$	Effective mass of holes	[-]
$\tilde{n}$	Complex refractive index	[-]
$n_1$	Electron trap density	[m <sup>-3</sup> ]
$n_{\text{eq}}$	Electron density at equilibrium	[m <sup>-3</sup> ]

$n_{\text{IPC,eq}}$	Electron density at the IPC under equilibrium	$[\text{m}^{-3}]$
$n_{\text{IPC}}$	Electron concentration at the inter-particle contact	$[\text{m}^{-3}]$
$n_{\text{mesh}}$	Mesh element number	$[-]$
$n_i$	Intrinsic carrier density	$[\text{m}^{-3}]$
$p_0$	Hole concentration at the bulk-SCR interface	$[\text{m}^{-3}]$
$p_1$	Hole trap density	$[\text{m}^{-3}]$
$p_{\text{eq}}$	Hole concentration at equilibrium	$[\text{m}^{-3}]$
$p_{\text{IPC,eq}}$	Hole concentration at the IPC under equilibrium	$[\text{m}^{-3}]$
$p_{\text{IPC}}$	Hole concentration at the inter-particle contact	$[\text{m}^{-3}]$
$p_s$	Hole concentration at the semiconductor surface	$[\text{m}^{-3}]$
$v_{\text{IPC},n}$	Electron inter-particle charge transfer velocity	$[\text{m s}^{-1}]$
$v_{\text{IPC},p}$	Hole inter-particle charge transfer velocity	$[\text{m s}^{-1}]$
$v_{s,n}$	Interfacial electron transfer velocity	$[\text{m s}^{-1}]$
$v_{s,p}$	Interfacial hole transfer velocity	$[\text{m s}^{-1}]$
$x_{\text{lim}}$	Thickness contributing to the photocurrent	$[\text{m}]$
$i_n$	Electron current density	$[\text{A m}^{-2}]$
$i_p$	Hole current density	$[\text{A m}^{-2}]$
$\alpha^*$	Effective absorption coefficient	$[\text{m}^{-1}]$
$\alpha_{500}$	Absorption coefficient at 500 nm	$[\text{m}^{-1}]$
$\alpha_{500}L_{0.95}$	Absorption coefficient times diffusion length $L_{0.95}$	$[-]$
$\alpha_{500}L$	Diffusion optical number	$[-]$
$\gamma_n$	Electron degeneracy factor	$[-]$
$\gamma_p$	Hole degeneracy factor	$[-]$
$\epsilon_0$	Vacuum permittivity	$[\text{F m}^{-1}]$
$\epsilon_r$	Relative permittivity	$[-]$
$\theta_i$	Incident angle of light	$[\circ]$
$\lambda_{\text{gap}}$	Wavelength corresponding to the bandgap	$[\text{m}]$
$\mu_{b,n}$	Bulk electron mobility	$[\text{m}^2 \text{V}^{-1} \text{s}^{-1}]$
$\mu_{\text{eff},n}$	Effective electron mobility	$[\text{m}^2 \text{V}^{-1} \text{s}^{-1}]$
$\mu_{\text{IPC},n}$	Inter-particle contact electron mobility	$[\text{m}^2 \text{V}^{-1} \text{s}^{-1}]$

## List of symbols

---

$\mu_n$	Electron mobility	$[\text{m}^2 \text{V}^{-1} \text{s}^{-1}]$
$\mu_p$	Hole mobility	$[\text{m}^2 \text{V}^{-1} \text{s}^{-1}]$
$\rho_c$	Corrected reflectance	[-]
$\rho_m$	Measured reflectance	[-]
$\tau_{\text{eff},n}$	Effective electron lifetime	[s]
$\tau_{\text{eff},p}$	Effective hole lifetime	[s]
$\tau_m$	Measured (total) transmittance	[-]
$\tau_{s,n}$	Surface electron lifetime	[s]
$\tau_{s,p}$	Surface hole lifetime	[s]
$\tau_n$	Bulk electron lifetime	[s]
$\tau_p$	Bulk hole lifetime	[s]
$\phi_H$	Helmholtz layer potential out of equilibrium	[V]
$\phi_H^0$	Helmholtz layer potential at equilibrium	[V]
$\phi_{\text{inj}}$	Injection yield of generated charges	[-]
$\phi_{\text{sc}}$	Space charge region potential out of equilibrium	[V]
$\phi_{\text{sc}}^0$	Space charge region potential at equilibrium	[V]
$\phi_{\text{sep}}$	Seperation yield of generated charges	[-]
$h$	Planck constant	[J s]
$\Phi$	Spectral photon flux	$[\text{m}^{-2} \text{s}^{-1} \text{nm}^{-1}]$
$A$	Surface area of photoelectrode	$[\text{m}^2]$
$C$	Capacitance	[F]
$D$	Film thickness	[m]
$D$	Diffusion coefficient	$[\text{m}^2 \text{s}^{-1}]$
$L$	Diffusion length	[m]
$N$	Spectral photon flux	$[\text{m}^{-2} \text{s}^{-1} \text{nm}^{-1}]$
$R$	Resistance	$[\Omega]$
$S$	Surface reaction velocity parameter	$[\text{m s}^{-1}]$
$T$	Temperature	[K]
$U$	Probability of charge in the bulk to reach the SCR	[-]
$W$	Width of space charge region or numerical domain	[m]
$d$	Photoelectrode material thickness	[m]

$d$	Height of numerical domain	[m]
$k$	Extinction coefficient	[-]
$n$	Electron concentration	[m <sup>-3</sup> ]
$n$	Refractive index	[-]
$p$	Hole concentration	[m <sup>-3</sup> ]
$q$	Elementary charge	[C]
$r$	Surface roughness factor	[-]
$E$	Electric field	[V m <sup>-1</sup> ]
$\alpha$	Frequency independent parameter of CPE	[F s <sup><math>\alpha</math>-1</sup> ]
$\alpha$	Absorbance	[-]
$\alpha$	Absorption coefficient	[m <sup>-1</sup> ]
$\alpha$	Charge transfer coefficient	[-]
$\beta$	Surface states energy distribution factor	[eV <sup>-1</sup> ]
$\varepsilon$	Complex permittivity	[F m <sup>-1</sup> ]
$\eta$	Photogeneration efficiency	[-]
$\eta$	Ratio of currents in the SCR	[-]
$\lambda$	Wavelength	[m]
$\nu$	Regular frequency	[Hz]
$\xi$	Correction term for finite photoelectrode thickness	[-]
$\rho$	Reflectance	[-]
$\rho$	Light intensity amount reflected	[-]
$\rho$	Particle density	[-]
$\rho$	Charge density	[cm <sup>-3</sup> ]
$\sigma$	Conductivity	[S m <sup>-1</sup> ]
$\tau$	Transmittance	[-]
$\tau$	Optical thickness	[-]
$\chi$	Electron affinity	[eV]
$\omega$	Radial frequency	[Hz]
$\phi$	Electrostatic potential	[V]

### ACRONYMS

1D	1-dimensional
2D	2-dimensional
3D	3-dimensional
AM	Air mass
CB	Conduction band
CNT	Carbon nanotube
CPE	Constant phase element
DFT	Density functional theory
DI	De-ionized
DSSC	Dye-sensitized solar cell
EIS	Electrochemical impedance spectroscopy
EL	Electrolyte
EMW	Electromagnetic wave
EQE	External quantum efficiency
FIB	Focused ion beam
FTO	Fluorine doped tin oxide
FVM	Finite volume method
HER	Hydrogen evolution reaction
HL	Helmholtz layer
IPC	Inter-particle contact
IPCE	Incident photon-to-current efficiency
IQE	Internal quantum efficiency
$I-V$	Photocurrent-voltage
K-M	Kubelka-Munk
LTON	LaTiO <sub>2</sub> N
MOCVD	Metal-organic chemical vapor deposition
MUMPS	Multifrontal massively parallel sparse direct solver
NIR	Near-infrared radiation
OCV	Open-circuit voltage



OER	Oxygen evolution reaction
PBPE	Particle-based photoelectrode
PC	Polymerized-complex
PDE	Partial differential equation
PE	Photoelectrode
PEC	Photoelectrochemical
PV	Photovoltaic
RHE	Reversible hydrogen electrode
SC	Semiconductor
SC-EL	Semiconductor-electrolyte
SCL	Space charge layer
SCR	Space charge region
SEM	Scanning electron microscopy
SHE	Standard hydrogen electrode
SRH	Shockley-Read-Hall
SS	Solid-state or surface states
STH	Solar-to-hydrogen
TRMC	Time-resolved microwave conductivity
UV	Ultraviolet
VB	Valance band
VIS	Visible

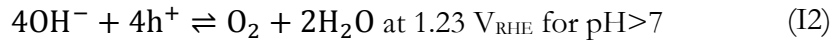
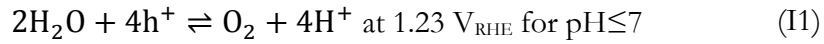
# Introduction

The accumulation of carbon dioxide in our atmosphere, in addition to carbon monoxide, oxides of nitrogen, un-burnt hydrocarbons and particulate matter, from fossil fuels threatens human health and environment. The global warming problem that is caused by burning fossil fuels mostly for electricity, heat and transportation applications is a major challenge to humankind[1], [2]. The transition to a sustainable society has become urgent. A complete transition includes a demographic transition, an economic transition that reflects full environmental costs, a societal transition for a better redistribution of wealth, a transition of the international institutions to develop arrangements among governments, and a technology transition[3]. The latter must cover the increase of the world energy demand along with a reduction of pollutant emissions.

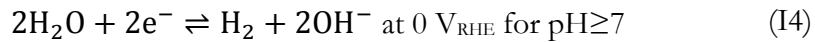
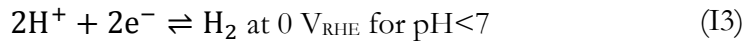
Solar energy received on the earth's surface can meet the current and future energy demand in a renewable way. However, solar energy is distributed and intermittent and thus must be stored for night energy demand or seasonal variations, and for usage at locations of demand which not necessarily co-inside with production locations[4]. Although lithium based batteries are starting to be massively produced, this technology is and might remain in the long-term too expensive to store large amount of electricity produced by photovoltaics. Moreover, lithium-based batteries are also partially self-discharging within 24 hours. Converting solar electricity to hydrogen by using electrolyzers could be an option for long-term solar energy storage but it induces considerable losses and additional cost that limits the economical viability of this approach[5]. However, this problem can be circumvented by directly converting solar energy into chemical fuels using photoelectrochemical (PEC) approaches, also called artificial photosynthesis. Indeed, PEC water splitting is a viable route for the direct conversion of solar energy into sustainable hydrogen, an energy carrier that can later be reconverted to electricity using fuel cells or used as a fuel for internal combustion engines[6].

### Photoelectrochemical water splitting devices

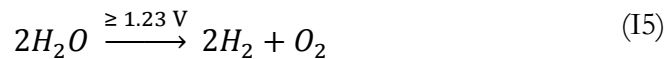
PEC water splitting devices require a photoabsorber made of a semiconductor material to generate electron-hole pairs and an electrolyte that conducts ions to have continuous water splitting (Fig. I1). Selective membranes that allows the transport of ions but not of electrons or gases are optional. However, membranes are very useful to avoid recombination and mixing of oxygen and hydrogen. Indeed, this recombination and mixing reduce the production yield of hydrogen, requiring subsequent separation of the oxygen and the hydrogen, and expose the device to a risk of explosion. As depicted in Fig. I1, the incoming light is absorbed by the photoabsorber and generates electron-hole pairs. Then, electrons and holes separately diffuse and/or migrate to their respective reaction sites in contact with the electrolyte to reduce or oxidize water. The generated electron and hole can partially or completely recombine during their transport. If they completely recombine, no photocurrent is present and water is not split. Holes (an unoccupied location of an electron) that reach the surface in contact with the electrolyte can oxidize the water if the reaction is favorable and generate oxygen (photoanodic reaction). This reaction, called the oxygen evolution reaction (OER), is given by[7]



Electrons reaching the electrolyte can reduce the water if the enthalpy of the reaction is favorable and generate hydrogen (photocathodic reaction). This reaction, called the hydrogen evolution reaction (HER), is given by



The two half-reactions (OER and HER) leads to the overall reaction of water splitting, given by



and requires a minimum thermodynamic potential difference of 1.23 V. Additional losses such as ohmic, activation, or concentration overpotentials[8][9] can occur in PEC water splitting devices leading to an overall water splitting potential of 1.57 V at best under  $10 \text{ mA cm}^{-2}$  (only considering activation overpotentials[10]). The OER requires usually a higher overpotential to initiate the transfer of electrons from the electrolyte to the semiconductor (the activation overpotential) than the HER since four electrons are involved in the OER compared to two electrons for the HER (eqns (I1) to (I4)). Once the amount of oxygen and hydrogen reaches the saturation level of the electrolyte, bubbles of oxygen and hydrogen are generated at their respective reaction sites and are collected either by forced or natural convection[11], [12].

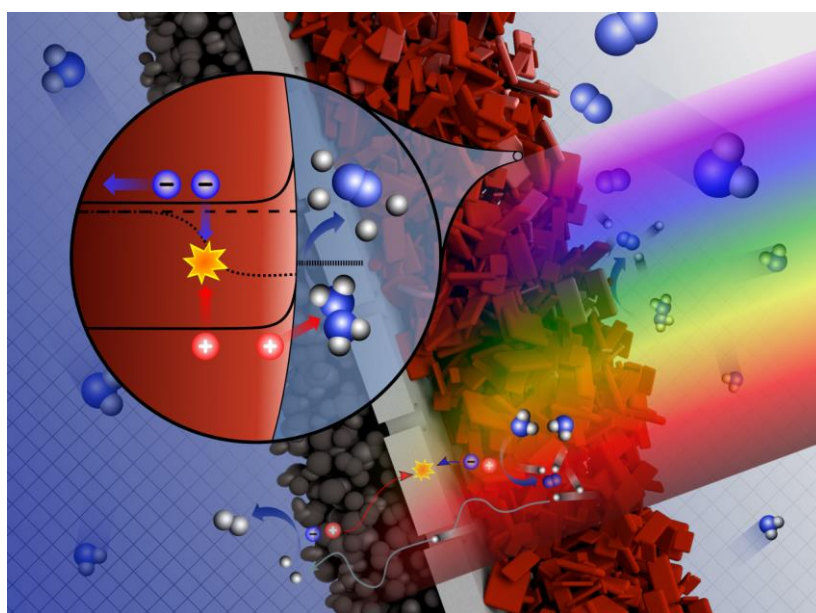


**Fig. I1.** Schematic of a particle-based tandem PEC water splitting system in an acidic electrolyte. A zoom of the semiconductor-electrolyte interface with an energy band diagram for the n-type semiconductor is included.

PEC water splitting devices can be classified into various types of devices with fundamental physical differences[13]. One of the key difference between them is the presence of a solid-liquid junction. The presence of a solid-liquid junction is essential in reaching the simplest PEC water splitting system: a system only composed of particles, called photocatalysts, dispersed into water and capable of splitting water. Photocatalyst systems could be extremely simple and cheap to implement since no

external wires would be required, only plastic bags ensuring that the produced gaseous hydrogen is captured. Photocatalyst systems are composed of either single or dual photoabsorbers. The single absorber system can be even cheaper and easier to implement than the dual absorber system but requires separating the oxygen and the hydrogen to avoid recombination or any risk of explosion, a separation process not trivial to implement. In contrast, the dual photoabsorber system has the advantage to separate directly the products by having the particles producing oxygen and the ones producing hydrogen in separated bags with a redox mediator shuttling the electrons back and forth and an ionic bridge between them. It has also the advantage of using potentially two photoabsorbers with two different bandgaps, which can theoretically overcome the efficiency of a single photoabsorber system[14]. The main drawback of the dual absorber system is the requirement of a redox mediator that can suffer from mass transport limitations and thus can highly impact the efficiency of the system[15]. Although, the simplest PEC water splitting system is photocatalysts it is possible to achieve economical and renewable production of hydrogen such as fixed panels with or without concentrated solar irradiation and with or without the presence of solid-solid junctions [6], [16]. Here, we only introduce PEC water splitting devices with a semiconductor-electrolyte interface, more specifically photoelectrodes that are composed of a single photoabsorber in contact with an electrolyte. There are two reasons for this choice. The first reason is that to improve photocatalyst systems, we need to understand the limitations of the semiconductor-electrolyte interface, an interface at the core of photocatalyst systems. The second reason is that the solid-liquid junction is simpler to construct than a solid-solid junction, a p-n junction. Indeed, a p-n junction requires to be able to dope positively and negatively the semiconducting material, a task often very challenging since the doping type or concentration can usually not be controlled during the material synthesis[17]. Thus, the semiconductor is naturally negatively or positively doped with an uncontrolled doping concentration. While a solid-liquid junction does not require controlling the doping type or concentration since only one type of doping is required for a single photocatalyst system[18], [19]. Indeed, the photogenerated electron and hole charges can diffuse to the half water splitting reaction sites independently of the doping type. However, an efficient diffusive charge transport mechanism requires the particle size or the photoelectrode thickness to be below the Debye length [20], a size too small to allow the development of a significant electric field in the semiconductor. This type of photoelectrodes are called nanostructured photoelectrodes in contrast to conventional photoelectrodes with particles or flat photoelectrodes larger than the Debye length. In the latter case, the charge carriers migrates to the semiconductor-electrolyte interface thanks to the presence of an electric field at the interface, a potential gradient induced by the band bending.

### Conventional photoelectrodes

Here, only the conventional photoelectrode is introduced since it is at the core of this work. A good introduction to photoelectrodes with only a diffusive transport mechanism can be found elsewhere [20], [21]. As mention in the previous section, conventional photoelectrode is required to have a thickness substantially larger than the Debye length,  $L_D$ , given by[20]

$$L_D = \sqrt{\frac{\epsilon_r \epsilon_0 k_B T}{2q^2 N_{A/D}^{+/-}}} . \quad (I6)$$

The Debye length measures the distance at which an electrostatic effect persists. Thus, a photoelectrode with a thickness smaller than the Debye length does not allow the electric field to develop completely. The Debye length shares some similarities with the thickness of the band bending, named the space chare region (SCR) width,  $W$ , given by

$$W = \sqrt{\frac{2\epsilon_0 \epsilon_r}{q N_{A/D}^{+/-}} (\phi_{SC} - V_{th})} . \quad (I7)$$

Similar to a semiconductor with a smaller thickness than the Debye length, a semiconductor with a smaller thickness than the SCR will not have a fully developed band bending and transport will be dominated by diffusion. For example, a photoanode of hematite with a permittivity of 30[22], a doping concentration of  $2.5 \cdot 10^{18} \text{ cm}^{-3}$ [23], and a flatband potential of 0.54 V<sub>RHE</sub>[23] leads to a SCR thickness of 31 nm at 1.23 V<sub>RHE</sub>. Thus, if the thickness of the hematite is below 31 nm, the band bending will not be fully developed.

One of the key point to understand the basic physical mechanism of conventional photoelectrodes is the formation of the band bending. The band bending is formed when the semiconductor is in contact with the electrolyte. When two isolated bodies such as the semiconductor and the electrolyte are in contact with a permeable boundary between them, both bodies reach a new state of thermodynamic equilibrium according to the second law of thermodynamic[24]. Thus, the electrochemical potential for electrons in the semiconductor and in the electrolyte will reach the same potential and there will be only one single potential for both the semiconductor and the electrolyte as depicted in Fig. 12.b. The electrochemical potential in the semiconductor is called the Fermi level and corresponds to a

hypothetical energy level which has 50 % probability of being occupied by an electron at any temperature. The electrochemical potential in the electrolyte corresponds to the redox potential. If the OER reaction is the predominant redox reaction, the Fermi level will align with the OER redox potential of  $1.23 \text{ V}_{\text{RHE}}$  and if the HER is predominant it will align at the HER redox potential of  $0 \text{ V}_{\text{RHE}}$ . If none of the reactions are predominant, the Fermi level will align somewhere between these two redox potential. Fig. 12.b depicts an ideal case where the band edge positions of the semiconductor are completely fixed (green points and dashed lines in Fig. 12.b). Moreover, the electrochemical potential alignment is only achieved by free charge carriers, electrons in n-type semiconductors (an holes in p-type semiconductor), moving out of the semiconductor leaving fixed positive charges, acceptors (or donors in p-type) at the dopant sites. This process forms the SCR, a charged region that induces the band bending through the Poisson's equation. However, a real semiconductor-electrolyte interface is much more complex with the presence of a Helmholtz layer in the electrolyte and with interface (or surface) states present at the surface of the semiconductor that can induce Fermi level pinning (Fig. 12.c)[25]. Since the band bending is very difficult to predict, the band bending is usually determined experimentally by a Mott-Schottky analysis[26] or by the inversion of photocurrents method[27]. The latter can provide more accurate results since it allows measuring the flatband potential, correlated to the band bending (section 1.2.3), with the presence of substantial Faradaic current for which capacitance measurements used in the Mott-Schottky analysis can become very complicated[27]. The flatband potential is the potential at which there is no band bending, the conduction and valence bands are flat. In Fig. 12.b and Fig. 12.c, the semiconductor-electrolyte system is in thermodynamic equilibrium. This thermodynamic equilibrium hold indefinitely until disturbed by a thermodynamic operation such as light (Fig. 12.d). Then, the photoelectrodes is not in thermodynamic equilibrium but in an excited state with energy and mass transfer. The band bending in dark condition or under illumination are usually not the same ( $\phi_{\text{sc,dark}} \neq \phi_{\text{sc,ill}}$ ) because minority charge carriers can accumulate at the surface or get trapped by interface states resulting in a change of the band bending and consequently also a change in the Helmholtz layer potential  $\phi_{\text{H}}$ . This effect can be interpreted as the movement of the band edges and is called unpinning of the band[28]. The vacuum energy level,  $E_{\text{vac}}$ , remains always continuous over the entire system even with the presence of the Helmholtz layer and interface states (Fig. 12).

The presence of a SCR in conventional photoelectrodes can be determined by running an open-circuit voltage (OCV) measurement under chopped light[29]. The OCV requires being different in dark condition and under illumination to reveal the presence of a SCR. If the OCV remains constant under chopped light, there is either

no SCR, or phenomena that are more complex are taking place such as tunneling effects under very high doping concentrations that can hinder having a varying OCV.

### **Key material properties for long-term high performing photoelectrodes**

Back in 1998, the record for a stand-alone water splitting device was 12.4 % solar-to-hydrogen (STH) efficiency under AM1.5G [30]. In 2018, Cheng et al.[31] achieved a new world record of 19 % STH efficiency under AM1.5G. Besides the great achievement of these records, these PEC water splitting devices were stable only over few hours and involves complex and expensive materials and fabrication processes. Moreover, these records were not obtained by using photoelectrodes or photocatalysts but by using a multi-junction solar cell in contact with rare metal catalysts. Thus, these records also highlight the challenges to achieve a mature system for economical large-scale production of hydrogen over the last two decades[32]. Here, we discuss the main challenges related to PEC water splitting devices, more specifically the key material properties for long-term high performing photoelectrodes with a semiconductor-electrolyte interface. The following discussion explains also, why word STH efficiency records were not obtained with devices having semiconductor-electrolyte interfaces and also why these devices might not reach high efficiency in the short-term.

The bandgap is one of the most important parameter for any photoabsorbing material. The bandgap determines the amount of light that can be converted to electron-hole pairs and the voltage the material can provide. A maximum theoretical efficiency limit can be determined by considering the bandgap of the material and a detailed energy balance, the Shockley-Queisser limit[33]. The Shockley-Queisser limit refers originally to the maximum theoretical efficiency of single junction solar cell but can also be applied to a single photoabsorber water splitting material by accounting for the minimum thermodynamic water splitting potential of 1.23 V and the different overpotential losses. Accordingly, a theoretical STH efficiency maximum of 11.2 % was obtained with a bandgap of 2.26 eV[16]. For tandem system, the STH efficiency can reach between 17 % and 22.8 % with a top photoabsorber bandgap between 1.65 eV and 2.1 eV and a bottom absorber between 0.8 eV and 1.5 eV[16]. The bandgap is a key parameter for the efficiency of photoelectrode materials and must be within a specific range for a given device configuration so that high efficiencies are feasible.



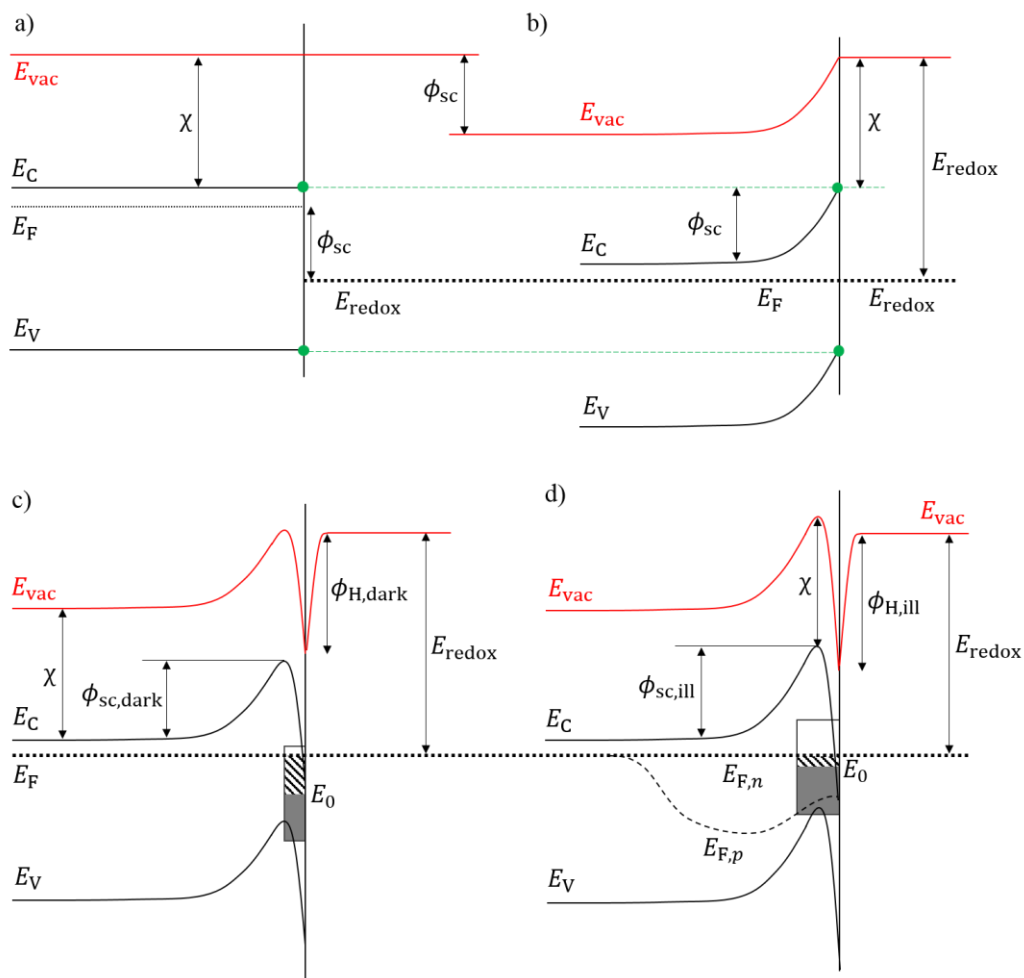


**Fig. 12.** Schematic of the energy band diagrams of a n-type semiconductor–electrolyte interface under dark a) before the semiconductor and the electrolyte are in contact, b) at thermodynamic equilibrium without any interface states or Helmholtz layer formation (ideal case), c) at thermodynamic equilibrium with p-type interface states and a Helmholtz layer (real case), and d) under illumination with p-type interface states and a Helmholtz layer. The thicknesses of the band bending related to the interface states and the Helmholtz layer are exaggerated for clarity. The subscript “dark” stands for dark condition and “ill” for illuminated condition.

The band-edge position must be well positioned for the water splitting reaction. The conduction band energy level should be greater than the OER energy level ( $\geq 1.23$  V vs RHE) and the valence band smaller than the HER energy level ( $\leq 0$  V vs RHE) to enable water splitting without the need of an applied bias for photoelectrode and

to enable the water splitting half reactions for photocatalysts. The band-edge position is a requirement that limits the number of material candidates for water splitting[34].

Defect tolerance is a very important property, although currently the least known criteria of nowadays photoelectrode material research. Indeed, defect tolerance is the tendency of a material to keep its properties unchanged despite the presence of crystallographic defects[35]. This property will determine if the fabrication process will need a very controlled and clean environment or not. It will not only affect the equipment needed to achieve the fabrication of the material, which is closely related to the cost, but also determine if the fabrication process is easily reproducible.

The catalytic activity for HER and OER must be high to reduce overpotential losses that can greatly affect the STH efficiency. The catalytic activity of a photoelectrode material can be enhanced by the deposition of co-catalysts. Nowadays, numerous catalysts for the HER and OER exist and have been successful in enhancing the catalytic activity[10], [36]. However, long-term stability of catalysts deposited on the surface of the semiconductor has not yet been shown[37]. Thus, a photoelectrode material with high catalytic activity avoids long-term stability issues related to the use of co-catalysts.

Photocorrosion is a major challenge to have long-term operating water splitting photoelectrodes[38]. Photocorrosion appears in materials that are not thermodynamically stable, i.e. the self-oxidation or reduction reaction are more favorable than the water splitting half reactions. Photocorrosion can be partially suppressed by decreasing the kinetics of self-oxidation or reduction reactions with a protective layer such as  $\text{TiO}_2/\text{NiCrO}_x$ [39] or by increasing the water splitting half reaction kinetics by depositing co-catalyst such as Pt[40] deposited on Si photoelectrodes or on multi-junction solar cell[31]. Despite significant progress made in the last years, protective layer stability issues must still be addressed for practical photoelectrodes[41], [42][43]. Semiconductor materials that are thermodynamically stable such as transition-metal oxides (no photocorrosion) are a much simpler option for long-term operating photoelectrodes. However, transition-metal oxides suffer from low charge transport properties because of the formation of polarons, i.e. the interaction of electrons with polarized phonon cloud (electron-phonon interaction) in the semiconductor[44], [45].

The transport of charge carriers is a key parameter for the performance of photoelectrode since it determines the capability of a material to transport the photogenerated charges towards the water splitting reaction sites without recombining. The charge transport properties of a photoelectrode material can be expressed by the diffusion length of minority charges carriers, given by

$$L = \sqrt{D\tau} . \quad (18)$$

The diffusion length is the average distance a photogenerated charge carrier moves between generation and recombination. However, this parameter cannot determine if a material has a diffusion length sufficient to transport charge carriers from its generation site to the water splitting reaction site. Indeed, a material with a high absorption coefficient requires a lower diffusion length to be efficient compared to a material with low absorption coefficient. The diffusion optical number introduced in section 4.2.1 as the product of the diffusion length and the absorption coefficient at 500 nm provides a dimensionless number capable of evaluating the efficiency of a material to convert light into charges that can reach the water splitting reaction sites. Nanostructuring or complex morphology can overcome the diffusion optical number limitation to a certain extent (chapter 4).

Surface energy is another important property. A high surface energy implies that charge carriers are trapped at the surface to form surface states (also called interface states). While surface states can be reduced by surface passivation[46], their presence suggest that similar states occur at other defects or at grain boundaries. Surface states further imply surface recombination sites that can affect the photocurrent of the semiconductor. High surface energy is also a sign of defect intolerance. A low surface energy is therefore a great advantage and reduces the need of surface treatments.

These different material properties are exemplified in a qualitative spider charts for Si and Fe<sub>2</sub>O<sub>3</sub> (Fig. I3). As depicted in Fig. I3, Si has very good diffusion optical number, surface energy, and bandgap, as well as a good band edge alignment for HER. The surface energy is very good because a nano-layer of silicon oxide naturally forms at the surface of Si that protects and stabilizes the Si beneath, a gift for the electronic industry. However, Si photocathodes are unstable in water and require a protective layer. Finally, the cost of monocrystalline Si is relatively high because it is not a defect tolerant material and thus require a fabrication process in a very clean environment. However, the price of monocrystalline (and polycrystalline) Si has highly decreased over the last decades[47]. In contrast, Fe<sub>2</sub>O<sub>3</sub> is a very abundant and cheap material with great stability in water. Its bandgap of 2.0 eV[23] and its band edge positions makes this material interesting for OER as a top absorber in a tandem device[48]. However, hematite suffers from low diffusion optical number, i.e. short hole diffusion length, and poor surface OER kinetic. Thus, hematite is currently poorly performing as photoanode[49], [50].

These two materials, Si and Fe<sub>2</sub>O<sub>3</sub>, as examples reveal the long list of requirements that a photoelectrode material must fulfil for viable hydrogen production.

Nowadays, having only one of these key parameters poorly performing is sufficient to hinder the viability of the material as a photoelectrode material.

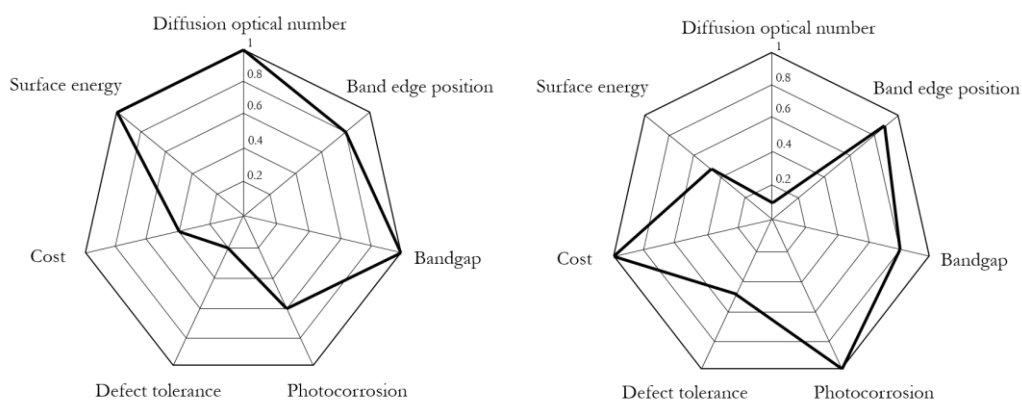


**Fig. I3.** Qualitative spider chart example of key properties for photoelectrode materials: a) Si and b) Fe<sub>2</sub>O<sub>3</sub>. A value of 1 means an excellent property and 0 a poor property.

Out of the different key material properties presented here, this work only focuses on two of them, the diffusion optical number and the surface energy. These two properties accounts for various coupled physical phenomena such as photoabsorption, charge transport and conservation, and charge transfer and recombination at the semiconductor-electrolyte interface. These coupled physical phenomena are difficult to access experimentally while numerical modelling can provide more systematic insights. Thus, different numerical models were developed and used in this work to investigate the limitation of morphologically complex photoelectrodes based on the diffusion optical number and the surface energy. The next section introduces a brief history of numerical modeling of photoelectrodes.

### Numerical modeling of photoelectrodes<sup>1</sup>

The water-splitting photoelectrode, more specifically the semiconductor-electrolyte interface, has been intensively studied and modeled over the last decades[51]–[55]. The first analytical model was based on a semiconductor-metal interface proposed by Gärtner[56] and was assumed to be valid for the semiconductor-electrolyte

<sup>1</sup> The material of this section is partially based on a book section published by the Royal Society of Chemistry under the reference ‘S. Haussener, Y. Gaudy, and S. Tembhurne, Modelling-derived Design Guidelines for Photo-electrochemical Devices, in *Advances in Photoelectrochemical Water Splitting: Theory, Experiment and Systems Analysis*, S. D. Tilley, S. Lany, and R. van de Krol, Eds. RSC, 2018’.

interface. This model assumed no majority carrier flux from the semiconductor to the electrolyte, no recombination in the space charge region and a minority concentration at the interface of zero. Sah et al.[57] introduced a model accounting for recombination in the space charge layer for a p-n junction that could also be applied to semiconductor-electrolyte interface. Reichman[58] proposed a more precise model than the Gärtner model by adding a hole concentration at the semiconductor-electrolyte interface and the possibility for electrons to flow from the semiconductor to the electrolyte. He also included the model of Sah et al. to take into account the space charge region recombination. This model has been extensively used to describe semiconductor-electrolyte interfaces and to explain, for example, the photocurrent's dependency on the doping concentration of an n-GaN photoanode[59]. Wilson[60] has developed a model to describe the  $I$ - $V$  curve of semiconductors that includes the effects of recombination with discrete or continuous distribution of surface states in the bandgap. Although these analytical models can provide some understanding of the semiconductor-electrolyte interface, they are 0D or 1D analytical models that cannot explain local behavior or geometrical effects. 1D numerical modelling of the semiconductor-electrolyte interface can provide additional insights and local effects that cannot be captured by analytical models or even experiments. One of the first 1D models integrating light absorption, charge transport in the semiconductor and in the electrolyte, and charge transfer to the metallic catalyst has been used to quantify the dependency of the device performance on the choice of the light absorber[61]. Mills et al.[62] have developed a 1D model that describes the  $I$ - $V$  behavior at various semiconductor-catalyst-electrolyte interfaces accounting for different types of catalysts, including metallic, adaptive, and molecular ones. Cendula et al.[63] have developed a 1D model of the charge transport in the semiconductor and have enhanced the understanding of the energy band dynamics of photoabsorbers in direct contact with an electrolyte. This work contributes to these modeling activities by the development of 1D and 2D models that combines charge generation, and charge transport and conservation in the semiconductor considering surface recombination.

### Aim

This work aims at identifying and providing potential improvements of photoelectrodes focused on light absorption, charge generation, transport and recombination in the bulk and at the semiconductor-electrolyte interface. More specifically, numerical models capable of reproducing  $I$ - $V$  curves of flat photoelectrodes and particle-based photoelectrodes were developed to provide material and morphology design guidelines for more efficient flat and morphologically complex photoelectrodes. Furthermore, a computational simpler numerical method based on the incident photon-to-current efficiency (IPCE) was

developed to accelerate the analysis of promising photoelectrode materials and synthesis methods.

## Scope

*Chapter 1* is essential for the understanding of this work and more generally for a detailed understanding of conventional photoelectrode physics. This chapter introduces the fundamental physical mechanisms occurring in water splitting photoelectrodes through the development of a multi-physics model of a planar GaN photoelectrode. The model is validated, and used to identify and quantify the most significant materials-related bottlenecks in photoelectrode performance. The model accounts for electromagnetic wave propagation within the electrolyte and semiconductor, and for charge carrier transport within the semiconductor and at the semiconductor-electrolyte interface. Interface states at the semiconductor-electrolyte interface were considered using an extended Schottky contact model. Numerical design of experiments and parametric analysis are conducted using the validated model in order to identify and optimize the key factors for water splitting photoelectrodes.

*Chapter 2* presents a validated numerical model capable of predicting the  $I$ - $V$  characteristics of oxide and oxynitride particle-based photoelectrodes and identifying the critical parameters affecting the performance of those photoelectrodes. We used particle-based LaTiO<sub>2</sub>N photoelectrodes as the model system. The necessary material parameters, namely complex refractive index, permittivity, density of states of the conduction and valence bands, charge mobilities, flatband potential, doping concentration, recombination lifetimes, and interfacial hole transfer velocity, are derived by density functional theory calculations, dedicated experiments, and fitting of the numerically determined photocurrent-voltage curves to the measured ones under back-side illumination.

*Chapter 3* investigates the inter-particle charge transfer mechanism of particle-based photoelectrode using particle-based LaTiO<sub>2</sub>N photoelectrode as model system. The front to back photocurrent ratio depending on the photoelectrode thickness was measured and compared to the numerical front to back photogenerated current ratio. This comparison proves indications of the presence of majority charge carrier transport limitation. Then, different theoretical inter-particle charge transfer mechanisms that could potentially occur in particle-based photoelectrode were introduced. Their related equations were implemented in a numerical model providing  $I$ - $V$  curves of particle-based LaTiO<sub>2</sub>N photoelectrodes.

*Chapter 4* reports the development of a rapid performance optimization method for photoelectrodes. The method requires as an input the IPCE of a material at two or

## Introduction

---

more wavelengths and calculates the diffusion length, optical losses, bulk recombination losses, space charge region losses, and surface losses. The diffusion optical number, defined as the product of the absorption coefficient and the diffusion length at 500 nm, was used to quantify the viability of the materials. The method was validated using planar  $\text{Cu}_2\text{O}$  water splitting photoelectrodes. Subsequently, it was applied to planar water splitting photoelectrodes made of  $\text{Cu}_2\text{O}$ ,  $\text{Si}$ ,  $\text{Fe}_2\text{O}_3$ ,  $\text{BiVO}_4$ ,  $\text{Cu}_2\text{V}_8\text{O}_3$ , and  $\text{CuFeO}_2$ , and to nanostructured photoelectrodes made of  $\text{Fe}_2\text{O}_3$  and  $\text{LaTiO}_2\text{N}$ .

*Chapter 5* investigates  $\text{In}_x\text{Ga}_{1-x}\text{N}$  photoelectrodes.  $\text{In}_x\text{Ga}_{1-x}\text{N}$  is a promising material for highly efficient water-splitting photoelectrodes since the bandgap is tunable by modifying the indium content. A maximum theoretical photogeneration efficiency is determined for  $\text{In}_x\text{Ga}_{1-x}\text{N}/\text{Si}$  tandem photoelectrodes by numerical simulation of electromagnetic wave propagation. Mott-Schottky analysis were performed to determine the doping concentration and the flatband potential of  $\text{In}_x\text{Ga}_{1-x}\text{N}$  photoanodes with varying indium content of 9.5 %, 16.5 %, 23.5 %, 33.3 %, and 41.4 %.  $I-V$  curves and IPCE spectra were measured in 1 M  $\text{H}_2\text{SO}_4$  and 1 M  $\text{Na}_2\text{SO}_4$ . The IPCE in 1 M  $\text{Na}_2\text{SO}_4$  was used with the software POPE to determine the diffusion length, the diffusion optical number, and the ratio of currents of  $\text{In}_x\text{Ga}_{1-x}\text{N}$ .

# Utilizing modeling, experiments, and statistics for the analysis of water-splitting photoelectrodes<sup>1</sup>

## 1.1. Introduction

Recently, numerical modelling of the charge transfer at the semiconductor-electrolyte interface and its coupling to multiphysical heat, mass, and charge transport phenomena in a complete PEC device has become of interest as it can provide insight into the coupled physical phenomena inaccessible to experiments. Models of charge transport in the semiconductor have enhanced the understanding of the energy band dynamics of photoabsorbers in direct contact with an electrolyte[63], insight that can only be captured by numerical calculations. A 1-dimensional model of a PEC water-splitting device integrating light absorption, charge transport in the semiconductor, charge transfer to the metallic catalyst, and charge transport in the electrolyte has quantified the dependency of the device performance on the choice of the light absorber[61]. Theory and numerical modeling of charge transfer at semiconductor-catalyst interfaces for solar water-splitting have been developed to describe current-voltage behavior of semiconductor-catalyst-solution systems with metallic, adaptive, and molecular catalysts[55]. These models do not simultaneously study electromagnetic wave propagation and charge transport in the semiconductor and/or do not consider all types of relevant recombination phenomena, such as surface recombination, which can be a major loss at semiconductor-electrolyte interfaces[55], [64], [65]. A detailed quantification and decoupling of the influence of the photon absorption, charge generation, charge

---

<sup>1</sup> The material from this chapter has been published in Journal of Materials Chemistry A under the reference ‘Y. K. Gaudy and S. Haussener, *J. Mater. Chem. A*, 2016, **4**, 3100’.



## 1: Utilizing modeling, experiments, and statistics for the analysis of water-splitting photoelectrodes

---

transport and recombination, and interface transport and recombination phenomena is missing.

In this chapter, we combine numerical modeling, experimental measurements, and statistical analysis for the development of an accurate water-splitting photoelectrode performance model, identification and quantification of the key performance parameters, and subsequent proposition of material and device optimization. First, we introduce the numerical model, which combines electromagnetic wave propagation, charge generation and transport in the semiconductor, and charge transfer across the catalytically active semiconductor-electrolyte interface. The numerical model is then applied to a model system composed of a planar gallium nitride photoanode and platinum wire cathode immersed in 1M sulfuric acid. The numerical model is completed with experimental investigations to determine missing material parameters of gallium nitride. The numerical model is subsequently experimentally validated using linear sweep voltammetry measurements. Statistical methods are used in combination with the validated model to identify the most important material and interface properties. Finally, parametric analyses are used to optimize identified key performance parameters of the water-splitting photoelectrode.

### 1.2. Governing equations and methodology

#### 1.2.1. Model domain and assumption

The modeled water-splitting photoelectrode consists of a planar photoanode (GaN) electrically connected to a wired counter electrode (Pt), both immersed in an electrolyte (sulfuric acid). The detailed arrangement of the planar photoelectrode, including substrate and highly-doped conduction layers, is depicted in [Fig. 1.1](#).

Electromagnetic wave (EMW) propagation is calculated in all components of the device (electrolyte and semiconductor), assuming solar irradiation at the top of the electrolyte and absorption at the back contact of the photoanode. The 2D model domain and its boundaries are indicated by a dotted frame in [Fig. 1.1.a](#). The radiation model attempts to be applicable to any type of photoelectrode or PEC device justifying the choice of the advanced light propagation model. The typically applied Beer-Lambert's law[55], [61], [63] limits the calculation of the charge generation rate to planar, homogeneous photoelectrodes, while detailed EMW propagation calculations provide solutions to the investigation and optimization of

# 1: Utilizing modeling, experiments, and statistics for the analysis of water-splitting photoelectrodes

morphologically-complex, nano-structured, heterogeneous, or multi-component water-splitting photoelectrodes. Similarly, ray-tracing methods are also limited to cases where geometrical optics are valid, i.e. the thickness of the absorber is larger than the light wavelength[66].

Charge transport and conservation is solved only in the semiconductor component, utilizing dedicated boundary conditions to ensure the physical coupling to the counter electrode and the electrolyte; the front semiconductor domain boundary consists of a semiconductor-electrolyte interface, and the back semiconductor domain interface consists of a semiconductor-metal ohmic contact. The 1D model domain and its boundaries are indicated by a red line in Fig. 1.1. The governing equations of chemical species transport and reactions in the electrolyte are well known[8], [9], [67] and have been previously studied[68]. Detailed analysis of the charge and species transport in the electrolyte was not considered in our study, assuming a highly conducting electrolyte with an excess availability of ions, no significant species concentration variations, and no mass transport limitations. Dissolved and gas-phase products such as oxygen and hydrogen were assumed to be quickly evacuated from the semiconductor-electrolyte interface. Generally, the electrolyte was assumed to be well stirred and purged. Flatband potentials were assumed to be unaffected by species adsorption at the semiconductor surface.

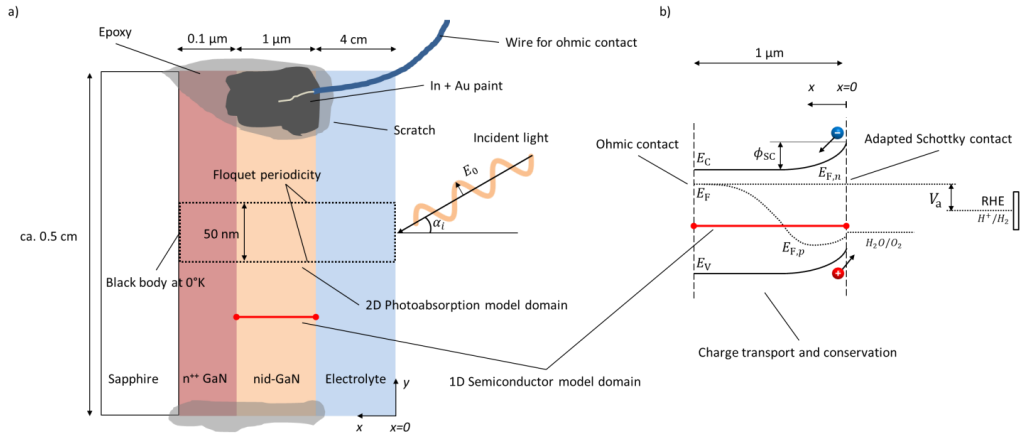


**Fig. 1.1.** Scheme of the model domain (not to scale) of the photoanode (GaN) immersed in electrolyte including the 2D EMW propagation model domain (dotted) and boundary conditions, and the 1D semiconductor model domain (red line). b) Detailed 1D semiconductor model domain and boundary conditions.

## 1: Utilizing modeling, experiments, and statistics for the analysis of water-splitting photoelectrodes

---

Our numerical model consists of two parts as depicted in Fig. 1.1: i) a 2D model of the EMW propagation in the electrolyte and semiconductor that allows determination of the generation rate of electron-hole pairs in the semiconductor, and ii) a 1D model of the charge transport and conservation in the semiconductor that allows determination of charge carrier concentrations, band positions, recombination rates, (photo)current, and potentials. The EMW propagation in 2D was developed to provide a general model enabling future study on more complex device structures. The advanced multi-dimensional EMW did not lead to significant additional computational expenses, as the electron-hole-pair generation rate was calculated only one time assuming that the complex refractive index was independent of the other semiconductor material properties. The 1D semiconductor model allowed for a computationally effective calculation and exploration of the material parameters of the semiconductor. Physical effects on charge transport due to multi-dimensionality of the sample were neglected and irrelevant for the planar sample with the highly conducting current collector.

The EMW propagation model assumed materials with a relative magnetic permeability of 1 and an electrical conductivity of zero. The various components were assumed rigid, homogeneous, and isotropic. Only steady state operation was considered, and time dependent effects such as photocorrosion were not considered.

### 1.2.2. Governing equations

The water-splitting photoelectrode model included EMW propagation, static and dynamic behavior of charge carriers in the semiconductor, and current transfer across the catalytically-active semiconductor-electrolyte interface.

**Photoabsorption.** The location-dependent charge carrier generation rate is calculated by solving the Maxwell's curl equations for each spectral band considered and the complex refractive index as relevant material property[69],

$$\nabla \times (\nabla \times \mathbf{E}(\mathbf{x}, \omega)) - k_0^2 \tilde{n}(\omega)^2 \mathbf{E}(\mathbf{x}, \omega) = 0. \quad (1.1)$$

The optical power absorbed per unit volume is calculated from the electric field and the imaginary part of the complex permittivity,

$$P_{\text{abs}}(\mathbf{x}, \omega) = -\frac{1}{2} \omega |\mathbf{E}(\mathbf{x}, \omega)|^2 \Im\{\varepsilon(\mathbf{x}, \omega)\}, \quad (1.2)$$

rather than by calculating the divergence of the Poynting vector, which is numerically less robust. The complex permittivity can be calculated from the complex refractive index and vacuum permittivity by  $\varepsilon = \varepsilon_r \varepsilon_0 = (n + ik)^2 \varepsilon_0$ . The total electron-hole generation rate,  $G$ , is calculated by integrating the spectral generation rate over the considered spectrum,

$$G_n = G_p = G(\mathbf{x}) = \int_{\infty}^{\omega_{\text{max}}} P_{\text{abs}}(\mathbf{x}, \omega) / h / \omega \, d\omega, \quad (1.3)$$

with the upper integration boundary  $\omega_{\text{max}} \geq E_{\text{gap}}/h$ .

**Charge transport and conservation.** The static behavior of the charge carriers in the semiconductor is calculated by solving Poisson's equation[70],

$$\nabla \cdot (\varepsilon_0 \varepsilon_r \nabla \phi) = -\rho = q(n - p + N_A^- - N_D^+), \quad (1.4)$$

The carrier density is given by integrating the product of the Fermi-Dirac distribution and the density of states over all possible states. For a non-degenerated semiconductor, i.e. when the Fermi level is at least  $3k_B T$  away from either band edge, the Fermi-Dirac distribution can be replaced by the Maxwell-Boltzmann distribution leading to electron and hole densities given by[70]:

$$n = N_C e^{-(E_C - E_F)/k_B T}, \quad (1.5)$$

$$p = N_V e^{-(E_F - E_V)/k_B T}. \quad (1.6)$$

The dynamic behavior of the carriers is calculated by solving the drift-diffusion equations for electrons and holes inside the semiconductor[70],

## 1: Utilizing modeling, experiments, and statistics for the analysis of water-splitting photoelectrodes

---

$$\mathbf{i}_n = \mu_n n \nabla E_C + \mu_n k_B T \nabla n, \quad (1.7)$$

$$\mathbf{i}_p = \mu_p p \nabla E_V - \mu_p k_B T \nabla p. \quad (1.8)$$

Isothermal device temperature and thermal equilibrium between the carrier and the lattice were assumed. The conduction band and valence energy levels,  $E_C$  and  $E_V$ , are given by  $E_C = E_{\text{vacuum}} - q\chi$  and  $E_V = E_{\text{vacuum}} - q\chi - E_{\text{gap}}$ . The total current density,  $\mathbf{i}_{\text{tot}}$ , is the sum of the electron and hole current densities. The steady state charge conservation is given by,

$$\frac{1}{q} \nabla \cdot \mathbf{i}_{n/p} = U_{n/p}, \quad (1.9)$$

where  $U_{n/p}$  is the net electron or hole recombination rate given by

$$U_{n/p} \equiv R_{n/p}^{\text{SRH}} + R_{n/p}^{\text{rad}} + R_{n/p}^{\text{Au}} + R_{s,n/p} - G_{n/p}, \quad (1.10)$$

composed of three types of recombination in the bulk, i.e. Shockley-Read-Hall, radiative and Auger recombination, and one surface recombination type. The Shockley-Read-Hall recombination is given by,

$$R_n^{\text{SRH}} = R_p^{\text{SRH}} = \frac{np - \gamma_n \gamma_p n_i^2}{\tau_p(n + n_1) + \tau_n(p + p_1)}, \quad (1.11)$$

where the electron and hole degeneracy factors are assumed equal to one for non-degenerated semiconductors. The intrinsic density is given by  $n_i = \sqrt{N_c N_v} \exp(-E_g/2/k_B T)$ . The electron and hole trap state densities are calculated according to

## 1: Utilizing modeling, experiments, and statistics for the analysis of water-splitting photoelectrodes

---

$$n_1 = \gamma_n n_i e^{(E_t - E_i)/k_B T}, \quad (1.12)$$

$$p_1 = \gamma_p n_i e^{-(E_t - E_i)/k_B T}, \quad (1.13)$$

where the intrinsic Fermi level is given by  $E_i = (E_c + E_v)/2 + k_B T/2 \cdot \ln(N_v/N_c)$ . The electron and hole lifetimes in eqn (1.11) were exchanged by effective electron and hole lifetimes,

$$\frac{1}{\tau_{\text{eff},n/p}} = \frac{1}{\tau_{n/p}} + \frac{1}{\tau_{s,n/p}}, \quad (1.14)$$

which combines SRH bulk recombination and single level surface recombination[71], [72]. Consequently, eqn (1.11) was updated with an effective SRH recombination rate,  $R_{\text{eff},n/p}^{\text{SRH}}$ , accounting also for surface recombination, and the surface recombination rate,  $R_{s,n/p}$ , was removed. This simplifying approach was chosen since surface recombination can be expressed through a single trap level that follows the typical SRH recombination expression[73]. The electron and hole surface lifetimes,  $\tau_{s,n/p}$ , are material dependent properties.

The direct band-to-band radiative recombination,

$$R_n^{\text{rad}} = R_p^{\text{rad}} = C_{\text{dir}}(np - \gamma_n \gamma_p n_i^2), \quad (1.15)$$

requires the direct recombination factor,  $C_{\text{dir}}$ , as material property. Auger recombination involves three carriers and becomes important at high non-equilibrium carrier densities,

$$R_n^{\text{Au}} = R_p^{\text{Au}} = (C_{\text{aug},n} n + C_{\text{aug},p} p)(np - \gamma_n \gamma_p n_i^2). \quad (1.16)$$

## 1: Utilizing modeling, experiments, and statistics for the analysis of water-splitting photoelectrodes

---

### 1.2.3. Boundary conditions

The boundary conditions for the electromagnetic waves are front illumination with collimated and uniform irradiation at  $x = 0$ , a black body at a temperature of 0 K at the back contact, and Floquet periodicity at the lateral walls (see Fig. 1.1). The spectral distribution of the illumination is detailed in section 1.3.3.

The boundary conditions for the charge transport were an ohmic contact for the semiconductor-metal interface and an adapted Schottky contact model for the semiconductor-electrolyte interface, both detailed below. The boundary conditions presented here are at steady-state.

**Ideal ohmic contact.** The ideal ohmic contact (requiring local thermodynamic equilibrium at the contact) assumes that electron and hole quasi-Fermi levels are equal. Under this condition, eqn (1.4) describes charge neutrality and is used with  $n_0 p_0 = \gamma_n \gamma_p n_{i,\text{eff}}^2$  to calculate the electron and hole equilibrium densities given as:

$$n_{\text{eq}} = \frac{1}{2}(N_D^+ - N_A^-) + \frac{1}{2}\sqrt{(N_D^+ - N_A^-)^2 + 4\gamma_n\gamma_p n_i^2}, \quad (1.17)$$

$$p_{\text{eq}} = -\frac{1}{2}(N_D^+ - N_A^-) + \frac{1}{2}\sqrt{(N_D^+ - N_A^-)^2 + 4\gamma_n\gamma_p n_i^2}. \quad (1.18)$$

The current, being conserved under steady-state, is determined by the current at the semiconductor-electrolyte interface, which must be equal to the current at the ohmic contact.

The electrostatic potential boundary condition for the ideal ohmic contact is given by:

$$\phi = V_a \text{ vs RHE}. \quad (1.19)$$

Under equilibrium and no applied potential, the potential for the ideal ohmic contact was chosen as zero vs Reversible Hydrogen Electrode (RHE).

**Adapted Schottky contact.** An adapted Schottky contact was used for the determination of the current density at the semiconductor-electrolyte interface. Our adapted Schottky contact model accounts for interface states which influence the potential barrier height,  $\phi_B$ , under dark and illumination, see Fig. 1.2. In the case of a majority carrier current, it also accounts for the interfacial potential drop distribution between the semiconductor space charge region (SCR) and the Helmholtz layer. Thus, the model enables prediction of band edge pinning or unpinning for majority carrier current.

An ideal Schottky describes the alignment of the Fermi level of the semiconductor with the dominant redox couple under equilibrium. This alignment provokes a depletion of negative charge (for n-type semiconductor), the SCR, which induces band bending[21]. If large concentrations of interface states exist within the bandgap at the surface of the semiconductor-electrolyte interface[25], the Fermi level of the semiconductor might align with the interface states energy level instead and be “pinned” at the interface states’ energy level. Upon illumination, the produced minority carriers might not cross the interface and therefore accumulate at the surface or get trapped by interface states[28] which results in a change of the SCR potential, and therefore, the Helmholtz layer (HL) (see Fig. 1.2). This effect is called “unpinning of the band” and can be interpreted as the movement of the band edges. These complex effects were considered in our adapted Schottky contact by adapting the barrier height,  $\phi_B$ , of the semiconductor SCR according to the flatband potential,  $V_{FB}$ , under illumination or dark condition. The flatband potential refers to the situation where the applied potential is such that there is no band bending or charge depletion[74]. The Mott-Schottky equation was used to determine the flatband potential of the semiconductor and therefore the barrier height. GaN has been reported to have strong interface states and therefore proves to be an excellent model material for our adapted Schottky contact model[75], [76].

The current density at the semiconductor-electrolyte interface was implemented as a Schottky contact mechanism with:

$$\mathbf{i}_n \cdot \hat{\mathbf{n}} = -qv_{s,n}(n - n_{eq}), \quad (1.20)$$

$$\mathbf{i}_p \cdot \hat{\mathbf{n}} = qv_{s,p}(p - p_{eq}), \quad (1.21)$$

$$i_{sc} = (\mathbf{i}_n + \mathbf{i}_p) \cdot \hat{\mathbf{n}} = i_H. \quad (1.22)$$



## 1: Utilizing modeling, experiments, and statistics for the analysis of water-splitting photoelectrodes

Under current conservation, the current in the semiconductor must be equal to the current in the electrolyte,  $i_H$ .  $n_{eq}$  and  $p_{eq}$  are given by:

$$n_{eq} = N_C e^{-\phi_B/V_{th}}, \quad (1.23)$$

$$p_{eq} = N_V e^{-(E_{gap}-\phi_B)/V_{th}}, \quad (1.24)$$

where the barrier height is  $\phi_B = \phi_{sc} + E_C - E_F$ , as depicted in Fig. 1.2.

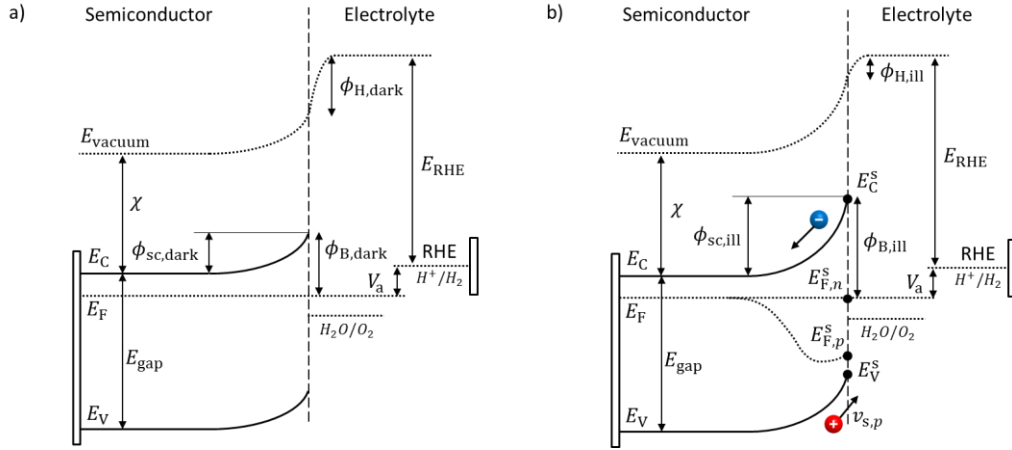


**Fig. 1.2.** Illustration of a n-type semiconductor-electrolyte interface under dark (a) and illumination (b). The applied potential  $V_a$  is between the ohmic contact at the back of the photoelectrode and the reference electrode vs RHE. The subscript “dark” stands for dark condition and “ill” for illuminated condition. The applied potential in this illustration is the same in the dark and illuminated conditions although it does not result in the same SCR. This situation is possible due to different flatband potentials in the dark and under illumination.

The electron and hole densities at the semiconductor-electrolyte interface (as required in eqns (1.20) and (1.21)) are expressed in terms of the quasi-Fermi levels, using eqns (1.5) and (1.6):

$$n = n_{\text{eq}} + \Delta n = N_C e^{-(E_C^S - E_{F,n}^S)/k_B T}, \quad (1.25)$$

$$p = p_{\text{eq}} + \Delta p = N_V e^{-(E_{F,p}^S - E_V^S)/k_B T}. \quad (1.26)$$

$\Delta n$  and  $\Delta p$  are the additional carriers created by illumination. The superscript “s” stands for properties at the semiconductor-electrolyte interface. The electron and hole densities inside the semiconductor upon illumination are also given by eqns (1.25) and (1.26) with the corresponding quasi-Fermi levels and conduction and valence energy levels at a specific location.

Under dark condition and illumination, the SCR potential has to be known to determine the carrier densities which determine the current density (eqns (1.20) and (1.21)). In the case where the applied potential equals the flatband potential,  $V_a = V_{\text{FB}}$  vs RHE, there is no band bending and the SCR potential,  $\phi_{\text{sc}}$ , equals zero. By assuming that the applied potential drops only into the SCR potential, in dark condition with no applied potential ( $V_a = 0$  vs RHE), the equilibrium SCR,  $\phi_{\text{sc,dark}}^0$ , is equal to the flatband potential under dark:

$$\phi_{\text{sc,dark}}^0 = -V_{\text{FB,dark}} \text{ vs RHE}. \quad (1.27)$$

The same assumption is used under illumination without an applied potential and therefore the SCR potential,  $\phi_{\text{sc,ill}}^0$ , equals the flatband potential under illumination:

$$\phi_{\text{sc,ill}}^0 = -V_{\text{FB,ill}} \text{ vs RHE}. \quad (1.28)$$

In the case of an applied potential, the applied potential drops in the SCR and/or in the HL:

$$V_a = \Delta\phi_{\text{sc}} + \Delta\phi_{\text{H}}, \quad (1.29)$$

## 1: Utilizing modeling, experiments, and statistics for the analysis of water-splitting photoelectrodes

---

where  $\Delta\phi_{\text{sc}}$  and  $\Delta\phi_{\text{H}}$  are the SCR and HL potential difference between no applied potential and applied potential:  $\Delta\phi_{\text{sc}} = \phi_{\text{sc}} - \phi_{\text{sc}}^0$  and  $\Delta\phi_{\text{H}} = \phi_{\text{H}} - \phi_{\text{H}}^0$ .

We distinguished two different cases for the SCR potential under an applied potential: minority current and majority current.

**Minority current.** For a minority current, i.e. a hole current in the case of a n-type material, the HL potential difference,  $\Delta\phi_{\text{H}}$ , is assumed to be negligible[21]. The SCR potential under dark or illumination is given by:

$$\phi_{\text{sc,dark}} = \Delta\phi_{\text{sc,dark}} - \phi_{\text{sc,dark}}^0 = V_{\text{a}} - V_{\text{FB,dark}}, \quad (1.30)$$

$$\phi_{\text{sc,ill}} = \Delta\phi_{\text{sc,ill}} - \phi_{\text{sc,ill}}^0 = V_{\text{a}} - V_{\text{FB,ill}}. \quad (1.31)$$

Generally, the minority current is influenced by the HL potential, species' concentration very close to the interface, and mass transport limits. Under such conditions, a detailed analysis based on the governing equation of chemical species transport and reactions in the electrolyte must be undertaken [8], [9], [67].

**Majority current.** For a majority current, i.e. an electron current in the case of a n-type material, the applied potential is assumed to drop in the SC and HL, and, consequently,  $\Delta\phi_{\text{H}}$  is assumed not equal to zero. We developed a simple analytical solution detailed in the ESI to determine  $\Delta\phi_{\text{H}}$  depending on the applied potential. In the case of a downward band bending for an n-type semiconductor, the HL potential is given by:

$$\Delta\phi_{\text{H}}(V_{\text{a}}) = \frac{V_{\text{th}} \ln\left(\frac{i_{\text{H}2}^0}{i_{\text{n}}^0}\right) + V_{\text{a}}}{1 + \alpha} < 0. \quad (1.32)$$

where the electron dark current densities is given by  $i_{\text{n}}^0 = qv_{\text{s,n}}n_{\text{eq}}$ , and the charge transfer coefficient is typically around  $\alpha \approx 0.5$ [25].

The SCR potential under dark condition and illumination in a case of a majority current in an n-type material is given by:

$$\phi_{\text{sc,dark}} = \Delta\phi_{\text{sc,dark}} - \phi_{\text{sc,dark}}^0 = V_a - \Delta\phi_{\text{H}}(V_a) - V_{\text{FB,dark}} \quad (1.33)$$

$$\phi_{\text{sc,ill}} = \Delta\phi_{\text{sc,ill}} - \phi_{\text{sc,ill}}^0 = V_a - \Delta\phi_{\text{H}}(V_a) - V_{\text{FB,ill}} \quad (1.34)$$

where the HL potential difference,  $\Delta\phi_{\text{H}}$ , depends on the applied potential given by eqn (1.32).

The same approach can be used for an upward band bending in a p-type material in the case of a majority carrier current.

A commercial finite-element solver, Comsol Multiphysics<sup>®</sup>[77], was used to solve the coupled equations with the corresponding boundary conditions.

#### 1.2.4. Numerical design of experiment

The numerical model described in the previous section depends on various parameters such as recombination rates, flatband potential, doping concentration, and charge transfer kinetics at the semiconductor-electrolyte interface, all of which significantly influence the efficiency of water-splitting photoelectrodes. We aimed at understanding the individual and coupled effects of these parameters on the performance of water-splitting photoelectrodes. A complete parameter sweep including all possible parameter combinations outgrew the resources ( $2^{14}$  combinations only considering the limiting parameter values). Consequently, we used a fractional factorial design (FFD) to statistically access the significance of the various parameters and their combinations. We chose a resolution five FFD study, reducing the number of combinations to  $2^{14-6}$  while allowing for an understanding of the main effects and first level interactions[78]. The data of the FFD were statistically analyzed using analysis of variance (ANOVA)[79] providing the ability to comment on the statistical significance of a parameter effect. We ensured the residuals were random, independent, normally-distributed, and homogeneous. We used Bonferroni limit and t-student limits to assess the significance[78].

The FFD was used to screen for the most influential parameters on the photocurrent. Specifically, we chose to investigate the influence of the various parameters on the photocurrent at *i*) a potential of 0.3 V<sub>RHE</sub>, and *ii*) a potential of 1.23 V<sub>RHE</sub>. These potentials were chosen in order to investigate two situations where different characteristics might be dominating the performance. For example, at a potential of 1.23 V<sub>RHE</sub>, i.e. at the thermodynamic oxygen evolution reaction potential,

## 1: Utilizing modeling, experiments, and statistics for the analysis of water-splitting photoelectrodes

---

the recombination rate is expected to be relatively small while at  $0.3 V_{\text{RHE}}$  it starts to be the dominating effect on the photocurrent. These two cases can also represent two characteristic PEC cell designs: *i)* a single cell design with one photo-absorber and a metallic counter electrode (the case at  $0.3 V_{\text{RHE}}$ ), or *ii)* a tandem cell design where an additional photo-electrode provides additional potential (the case at  $1.23 V_{\text{RHE}}$ ).

The FFD only revealed the most significant parameters and (linear) interactions on the photocurrent. In order to gain information about the optimum values, we subsequently conducted a parametric study on the most relevant parameters to fully understand the effect of these parameters, their interactions, and their non-linear functional dependences.

### 1.3. Application to Gallium Nitride

A single layer of  $1 \mu\text{m}$  of non-intentionally doped (nid) Gallium Nitride (GaN) with Wurtzite crystal structure was used as a model system. The planar GaN sample was immersed in  $1\text{M H}_2\text{SO}_4$  with front illumination, as depicted in Fig. 1.1. A 2D model ( $x$ - $y$  plane) was used for EMW propagation and the same optical properties were used for nid-GaN and  $n^{++}$  GaN. The electrolyte was considered in the EMW propagation. The 1D semiconductor model was only considering nid-GaN since the  $n^{++}$  GaN was used to provide a conducting layer for the ohmic contact with a sheet resistance of approximately  $50 \Omega \square^{-1}$ . The 1D model accounted for a semi-infinite layer neglecting current variations in the other directions.

#### 1.3.1. Computational details

**Electromagnetic wave propagation.** The electromagnetic wave propagation model was applied to the infinite slab of a GaN photoanode immersed into  $1\text{M H}_2\text{SO}_4$  (assumed as water). Fig. 1.1 depicts the boundary conditions that were used in the computational modeling. The light was considered as a transverse electric wave. The EMW wavelengths were varied from  $346.2\text{nm}$  to  $361.3\text{nm}$  with  $\Delta\lambda = 0.27 \text{ nm}$ . The incident angle  $\alpha_i$  was set to  $0^\circ$ . Bloch-Floquet theory was assumed for the periodicity on both side of the computational domain which is typically used for infinite stab models where no boundary effects appear and where the phase shift is determined by a wave vector and the distance between the source and the destination[80], [81]. Convergence was obtained with a direct MUMPS solver fully coupled for the corresponding variables. A relative tolerance of  $10^{-3}$  in the three

components of the electric field was used as convergence criteria. Mesh convergence was obtained for quadratic mesh elements with size ratio of 4 and element numbers,  $n_{el}$ , depending on the irradiation wavelength,  $\lambda$ , the maximum refractive index  $n_{max}$  and the layer thickness,  $d$ :  $n_{el} = n_{max}d/10/\lambda$ . The number of mesh elements perpendicularly to the direction of light propagation was fixed to 20.

**Semiconductor physics.** A 1D model was chosen for the solution of the semiconductor model with a single semiconductor layer and a semiconductor-electrolyte interface on the front side and an ohmic contact on the back side, as depicted in Fig. 1.1. The standard thickness of GaN was  $1\mu\text{m}$ . The model was calculated at steady-state. A uniform isothermal device temperature of  $25^\circ\text{C}$  was assumed. A non-degenerate semiconductor was assumed using the Maxwell-Boltzmann distribution to calculate the carrier density. Convergence was obtained with a direct MUMPS solver fully coupled for the corresponding variables. A relative tolerance in the hole and electron concentrations and the electric potential of  $10^{-3}$  was used as a convergence criteria. A segregated approach to solving electron and potential in one group, and electron, hole, and potential in the second group, appeared to be a good and fast alternative when convergence could not be obtained with the fully coupled approach. Mesh convergence was obtained for mesh element number,  $n_{mesh} = d/20\text{ nm}$ , with symmetric and linear mesh distributions and an element ratio of 7. The symmetric distribution ensured a highly resolved mesh at each interface in the model.

### 1.3.2. Material properties

The spectrally resolved refractive index,  $n$ , and the extinction coefficient (i.e. imaginary part of refractive index),  $k$ , for Wurtzite GaN were taken from Adachi[82]. The complex refractive index data of  $1\text{M H}_2\text{SO}_4$  was assumed to be of water and was taken from literature[83]. The electrolyte height was set to  $1\mu\text{m}$  in order to ensure correct calculation of the reflection behavior (for very small absorption in the wavelength range considered) while minimizing computational efforts.

GaN Wurtzite crystal structure has been studied in the last decades for applications like LEDs[84]. Parameters such as density of states for valence and conduction band, bandgap, electron affinity, relative permittivity, and recombination factors have been reported and are summarized in Table 1.1.

# 1: Utilizing modeling, experiments, and statistics for the analysis of water-splitting photoelectrodes

**Table 1.1.** Material parameters and numerical values used for the model system made of n-d-GaN

Parameters for semiconductor	Electron mobility, $\mu_n$	$682 \text{ cm}^2 \text{ V}^{-1} \text{ s}^{-1}$ [eqn (1.35)]
	Hole mobility, $\mu_p$	$143 \text{ cm}^2 \text{ V}^{-1} \text{ s}^{-1}$ [eqn (1.36)]
	Density of states, valence band, $N_V$	$T^{3/2} \cdot 8.9 \cdot 10^{15} \text{ cm}^{-3}$ [85]
	Density of states, conduction band, $N_C$	$T^{3/2} \cdot 4.3 \cdot 10^{14} \text{ cm}^{-3}$ [86]
	Direct recombination factors, $C_{\text{dir}}$	$1.1 \cdot 10^{-8} \text{ cm}^3 \text{ s}^{-1}$ [87]
	Electron Shockley-Read-Hall lifetime, $\tau_n$	$1 \cdot 10^{-9} \text{ s}$ [88]
	Hole Shockley-Read-Hall lifetime, $\tau_p$	$1 \cdot 10^{-9} \text{ s}$ [88]
	Auger recombination factor, $C_{\text{au},n/p}$	$2 \cdot 10^{-31} \text{ cm}^6 \text{ s}^{-1}$ [88], [89]
	Relative permittivity, $\epsilon_r$	8.9 [90]
	Band gap, $E_{\text{gap}}$	3.39 eV [91]
	Electron affinity, $\chi$	4.1 eV [90]
	Electron degeneracy factor, $\gamma_n$	1
	Hole degeneracy factor, $\gamma_p$	1
Determined parameters	Flatband potential under dark, $V_{\text{FB,dark}}$	$-0.49 V_{\text{RHE}}$ [eqn (1.37)]
	Flatband potential under dark, $V_{\text{FB,ill}}$	$-0.66 V_{\text{RHE}}$ [eqn (1.37)]
	Donor concentration, $N_D^+$	$4 \cdot 10^{16} \text{ cm}^{-3}$ [eqn (1.37)]
	Electron effective lifetime, $\tau_{\text{eff}}$	$8 \cdot 10^{-13} \text{ s}$ [eqn (1.14)]
	Hole effective lifetime, $\tau_{\text{eff}}$	$8 \cdot 10^{-13} \text{ s}$ [eqn (1.14)]
	Electron dark current, $i_n^0$	$1.1 \cdot 10^{-10} \text{ mA cm}^{-2}$ [eqn (A1.1)]
	Hole dark current, $i_p^0$	$1.4 \cdot 10^{-41} \text{ mA cm}^{-2}$ [eqn (A1.2)]
	Trap energy level, $\Delta E_t$	0 eV [eqns (1.12) and (1.13)]
Operating conditions	Temperature, $T$	298.15 K

The carrier concentration-dependent electron mobility for n-type GaN was approximated as [92]:

$$\mu_n(\text{cm}^2\text{V}^{-1}\text{s}^{-1}) = -98.02 \cdot \ln(N_D^+(\text{cm}^{-3})) + 4429.2, \quad (1.35)$$

the temperature-dependent hole mobility was assumed similar to p-type GaN[93]:

$$\mu_p(\text{cm}^2\text{V}^{-1}\text{s}^{-1}) = 0.039 \cdot (T(\text{K}))^2 - 26.945 \cdot T(\text{K}) + 4709.7. \quad (1.36)$$

## 1: Utilizing modeling, experiments, and statistics for the analysis of water-splitting photoelectrodes

---

The n-doped GaN used as a model system was a naturally n-type semiconductor with a donor concentration of  $4 \cdot 10^{16} \text{ cm}^{-3}$  determined through electrochemical impedance spectroscopy (see section 1.3.4). Hence, the acceptor concentration was assumed to be zero. The flatband potentials, the effective lifetimes, and the dark currents are discussed in section 1.3.4.

### 1.3.3. Experimental details

**GaN sample preparation.** GaN was deposited on a sapphire (0001) substrate using a Metal-Organic Vapor Phase Epitaxy (MOVPE) reactor of the laboratory LASPE, EPFL. A layer of 100nm Si-doped GaN with doping concentration of  $3 \cdot 10^{18} \text{ cm}^{-3}$  was deposited on the sapphire substrate followed by  $1 \mu\text{m}$  of n-doped GaN. The ohmic contact was made with indium in contact with the highly doped layer of GaN. Copper wires were fixed to indium using conductive liquid silver paint. GaN edges and ohmic contacts were protected from the electrolyte and light by applying white opaque epoxy. A photo of the GaN electrode is shown in Fig. 1.3.

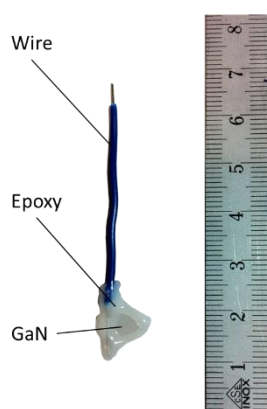


Fig. 1.3. Photo of the GaN photoelectrode.

**Light source characteristics.** A 1W UV light-emitting diode (LED) with a nominal wavelength at 368nm and with high temporal stability was used as a light source. Back and front illuminations were possible with our new PEC experimental cell with a GE 124 quartz glass (94% transmittance in the range of 300-750nm) of 2.54cm x 2.54cm-area placed on either side of the working electrode chamber (presented in Fig. 1.4). This additionally allowed for observation of the gas bubble formation. The



## 1: Utilizing modeling, experiments, and statistics for the analysis of water-splitting photoelectrodes

---

LED's spectrum was measured using a spectral-stepping of 0.27nm using a UV-Vis spectrometer (HR4000CG-UV-NIR from Ocean Optics). The total irradiance was measured with a thermal power sensor (S302C from Thorlabs). Both measurements were corrected for the absorption of the glass.

The spectral irradiance is shown in Fig. A1.1. The total measured irradiance was 9.9 mW/cm<sup>2</sup> at a distance of 4cm from the LED of which 2.45 mW/cm<sup>2</sup> could actually be absorbed by GaN with a bandgap of 3.39 eV (equivalent to a band gap wavelength of 365.6nm).

***PEC experimental setup and measurements.*** A newly developed type of PEC experimental cell presented in Fig. 1.4 was used for the experimental measurements. This cell was 3D printed using an acrylic-based photo-polymer, VeroWhite. The design of the cell allowed placement of the reference electrode very close to the working electrode and prevented gas crossovers between the working electrode and the counter electrode's chamber utilizing a Nafion membrane. Electrochemical experiments were carried out in a three-electrode setup to refer the potential of our measurements to the reversible hydrogen electrode. The electrodes were connected to a potentiostat (Bio-Logic VSP-300 controlled by the EC-lab software) for linear sweep voltammetry and impedance spectroscopy measurements. The reference electrode was Ag/AgCl (sat. KCl) and the counter electrode was Pt. The aqueous electrolyte solution was 1M H<sub>2</sub>SO<sub>4</sub>.

## 1: Utilizing modeling, experiments, and statistics for the analysis of water-splitting photoelectrodes

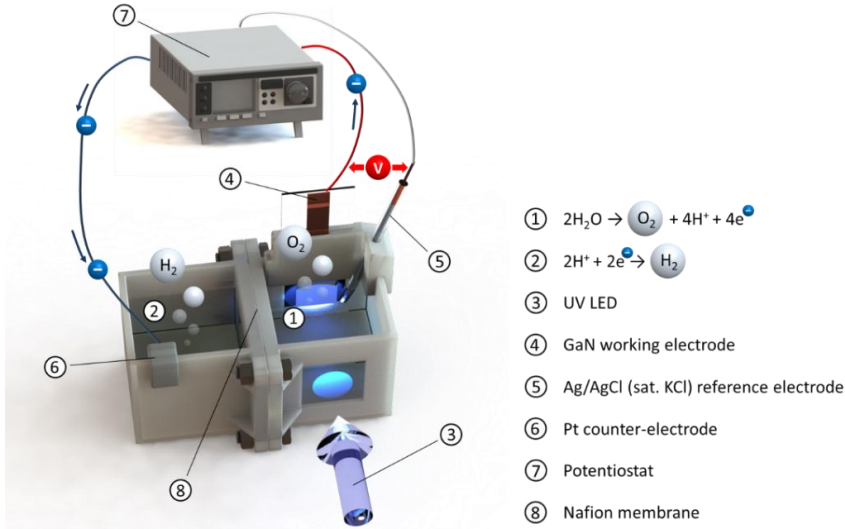


**Fig. 1.4.** Scheme of the experimental PEC water-splitting test cell connected to the potentiostat. The UV LED illuminates the working electrode through air, quartz glass, and electrolyte.

The current-voltage curves were obtained using linear sweep voltammetry with a varying voltage rate of  $10 \text{ mV s}^{-1}$  (typically in a voltage range of  $-1$  to  $1.5 V_{\text{RHE}}$ ). The voltage rate of  $10 \text{ mV s}^{-1}$  gave a stable steady-state current without any hysteresis on the photocurrent. Impedance spectra were measured at varying potentials which were scanned from  $-0.6$  to  $1 V_{\text{RHE}}$  covering a frequency range of  $300 \text{ mHz}$  to  $1 \text{ MHz}$ . The first run of the measurements are used (which ensured stable current conditions, Fig. A1.2) since GaN dissolves in the electrolyte after a few minutes under small current densities, i.e. around  $0.5 \text{ mA cm}^{-2}$ .

### 1.3.4. Experimental parameter value estimation

The flatband potential and doping concentration were experimentally estimated by electrochemical impedance spectroscopy (EIS) using Mott-Schottky theory[21], [74]:

$$\frac{1}{C_{sc}^2} = \left( \frac{dQ_{sc}}{d\phi_{sc}} \right)^{-2} = \frac{2}{\epsilon_0 \epsilon_r q N_D^+ A^2} \left( V_a - V_{FB} - \frac{k_B T}{q} \right). \quad (1.37)$$

## 1: Utilizing modeling, experiments, and statistics for the analysis of water-splitting photoelectrodes

Only frequencies higher than 50 Hz were considered in order to eliminate the effect of slow carrier processes[94]. The Mott-Schottky plot for n-doped GaN at different frequencies under dark condition is depicted in Fig. 1.5.a. The Mott-Schottky plot shows a linear relationship between  $1/C^2$  and  $V_a$ , which ensured the pinning of the band edge[95]. The Mott-Schottky plot showed only very little frequency dispersion in the frequency range of 500 Hz to 10 kHz and therefore we did not fit the impedance spectra to an equivalent circuit. Instead, a linear function was fitted to the average Mott-Schottky plot for all frequencies depicted in Fig. 1.5.a and used to determine the flatband potential and the doping concentration. The flatband potential under dark is  $-0.49 V_{RHE}$  in 1M  $H_2SO_4$  and the doping concentration  $4 \cdot 10^{16} cm^{-3}$ . The Mott-Schottky plot also confirms that non-intentionally doped GaN is naturally n-type. The flatband potential is similar to previous values found in the literature ( $-0.49 V_{RHE}$ ,  $-0.5 V_{RHE}$  and  $-0.52 V_{RHE}$  [93], [95], [96]). The doping concentration of undoped GaN can vary significantly by unintentional incorporation of extrinsic impurities, mainly silicon and oxygen. Nevertheless, the doping concentration that we found is similar to n-doped GaN with low impurities reported as  $5 \cdot 10^{16} cm^{-3}$  [96].

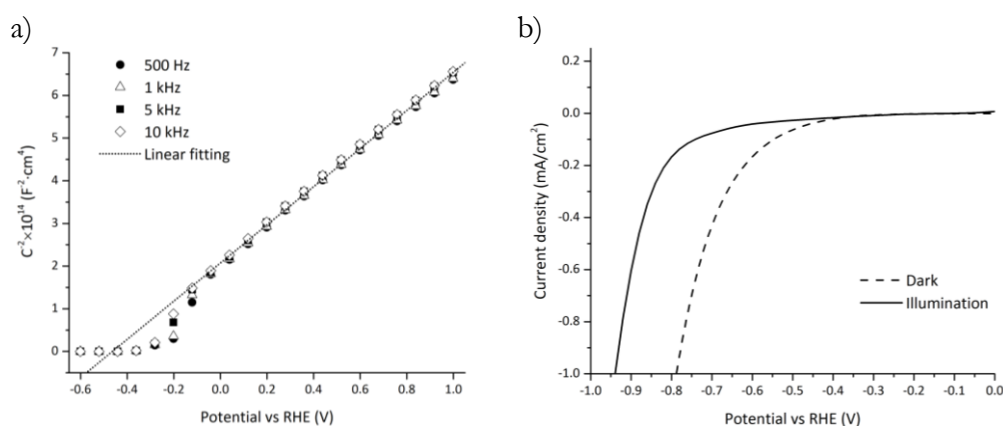


**Fig. 1.5.** a) Mott-Schottky plot for four frequencies (500 Hz, 1 kHz, 5 kHz, 10 kHz) of a 1  $\mu m$ -thick n-doped GaN sample immersed in 1M  $H_2SO_4$  electrolyte under dark. b) Experimental dark current density (dashed line) and photocurrent density (solid line) vs RHE.

The small trough around  $-0.5 V_{RHE}$  to  $-0.1 V_{RHE}$  depicted in Fig. 1.5.a is assumed to result from interface states near the conduction band, i.e. the measured capacitance being the sum of the SC and the interface states capacitance [97]. Interface states

## 1: Utilizing modeling, experiments, and statistics for the analysis of water-splitting photoelectrodes

usually follow a Gaussian distribution which is in accordance with the observed trough (see Fig. 1.5.a).

Interface states charging under illumination can cause a change in the flatband potential as previously mentioned and this effect has been observed for GaN in previous work[98]. The shift in the flatband potential was measured by comparing the current for water reduction under dark and illumination depicted in Fig. 1.5.b. The flatband potential shift was -0.17 V, which gave a flatband potential of -0.66 V<sub>RHE</sub> under illumination.

### 1.3.5. Numerical model validation

Linear sweep voltammetry measurements and numerical simulations on GaN were used for the comparison between the steady-state numerical model and the experimental results. The surface charge transfer kinetic velocities for holes and electrons (see eqns (1.20) and (1.21)), electron and hole surface recombination lifetimes (see eqn (1.14)), and HER exchange current density (see eqn (1.32)) were estimated from linear sweep voltammetry by parameter fitting and are summarized in Table 1.2. The surface charge transfer velocities are smaller compared to typical semiconductor-metal interface velocities (usually in the range of  $1\text{-}10^4 \text{ m}\cdot\text{s}^{-1}$ )[70] as the catalytically-driven electrochemical reaction slows down the charge transfer. The small surface recombination lifetimes indicated that surface recombination is a major loss in the case of n-d-GaN. The exchange current density is three orders of magnitude below state-of-art HER catalysts[68]. The modeled case using parameter values indicated in Table 1.1 and Table 1.2 is considered as our reference case.

**Table 1.2.** Material parameters determined by fitting to the linear sweep voltammetry measurement.

Fitting parameters	Electron surface transfer kinetic velocity, $v_{s,n}$	$1 \cdot 10^{-3} \text{ m} \cdot \text{s}^{-1}$
	Hole surface transfer kinetic velocity, $v_{s,p}$	$5 \cdot 10^{-2} \text{ m} \cdot \text{s}^{-1}$
	Electron surface recombination lifetime, $\tau_{s,n}$	$8 \cdot 10^{-13} \text{ s}$
	Hole surface recombination lifetime, $\tau_{s,p}$	$8 \cdot 10^{-13} \text{ s}$
	HER exchange current density, $i_{\text{H}_2}^0$	$1 \cdot 10^{-3} \text{ mA} \cdot \text{cm}^{-2}$

The only parameter that is changed in the experiment is the applied potential. Therefore, we compared the numerical current-potential dependency under dark and illumination with the experimental current-potential measurements. The

## 1: Utilizing modeling, experiments, and statistics for the analysis of water-splitting photoelectrodes

measurements of n-GaN were stable over eight minutes during linear sweep voltammetry and at photocurrent densities below one  $\text{mA cm}^{-2}$  (see Fig. A1.2). We used the first linear sweep voltammetry measurements (from 1.5  $V_{\text{RHE}}$  to  $-1 V_{\text{RHE}}$ , in about 2 minutes) for experimental-numerical comparison because GaN suffers from photocorrosion in acidic solutions although it is known to be resistant to corrosion[99], [100]. The numerically calculated dark current compares well to the experimentally measured current as depicted in Fig. 1.6. The calculated slope in the photocurrent is steeper at the onset potential than the measured one. This is explained by the losses within the highly doped GaN layer used for the charge collection, which were not accounted for in the model.

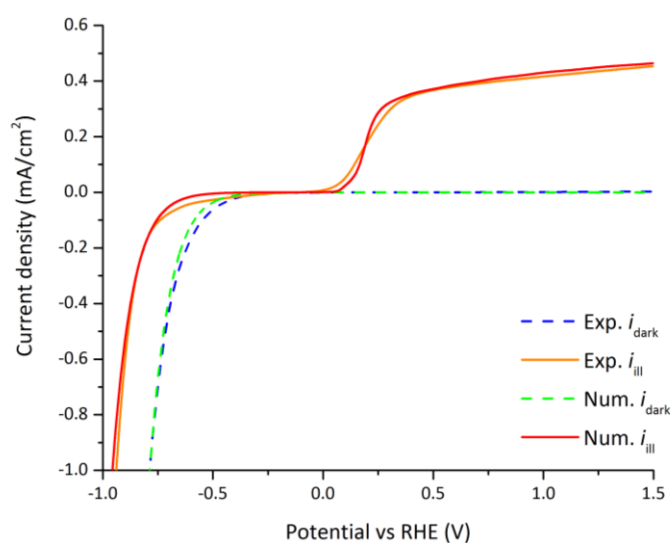


**Fig. 1.6.** Dark current densities (dashed lines) and photocurrent densities (solid lines) vs RHE, and comparison between experimentally measured values and numerically calculated values.

Two different dark current regimes can be distinguished in Fig. 1.6. Above the flatband potential ( $-0.49 V_{\text{RHE}}$ ) the dark current is a minority current of only a few nA since n-GaN is naturally n-type with a negligible amount of holes to actually enable the water oxidation. Indeed, the hole dark current density is only  $1.4 \cdot 10^{-41} \text{ mA cm}^{-2}$  (see Table 1.1) producing a negligible dark current. Around and below the flatband potential, the current shifts to a majority current as there is no more

## 1: Utilizing modeling, experiments, and statistics for the analysis of water-splitting photoelectrodes

---

potential barrier with a downward bending band. In this case, the applied potential drops not only in the SC layer but also in the H layer in accordance with eqn (1.32).

Four different photocurrent regimes can be distinguished in Fig. 1.6. In the first regime at potentials between 0.4 to 1.5 V<sub>RHE</sub>, the photocurrent slightly decreases from the maximum photocurrent of 0.42 mA cm<sup>-2</sup> at 1.5 V<sub>RHE</sub> to 0.37 mA cm<sup>-2</sup> at 0.5 V<sub>RHE</sub>. In this regime the current density is a minority charge carrier current, holes are transferred from the semiconductor to the electrolyte for the water oxidation reaction. The applied potential and the band bending at the semiconductor-electrolyte interface provides an electric field large enough to allow for efficient charge separation. Recombination rates represented a 27% loss on the total photo-generation rate at 1.5 V<sub>RHE</sub> and 44 % loss at 0.4 V<sub>RHE</sub>. This non-linear current drop is mainly associated to surface recombination since  $\tau_{s,n/p} \ll \tau_{bulk,n/p}$  and consequently  $\tau_{eff,n/p} \approx \tau_{s,n/p}$  (see eqn (1.14), and Table 1.1 and Table 1.2) and is explained in detail in section 1.3.7. Above 0 vs RHE, the potential drops only in the semiconductor SCR.

In the second regime at potentials between 0.4 and 0 V<sub>RHE</sub>, the photocurrent abruptly decreases to zero at around 0 V<sub>RHE</sub>. The electric field created by the potential and the band bending is not sufficient for charge separation and electron-hole recombination starts to dominate. Recombination rates represent a 50% loss on the total photo-generation rate at 0.28 V<sub>RHE</sub> and a 100% loss at 0.05 V<sub>RHE</sub>.

In the third regime between potentials at 0 V<sub>RHE</sub> and -0.66 V<sub>RHE</sub>, the band bending starts to decrease until reaching the flatband potential conditions at -0.66 V<sub>RHE</sub>. The recombination of electron and holes is complete and there is no photocurrent.

In the fourth regime between potentials -0.66 V<sub>RHE</sub> and -1.0 V<sub>RHE</sub>, the current becomes a majority carrier current because of the downward band bending. Electrons are transferred from the semiconductor to the electrolyte for the water reduction reaction. The current decreases exponentially following eqn (1.21). The applied potential below the flatband potential drops not only in the SCR, but also in the HL layer in accordance with eqn (1.32). This behavior is consistent with the dark condition, only the flatband potential shifts between dark and illumination.

In addition to predicting the experimental values accessible by measurements, the benefit of the numerical model is that it allows for the prediction of the depth-dependent charge carrier generation, the depth-dependent electron and hole concentrations, and the depth-dependent energy levels of the quasi-Fermi levels, conduction band, and valence band in the semiconductor. Fig. A1.3 to Fig. A1.5

## 1: Utilizing modeling, experiments, and statistics for the analysis of water-splitting photoelectrodes

show the distribution of these parameters for the reference case under illumination at 0 V<sub>RHE</sub>. The current is also depicted in Fig. 1.6 (red curve at 0 V<sub>RHE</sub>). The accessibility of such concentration and energy profiles greatly supports the understanding and interpretation of the observed current-voltage behavior.

### 1.3.6. Numerical design of experiment

The FFD was used to screen for the most influential semiconductor and semiconductor-electrolyte interface parameters on the photocurrent, i.e. fourteen parameters with two levels as presented in Table 1.3. The minimum and maximum values were carefully chosen to lie within realistic limits as otherwise no convergence in the numerical solution was achieved. The baseline parameters were required to lie between the upper and lower limits.

**Table 1.3.** Minimum and maximum parameter values used in the FFD under illumination

Parameters	Unit	Minimum	Maximum
Electron surface transfer kinetic velocity, $v_{s,n}$	m s <sup>-1</sup>	$1 \cdot 10^{-4}$	$1 \cdot 10^{-2}$
Hole surface transfer kinetic velocity, $v_{s,p}$	m s <sup>-1</sup>	$1 \cdot 10^{-2}$	$1 \cdot 10^{-1}$
Direct recombination factor, $C_{dir}$	cm <sup>3</sup> s <sup>-1</sup>	$1 \cdot 10^{-9}$	$1 \cdot 10^{-7}$
Effective electron lifetime, $\tau_{eff,n}$	s	$1 \cdot 10^{-13}$	$1 \cdot 10^{-11}$
Effective hole lifetime, $\tau_{eff,p}$	s	$1 \cdot 10^{-13}$	$1 \cdot 10^{-11}$
Electron Auger recombination factor, $C_{aug,n}$	cm <sup>6</sup> s <sup>-1</sup>	$1 \cdot 10^{-33}$	$1 \cdot 10^{-31}$
Hole Auger recombination factor, $C_{aug,p}$	cm <sup>6</sup> s <sup>-1</sup>	$1 \cdot 10^{-33}$	$1 \cdot 10^{-31}$
Donor concentration, $N_D^+$	cm <sup>-3</sup>	$1 \cdot 10^{16}$	$1 \cdot 10^{17}$
Flatband potential, $V_{FB}$	V <sub>RHE</sub>	-0.5	-0.7
Relative permittivity, $\epsilon_r$	-	7	11
Semiconductor film thickness, $d$	μm	0.8	1.2
Hole mobility, $\mu_p$	V <sup>-1</sup> s <sup>-1</sup>	50	200
Effective density of states, valence band, $N_V$	cm <sup>-3</sup>	$8 \cdot 10^{17}$	$6 \cdot 10^{18}$
Effective density of states, conduction band, $N_C$	cm <sup>-3</sup>	$1 \cdot 10^{19}$	$8 \cdot 10^{19}$

In order to ensure that the residuals were normally distributed, transformations in the photocurrent results were performed at both potentials investigated, i.e. 0.3V and 1.23 vs RHE. At 0.3 V<sub>RHE</sub>, a power function,  $y' = (y + k)^\lambda$ , with  $k = 0.0057$  and  $\lambda = 0.61$  was used as the transformation function. At a potential of 1.23 V<sub>RHE</sub>, a power function with  $k = 0$  and  $\lambda = 1.99$  was used. At both potentials, the normal plot of the residuals indicated no abnormalities and the R<sup>2</sup> coefficients for a normal distribution were reasonable (0.95 for 1.23 V<sub>RHE</sub> and 0.88 for 0.3 V<sub>RHE</sub>). The residuals

## 1: Utilizing modeling, experiments, and statistics for the analysis of water-splitting photoelectrodes

---

versus predicted values plots showed an approximately constant level of the studentized residuals across all predicted values and no outliers were found outside of the 95% confidence control limit in the studentized residuals versus run plot. Hence, the multiple regression model could be validated and the influence of each parameter could be safely investigated.

The Pareto charts depicted in Fig. 1.7 show the significant parameters or interactions, i.e. parameters or interactions with an effect above the Bonferroni limit. The most relevant factors at 1.23 V<sub>RHE</sub> are, from the largest to the smallest influence:  $\tau_{\text{eff},p}$ ,  $\tau_{\text{eff},n}$ , the interaction between effective hole and doping concentration  $\tau_{\text{eff},n} \cdot N_{\text{D}}^+$ , and  $N_{\text{D}}^+$  (Fig. 1.7.a). The other significant effects like the interaction between effective electron and hole lifetime,  $\tau_{\text{eff},n} \cdot \tau_{\text{eff},p}$ , and  $\mu_p$  are also presented in Fig. 1.7.a although their effects are lower compared to the effective lifetimes and the doping concentration. The bulk lifetimes are measured values[88] which are intrinsic properties of GaN, but the lifetimes related to the surface recombination process depend on the semiconductor-electrolyte interface. The surface recombination lifetimes were more than three orders of magnitude lower than the bulk recombination and dominated the effective lifetimes (Table 1.1 and Table 1.2). Increasing the surface recombination lifetimes has a positive effect on the photocurrent (white bar in Fig. 1.7.a) and can practically be obtained by surface passivation or by application of catalyst. The negative effect on photocurrent of the combined effective electron and hole lifetime ( $\tau_{\text{eff},n} \cdot \tau_{\text{eff},p}$ ) is explained by the non-linear dependence of these parameters on the photocurrent, inconsistent with the FFD assumption of linearity.

For the combined effect of effective electron lifetime and doping concentration ( $\tau_{\text{eff},n} \cdot N_{\text{D}}^+$ ), the negative effect of the doping concentration on the photocurrent is dominant. A more clear dependence of the most significant parameters on the photocurrent is investigated in the parametric study in the next section.



# 1: Utilizing modeling, experiments, and statistics for the analysis of water-splitting photoelectrodes

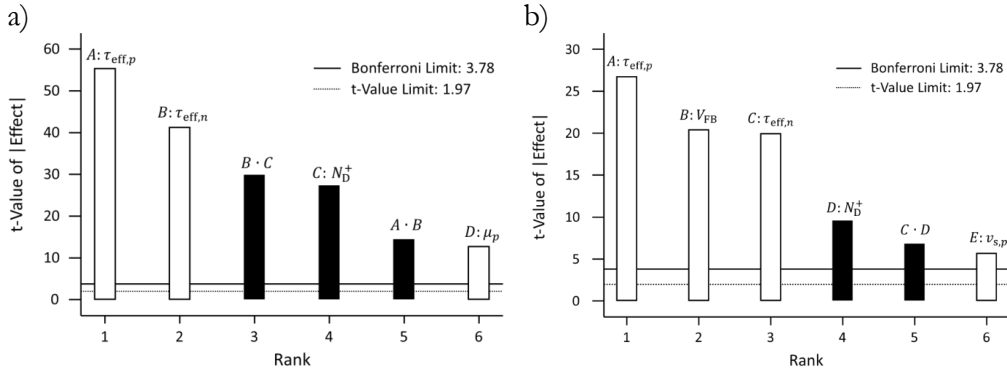


**Fig. 1.7.** Pareto plots indicating the significance of the photocurrent response at a potential of 1.23 V<sub>RHE</sub> (a) and 0.3 V<sub>RHE</sub> (b) vs RHE calculated utilizing the FFD of experiment. White bars indicate an increase and black bars a decrease, respectively, of the photocurrent when increasing the corresponding parameter.  $\tau_{eff,n}$  and  $\tau_{eff,p}$  are effective electron and hole lifetimes,  $N_D^+$  is the doping concentration, and  $\mu_p$  is the hole mobility,  $V_{FB}$  is the flatband potential, and  $v_{s,p}$  is the hole surface transfer kinetic velocity.

We used an effective lifetime combining surface recombination and SRH bulk recombination (see eqn (1.14)) and therefore the charge carrier concentration in the semiconductor is related to the surface lifetimes. Consequently, the observed strong dependence on doping concentration is a result of the effective lifetime assumption and not necessarily a physical result.

The most significant parameters influencing the photocurrent at 0.3 V<sub>RHE</sub> are, from the largest to the smallest influence:  $\tau_{eff,p}$ ,  $V_{FB}$ , and  $\tau_{eff,n}$  (Fig. 1.7.b). The other significant effects are also indicated:  $N_D^+$  the interaction between effective electron lifetime and doping concentration  $\tau_{eff,n} \cdot N_D^+$ , and  $v_{s,p}$ . According to FFD, it is beneficial for the photocurrent at 0.3 V<sub>RHE</sub> to reduce the effective recombination of electrons and holes (dominated by surface lifetimes), and to increase the flatband potential.

## 1.3.7. Parametric analysis on key factors

A parametric study was done to precisely understand the functional dependence of the photocurrent on the most significant parameters according to FFD, i.e. the surface lifetimes of electrons and holes and the doping concentration at 1.23 V<sub>RHE</sub>, and the surface lifetimes of the electrons and holes and the flatband potential at 0.3 V<sub>RHE</sub>.

## 1: Utilizing modeling, experiments, and statistics for the analysis of water-splitting photoelectrodes

The influence of the hole surface lifetime on the photocurrent for varying applied potential is presented in Fig. 1.8. An increase of the hole surface lifetime has not only the beneficial effect of shifting the onset potential but also allows the further increase of the photocurrent at larger applied potentials. This unusual effect for an OER photocatalyst has been observed for hematite and TiO<sub>2</sub> photoelectrodes whose surfaces were modified with phosphate ions[48], [101]. In both cases surface phosphate ions appeared to prolong the lifetime of holes on the surface. Interestingly, our numerical model is consistent with this effect using GaN as a reference model system for small hole surface lifetimes (around 1ps). At larger hole surface lifetimes (above 0.1 to 1ns), the current-potential dependency follows the expected behavior, namely that surface recombination is negligible for an applied potential above 0.2 V<sub>RHE</sub>.

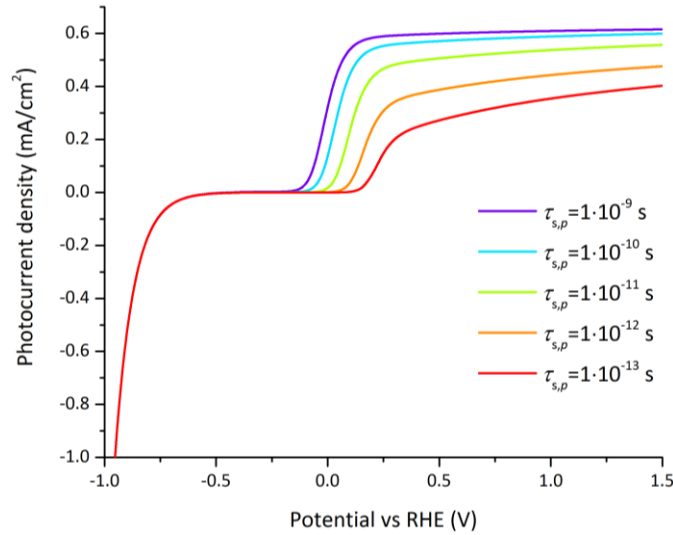


**Fig. 1.8.** Photocurrent-voltage curves for varying hole surface lifetimes for the reference case (parameters indicated in Table 1.1 and Table 1.2. For large hole surface lifetimes (above 0.1 to 1 ns), surface recombination is negligible at large applied potentials. For small hole surface lifetimes (around 1 ps), the photocurrent is still affected by surface recombination at large potentials.

The dependence of the photocurrent densities at 1.23 V<sub>RHE</sub> on surface lifetimes and doping concentration are depicted in Fig. 1.9. At low doping concentration, i.e.  $1 \cdot 10^{16}$  cm<sup>-3</sup> for GaN, an increase of the effective hole and electron surface lifetimes results in an increase in photocurrent (Fig. 1.9). If the electron surface lifetime is

## 1: Utilizing modeling, experiments, and statistics for the analysis of water-splitting photoelectrodes

---

large enough, e.g. 1 ns, the hole surface lifetime has a less significant impact on the photocurrent; a relative increase by 9.5% ( $0.06 \text{ mA cm}^{-2}$ ) for 4 orders of magnitude difference of hole surface lifetime is observed (violet line in Fig. 1.9). For low electron surface lifetime, e.g. 0.1 ps, increasing the hole surface lifetime from 1ps to 0.1ns increases the photocurrent by  $0.34 \text{ mA cm}^{-2}$ , which represents a relative increase of 58%. Increasing the doping concentration to  $1 \cdot 10^{18} \text{ cm}^{-3}$  results in a photocurrent which is not affected by the electron surface lifetime (Fig. 1.9). On the other hand, the hole surface lifetime is still significant at these larger doping concentrations, i.e. increasing the hole surface lifetime from 1ps to 1ns increases the photocurrent by  $0.21 \text{ mA cm}^{-2}$ .

The photocurrent, being a minority current, is generally more influenced by the hole surface lifetime. Especially at large hole surface lifetimes, the influence of electron surface lifetime becomes negligible. The insensitivity of the photocurrent on electron surface lifetime at high doping concentrations results from the dominating terms in the recombination, namely the electron concentration and hole surface lifetime (see eqn (1.11)). As mentioned, the photocurrent results from the combined influence of the numerical value of the hole surface lifetime, electron surface lifetime, and doping concentration. Therefore under low doping and low hole surface lifetime the electron surface lifetime can still have an impact on the photocurrent at  $1.23 \text{ V}_{\text{RHE}}$  which appears counterintuitive.

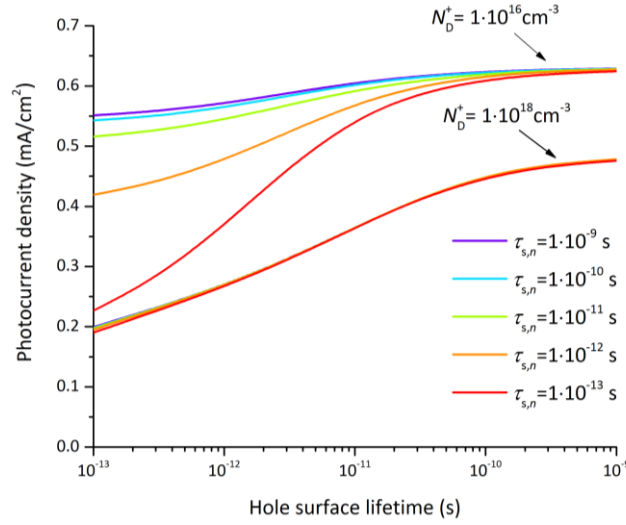


**Fig. 1.9.** Photocurrent density at 1.23 V<sub>RHE</sub> as a function of the hole surface lifetime for various electron lifetimes ( $\tau_{s,n} = 10^{-9}, 10^{-10}, 10^{-11}, 10^{-12}, 10^{-13}$  s) and two doping concentrations ( $N_D^+ = 10^{16} \text{ cm}^{-3}$  and  $N_D^+ = 10^{18} \text{ cm}^{-3}$ ).

The doping concentration-dependent current-voltage behavior under illumination is depicted in Fig. 1.10. An optimal doping concentration is found at a value of  $N_D^+ = 10^{16} \text{ cm}^{-3}$  above about 0.2 V<sub>RHE</sub> as depicted in Fig. A1.6. The optimum is caused by different and opposing effects. On one hand a decrease of the doping concentration leads to a lower Fermi level. Since the Fermi level aligns with the interface states located at the semiconductor-electrolyte interface, it leads to a higher band bending at the semiconductor-electrolyte interface and therefore a positive shift of the onset potential and an increase of the photocurrent (can be clearly observed on the negative potential side). On the other hand, the recombination rate increases with larger doping concentrations simply because of the increased electron concentration which reduces the photocurrent. At very low doping concentrations, the semiconductor is completely depleted and there is no band bending but instead a linearly increasing band potential throughout the entire semiconductor. By assuming locally a constant potential change and by integrating the drift-diffusion equations (eqns (1.7) and (1.8)) within the semiconductor, the current-potential relation is predicted by Ohm's law. This situation is depicted Fig. 1.10 at a doping concentration of  $N_D^+ = 10^{14} \text{ cm}^{-3}$  where the photocurrent versus potential starts to show a linear trend. These effects must be considered when optimizing the photocurrent density by variations in doping concentration and operating potential.

## 1: Utilizing modeling, experiments, and statistics for the analysis of water-splitting photoelectrodes

For example at an operating potential of  $0.3 \text{ V}_{\text{RHE}}$ , the photocurrent density increases by  $0.25 \text{ mA cm}^{-2}$  by changing the doping concentration from  $10^{14} \text{ cm}^{-3}$  to  $10^{16} \text{ cm}^{-3}$  which represents a relative gain of 69 %.

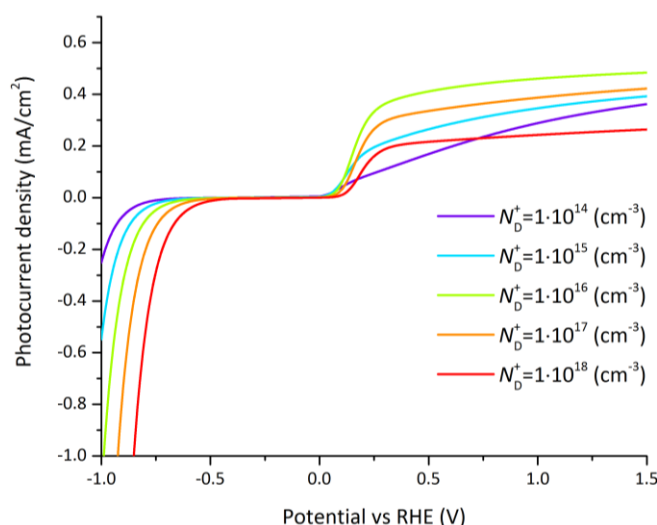


**Fig. 1.10.** Photocurrent-voltage curves for varying doping concentration for the reference case (parameters indicated in Table 1.1 and Table 1.2. For small doping concentrations (below  $10^{14} \text{ cm}^{-3}$ ), the photocurrent-potential relation is linear. For intermediate doping concentrations (around  $10^{16} \text{ cm}^{-3}$ ), the photocurrent shows an optimum at which the band bending is maximized and recombination is reasonable. At large doping concentrations (above  $10^{18} \text{ cm}^{-3}$ ) recombination dominates.

The photocurrent densities at  $0.3 \text{ V}_{\text{RHE}}$  depend most significantly on the flatband potential, electron lifetime, and hole surface lifetime. The variation of the flatband potential gives rise to a shift of the onset potential (see Fig. A1.7). A more complex behavior is observed when also varying the surface lifetimes as depicted in Fig. 1.11. At a flatband potential of  $-0.5 \text{ V}_{\text{RHE}}$ , the band bending is reduced resulting in a decreased electric field and consequently a decreased hole transfer from the semiconductor to the electrolyte (the photocurrent). Since the electric field is lower, recombination becomes the dominating loss which is directly related to the hole and electron surface lifetimes (Fig. 1.11.a).

A significant effect of the hole surface lifetime on the photocurrent is observed at a flatband potential of  $-0.5 \text{ V}_{\text{RHE}}$  (Fig. 1.11.a). At low electron lifetime, i.e.  $0.1 \text{ ps}$ , the

## 1: Utilizing modeling, experiments, and statistics for the analysis of water-splitting photoelectrodes

photocurrent increases from 0 mA cm<sup>-2</sup> to 0.56 mA cm<sup>-2</sup> when changing the hole surface lifetime by four orders of magnitude, i.e. from 0.1 ps to 1 ns. Even at higher electron surface lifetime, i.e 1ns, the photocurrent increases from 0.24 mA cm<sup>-2</sup> to 0.54 mA cm<sup>-2</sup> (a relative increase of 55 %) when increasing the hole surface lifetime from 0.1 ps to 1 ns. The behavior is similar at a flatband potential of -0.7 V<sub>RHE</sub> (Fig. 1.11.b), although the electron and hole surface lifetimes have a smaller impact: the photocurrent increases by 0.4 mA cm<sup>-2</sup> (from 0.18 mA cm<sup>-2</sup> to 0.58 mA cm<sup>-2</sup>, i.e a relative increase of 69 %) when increasing the hole surface lifetime from 0.1 ps to 1ns at an electron surface lifetime of 0.1 ps. At an electron surface lifetime of 1ns, the photocurrent increases by 0.29 mA cm<sup>-2</sup> (a relative increase of 48 %) when increasing the hole surface lifetime from 0.1 ps to 1 ns.

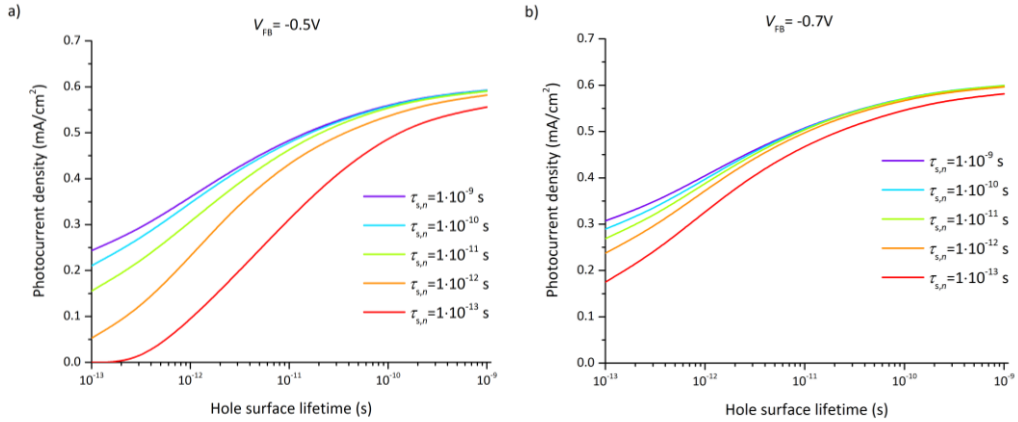


**Fig. 1.11.** Photocurrent density at 0.3 V<sub>RHE</sub> as a function of the hole surface lifetime for various electron lifetimes ( $\tau_{s,n} = 10^{-9}, 10^{-10}, 10^{-11}, 10^{-12}, 10^{-13}$  s) and two flatband potentials: a)  $V_{FB} = -0.5$  V<sub>RHE</sub>, and b)  $V_{FB} = -0.7$  V<sub>RHE</sub>.

### 1.4. Summary and conclusion

A multi-physics model of a semiconductor water-splitting photoelectrode immersed in electrolyte was developed. The model coupled electromagnetic wave propagation, charge carrier generation and transport, and charge transfer at the semiconductor-electrolyte interface. The model provided, among others, spatially resolved energy band diagrams, charge carrier concentrations, and generation and recombination profiles in the semiconductor. The model incorporated an adapted Schottky contact

## 1: Utilizing modeling, experiments, and statistics for the analysis of water-splitting photoelectrodes

---

at the semiconductor-electrolyte interface, accounting for pinning and unpinning of the band edges and for potential drop within the SCR as well as the HL. The interface model presented allows for a straightforward extension to semiconductor-catalyst-solution systems with metallic, adaptive and molecular catalysts by using the boundary conditions presented in the work of Mills et al.[55]. The HL played only a role in charge transfer at the semiconductor-electrolyte interface for majority carrier currents. In this case, the potential distribution between the HL and the SCR was determined by a newly derived analytical solution.

The numerical model was applied to our model system composed of a non-intentionally doped n-type Gallium Nitride (GaN) with Wurtzite crystal structure photoelectrode layer immersed in 1M sulfuric acid. GaN was chosen here as it allows for unbiased photoelectrochemical water-splitting. Additionally, GaN has been shown to be considerably resistant to corrosion in many solutions in the dark[92] although it gradually dissolves under illumination. GaN has been known to have interface states, therefore flatband potentials under dark and illumination were experimentally determined by electrochemical impedance spectroscopy using Mott-Schottky theory. Flatband potentials under dark and illumination were found to be  $-0.49 V_{\text{RHE}}$  and  $-0.66 V_{\text{RHE}}$ . Impedance spectroscopy was also used to estimate the intrinsic doping concentration of n-doped GaN, estimated as  $4 \cdot 10^{16} \text{ cm}^{-3}$ . Linear sweep voltammetry was then used to determine photocurrent response as a function of the applied potential to which the modeled photocurrent-potential response was compared in order to validate the multi-physics model.

The multi-physics model allowed representation of numerous semiconductor materials with numerous semiconductor-electrolyte interface properties such as electron and hole mobilities, surface lifetimes, flatband potential, permittivity, doping concentration, bulk SRH recombination, and hole and electron interface kinetics. The large number of relevant material and interface characteristics renders the identification of the most significant parameter(s) challenging. Statistical tools provide a pathway for solving this challenge as demonstrated in this study. The validated model was used in a FFD of experiment to statistically identify the most significant material and interface parameters and device dimensions on the photocurrent. Key factors were identified at two different potentials:  $0.3 V_{\text{RHE}}$  and  $1.23 V_{\text{RHE}}$ . Hole and electron surface lifetimes and doping concentration appeared to be the most significant factors at  $1.23 V_{\text{RHE}}$ . At  $0.3 V_{\text{RHE}}$ , hole and electron surface lifetimes and flatband potential were the most significant factors. The statistically identified most significant parameters were further investigated and theoretically optimized in a detailed parameter study. The parametric analysis provided

## **1: Utilizing modeling, experiments, and statistics for the analysis of water-splitting photoelectrodes**

---

quantifiable effects and functional dependence of the photocurrent on the predominant factors previously determined by FFD analysis.

The developed methodology uses an experimentally-validated numerical model and statistical analysis to provide understanding of the performance of water-splitting photoelectrodes. It allows for the identification of the most significant parameters on performance. Subsequent in-depth parametric analysis of the most significant parameters allows for the quantification of their effect and subsequent optimization of the device for maximum performance. The presented methodology provides a general approach to identify and quantify main material challenges and design considerations in functioning water-splitting photoelectrodes. The predictive character of the validated model can be further exploited with confidence to approach and investigate morphologically complex electrodes and material classes for which research-related questions are not yet answered.



# Determination and optimization of material parameters of particle-based LaTiO<sub>2</sub>N photoelectrodes<sup>1</sup>

## 2.1. Introduction

PEC approaches using particle-based photoelectrodes (PEs), which can be fabricated with simple dip or slurry coating procedures that are already scaled in industrial battery production, can be a route to efficient and economic solar hydrogen. LaTiO<sub>2</sub>N (LTON) is a promising PEC material with a suitable bandgap of 2.1 eV[19], [102] which enables the absorption of visible light up to 590 nm. Indeed, highly performing particle-based LTON PEs with a photocurrent density up to 8.9 mA cm<sup>-2</sup> at 1.23 V<sub>RHE</sub> were recently reported[103]. However, the various material parameters of particle-based LTON PEs must be determined, and the impact of each parameter on the photocurrent and their underlying multi-physical phenomena must be investigated and understood to further improve the performance of particle-based LTON PEs.

Numerical modelling can help in identifying crucial material, processing, and design challenges for PEs, not accessible and identifiable by experimental investigations. Berger et al. introduced the first 1D PEC electrode model for investigating the light absorber's role on the device performance by accounting for the charge transport in the electrolyte and in the semiconductor[61]. This model was developed for

---

<sup>1</sup> The material from this chapter has been published in Journal of Materials Chemistry A under the reference 'Y. K. Gaudy, S. Dilger, S. Landsmann, U. Aschauer, S. Pokrant and S. Haussener, *J. Mater. Chem. A*, 2018, 6, 17337'.

## 2: Determination and optimization of material parameters of particle-based LaTiO<sub>2</sub>N photoelectrodes

---

homogeneous, thin-film photoabsorber materials and metallic catalysts and was compared to a crystalline-Si PEC cell with Pt as a hydrogen evolution reaction catalyst, two materials with well-known material parameters. These parameters were either taken from literature or assumed (for example, the charge transfer rate constant from the semiconductor to the electrode). Cendula et al.[63] introduced a 1D model capable of describing  $I$ - $V$  curves and energy band dynamics of photoabsorbers in direct contact with an electrolyte. Their work was based on n-type hematite and p-type cuprous oxide, two known semiconductor materials. However, some material parameters such as the densities of states of the conduction and valence band and the relative permittivity of cuprous oxide were assumed. The 1D numerical model of charge transfer at the semiconductor-catalyst-electrolyte interface by Mills et al. provided the flexibility to account for different types of catalysts (metallic, adaptive, and molecular), and has provided insights into the  $I$ - $V$  characteristics of semiconductor-catalyst-solution systems[55]. Their model was based on semi-classical macroscopic semiconductor physics, similarly to what we use here. They assumed numerous parameters (for example, the hole/electron transfer rate constants) and compared their results to experiments with a n-TiO<sub>2</sub> photoabsorber and IrOx, hydrous Ni(OH)<sub>2</sub>/NiOOH, and NiOx catalysts. Our previous work with a 1D validated numerical model, accounting for EMW within the electrolyte and semiconductor and for charge carrier transport and conservation within the semiconductor and at the semiconductor-electrolyte interface, has shown the significant impact of surface lifetimes on the photocurrent for a thin-film GaN photoanode, a well-defined material with known material parameters[104]. It becomes obvious from these early modelling works that the knowledge of the material parameters is key for model accuracy. However, determining the material parameters of many well-known, well-defined materials and films is already a challenge. For this reason, successful models have been mostly limited to classical semiconductor materials such as Si, GaAs, GaInP, TiO<sub>2</sub> or GaN[61], [104]–[107], in monocrystalline and almost defect free thin films. Detailed experimental characterization of these materials has been done for decades, and essential material parameters (e.g. electrical transport properties or electron and hole recombination lifetimes) are well documented in literature[70], [108]–[110] or in well referenced electronic archives[111]. However, many of the recent materials (e.g. BiVO<sub>4</sub>[112], [113], SrTiO<sub>3</sub>[114], [115] and LTON) used in high performing PEs are complex oxides or oxynitrides. The parameters of these materials are less investigated and also less straight forward to determine since variations in the synthesis procedure induce significant differences in terms of defect density and morphology for the same compound. Transport properties are especially difficult to assess since the

## 2: Determination and optimization of material parameters of particle-based LaTiO<sub>2</sub>N photoelectrodes

---

preparation of comparable thin films is not yet possible for some complex oxides and oxynitrides like LTON[116]. This is one of the significant challenges in building a realistic numerical model of particle-based PEs of oxides and oxynitrides.

The second challenge is related to the multi-physical nature of PEs[14], [117]. Most of the material parameters are difficult to determine since they depend on multi-physical interactions. It is often not possible to determine them with one dedicated experiment or numerical model. Instead, a combination of experiments and numerical modeling must be used to isolate each physical process with its related parameters. Numerous experiments, such as spectrophotometry, EIS, and conduction measurements, are required and need to be carefully combined with molecular and macroscopic numerical models in order to build a complete model capable of describing the  $I$ - $V$  characteristics of oxide and oxynitride PEs.

The third challenge is related to the morphological complexity of particle-based PEs for which a traditional 1D model is not appropriate and a 3D discrete model is not yet practical. In such a complex PE, each photocatalytic particle is almost fully surrounded by an electrolyte enabling the OER. The use of a 1D model would reduce this continuous interface to a single one at the model's boundary. Therefore, a 1D model requires to determine an average path for charge transport and conservation which can only be found once all other material parameters are known. In contrast, a 3D-scale model based on the exact morphology can fully capture the physical behavior of particle-based PEs, but the morphological complexity of LTON particles, including nanopores inside and at the surface of particles, introduce considerable computational efforts and require nano-scale transport modeling. Additionally, inter-particle charge transfer mechanism have not been investigated for our PEs. Therefore, it is challenging to develop a model with a simplified morphology that can still capture the physical behavior of LTON particle-based PEs and allows for understanding the interplay of multi-physics processes and identifying key factors in the performance of LTON PEs.

Here, we describe the development of a 2D model which is able to predict the performance of particle-based PEs made of oxynitrides, specifically LTON particles. LTON particle-based PEs were chosen as the model system because of the monocrystallinity of the particles[118], reproducibility by simple dipping procedures[102], and potential for high performance[103]. The 2D PE model accounts for the EMW propagation, charge generation and transport, and semiconductor-electrolyte interface charge transfer. Bulk material parameters, namely the density of states of the valence and conduction bands and the relative

## 2: Determination and optimization of material parameters of particle-based LaTiO<sub>2</sub>N photoelectrodes

---

permittivity, were calculated by density functional theory (DFT). Consequently, our approach provides a link between the macroscopic and molecular simulation approaches in PEC materials and devices. Additional material parameters, such as spectrally-resolved complex refractive index, charge mobilities, flatband potential and doping concentration, are extracted from dedicated experiments. The numerical model is used in combination with back-side illumination experiments to inversely determine missing material parameters, such as recombination lifetimes and interfacial hole transfer velocity, parameters not accessible experimentally. By doing so, we identify simultaneously the critical parameters affecting the performance of LTON particle-based PEs while showing the predictive character of the model (specifically predicting the  $I$ - $V$  curve under front-side illumination). Finally, we provide pathways for the improvement of LTON PEs by identifying the key parameters contributing to performance enhancement.

### 2.2. Numerical $I$ - $V$ curve model

The numerical model to predict the  $I$ - $V$  characteristics accounts for EMW propagation, charge transport and conservation, and semiconductor-electrolyte interface charge transfer. All equations are presented in detail in our previous work[104]. Here, we only review the equations relevant to key material parameters for the performance of the LTON particle-based PEs.

#### 2.2.1. Model domain and general assumptions

The complex morphology of LTON PEs is simplified by an equivalent homogeneous domain (Fig. 2.1) relying on two approximations. First, the light absorption model considers the particle-based PEs as a thin film (Fig. 2.1.b) of the same thickness as the particle-based PEs with a weighting according to the solid-phase density profile along the thickness. Second, the domain for the semiconductor physics was reduced to the dimensions of an average-sized single particle, approximated by a rectangular domain with two semiconductor-electrolyte interfaces, one ohmic contact between LTON and the fluorine-doped tin oxide (FTO) and one insulation interface to account for contacts with upper particles (Fig. 2.1.c). Only a single particle in direct contact with the FTO is assumed to significantly contribute to the photocurrent. This approximation can be justified by considering that the inter-particle contact introduces a resistance due to the formation of a double Schottky barrier[119], [120], reducing the space charge layer (SCL) potential,  $V_{\text{SCL}}$ , at the semiconductor-electrolyte [121] as given by  $V_{\text{SCL}} = V_a - \sum_i^n V_{\text{IPC},i}$ ,

## 2: Determination and optimization of material parameters of particle-based LaTiO<sub>2</sub>N photoelectrodes

---

with  $V_a$  the applied potential,  $V_{IPC}$  the potential drop at the inter-particle contact, and  $n$  the number of inter-particle contacts the electron goes through. Additionally, the inter-particle contact reduces the effective electron mobility ( $1/\mu_{eff,n} = 1/\mu_b + \sum_i^n 1/\mu_{IPC,i}$ ) as observed for polycrystalline silicon[122], [123] or mesoporous TiO<sub>2</sub>. In the latter case, it was observed that the electron diffusion coefficient in the mesoporous TiO<sub>2</sub> dropped when the particles were not well sintered leading to poor performance of dye sensitized solar cells[124]. Generally, photoelectrodes containing only one layer of LTON particles have shown equal or even better performance than multilayer particle-based photoelectrodes, pointing to the vital role of the first particle layer for the performance of the PE[102], [103].

The dimensions of the approximated particle size, namely 1.42  $\mu\text{m}$  thickness and 0.6 $\mu\text{m}$  width, are based on the average dimensions and orientations of particles calculated by a detailed quantitative structural analysis of LTON particle-based PEs utilizing 3D nano-tomography data of the actual electrodes[125]. A particle identification algorithm based on fitting ellipsoids inside LTON particles was applied to focused ion beam scanning electron microscopy (SEM) data. Particle characterization such as nominal sizes of particles were then determined by fitting a log-normal distribution of particle size in  $x$ ,  $y$ , and  $z$  directions. The average orientation of particles in all directions was also determined. The length of the model domain is 1.42 $\mu\text{m}$ , corresponding to the average particle size of the longest axis of 1.79  $\mu\text{m}$  (Fig. A2.1) and the average orientation angle of 37.4° (Fig. A2.2), i.e. the angle between the normal of the FTO plan and the direction of the particle in the longest direction. The width of the model domain is 0.6 $\mu\text{m}$ , corresponding to the average particle size of the medium and shortest direction.

### 2.2.2. Radiation absorption

The electron-hole pair generation rate was calculated considering a 2D EMW propagation model with irradiation wavelengths from 400nm to 590nm, corresponding to the spectrum of the solar simulator, up to the bandgap of LTON (2.1eV=590nm). The irradiation was considered as transverse electric field, and therefore, only the out-of-plane electric field was calculated. Bloch-Floquet theory was assumed for the periodicity on both lateral sides of the computational domain with a width of 5 $\mu\text{m}$ , ensuring convergence of the model[80], [81]. Fig. 2.1.b depicts the computational domain, the dimensions, and the boundary conditions of the model.

## 2: Determination and optimization of material parameters of particle-based LaTiO<sub>2</sub>N photoelectrodes

---

The location-dependent charge carrier generation rate in LTON particle-based PEs was calculated by solving the Maxwell's curl equation[69] for each spectral band of the irradiation for the given spectrally-resolved complex refractive index and the particle density profile. A spectral band of  $\Delta\lambda = 4\text{nm}$  was carefully chosen to reduce calculation time without losing accuracy of the calculated generation rate. For non-chromatic sources of light, the total generation rate is the spectral integration of the fraction of the absorbed optical power and the energy of the corresponding photon.

EMW propagation was calculated considering the electrolyte (assumed to have the optical properties of water), the FTO glass, and LTON, with the spectral irradiance of the solar simulator Verasol-2 from Oriel and an incident angle of  $0^\circ$  (Fig. A2.4). The reflection losses at the semiconductor-electrolyte interface can greatly influence the photogeneration efficiency and were accounted for by adding a 2mm-thin layer of water at the back- and the front-side of the PE. The absorption losses due to the electrolyte are negligible since the water extinction coefficient is below  $4 \cdot 10^{-6}$  in the visible range[83], [126]. Indeed, the same photogenerated current density was calculated using a smaller thickness of the water layer. The spectral complex refractive index,  $\tilde{n}$ , of LTON is a material parameter required for the numerical model based on EMW propagation and was extracted from spectrophotometry measurements (see section 2.3).

## 2: Determination and optimization of material parameters of particle-based LaTiO<sub>2</sub>N photoelectrodes

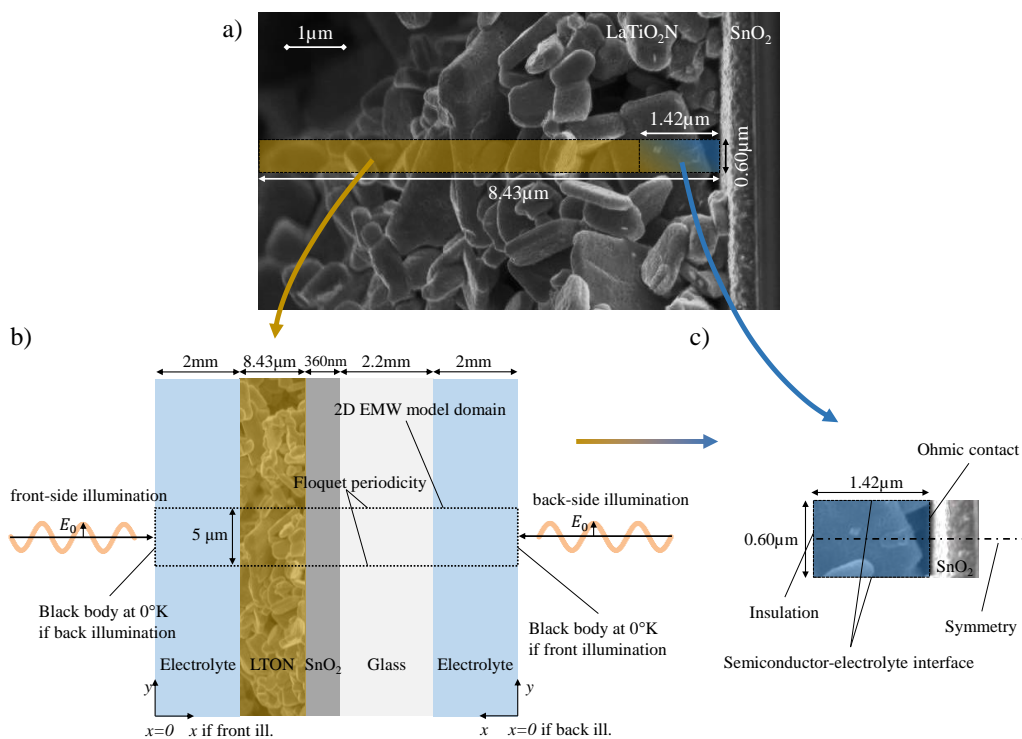


**Fig. 2.1.** a) Scanning electron microscopy picture of a LTON particle-based PE and indication of the domain sizes used for the numerical model (yellow for the EMW simulations, blue for the semiconductor physics simulations), b) EMW propagation model domain and boundary conditions, and c) semiconductor physics model domain and boundary conditions. The generation rate calculated with model b) is used as an input in model c).

### 2.2.3. Charge transport and conservation

The charge transport and conservation were calculated considering a 2D continuum model within the calculation domain. The 2D model, representing an average LTON particle, ensures that the OER can occur along a typical particle surface. The numerical model fully couples the static and the dynamic behavior of charge carriers in the semiconductor. The static behavior was calculated by solving the Poisson's equation[70] with the permittivity and the doping concentration as relevant material parameters. The dynamic behavior of the carriers was calculated by solving the drift-diffusion equation with the electron and hole mobilities as relevant material parameters. The charge carrier density in the semiconductor was determined by the



## 2: Determination and optimization of material parameters of particle-based LaTiO<sub>2</sub>N photoelectrodes

---

product of the Fermi-Dirac distribution and the density of states of the conduction and valence bands as material parameters. The governing equations were solved at steady-state with a uniform isothermal device temperature of 20°C. The steady-state charge conservation is given by the sum of all recombination and the generation rate, the latter being calculated through the EMW model. Only Shockley–Read–Hall (SRH) recombination was considered and modeled using effective electron and hole lifetimes given by eqn (1.11). The effective electron and hole lifetimes are given in eqn (1.14). We used effective lifetimes to account for both the bulk and the surface recombination, which is in accordance with the general practice of modeling surface recombination[71], [72]. This approximation still accurately predicts the  $I$ - $V$  characteristics of water-splitting photoelectrodes, as shown in our previous work[104].

The charge transport at the particle-FTO interface was modeled as an ideal ohmic contact. The current density at the semiconductor-electrolyte interface along the side of the particle was determined by using a Schottky contact with the interfacial hole transfer velocity and the flatband potential as relevant material surface parameters. The interfacial hole transfer velocity dictates the kinetics of the oxygen evolution reaction at the semiconductor-electrolyte interface. The hole current in a Schottky contact (the photocurrent in an n-type semiconductor) is given by eqn (1.21). The use of a Schottky contact to describe the charge transfer mechanism at the semiconductor-electrolyte interface simplifies the actual charge transfer mechanisms involved in a photoelectrode with co-catalyst and surface states (SS). A charge carrier can be transferred across different interfaces and paths, such as a direct transfer from the LTON bulk states to the electrolyte, through SS, and/or through co-catalysts. Each path, with its own kinetic characteristics, is competing with the others. Moreover, SS or co-catalyst might lead to Fermi level pinning, inducing a potential drop not only in the SCL but also in the electrolyte[127]. However, if the band bending due to the semiconductor-electrolyte interface is fully developed and if there is no mass transport limitation from the electrolyte side, the use of a Schottky contact has shown to fit experimental  $I$ - $V$  curves well (for example for GaN[104]). We confirmed that an electric field was present at the semiconductor-electrolyte interface by conducting open-circuit voltage measurements for the LTON particle-based PEs (Fig. A2.5). We also used a highly alkaline solution to ensure that mass transport limits were not present. Furthermore, the Helmholtz layer (HL) capacitance is usually much larger than the SCL capacitance, thus ensuring that the applied potential drops only in the SCL and not in the HL[51], [99]. Therefore, the Schottky contact approximation was justified in the present study. Further details



## 2: Determination and optimization of material parameters of particle-based LaTiO<sub>2</sub>N photoelectrodes

---

and equations related to the Schottky contact mechanism can be found in our previous work[104].

Flatband potential, doping concentration, densities of states, permittivity, charge mobilities, effective lifetimes, and interfacial hole transfer velocity are required material parameters for the charge transport and conservation numerical model and were extracted from molecular numerical model, various experimental measurements, and the inverse analysis (see section 2.3).

### 2.3. Determination of material parameters

#### 2.3.1. Complex refractive index

The complex refractive index of LTON was extracted from spectrophotometry measurements. Spectral reflectance and transmittance were acquired in an air environment with a UV-3600 Shimadzu UV-VIS-NIR spectrophotometer using an integrating sphere to account for diffuse reflectance and transmittance.

The real part of the complex refractive index, the refractive index,  $n$ , of LTON particle-based PEs was determined by using the total reflectance,  $\rho_m$ , measured under front-side illumination and using the Fresnel's equations[66] under normal incident, unpolarized light with  $n \gg k$ , given by

$$n = \frac{n_{\text{air}}(\rho_m + 2\sqrt{\rho_m} + 1)}{1 - \rho_m} \cong \frac{\sqrt{\rho_m} + 1}{1 - \sqrt{\rho_m}} \text{ with } n_{\text{air}} \cong 1. \quad (2.1)$$

The imaginary part of the complex refractive index, the extinction coefficient,  $k$ , was determined by using the total transmittance,  $\tau_m$ , and reflectance,  $\rho_m$ , measured under back-side illumination. The reflectance measurement was corrected for the absorbance of the FTO glass by  $\rho_c = \rho_m + a_{\text{FTO}}$ . The absorbance of the FTO glass was determined by transmittance and reflectance measurements using  $a_{\text{FTO}} = 1 - \rho_{\text{FTO}} - \tau_{\text{FTO}}$ . Following the multiple internal reflections for a single partially transmitting layer with a film thickness much larger than the irradiation wavelength,  $D > \lambda$ , the reflectance and transmittance are given by[66]

## 2: Determination and optimization of material parameters of particle-based LaTiO<sub>2</sub>N photoelectrodes

---

$$\rho_c = \rho_m + \alpha_{\text{FTO}} = \rho \left[ 1 + \frac{(1-\rho)^2 \sigma^2}{1-\rho^2 \sigma^2} \right] \quad (2.2)$$

$$\text{and } \tau_m = \frac{\sigma(1-\rho)^2}{1-\rho^2 \sigma^2}. \quad (2.3)$$

where  $1-\rho$  is the amount of light refracted. The transmitted amount of light is given by  $\sigma = e^{-\tau/\cos \theta_i}$ . The absorption coefficient was assumed to depend on the particle density distribution,  $\rho(z)$ , along the height,  $a(z)=a^* \rho(z)$ . The particle density distribution was calculated by a detailed quantitative structural analysis of LTON particle-based PEs utilizing 3D nano-tomography data of the actual electrodes[125] (Fig. A2.3). The effective depth,  $D^*$ , of particle-based photoelectrode using the particle density distribution is given by

$$\tau = \alpha^* \int_0^D \rho(z) dz = \alpha^* \cdot D^*. \quad (2.4)$$

By rearranging eqns (2.2) to (2.4) and considering an incident angle of  $\theta_i=0^\circ$ , the absorption coefficient,  $\alpha^*$ , can be expressed in function of the measured transmittance and the corrected reflectance, given by

$$\alpha^* = -\frac{1}{D^*} \ln \left( \frac{\sqrt{(-\rho_c^2 + 2\rho_c + \tau_m^2 - 1)^2 + 4\tau_m^2} - \rho_c^2 + 2\rho_c + \tau_m^2 - 1}{2\tau_m} \right). \quad (2.5)$$

Finally, the extinction coefficient depending on the PE's thickness is given by  $k(z)=k^* \rho(z)$ , where  $k^*=a^* \lambda / 4 / \pi$ .

### 2.3.2. Density of states of the valence and conduction bands, and relative permittivity

Assuming parabolic bands in the electronic band structure, the density of states of the valence and conduction bands are given by[21]

## 2: Determination and optimization of material parameters of particle-based LaTiO<sub>2</sub>N photoelectrodes

---

$$N_{V/C} = 2 \left( \frac{2\pi m_{h/e}^* k_B T}{h^2} \right)^{3/2}. \quad (2.6)$$

The electron and hole effective masses of LTON were computed using DFT calculations with the Quantum ESPRESSO[128] package using the PBE[129] exchange-correlation functional with a Hubbard U correction[130] of 3.0 eV applied to the Ti 3d states and using the virtual crystal approximation to describe a  $1/3$  N  $2/3$  O disorder on the anion sublattice (for additional computational details, see the supporting information). Based on band structure calculations, we determined the electron and hole effective mass tensors using finite differences with a stencil grid of step size  $0.01 \text{ Bohr}^{-1}$  by means of the EMC utility[131]. For our orthorhombic cell (b is the long axis), we converted the effective masses in all direction into conduction effective masses via

$$m_{\text{cond}}^* = 3 \left( \frac{1}{m_a} + \frac{1}{m_b} + \frac{1}{m_c} \right)^{-1}. \quad (2.7)$$

The permittivity of LTON was computed using functional perturbation theory, considering both electronic and ionic contributions.

### 2.3.3. Flatband potential and doping concentration

The flatband potential and the doping concentration were determined by EIS and Mott-Schottky analysis of LTON PEs. The Mott-Schottky plot of LTON PEs using only a capacitance showed a high frequency dispersion (Fig. A2.6). This frequency dispersion is commonly found in practical electrodes and is attributed to various physico-chemical phenomena, such as surface roughness, surface defects, local charge inhomogeneity, absorbed species, different phase region, variations in composition and stoichiometry, doping inhomogeneity, dielectric relaxation, electric double layer, and deep donor levels [132]–[134].

Frequency-independent Mott-Schottky plots using Mott-Schottky theory[21], [133] can be obtained by using a constant phase element (CPE) combined with the appropriate EIS model. Zoltowski suggested using the following admittance of the CPE[135]:

## 2: Determination and optimization of material parameters of particle-based LaTiO<sub>2</sub>N photoelectrodes

---

$$Y_{\text{CPE}} = Y_0(i\omega)^\alpha. \quad (2.8)$$

$Y_0$  cannot be approximated as a capacitance since a small deviation of  $\alpha$  from 1 would lead to large error in the capacitance[134], and  $Y_0$  does not have the unit of a capacitance as mentioned by Zoltowski[135]. The capacitance without any frequency dispersion is obtained from  $Y_0$  and the related resistance,  $R$  [132], [136], given by

$$C = \frac{(R \cdot Y_0)^{1/\alpha}}{R}. \quad (2.9)$$

The model for EIS fitting and for determining the flatband potentials and doping concentrations of the best-LTON PEs is depicted in Fig. 2.4. LTON PEs with co-catalysts were used for the impedance analysis instead of LTON without co-catalysts due to better performance and more reliable results.  $R_s$  in the equivalent circuit model denotes a series resistance of the electrolyte and the semiconductor.  $R_{sc}$  and  $\text{CPE}_{sc}$  denote the resistance and the CPE in the SCL.  $R_{ss}$  and  $\text{CPE}_{ss}$  denote the resistance and the CPE caused by SS at the semiconductor-electrolyte interface. This equivalent circuit is usually used for a semiconductor-electrolyte interface with species adsorption at the interface[133] and was previously used for n-type GaN[92].

The model was fitted to a frequency range of 2-16kHz to 50Hz to avoid the slow diffusion component, which is not related to the SCL capacitance[92]. The varying upper frequency limit is due to an abrupt change in the impedance spectra of the best-LTON PEs appearing in all our electrodes at a frequency of 10kHz at 0.12V vs reversible hydrogen electrode (RHE) (Fig. A2.7). The flatband potential is often determined using the Mott-Schottky equation, which requires that the HL capacitance is much larger than the SCL capacitance. Since the HL capacitance is unknown, the flatband potential is reported without considering any potential shift due to the HL capacitance, in accordance with the general practice[132].

### 2.3.4. Electron and hole mobilities

The conductivity of LTON particle-based PE was measured by 4-point probes with a sourcemeter (Keithley 2450). The mobilities of electron and holes are estimated by conductivity measurements and using the DFT-calculated effective mass of electrons and holes. The conductivity of a semiconductor material is given by

## 2: Determination and optimization of material parameters of particle-based LaTiO<sub>2</sub>N photoelectrodes

---

$$\sigma = q(n\mu_n + p\mu_p). \quad (2.10)$$

Since LTON is naturally a n-type semiconductor material, the hole density in the material is negligible compared to the electron density. Consequently, the hole density term in the conductivity equation (eqn (2.10)) was neglected. The charge density in the bulk of the semiconductor was assumed to be zero, hence  $n \approx N_D^+$ , and the electron mobility is given as  $\mu_n = \sigma/(qN_D^+)$ . By assuming that the average scattering time of electrons and holes is equal, the hole mobility is calculated by

$$\mu_p = \mu_n \frac{m_e^*}{m_h^*}. \quad (2.11)$$

### 2.3.5. Electron and hole effective lifetimes and interfacial hole transfer velocity

The interfacial hole transfer velocity and effective lifetimes (combination of surface lifetimes at the semiconductor-electrolyte interface, inter-particle contact, and bulk lifetimes) are difficult to access experimentally. Here, we used an inverse analysis for their determination. First, we measured  $I-V$  curves under back- and front-side illumination and provided experimental error bars. Then, we applied our inverse analysis which consisted in varying these parameters until the numerical  $I-V$  curves fitted the experimental  $I-V$  curves under back-side illumination within the error bars. Once, a parameter had been determined under back-side illumination, the numerical photocurrent under front-side illumination was calculated and compared with the corresponding measurement. If the numerical photocurrent under front-side illumination followed the experimental one, the determined parameter was approved, and the model was considered validated and of predictive character. Finally, the exact value of the parameter was determined by minimizing the R-square value of the numerical fitting to the averaged experimental  $I-V$  curve above 1 V<sub>RHE</sub> under front-side illumination.

### 2.4. Experimental section

#### 2.4.1. Photoelectrode preparation and characterization

Two types of LTON PEs were prepared following the procedure of Landsmann et al.[102]: best-LTON with multiple coating processes and bare-LTON with a single dipping procedure. In both configurations, the LTON PEs were fabricated using LTON suspended particles deposited on a FTO glass substrate by electrophoretic deposition. Subsequently, the LTON PEs were dipped in an ethanol solution of Ti(OEt)<sub>4</sub> and then annealed under a NH<sub>3</sub> flow. This last process ensures ohmic contact between the LTON particles and the FTO glass substrate. These electrodes were called bare-LTON PEs. Best-LTON PEs were obtained by additional dipping of the electrodes firstly in an ethanol solution of Ta(OEt)<sub>4</sub> followed by annealing under NH<sub>3</sub> flow to form a passivation layer of Ta<sub>2</sub>O<sub>5</sub>. NiO<sub>x</sub> co-catalysts were then deposited by dipping the electrode in an ethanol solution of Ni(NO<sub>3</sub>)<sub>2</sub> and subsequently annealed in normal air environment. A similar procedure was used to deposit the CoO<sub>x</sub> co-catalyst. Finally, the Co(OH)<sub>2</sub> co-catalyst was also deposited by a dipping procedure. SEM images of the electrodes were acquired with a FEI NovaNanoSEM using a through-the lens detector at 5 kV acceleration voltage.

The thickness of the PEs were determined by taking the average thickness along 1μm of the PEs, measured by profilometry using a Bruker DektakX with a 60° tip and an applied contact weight of 1mg. The best-LTON PEs have an average thickness of 8.43μm, and the bare-LTON PEs have an average thickness of 5.51μm. All LTON PEs in this work have an illuminated surface area of 1±0.3cm<sup>2</sup>.

#### 2.4.2. Photoelectrochemical measurements

Photoelectrochemical experiments were conducted in a three-electrode setup to refer the potential of our measurements to the RHE. The electrodes were connected to a potentiostat (Bio-Logic VSP-300 controlled by the EC-lab software) for *I-V* curve measurements and EIS measurements. The reference electrode was Ag/AgCl (sat. KCl), and the counter electrode was Pt. The aqueous electrolyte solutions used were 0.1M Na<sub>2</sub>SO<sub>4</sub> and NaOH at pH= 13.2±0.2. The sample was illuminated by the solar simulator VeraSol-2 from Oriel corresponding to AM1.5G in the visible and near-infrared region (400-1100nm) with a light irradiance of 76±3 mW/cm<sup>2</sup> (Fig. A2.4). The PEs were measured under front-side illumination with the irradiance transmitted through the electrolyte and absorbed by the LTON and under back-side

## 2: Determination and optimization of material parameters of particle-based LaTiO<sub>2</sub>N photoelectrodes

---

illumination with the irradiance transmitted through the electrolyte and the FTO glass substrate before being absorbed by the LTON (Fig. 2.1).  $I$ - $V$  curves were measured with a potential sweep of 10mV/s in the potential range of 0.5 to 1.5 V<sub>RHE</sub>. A small hysteresis could be observed between forward and backward swept voltage even at this low voltage sweep rate. Therefore, the current density was averaged between forward and backward swept voltage. The final  $I$ - $V$  curves depicted in this work for best-LTON and bare-LTON under back- and front-side illumination are the measurement averages of eight fresh PEs each to ensure representative results and stable current conditions (LTON corroded in the electrolyte after a few minutes under illumination). The error bars of the experimental  $I$ - $V$  curves are the minimum and maximum photocurrent densities measured for the eight PEs. EIS was done under dark conditions at potentials varying from 0 to 0.6 V<sub>RHE</sub> and covering a frequency range of 50Hz to 20kHz.

### 2.5. Results and discussion

#### 2.5.1. Determination of material parameters

**Complex refractive index.** The complex refractive index of bulk LTON calculated with eqns (2.1) and (2.5) from transmittance and reflectance measurements are depicted in Fig. 2.2. The Tauc plot of LTON is given in the supporting information (Fig. A2.8). The refractive index based on the total reflectance using eqn (2.1) has a drop below 600nm. This drop can be interpreted as the bandgap value of LTON (600nm  $\approx$  2.1eV) using the Kubelka-Munk (K-M) transform based on the total reflectance (Fig. A2.9). It is therefore often used to determine the bandgap of semiconductors, for which transmittance cannot be measured. The complex refractive of the glass substrate and the FTO layer can be found in the supporting information (Fig. A2.10 and Fig. A2.11).

For validation purposes, the transmittance was numerically simulated using the obtained optical parameters and compared to the experimental one (Fig. A2.12). The transmittance was also calculated by utilizing Beer-Lambert's law and additionally accounting for reflectance and absorptance of the FTO glass substrate (Fig. A2.13). The calculated transmittance for both methods was below 2 % error compared to the measured transmittance in a spectral range of 400 nm to 590 nm. This gave us confidence in the accuracy of the extracted complex refractive index of LTON PEs. The model based on Beer-Lambert's law is very efficient and simple compared to EMW propagation model but should be used with care in the UV region where over

## 2: Determination and optimization of material parameters of particle-based LaTiO<sub>2</sub>N photoelectrodes

3 % error in the transmittance under back-side illumination was observed (relative error of 100 % at 340nm, Fig. A2.13.a).

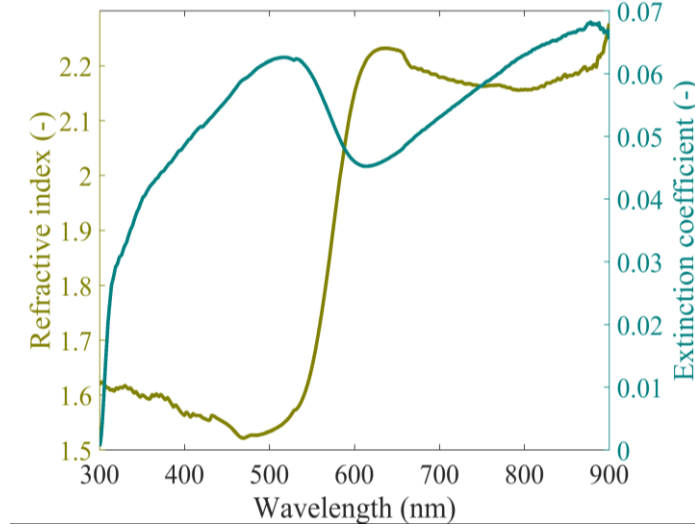


**Fig. 2.2.** Complex refractive index of LTON particle-based PE using reflectance and transmittance measurements with an integrating sphere. The refractive index (left  $y$ -axis) is calculated using Fresnel's equation (eqn (2.1)) in conjunction with total reflectance measurements. The extinction coefficient (right  $y$ -axis) is determined using reflectance and transmittance measurements in conjunction with eqn (2.5) derived by considering multiple internal reflections in a single, partially transmitting thick layer ( $D > \lambda$ ).

**Generation rate.** The calculated generation rate and photogenerated current density under back- and front-side illumination of the solar simulator is depicted in Fig. 2.3. Under back-side illumination, the generation rate follows an exponential decay given by the constant extinction coefficient, resulting from a constant density of particles within the first 1.5  $\mu\text{m}$  (Fig. A2.3). The ratio between the front- and back-side illumination photogenerated current density reproduces the experimental front- and back-side photocurrent ratio. The numerical model, considering only the first layer of particles in direct contact with the FTO, is already partially validated, based only on light absorption. As depicted in Fig. 2.3, the front-side illumination's photogenerated current is more affected by the use of only the first layer of particles. The photogenerated current densities of the front- and back-side illuminations are 0.8  $\text{mA cm}^{-2}$  and 4.4  $\text{mA cm}^{-2}$  respectively.



## 2: Determination and optimization of material parameters of particle-based LaTiO<sub>2</sub>N photoelectrodes

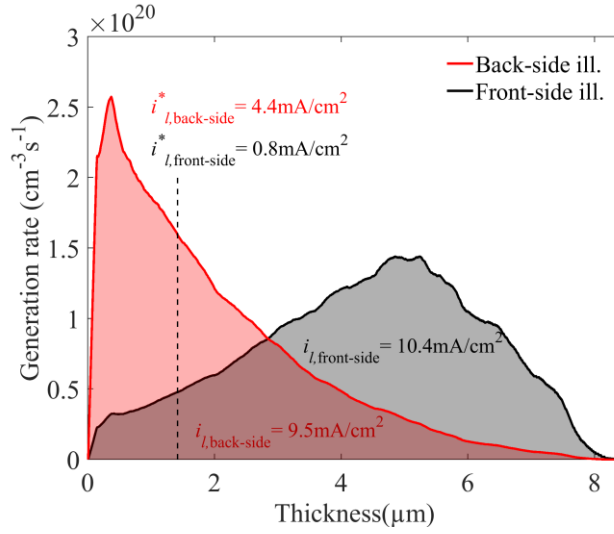


**Fig. 2.3.** Generation rate of LTON particle-based PEs under back- and front-side illumination with the AM1.5G solar simulator's spectral irradiance. The integrated photogenerated current density is indicated for PEs of thickness 1.42  $\mu\text{m}$  (dashed line) and 8.43  $\mu\text{m}$ .

**Density of states of the valence and conduction bands.** For our orthorhombic cell ( $b$  is the long axis), the electron effective masses are 0.788, 4.553 and  $0.390m_e$  along the  $a$ ,  $b$  and  $c$  axes, respectively, whereas the hole effective masses are 0.714, 0.956 and  $0.341m_e$ , respectively,  $m_e$  being the electron mass at rest. We converted these into conduction effective masses via eqn (2.7), resulting in  $0.740m_e$  for the electrons and  $0.558m_e$  for the holes. These values agree well with  $0.750m_e$  and  $0.517m_e$  obtained by averaging over conduction effective masses for explicit disorder models[137]. The light holes in oxynitrides can be explained from their electronic structure. While the top of the valence band is N 2p dominated, the Ti 3d dominated bottom of the conduction band is hybridized more with O 2p than N 2p orbitals. Given the stronger covalent Ti-N bond compared to Ti-O, a stronger band dispersion for the N-derived states at the top of the valence band compared to the bottom of the conduction band is expected. Therefore, we observe a lighter mass of the holes compared to the electrons. In pure oxides or nitrides, such an effect would be absent, but we see similar trends for layered Ruddlesden-Popper oxynitrides[138]. The density of states of the valence and conduction bands using eqn (2.6) are  $1.01 \times 10^{19} \text{ cm}^{-3}$  and  $1.54 \times 10^{19} \text{ cm}^{-3}$ , respectively, at a temperature of 20°C. The

## 2: Determination and optimization of material parameters of particle-based LaTiO<sub>2</sub>N photoelectrodes

---

electronic band structure of orthorhombic LTON can be found in the supporting information (Fig. A2.14).

**Relative permittivity.** The full tensor of the relative permittivity of LTON is given in the supporting information. We converted it to a single value via an effective medium theory[139] and obtained a value of 14.94 without the second order correction and 15.19 with second order corrections. For the macroscopic model, we assumed an approximate relative permittivity of  $\epsilon_r=15$ .

**Flatband potential and doping concentration.** Fig. 2.4 shows the Mott-Schottky plot for best-LTON PEs in the dark with a resulting flatband potential of 0.1 V<sub>RHE</sub> (in accordance with the work of Feng et al.[140]) and a doping concentration of  $7.43 \cdot 10^{17} \text{ cm}^{-3}$ . The flatband potential of 0.1 V<sub>RHE</sub> is also in accordance with the  $I-V$  curve found in a previous paper[141]. A flatband potential of 0.1 V<sub>RHE</sub> and a doping concentration of  $7.4 \cdot 10^{17} \text{ cm}^{-3}$  result in a conduction band situated at 0.02 V<sub>RHE</sub>, below the hydrogen evolution reaction (HER) potential. However, hydrogen production with LTON particles has been reported by Kasahara et al.[19]. We think that the HER can still occur with the conduction band below the HER potential because these redox systems have a continuous distribution of energy states and not a single discrete state[53]. Nevertheless, this situation will lead to very poor hydrogen production as reported by Kasahara et al. (one order of magnitude lower production of hydrogen than oxygen). The same situation is observed with BiVO<sub>4</sub> with a flatband potential of 0.1 V<sub>RHE</sub> [142] and the ability to produce hydrogen[143] or La<sub>5</sub>Ti<sub>2</sub>CuS<sub>5</sub>O<sub>7</sub> with a valence band above the OER potential[144] and the ability to produce oxygen[145]. The normal surface of the electrode used to calculate the doping concentration with the Mott-Schottky equation[133], [146] was 0.79 cm<sup>2</sup>. The active area,  $A_{\text{active}}$ , was 14.39 cm<sup>2</sup>, utilizing a surface roughness factor of 18.2, obtained from the structural analysis[125] (Table 2.1). The flatband potential obtained with the best-LTON PEs gives the same result as the one obtained from a Mott-Schottky plot with frequency dispersion (Fig. A2.6). We can expect to see the effect of SS recombination on the photocurrent up to a potential of 0.6 V<sub>RHE</sub> (Fig. 2.4) and higher, since the onset potential is at 0.9 V<sub>RHE</sub> (Fig. 2.5). Similar distributions of  $1/C_{\text{ss}}^2$  have been shown for other semiconductor materials such as TiO<sub>2</sub> in aqueous electrolyte[147].

We obtained a doping concentration variation of  $\pm 5 \cdot 10^{17} \text{ cm}^{-3}$  based on two measurements with newly prepared best-LTON PEs.

## 2: Determination and optimization of material parameters of particle-based LaTiO<sub>2</sub>N photoelectrodes

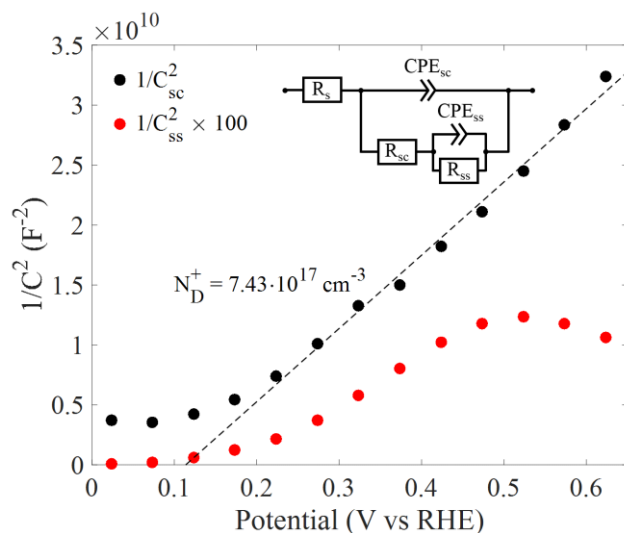


**Fig. 2.4.** Frequency-independent Mott-Schottky plots for best-LTON photoelectrodes with the determined doping concentration. The equivalent circuit for the electrochemical impedance analysis is also indicated.

**Hole and electron mobilities.** The electron mobility of the LTON particle-based PEs is  $46 \text{ cm}^2\text{V}^{-1}\text{s}^{-1}$  with a doping concentration of  $7.43 \cdot 10^{17} \text{ cm}^{-3}$  and with a measured conductivity of  $5.51 \text{ S/cm}$  (eqn (2.10)). By using the effective masses determined by DFT calculations and using eqn (2.11), the hole mobility of LTON is  $61 \text{ cm}^2\text{V}^{-1}\text{s}^{-1}$ .

**Effective electron lifetimes.** The numerical  $I$ - $V$  curves for varying effective electron lifetimes under back- and front-side illumination are presented in Fig. 2.5, together with the experimentally measured ones. The experimental relative error of the photocurrent is  $\pm 17\%$  at  $1.23 \text{ V}_{\text{RHE}}$  for the best-LTON PEs under back-side illumination and  $\pm 30\%$  under front-side illumination. A numerical photocurrent density within the experimental variations above  $1 \text{ V}_{\text{RHE}}$  under both illuminations' sides is obtained for an electron lifetime of  $5 \cdot 10^{-10} \text{ s}$ . We can conclude that our numerical model can reproduce the experimental  $I$ - $V$  curves well and is predictive by reproducing the front-side illumination  $I$ - $V$  curve. The photocurrent density below  $1 \text{ V}_{\text{RHE}}$  was not considered for the fitting of the experimental  $I$ - $V$  curves since the modeling of the photocurrent in the potential region below  $1 \text{ V}_{\text{RHE}}$  is highly complex. Indeed, surface recombination is present at low applied potential and any attempt to simulate the photocurrent in this region requires precise knowledge of the surface recombination phenomena with all the related parameters. Thus, this work, in conjunction with state-of-the-art modeling work[55], [63], does not address

## 2: Determination and optimization of material parameters of particle-based LaTiO<sub>2</sub>N photoelectrodes

this issue nor reproduces well the  $I$ - $V$  curves in the regions where surface recombination occurs (potential below 1 V<sub>RHE</sub>). An in-depth understanding and modeling of surface recombination phenomena at the semiconductor-electrolyte interface would greatly help the community to improve the performance of photoelectrodes but is still missing. The numerical model was also compared to experimental  $I$ - $V$  curves under back illumination for different light intensities: 1 sun, 0.1 sun and 0.01 sun. Although some discrepancies between the numerical and the experimental  $I$ - $V$  curves occur at a potential between 0.9 V<sub>RHE</sub> to 1.3 V<sub>RHE</sub>—most probably due to the surface recombination—the numerical model is able to follow the experimental  $I$ - $V$  curves for different light intensities (Fig. A2.15).

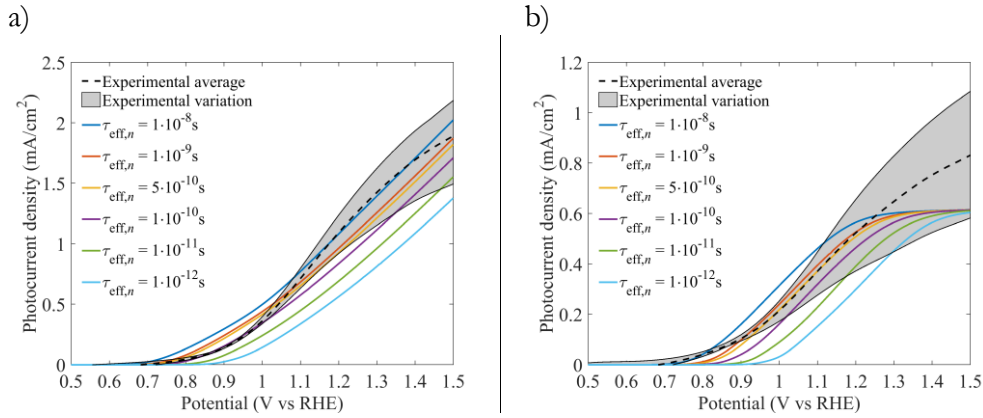


**Fig. 2.5.** Numerical and experimental photocurrent-voltage curves of best-LTON under a) back- and b) front-side illumination for varying effective electron lifetimes. The photocurrent density was reduced from 1.18 mA cm<sup>-2</sup> to 0.63 mA cm<sup>-2</sup> at 1.23 V<sub>RHE</sub> when reducing the effective electron lifetime by four orders of magnitude under back-side illumination (from 10 ns to 1 ps). Under front-side illumination, the photocurrent density was reduced from 0.55 mA cm<sup>-2</sup> to 0.34 mA cm<sup>-2</sup> at 1.23 V<sub>RHE</sub> when reducing the effective electron lifetime by four orders of magnitude.

The back-side illumination photocurrent of best-LTON PEs is around 2.5 times higher than the front-side illumination photocurrent at 1.23 V<sub>RHE</sub>, although part of the light is absorbed by the FTO glass under back-side illumination and not under front-side illumination. Since electrons are collected at the FTO substrate, electrons generated closer to it have a higher chance to be collected before recombining, leading to a higher photocurrent under back-side illumination. As previously

## 2: Determination and optimization of material parameters of particle-based LaTiO<sub>2</sub>N photoelectrodes

---

mentioned, we assumed for the modeling that only the first layer of particles in direct contact with the FTO substrate is significantly contributing to the photocurrent. This approximation is supported by the experimental  $I$ - $V$  curves (Fig. 2.5) since the upper particles (not contributing to the photocurrent) are parasitically reducing the light under front-side illumination. This unexpected behavior was attributed in previous work to electron transport limitations due to poor inter-particle conductivity [102], [140], [148], [149]. The numerical photocurrent reaches saturation already at  $1.3 V_{\text{RHE}}$  while the experimental photocurrent does not show saturation below  $1.5 V_{\text{RHE}}$  (Fig. 2.5.b). We hypothesize that this discrepancy is caused by the upper particles of the PE starting to contribute to the photocurrent under large applied potential (above  $1.3 V_{\text{RHE}}$ ). Such a large applied potential might help to overcome the potential losses appearing at the inter-particle contacts of the upper particles. In the case where there is no potential loss for the upper particles and, thus, the entire thickness of the photoelectrode becomes active, the front-side illumination photocurrent would be larger than the back-side illumination (Fig. A2.16). This is not observed for our particle-based LTON photoelectrodes. We recognize that in reality a smoother potential drop for the top particles might be experienced, instead of our assumed complete loss of the applied potential above the first layer of particle. Future work will be devoted to investigate this assumption and variations thereof.

**Effective hole lifetimes.** The impact of effective hole lifetime under back- and front-side illumination on the calculated photocurrents is depicted in Fig. 2.6, together with the experimentally measured ones. The effective hole lifetime affects both the photocurrent and the onset potential. A hole lifetime of  $5 \cdot 10^{-10}$  s gave a photocurrent density within the experimental variation for both illuminations' sides above  $1 V_{\text{RHE}}$ .

## 2: Determination and optimization of material parameters of particle-based LaTiO<sub>2</sub>N photoelectrodes

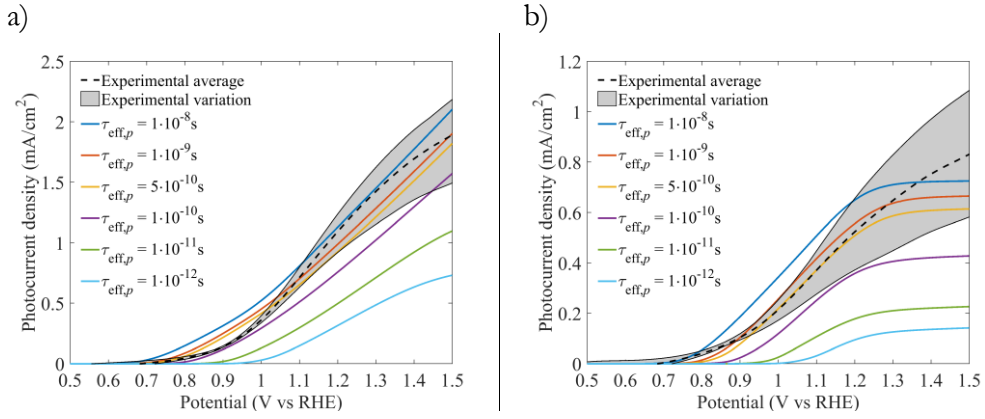


**Fig. 2.6.** Numerical and experimental photocurrent-voltage curves of best-LTON under a) back- and b) front-side illumination for varying effective hole lifetimes. The photocurrent density was reduced from 1.01 mA cm<sup>-2</sup> to 0.37 mA cm<sup>-2</sup> at 1.23 V<sub>RHE</sub> when reducing the effective hole lifetime by four orders of magnitude under back-side illumination (from 10 ns to 1 ps). Under front-side illumination, the photocurrent density was reduced from 0.68 mA cm<sup>-2</sup> to 0.11 mA cm<sup>-2</sup> at 1.23 V<sub>RHE</sub> when reducing the effective hole lifetime by four orders of magnitude.

**Interfacial hole transfer velocity.** The numerical  $I$ - $V$  curves for varying interfacial hole transfer velocities under back- and front-side illumination are presented in Fig. 2.7, together with the experimentally measured ones. The interfacial hole transfer velocity significantly affected the photocurrent under back- and front-side illumination. A hole transfer velocity of  $v_{sp} = 3.5 \cdot 10^{-6}$  cm s<sup>-1</sup> provided a numerical photocurrent within the experimental variation under back-side illumination above 1 V<sub>RHE</sub>. The same hole transfer velocity was within the experimental error under front-side illumination.

## 2: Determination and optimization of material parameters of particle-based LaTiO<sub>2</sub>N photoelectrodes

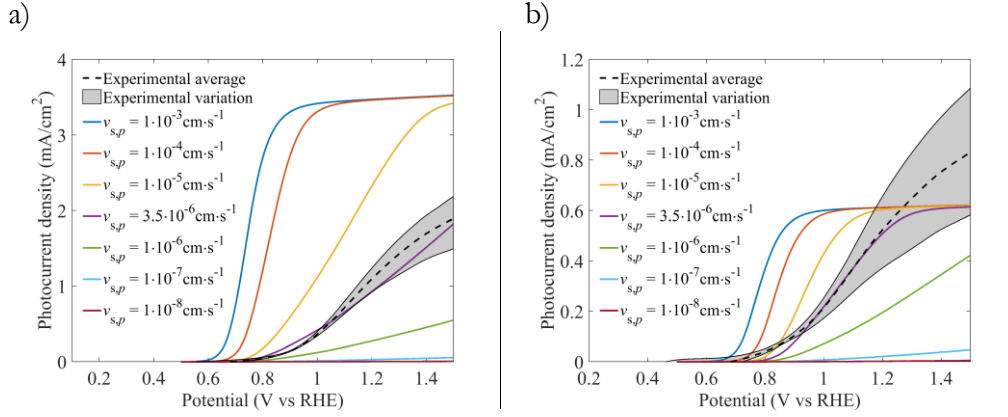


**Fig. 2.7.** Numerical and experimental photocurrent-voltage curves of best-LTON PEs under a) back- and b) front-side illumination for varying interfacial hole transfer velocities. The hole transfer velocity was significantly affecting the photocurrent under back-side illumination: a photocurrent of 3.48 mA cm<sup>-2</sup> at 1.23 V<sub>RHE</sub> with  $v_{sp}=1\cdot10^{-4}$  cm s<sup>-1</sup> and of 1.01 mA cm<sup>-2</sup> with  $v_{sp}=3.5\cdot10^{-6}$  cm s<sup>-1</sup>. Under front-side illumination, the hole transfer velocity was less affecting the photocurrent since the photocurrent reached almost saturation at 1.23 V<sub>RHE</sub> with  $v_{sp}=3.5\cdot10^{-6}$  cm s<sup>-1</sup>, a photocurrent density of 0.61 mA cm<sup>-2</sup> at 1.23 V<sub>RHE</sub> with  $v_{sp}=1\cdot10^{-4}$  cm s<sup>-1</sup> and of 0.54 mA cm<sup>-2</sup> for  $v_{sp}=3.5\cdot10^{-6}$  cm s<sup>-1</sup>.

All material parameters of LTON particle-based PE used in this work are summarized in [Table 2.1](#).

## 2: Determination and optimization of material parameters of particle-based LaTiO<sub>2</sub>N photoelectrodes

**Table 2.1.** Material parameters of LTON particle-based PE determined by dedicated experiments (Mott-Schottky analysis and conductivity measurements), DFT calculations, and inverse analysis.

Literature	Band gap, $E_{\text{gap}}$	2.1eV[19], [102], [148], [150]–[153]	
	Electron affinity, $\chi$	4.3 eV[152]	
Mott-Schottky analysis	Flatband potential, $V_{\text{FB}}$	0.1 $V_{\text{RHE}}$	
	Donor concentration, $N_{\text{D}}^{+}$	$7.43 \cdot 10^{17} \text{ cm}^{-3}$	
DFT calculation	Relative permittivity, $\epsilon_{\text{r}}$	15	
	Effective mass of electron, $m_{\text{e}}^{*}$	0.74	
	Effective mass of holes, $m_{\text{h}}^{*}$	0.558	
	Density of states of the conduction band, $N_{\text{C}}$	$1.54 \cdot 10^{19} \text{ cm}^{-3}$	
	Density of states of the valence band, $N_{\text{V}}$	$1.01 \cdot 10^{19} \text{ cm}^{-3}$	
Conductivity measurements + DFT calculation	Electron mobility, $\mu_{\text{n}}$	$46 \text{ cm}^2 \text{ V}^{-1} \text{ s}^{-1}$	
	Hole mobility, $\mu_{\text{p}}$	$61 \text{ cm}^2 \text{ V}^{-1} \text{ s}^{-1}$	
Inverse analysis	Best-LTON	Electron effective lifetime, $\tau_{\text{eff},\text{n}}$	$5 \cdot 10^{-10} \text{ s}$
	Bare-LTON	Electron effective lifetime, $\tau_{\text{eff},\text{n}}$	$1 \cdot 10^{-11} \text{ s}$
	Best-LTON	Hole effective lifetime, $\tau_{\text{eff},\text{p}}$	$5 \cdot 10^{-10} \text{ s}$
	Bare-LTON	Hole effective lifetime, $\tau_{\text{eff},\text{p}}$	$1 \cdot 10^{-11} \text{ s}$
	Best-LTON	Interfacial hole transfer velocity, $v_{\text{s},\text{p}}$	$3.5 \cdot 10^{-8} \text{ m} \cdot \text{s}^{-1}$
	Bare-LTON	Interfacial hole transfer velocity, $v_{\text{s},\text{p}}$	$8.2 \cdot 10^{-9} \text{ m} \cdot \text{s}^{-1}$
Quantitative structural analysis	Height of model domain, $d$	$1.42 \mu\text{m}$ [125]	
	Width of model domain, $W$	$0.6 \mu\text{m}$ [125]	
	Surface roughness factor, $r$	18.2[125]	
Assumption	Interfacial electron transfer velocity, $v_{\text{s},\text{n}}$	$1 \cdot 10^{-12} \text{ m s}^{-1*}$	

\*An interfacial electron transfer velocity of  $1 \cdot 10^{-12} \text{ m/s}$  is assumed to avoid having the back reaction of oxygen reduction.

### 2.5.2. Identifying key material parameters

**Interfacial hole transfer velocity.** The interfacial hole transfer velocity is highly affecting the performance of the particle-based LTON PEs, as depicted in Fig. 2.7.a. Indeed, we observed a potential photocurrent increase of  $2.3 \text{ mA cm}^{-2}$  at  $1.23 \text{ V}_{\text{RHE}}$  compared to our current experimental results when increasing the interfacial hole transfer velocity under back-side illumination by a factor of 10. Similar trends were observed for photocurrent densities under front-side illumination, although the improvement was limited to  $0.07 \text{ mA cm}^{-2}$  at  $1.23 \text{ V}_{\text{RHE}}$  (Fig. 2.7.b). The interfacial hole transfer velocity also reduces the onset potential since it reduces the recombination rate and, thus, the need of a higher band bending at the semiconductor-electrolyte interface. Therefore, less applied potential is required to overcome the recombination present in the SCL. The shape of the photocurrent's curve also changes with varying interfacial hole transfer velocity, i.e. decreasing the slope of the photocurrent curve with smaller velocities. The photocurrent density increased from  $2.5 \text{ mA cm}^{-2}$  to  $3.5 \text{ mA cm}^{-2}$  at  $1.23 \text{ V}_{\text{RHE}}$  with  $v_{s,p}$  increasing from



## 2: Determination and optimization of material parameters of particle-based LaTiO<sub>2</sub>N photoelectrodes

---

$10^{-5}$  to  $10^{-4}$  cm s<sup>-1</sup>, respectively. Above a value of  $\nu_{sp} = 1 \cdot 10^{-4}$  cm s<sup>-1</sup>, the photocurrent density remained constant at 3.5 mA cm<sup>-2</sup> at potentials above 1.23 V<sub>RHE</sub>, only the onset potential was improved. The interfacial hole transfer velocity is the parameter affecting most significantly the performance of LTON particle-based PEs in terms of photocurrent and onset potential.

**Hole and electron mobilities.** Improving the hole mobility from 10 cm<sup>2</sup> V<sup>-1</sup> s<sup>-1</sup> to 500 cm<sup>2</sup> V<sup>-1</sup> s<sup>-1</sup> does not significantly affect the photocurrent density, i.e. it increased the photocurrent by 0.1 mA cm<sup>-2</sup> at 1.23 V<sub>RHE</sub>, 10 % relative increase (Fig. 2.8). Under back-side illumination, the impact of the hole mobility was higher, with an increase of 0.22 mA cm<sup>-2</sup> at 1.23 V<sub>RHE</sub> (37 % relative increase) for a hole mobility increase from 10 cm<sup>2</sup> V<sup>-1</sup> s<sup>-1</sup> to 500 cm<sup>2</sup> V<sup>-1</sup> s<sup>-1</sup>. LTON particles have a high hole mobility, 61 cm<sup>2</sup> V<sup>-1</sup> s<sup>-1</sup>, and this is confirmed by the numerical  $I$ - $V$  curves within the experimental error bars (Fig. 2.8). Therefore, the hole mobility is not a limiting parameters for the performance of the PEs and any further improvement of it by, for example, reducing the doping concentration of the material[154] would not lead to any performance improvement of the LTON PEs.

The photocurrent was insensitive to variations of the electron mobility (tested for 0.1 cm<sup>2</sup> V<sup>-1</sup> s<sup>-1</sup> to 500 cm<sup>2</sup> V<sup>-1</sup> s<sup>-1</sup>) under both illuminations' sides (Fig. A2.17). The photocurrent is a hole current and the electrons are only here to balance the hole current under steady-state, but are not the limiting factor. Only if the electron mobility becomes too small would the electrons not be able to balance the hole current, resulting in the photocurrent abruptly dropping to zero. This was the case under front-side illumination for an electron mobility of 0.1 cm<sup>2</sup> V<sup>-1</sup> s<sup>-1</sup> and below.

## 2: Determination and optimization of material parameters of particle-based LaTiO<sub>2</sub>N photoelectrodes

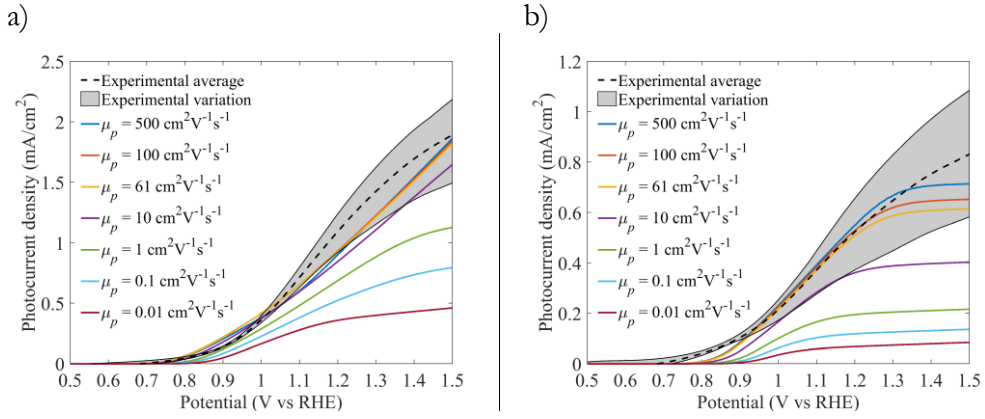


**Fig. 2.8.** Numerical and experimental photocurrent-voltage curves of best-LTON under a) back- and b) front-side illumination for varying hole mobilities. The photocurrent density was reduced from 1.02 mA cm<sup>-2</sup> to 0.37 mA cm<sup>-2</sup> at 1.23 V<sub>RHE</sub> when reducing the hole mobility from 500 cm<sup>2</sup> V<sup>-1</sup> s<sup>-1</sup> to 0.01 cm<sup>2</sup> V<sup>-1</sup> s<sup>-1</sup>. Under front-side illumination, the photocurrent density was reduced from 0.59 mA cm<sup>-2</sup> to 0.07 mA cm<sup>-2</sup> at 1.23 V<sub>RHE</sub> when reducing the hole mobility from 500 cm<sup>2</sup> V<sup>-1</sup> s<sup>-1</sup> to 0.01 cm<sup>2</sup> V<sup>-1</sup> s<sup>-1</sup>.

**Electron and hole effective lifetimes.** Both electron and hole lifetimes are affecting the photocurrent and the onset potential (Fig. 2.5 and Fig. 2.6). The impact of effective hole lifetime on the photocurrent, however, was greater than for the effective electron lifetime, i.e. the photocurrent increased by 0.5 mA cm<sup>-2</sup> at 1.23 V<sub>RHE</sub> for an increase of two orders of magnitude in hole lifetime compared to an increase of 0.3 mA cm<sup>-2</sup> for an increase of two orders of magnitude in electron lifetime. The impact of the effective hole lifetimes on the photocurrent was less significant compared to the effect of the interfacial hole transfer velocity. The most pronounced effect of increasing effective lifetimes was the downshift of the onset potential for both illumination sides. The applied potential directly changed the band bending at the semiconductor-electrolyte interface, and this bending was reduced with a higher effective electron lifetime.

**Doping concentration.** Modifying only the doping concentration without changing any other parameters did not influence the performance of LTON PEs under back-side illumination (Fig. A2.18.a). Under front-side illumination, the photocurrent was slightly increased, 0.1 mA cm<sup>-2</sup> at 1.23 V<sub>RHE</sub>, by reducing the doping concentration from 10<sup>19</sup> cm<sup>-3</sup> to 10<sup>16</sup> cm<sup>-3</sup> (Fig. A2.18.b). Therefore, the doping concentration must be varied together with other parameters to see an increase in the performance.

## 2: Determination and optimization of material parameters of particle-based LaTiO<sub>2</sub>N photoelectrodes

---

### 2.5.3. Pathways to improved performance

Properties such as the effective lifetimes, the interfacial hole transfer velocity, and the doping concentration can be modified experimentally to improve the photocurrent. The interfacial hole transfer velocity for best-LTON PEs with CoO<sub>x</sub> and CoOH as co-catalysts was still six orders of magnitude smaller than the interfacial hole transfer for n-GaN ( $5 \cdot 10^{-2} \text{ m s}^{-1}$ ) [104] pointing to the need for co-catalyst improvement. Moreover, the hole transfer velocity of the bare-LTON PE was one order of magnitude smaller than the best-LTON PE, i.e.  $8.2 \cdot 10^{-9} \text{ cm s}^{-1}$  for bare-LTON and  $3.5 \cdot 10^{-8} \text{ cm s}^{-1}$  for best-LTON (Table 2.1 and Fig. A2.19). Thus, we conclude that either the role of the catalyst is not a truly catalytic one or that the dipping deposition method is not providing a good contact between the catalyst and the photoabsorber. Recently, the deposition of CoO<sub>x</sub> co-catalyst on LTON particle-based PEs with microwave annealing showed significantly higher photocurrent ( $8.9 \text{ mA cm}^{-2}$  at  $1.23 V_{\text{RHE}}$ ) [103] than the PEs presented in this work. Therefore, different co-catalyst deposition should be investigated in the future to determine if the deposition method is truly the key factor for the performance of LTON particle-based PEs.

The effective lifetimes include surface and bulk lifetimes. The effective lifetimes with a value of 0.5 ns for the best-LTON PEs were high compared to other materials with high surface recombination such as GaN [104] (2-3 orders of magnitude higher) but low compared to well-known and efficient material such as Si (effective lifetimes above 1  $\mu\text{s}$  [155]). The effective lifetime of the best-LTON PE was improved by one order of magnitude compared to the bare-LTON PEs (Table 2.1). Thus, surface passivation treatments by the deposition of Ta<sub>2</sub>O<sub>5</sub>, or surface lifetime improvement by deposition of NiO<sub>x</sub> of our best-LTON PEs is confirmed to increase the photocurrent.

The key parameters on the performance of PEs are the effective lifetimes and interfacial hole transfer. These properties were optimized to improve photocurrent densities as depicted in Fig. 2.9. Additionally, the doping concentration was adapted and optimized accordingly to the new conditions. An internal quantum efficiency (IQE) of 46 % (integrated from 400 nm to 590 nm) was obtained at  $1.23 V_{\text{RHE}}$  by improving the hole transfer velocity from  $3.5 \cdot 10^{-6} \text{ cm s}^{-1}$  to  $1 \cdot 10^{-4} \text{ cm s}^{-1}$ , increasing the hole and electron lifetimes from 5 ns to 1 ns, and reducing the doping concentration from  $7.43 \cdot 10^{17} \text{ cm}^{-3}$  to  $1 \cdot 10^{16} \text{ cm}^{-3}$ . Indeed, the photocurrent was increased from  $1.2 \text{ mA cm}^{-2}$  to  $4.33 \text{ mA cm}^{-2}$  at  $1.23 V_{\text{RHE}}$ , which corresponds to an incident photon-to-current efficiency (IPCE) of 10 % by considering the entire solar

## 2: Determination and optimization of material parameters of particle-based LaTiO<sub>2</sub>N photoelectrodes

---

simulator's spectral irradiance (photon flux current density of 41.56 mA cm<sup>-2</sup>). An effective lifetime of 1 ns corresponds to a pure bulk lifetime with complete removal of surface recombination if we assume a bulk lifetime of 1ns like for GaN[104]. The onset can be reduced to 0.1 V<sub>RHE</sub> with a strong photocurrent increase at 0.3 V<sub>RHE</sub> by further increasing the hole transfer velocity to 100 cm s<sup>-1</sup>. Nevertheless, such a high charge transfer velocity is unlikely to be achieved even with highly performing co-catalysts.

By only increasing the surface properties of LTON particles, we reached an IQE of 40% at 1.23 V<sub>RHE</sub> which corresponds to a photocurrent increase of 2.56 mA cm<sup>-2</sup>, from 1.2 mA cm<sup>-2</sup> to 3.76 mA cm<sup>-2</sup>. This photocurrent density corresponds to an IPCE of 9 %, three times larger compared to our current experimental value of 3 %.

Although these improvements are important, they are greatly limited by the fact that only the first layer of particles is contributing to the photocurrent. Much higher improvement could be achieved if the entire film thickness of the LTON PEs would contribute to the photocurrent and will be investigated in the future.

## 2: Determination and optimization of material parameters of particle-based LaTiO<sub>2</sub>N photoelectrodes

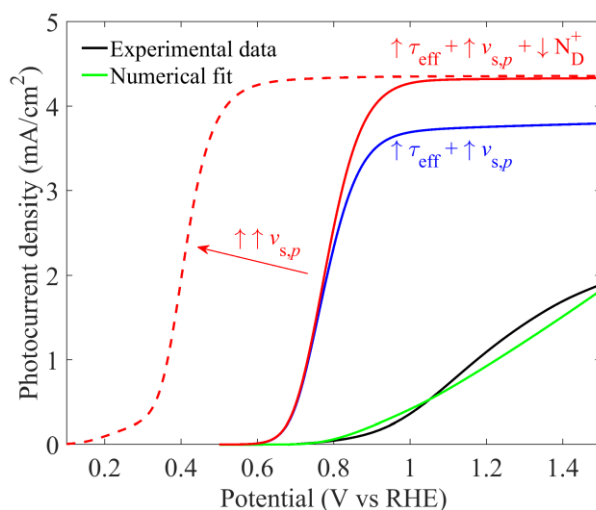


**Fig. 2.9.** Numerical and experimental photocurrent-voltage curves of best-LTON under back-side illumination for effective lifetime and interfacial hole transfer velocity optimization (blue line) and for additionally doping concentration optimization (red line). The current IPCE is 3 % (black or green line) and is improved to 9 % (blue line) by only improving the effective lifetimes of hole and electron from 0.5 ns to 1 ns and the interfacial hole transfer velocity from  $3.5 \cdot 10^{-6} \text{ cm} \cdot \text{s}^{-1}$  to  $1.10^{-4} \text{ cm} \cdot \text{s}^{-1}$ . The IPCE can be further improved to an IPCE of 10 % by reducing the doping concentration from  $7.43 \cdot 10^{17} \text{ cm}^{-3}$  to  $1.10^{16} \text{ cm}^{-3}$ . The onset potential can be reduced to 0.1 V<sub>RHE</sub> by increasing the interfacial hole transfer velocity to  $100 \text{ cm} \cdot \text{s}^{-1}$  (red dashed line).

### 2.6. Conclusion

We presented an experimental-numerical approach for determining material parameters that are not easily accessible otherwise. We successfully connected macro-scale and molecular-scale modeling with optical, transport, and electrochemical experiments to provide—for the first time—all necessary parameters to build a 2D numerical model capable of predicting the  $I$ - $V$  curve of particle-based LTON PEs. Furthermore, this numerical model provides a predictive tool for the performance of morphologically complex, multi-component LTON PEs. It allowed us to identify and to study the impact of key parameters on the photoelectrode's performance in order to deduce material design guidelines for materials scientists and give recommendations for pathways to photoelectrode performance engagements. We found that the interfacial hole transfer velocity was the most important parameter, and its improvement should be prioritized. Indeed,

## 2: Determination and optimization of material parameters of particle-based LaTiO<sub>2</sub>N photoelectrodes

---

photocurrent density was numerically improved by 2.3 mA cm<sup>-2</sup> at 1.23 V<sub>RHE</sub> (from 1.2 mA cm<sup>-2</sup> to 3.5 mA cm<sup>-2</sup>) by boosting only the interfacial hole transfer velocity. Further improvements up to a photocurrent of 4.3 mA cm<sup>-2</sup> (IPCE of 10 %) were achieved by additionally reducing the doping concentration and increasing the effective lifetime.

The numerical model developed in this work can be further used to study numerically the impact of particle size on the photocurrent, which can be modified using different synthesis routes[102], and on particle density, which can vary with the deposition method of particles. Thus, design guidelines on the particle arrangement and size of particle-based PEs can be determined with this model. Furthermore, a numerical model of the inter-particle charge transfer mechanism between LTON particles can be added to the current model to provide additional understandings of particle-based PEs and the role of inter-particle necking that is still not elucidated.

# Majority charge carrier transport in particle-based photoelectrodes<sup>1</sup>

## 3.1. Introduction

The direct conversion of solar energy to hydrogen by using photoelectrochemical (PEC) water splitting approaches has been theoretically calculated to reach up to 40% solar-to-fuel efficiency using a dual bandgap tandem device[156]. Techno-economic calculations indicate that hydrogen produced by photocatalyst particle-suspension devices based on cheap photoabsorbers with a solar-to-fuel efficiency of only 5% can be cost-competitive with hydrogen produced by steam reforming of fossil fuels[16]. However, it has been very challenging to demonstrate experimentally efficiencies even as low as 5%. Experimentally, more successful approaches utilize immobilized photocatalyst particles on conducting substrates, termed particle-based photoelectrodes (PBPE). Such PBPEs are especially interesting as they can be fabricated by low cost dipping procedures, procedures currently used in commercial large-scale battery production[102]. Consequently, PBPEs might show an interesting cost-efficiency tradeoff. PBPEs can use different immobilization approaches, providing a large variety of PE mesostructure designs, which can influence photoabsorption, charge transport, surface charge transfer, independently of the material composition of the individual particles. Moreover, the shape, size, surface area and roughness, and crystallinity of the individual particles can be modified, which greatly impact the performance of PBPEs[102]. One important element influencing the performance of PBPE is the inter-particle conductivity. Different approaches have been tested to improve the inter-particle conductivity, for example by adding a, so-called, necking material to connect particles[153] or by adding a

---

<sup>1</sup> A manuscript of this chapter is under review, 'Y. K. Gaudy, S. Dilger, S. Pokrant, and S. Haussener, Majority charge carrier transport in particle-based photoelectrodes, 2019, under review.

carbon containing conductive network linking particles and the conductive substrate[148]. Although the impact of the inter-particle conductivity on the performance of PBPE has been reported[140], [149], [153], the inter-particle charge transport has never been investigated in details. Nishimura et al. reported a performance increase of PBPEs when applying TiO<sub>2</sub> necking but without attempting to describe or discriminate the inter-particle charge transport [153]. Landsman et al. tried different necking materials such as TiO<sub>2</sub>, SnO<sub>2</sub>, Ta<sub>2</sub>O<sub>5</sub>, Nb<sub>2</sub>O<sub>5</sub>, and Al<sub>2</sub>O<sub>3</sub> and observed that PBPEs with TiO<sub>2</sub> necking exhibited the highest photocurrent[102]. Higashi et al. attributed the increase of the photocurrent through necking treatment to the improvement of electron transport between the TaON particles[149]. There was no investigation to determine if the improvement was actually caused by inter-particle conductivity improvement or simply by an improved contact of TaON particles with the fluorine tin doped (FTO) glass substrate. Moreover, a comparison of the photocurrent density under back-side illumination (illuminated from the FTO-side) and front-side illumination (illuminated from the semiconductor-side through the electrolyte) to strengthen or to disprove their hypothesis was missing. Dilger et al.[148] observed that adding a carbon containing conductive network in PBPEs without co-catalysts led to higher front-side illumination photocurrent (front photocurrent) than back-side illumination photocurrent (back photocurrent). They attributed this result to improved majority charge carrier transport, resulting from the added conductive network. Adding co-catalysts inverted the front- to back-side illumination (front to back) photocurrent ratio[21] and was attributed to a limited charge transport capacity of the conductive network for high performing PBPEs[148]. Feng et al.[140] decreased the size of particles in particle-based LaTiO<sub>2</sub>N (LTON) PEs in order to increase the active surface area and, thus, the efficiency, as was expected from observations in mesoporous TiO<sub>2</sub> in dye-sensitized solar cells (DSSCs)[157]. Unexpectedly, PBPEs made of smaller particles resulted in lower efficiency. Moreover, the back photocurrent was much higher than the front one for small particles while the illumination side did not influence the performance for larger particles. They attributed this result to the larger number of inter-particle contacts present within the PBPEs made of smaller particles that reduced the electron transport. However, the PBPEs made of larger particles appeared to have only about a single layer of particles and therefore no contribution of upper particles to the photocurrent where observed.

Modeling and theoretical work of particle-based semiconductor substrates such as the mesoporous anatase TiO<sub>2</sub> in DSSCs have been developed over decades. Bisquert and Marcus reviewed the state-of-the-art modeling of DSSCs, which provided



### 3: Majority charge carrier transport in particle-based photoelectrodes

---

insights into the various, coupled transport phenomena occurring in DSSCs and allowed for DSSC's precise characterization[158]. Furthermore, Bisquert developed equivalent-electrical circuits-based transient numerical models to assess the charge transport, generation and recombination behavior of DSSCs. Time constants of charge transfer, trapping, and detrapping were determined by fitting the equivalent circuits to measured impedance spectra of DSSCs[159]. Peter presented the main physico-chemical principles behind DSSCs in order to outline the differences between DSSCs and conventional photovoltaic solar cells. He also analyzed and quantified the different loss mechanisms of DSSCs[160]. In all these modeling and theoretical works, the mesoporous anatase  $\text{TiO}_2$  was systematically treated as a low-resistance structure for the transport of electrons where the electron transport follows a diffusion current only. Thus, the mesoporous  $\text{TiO}_2$  is neither working as a photoabsorber nor as a material with an internal electric field described by the drift-diffusion current equation. In contrast, the semiconducting particles in PBPEs are photoabsorbers that convert light into electron-hole pairs in the presence of an electric field (the space charge layer) resulting from the energy level equilibration at the semiconductor-electrolyte interface[161]. Therefore, we cannot treat PBPEs in the same way as mesoporous  $\text{TiO}_2$  networks of DSSCs. Particles in PBPE must be treated as photoabsorbers encountering electron-hole pair generation and the charge transport must be described by a drift-diffusion current equation. In our previous work, we developed a numerical model solving the drift-diffusion current equations for holes and electrons to reproduce and predict photocurrent-potential ( $I$ - $V$ ) curves of particle-based LTON PEs[161]. Our model was able to predict the experimental  $I$ - $V$  curves only when a single layer of particles in contact with the FTO was considered, excluding the contribution to the photocurrent of upper particles. Nevertheless, we did not investigate the reason for this exclusive contribution of the first particle layer to the photocurrent nor the related inter-particle charge transfer.

It becomes obvious from these previous works that the inter-particle charge transfer in PBPEs remains largely unknown and the approach of inter-connecting particles undiscussed. A better understanding is needed to guide research towards high-performing PBPEs. Here, we investigated the inter-particle charge transfer of PBPEs using LTON as model system. First, we experimentally investigated the thickness-dependence and front- and back-side illumination dependence on the photocurrent of the PBPEs in order to provide information about charge transport limitations. The limiting front to back photocurrent ratio depending on the PE's thickness was then computed and compared to the experimental data. This comparison indicated the thickness of the particle-based film that contributes to the

photocurrent. Then, we introduced three different theoretical inter-particle charge transfer mechanisms that could describe the inter-particle charge transport of PBPEs. Their related equations were implemented in a numerical model accounting for non-ideal transport behavior and used to calculate  $I$ - $V$  curves[161]. The numerical  $I$ - $V$  curves were subsequently compared to experimental  $I$ - $V$  curves to determine which of the inter-particle charge transfer mechanisms most likely occurred and also if only the particles in direct contact with the FTO were contributing to the photocurrent. In addition, quantification of the potential performance improvements were provided, assuming the different inter-particle charge transfer mechanisms were actually occurring. We finish by discussing the most likely transport between particles and provide design guidance for higher performing PBPEs.

## 3.2. Methodology

### 3.2.1. Estimated thickness contributing to the photocurrent

The thickness of the LTON PBPEs was controlled by varying the electrophoretic deposition (EPD) time as done by Dilger et al.[148]. The photocurrent density of the PBPEs with different thickness was measured under front and back-side illumination at a potential of 1.23 V vs the reversible hydrogen electrode ( $V_{\text{RHE}}$ ) under the same experimental conditions as Dilger et al.[148]. Bare-LTON electrodes were used for these measurements since adding catalysts would introduce additional effects (section 3.2.4). The measured thickness-dependent front to back photocurrent ratios of the PBPE were compared to the numerical front to back photogenerated current ratio. The photocurrent is the product of the photogenerated current,  $i_l$ , representing the maximum possible current that can be extracted of the photoelectrode (considering realistic absorption behavior and perfect charge transport), and the separation and the injection yields[162], [163]:

$$i_{\text{ph}} = i_l \times \phi_{\text{sep}} \times \phi_{\text{inj}}, \quad (3.1)$$

where the separation yield,  $\phi_{\text{sep}}$ , is the yield of photogenerated minority charge carriers reaching the semiconductor-electrolyte interface, and the injection yield,  $\phi_{\text{inj}}$ , is the yield of these charges injected into the electrolyte for the water reduction

### 3: Majority charge carrier transport in particle-based photoelectrodes

---

or oxidation reaction. These yields are depending on the charge recombination and transport in the bulk and at the semiconductor-electrolyte interface, but not on the illumination side for holes since they can be extracted orthogonally to the irradiation direction (along the radius of the particle). However, electrons are extracted along the direction of the irradiation. Therefore, the numerical photogenerated current was calculated by integrating the generation rate solved by Beer-Lambert law along the thickness,  $x_{\text{lim}}$ .  $x_{\text{lim}}$  is defined as the maximum thickness which still allows electrons to reach the FTO substrate. In other words,  $x_{\text{lim}}$  corresponds to the thickness of particles contributing to the photogenerated current. Particles below  $x_{\text{lim}}$  are contributing to the photogenerated current while particles above  $x_{\text{lim}}$  are not contributing to the photogenerated current. The numerical photogenerated current is given by

$$i_{\text{l,front}} = q \int_0^{x_{\text{lim}}} \int_0^{\lambda_{\text{gap}}} [1 - R_{\text{front}}(\lambda)] N(\lambda) e^{-\alpha(\lambda)\rho(d-x)} d\lambda dx, \quad (3.2)$$

under front-side illumination and given by

$$i_{\text{l,back}} = q \int_0^{x_{\text{lim}}} \int_0^{\lambda_{\text{gap}}} [1 - R_{\text{back}}(\lambda) - A_{\text{FTO}}(\lambda)] N(\lambda) e^{-\alpha(\lambda)\rho x} d\lambda dx, \quad (3.3)$$

under back-side illumination.  $x$  is the location through the thickness of the PBPE (along the substrate's surface normal) according to Fig. 3.1, with the FTO-LTON interface corresponding to  $x=0$  and the top of the PBPE corresponding to  $x=d$ .  $N$  is the spectral photon flux hitting the PBPE following the global standard spectrum AM1.5G.  $\alpha$  is the spectral absorption coefficient of LTON taken from Gaudy et al.[161].  $\rho$  is the solid phase density in the PBPE. The spectral reflectance under front- and back-side illumination,  $R_{\text{front}}$  and  $R_{\text{back}}$ , and the absorptance of the FTO glass substrate under back illumination,  $A_{\text{FTO}}$ , were also taken from Gaudy et al.[161]. For front- and back-side illumination, the absorption in the electrolyte was neglected. The integrals over the wavelength and over the thickness were solved numerically with a resolution of 1 nm. The bandgap wavelength,  $\lambda_{\text{gap}}$ , was 590 nm for LTON (bandgap of 2.1 eV).

The front to back photocurrent ratio can be compared to the front to back photogenerated current

$$\frac{i_{ph,front}}{i_{ph,back}} = \frac{i_{l,front} \times \phi_{sep} \times \phi_{inj}}{i_{l,back} \times \phi_{sep} \times \phi_{inj}} = \frac{i_{l,front}}{i_{l,back}} \quad (3.4)$$

As previously mentioned, the separation and the injection yields of the holes are the same for both illumination directions. These yields depend on the illumination direction for electrons and are included in the photogenerated current calculations (eqns (3.2) and (3.3)). If a  $x_{lim}$  provides a numerical front to back photogenerated current ratio that matches the experimental photocurrent ratio, we assume that this  $x_{lim}$  is the thickness of the film that contributes to the photocurrent. However, this  $x_{lim}$  is only an estimation of the actual thickness of particles contributing to the photocurrent. Indeed, the solid phase density was not measured for each of the PBPE thicknesses but assumed to be constant at 0.28 according to the density profile in the first 4  $\mu\text{m}$  of a 8.43  $\mu\text{m}$  LTON PBPE from Suter et al.[125]. However, the density profile from Suter et al. is not constant and decreases after 4  $\mu\text{m}$ . Thus, the numerical photogenerated current ratio (eqns (3.2) and (3.3)) in PBPE is only an estimation, and so is  $x_{lim}$ . A more precise estimation of  $x_{lim}$  could incorporate the measured solid phase density for each of the PBPE thicknesses and by calculating the generation rate using an EMW propagation model with the exact morphology of the PBPE.

#### 3.2.2. Theoretical inter-particle charge transfer mechanisms

The charge transfer at the LTON particle-TiO<sub>2</sub> necking-FTO substrate interface is briefly introduced, before discussing the inter-particle transfer. We hypothesize that the LTON-TiO<sub>2</sub> contact provides a built-in field that promotes the electron transfer because the conduction band level of LTON is  $-4.2 \pm 0.1$  V vs vacuum ( $V_{vac}$ )[152] and the conduction band of TiO<sub>2</sub> is  $-4.8 V_{vac}$  or  $-5.1 V_{vac}$ , depending on its crystal structure[164]. The electron charge transfer from TiO<sub>2</sub> to FTO follows a charge transfer by tunneling rather than a Schottky barrier since the potential barrier width is only 1 nm[165]. Therefore, electrons can transfer from the LTON to the FTO effectively. Whereas, electrons would transfer by a Schottky barrier from LTON to FTO without the TiO<sub>2</sub> necking. The potential barrier width would be too large (25 nm for LTON with a potential barrier of 0.3 V and a doping concentration of  $7.4 \times 10^{17} \text{ cm}^{-3}$  and a permittivity of 15[161]) to allow electron tunneling and thus

### 3: Majority charge carrier transport in particle-based photoelectrodes

---

would severely impact the performance of LTON PBPE, as observed by Landsmann et al.[102]. The inter-particle interface, LTON-TiO<sub>2</sub>-LTON, is radically different from the LTON-TiO<sub>2</sub>-FTO contact since there is no FTO. Here, we discuss this difference by introducing three different models for describing the inter-particle charge transfer mechanism. The first inter-particle charge transfer mechanism case, depicted in Fig. 3.1.c case 1, assumes that the majority charge carriers cannot be transported from one particle to the other. Only the photogenerated electrons of the first layer of particles that are in direct contact with the FTO can be collected. This implies that under front-side illumination any additional particles lying on top of the first layer of particles will hinder the light absorbed by the first layer of particles while under back illumination there is simply no additional gain of adding particles on top of the first layer of particles. The energy band diagram of the inter-particle contact in case 1, as depicted schematically in Fig. 3.1.d, can be compared to a double Schottky barrier present at the grain boundary of polycrystalline semiconductors[119], [120]. The surface in contact between the particles is much smaller than the surface between grains in well performing polycrystalline semiconductors. Indeed, the grain sizes and boundaries in well performing polycrystalline Si varies from few millimeters to centimeters, while the size of particles and inter-particle contacts in LTON PBPEs varies from nanometers to micrometers[102], [125]. Polycrystalline silicon solar cells are poorly performing when the grains are randomly oriented, as is the case for particles in LTON PBPEs, compared to columnar or dendritic orientation having a single crystalline grain from the top to the bottom of the solar cell[166], [167]. In analogy to the transport behavior known from Si grains, case 1 assumes a double Schottky barrier that is too high to allow any majority charge carrier transfer between particles. The boundary between the first and the second particle assumes no charge transfer, given by

$$\mathbf{i}_n \cdot \hat{\mathbf{n}} = \mathbf{i}_p \cdot \hat{\mathbf{n}} = 0, \quad (3.5)$$

The second inter-particle charge transfer mechanisms case, depicted in Fig. 3.1.c case 2, assumes an ohmic contact between particles with a potential drop due to the contact resistance,  $V_{IPC}$ . The energy band diagram of the inter-particle contact in case 2, as schematically depicted in Fig. 3.1.d, is treated as grain boundaries in cauliflower-type structures of hematite photoanodes[121], given by[104]

### 3: Majority charge carrier transport in particle-based photoelectrodes

---

$$V_{\text{SCR}} = V_a - V_{\text{FB}} - \sum_i^m V_{\text{IPC},i}, \quad (3.6)$$

where  $V_{\text{SCR}}$  is the space charge region (SCR) potential (a discrete function) and  $m$  is the number of inter-particle contacts. If  $V_{\text{IPC}}$  is too high, the upper particles do not feel the effect of the applied potential,  $V_a$ , and, correspondingly, the upper particles do not contribute to the photocurrent. If the inter-particle contact resistance is of medium magnitude and the upper particles are contributing to the photocurrent, we use eqn (3.6) to compute the SCR potential depending on the height of the particle. Since the potential  $V_{\text{IPC}}$  is not known, we assumed a linear SCR potential drop depending on the height,  $x$ , given by

$$V_{\text{SCR}}(x) = V_a \left(1 - \frac{x}{d}\right). \quad (3.7)$$

$d$  is the PBPE thickness and equals to 8.43  $\mu\text{m}$  as determined in Gaudy et al.[161]. In this case, we assumed a continuous quasi-Fermi level over the height of the PBPE since this model is only driven by the SCR potential drop along every inter-particle contact. In a perfect inter-particle contact,  $V_{\text{IPC}}$  is negligible. In this case, we tested different situations: *i)* one for which the effective electron mobility is not influenced by any inter-particles contacts ( $\mu_{\text{eff},n} = \mu_{\text{b},n}$ ), *ii)* one for which the mobility drops over the height of the PBPE (see eqns (3.8) and (3.9)), and *iii)* one for which the mobility completely drops after the first particle in contact with the FTO. We treated the electron mobility drop over the height in analogy to polycrystalline silicon[122] or mesoporous  $\text{TiO}_2$  in DSSC[123], given by

$$1/\mu_{\text{eff},n} = 1/\mu_{\text{b},n} + \sum_i^m 1/\mu_{\text{IPC},n,i}, \quad (3.8)$$

Since  $\mu_{\text{IPC},n}$  is not known, two different mobility drops vs height were assumed. The mobility drop type I of situation *ii)* is given by

$$\mu_{\text{eff},n}(x) = \mu_{\text{b},n} \left(1 - \frac{x}{d}\right), \quad (3.9)$$

### 3: Majority charge carrier transport in particle-based photoelectrodes

---

and the mobility drop type II of situation *ii*) is given by

$$\mu_{\text{eff},n}(x) = \mu_{b,n} \left(1 - \frac{2x}{d}\right) \text{ for } x \leq \frac{d}{2} \text{ and } \mu_{\text{eff},n} = 0 \text{ for } x > \frac{d}{2}, \quad (3.10)$$

where  $\mu_{b,n}$  is  $46 \text{ cm}^2 \text{ V}^{-1} \text{ s}^{-1}$  [161]. The situation *iii*) of case 2 with a complete drop of mobility results in electrons of upper particles that cannot travel to the FTO glass substrate and leads to the same situation as case 1 (first layer of particle only contributing to the photocurrent).

The third inter-particle charge transfer mechanism case, depicted in Fig. 3.1.c case 3), considers particles in *pseudo-series* with holes and electrons recombining at each inter-particle contact. The term *pseudo-series* is used because every particle is surrounded by the same electrolyte while the contact between particles is in series. In this case, the inter-particle contact is modeled as a Schottky contact with negligible tunneling pinned to an inter-particle contact energy level. The electron and hole current densities are given by

$$\mathbf{i}_p \cdot \hat{\mathbf{n}} = qv_{\text{IPC},p}(p_{\text{IPC}} - p_{\text{IPC,eq}}), \quad (3.11)$$

$$\mathbf{i}_n \cdot \hat{\mathbf{n}} = qv_{\text{IPC},n}(n_{\text{IPC}} - n_{\text{IPC,eq}}), \quad (3.12)$$

As depicted in Fig. 3.1.c case 3), this charge transfer mechanism requires that the inter-particle SCL potential,  $V_{\text{IPSC}}$ , is sufficiently low to have electrons able to reach the inter-particle contact. If  $V_{\text{IPSC}}$  is too high, the charge transport is suppressed and situation is similar as in case 1 where only the first layer of particles contributes to the photocurrent. If tunneling at the inter-particle contact is high, the inter-particle charge transfer becomes similar to case 2.

This third inter-particle charge transfer mechanism case requires a perfect balance between photogenerated holes from the first particle and photogenerated electrons from the second particle at the inter-particle contact to recombine together. If there is only one type of charge carriers at the interface, this charge transfer mechanism cannot occur. The presence of the electric field in the SCR pushes electron away from the semiconductor-electrolyte (SC-EL) interface while attracting holes. For

### 3: Majority charge carrier transport in particle-based photoelectrodes

---

example the concentration of electrons is five times lower than the one of holes at the SC-EL interface in GaN photoanodes[104]. Thus, mostly electrons are present at the inter-particle contacts and holes at the SC-EL interface. However, the first layer of particles is not only in contact with particles but also with the TiO<sub>2</sub> necking-FTO substrate. In this case, electrons are pushed to the FTO substrate, as previously described, while holes are attracted to the SC-EL interface and to the inter-particle contact (if the electric field is favorable or if there is no electric field by diffusion transport). Moreover, holes at the inter-particle contact in the first particle recombine with electrons from the second particle. Therefore, it is a reasonable assumption that the third layer of particles as well as upper layers do not contribute to the photocurrent since mostly electrons will be present at their inter-particle contacts and holes at the SC-EL interface. Under these conditions, the charge transfer mechanism case 3 implies that the photocurrent remains limited to the photogenerated current in the first layer of particles and that the only benefit of this mechanism is to distribute the photocurrent within the first and second layer of particles.



### 3: Majority charge carrier transport in particle-based photoelectrodes

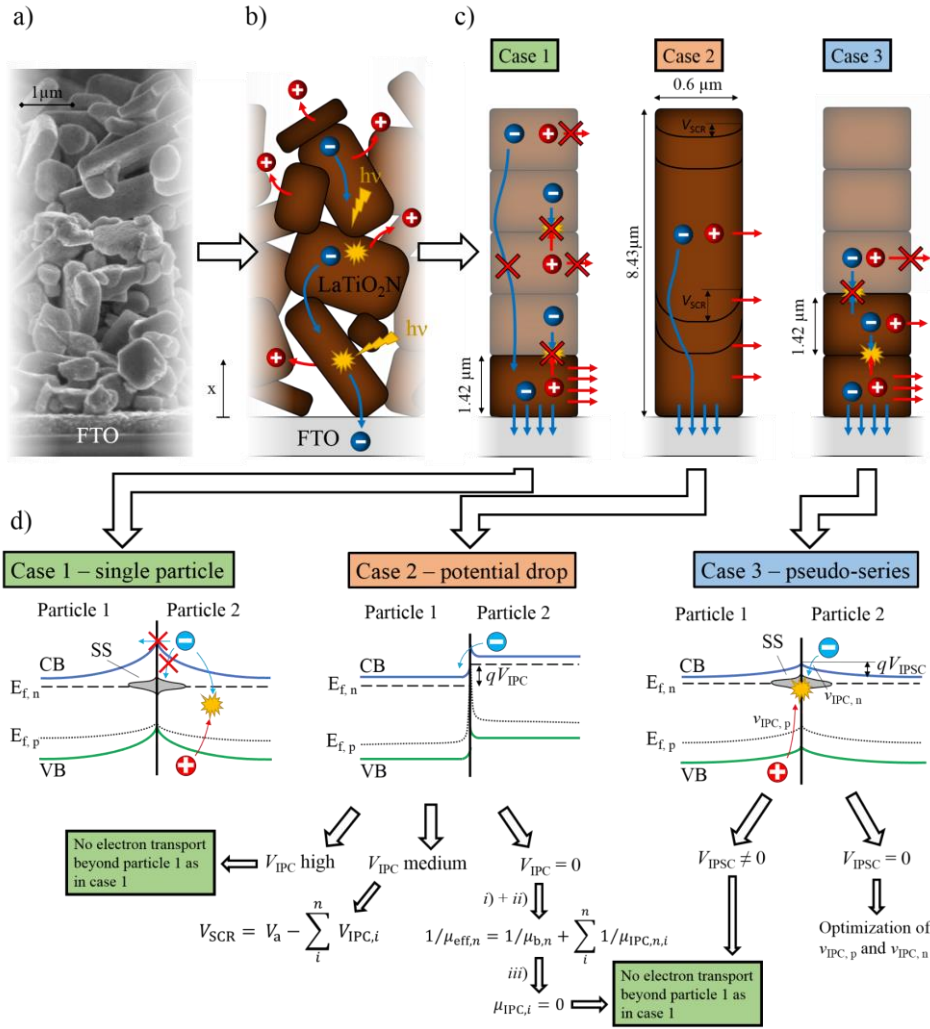


**Fig. 3.1.** a) SEM of LTON PBPEs, b) schematic of electron and hole generation and transport in LTON particles, c) simplified morphology model considering case 1: only the first layer of particles contributes to the photocurrent, case 2: quasi-Fermi level continuity between the particles, and case 3: particles in “pseudo-series” with computational domain dimensions. d) Details about each case with a scheme of the corresponding energy band diagram.

**Computational photoelectrode performance model.** The three different inter-particle charge transfer mechanisms cases were implemented in the computational photoelectrode model of Gaudy et al.[161], a 2-dimensional (2D), steady-state multi-physical continuum model that combines electromagnetic wave (EMW) propagation

model, charge transfer at the SC-EL interface, charge transport and conservation under steady-state for best-LTON PBPE. The EMW model considered a layer of 2 mm of electrolyte, 8.43  $\mu\text{m}$  of LTON particles with a solid phase density profile taken from Gaudy et al., 360 nm of  $\text{SnO}_2$ , 2.2 mm of glass, and 2 mm of electrolyte. The domain sizes of the charge transport and conservation model were approximated by rectangular model domains 1.42 x 0.6  $\mu\text{m}$  for case 1, 8.43 x 0.6  $\mu\text{m}$  for case 2, and (2x1.42) x 0.6  $\mu\text{m}$  for case 3 (see Fig. 3.1). An ohmic contact with thermodynamic equilibrium is present as the bottom boundary for all cases. The SC-EL interfaces were modeled by an adapted Schottky contact[104]. For case 1, SC-EL interfaces are present only on both side boundaries and the top boundary is assumed electronically insulated, i.e. no charge transfer occurred. For case 2, SC-EL interfaces are present on both sides and at the top of the domain's boundary. For case 3, SC-EL interfaces are present at the side boundaries of both particles and the inter-particle contact between the first and the second particle is modeled by a double Schottky contact given by eqns (3.11) and (3.12). The top boundary of the second particle is assumed to be insulated (without any charge transfer). The same interfacial hole transfer velocity at the SC-EL interface of  $3.5 \times 10^{-6} \text{ cm s}^{-1}$  is assumed for all three cases[161]. All the related equations, material parameters, numerical domain sizes, convergence criteria, and mesh discretization of best-LTON PBPE are presented in Gaudy et al.[161].

#### 3.2.3. Expected impact of particle size on the photocurrent

The impact of the particle size on the front to back photocurrent ratio is correlated to the majority charge transfer limitation in PBPEs. If only the first layer of particles in direct contact with the FTO substrate is contributing to the photocurrent, we should observe a decrease of the photocurrent with smaller particle sizes. Moreover, the front photocurrent should be more strongly reduced than the back photocurrent and lead to a smaller front to back photocurrent ratio. However, if the entire film thickness is contributing to the photocurrent, the size of particles should neither impact the photocurrent nor the front to back photocurrent ratio. The impact of particle size on the photocurrent in PBPEs is discussed in section 3.3.3 using published experimental studies of PBPEs with different LTON particle sizes[125], [140], [168].

#### 3.2.4. Photoelectrode preparation and characterization

The LTON particles in this work were synthesized by a solid-state reaction, named SS-LTON[102]. Two types of LTON PBPEs were prepared: the so-called best-LTON with multiple coating process and photocurrent density up to  $1.2 \text{ mA cm}^{-2}$  at  $1.23 \text{ V}_{\text{RHE}}$  under standard irradiance AM1.5G, and the so-called bare-LTON with a single dipping procedure and lower photocurrent density (ca.  $0.1 \text{ mA cm}^{-2}$  at  $1.23 \text{ V}_{\text{RHE}}$ ). The fabrication of both configurations is described in Gaudy et al.[161] and Landsmann et al.[141].

Electrochemical experiments were conducted in a three-electrode setup to refer the potential of our measurements to the RHE. The reference electrode was Ag/AgCl (sat. KCl) and the counter electrode was Pt. The aqueous electrolyte solution was  $0.1 \text{ M Na}_2\text{SO}_4$  as a buffer solution with  $\text{pH}=13.2\pm0.2$  by adding NaOH. The sample was illuminated by a solar simulator corresponding to the spectral irradiance of the AM1.5G spectrum. The PBPE's photocurrent thickness dependency was investigated by preparing different electrodes with varying EPD times (i.e. 30, 60, 120, 180, and 240 s), only for bare-LTON PBPEs. Adding catalysts would have added additional effects affecting the photocurrent thickness dependency measurements. The PE thickness was determined by taking the average thickness measured by profilometry. Measurements were done for one sample and current densities are averaged between forward and backward sweeps.

The photocurrent density at  $1.23 \text{ V}_{\text{RHE}}$  was taken as reference value on the forward linear sweep voltammograms. The experimental  $I-V$  curves of best-LTON PBPEs used in this work were taken from Gaudy et al.[161]. These results were obtained by averaging forward and backward sweeps of eight samples.

### 3.3. Results and discussion

#### 3.3.1. Thickness dependency of the front and back photocurrent

We expect the following thickness-dependent photocurrent response for the PBPEs. A poor majority charge carrier transport in PBPEs should lead to an optimum thickness under front-side illumination. At low thicknesses, the photocurrent increases with increasing thickness because photoabsorption is dominating, i.e. thicker films absorb more light. Above a certain thickness, the poor majority charge carrier transport is starting to limit and the photocurrent starts to decrease. An optimum thickness is observed under front-side illumination for photoelectrodes

### 3: Majority charge carrier transport in particle-based photoelectrodes

---

independent of the presence of SCR such as in  $\text{Cu}_2\text{O}$  photocathodes with a SCR[169] or  $\text{BiVO}_4$  photoanodes without a SCR[170] (purely diffusive charge carrier transport). If no optimum thickness is observed under front-side illumination and the photocurrent is only increasing with the thickness until it reaches a plateau, we can conclude that the majority charge carrier transport is not a limiting factor. If no optimum thickness is observed and the photocurrent is only decreasing, the majority charge carrier transport is limiting but the optimum thickness is below the range of investigated thicknesses. Under back-side illumination, the photocurrent increases limited by absorption. Above a certain thickness, the photocurrent reaches a plateau limited by majority carrier transport, i.e. the upper region is not contributing to the photocurrent anymore.

In the case of PBPEs, a decrease of the photocurrent with the thickness can be caused either by a poor majority charge carrier transport in the bulk or by a poor inter-particle majority charge carrier transport. Moreover, the thickness cannot be below a single layer of particles, a thickness of  $1.42\text{ }\mu\text{m}$  for LTON PBPE, because the particle-based film becomes highly inhomogeneous[148]. As depicted in Fig. 3.2, no optimum thickness was found for experimental front or back photocurrents of bare-LTON PBPEs. Indeed, the photocurrent decreased with increasing thickness under both illumination conditions (front and back). The decrease for front illumination is consistent with the explanation of strong majority carrier transport limitations. We attribute the progressive decrease of the photocurrent with increasing PBPE thickness under back illumination sides to a reduced amount of necking material at the LTON-FTO contacts with thicker films. We hypothesize that the amount of  $\text{TiO}_2$  necking is more distributed over the entire film for thicker films and more concentrated at the FTO-LTON contacts for thinner films. Thus, the photocurrent in thicker films is reduced compared to thinner films. This necking inhomogeneity also affects the front illumination current and, together with the majority current transport limitation, leads to its strong decrease with thickness.

### 3: Majority charge carrier transport in particle-based photoelectrodes

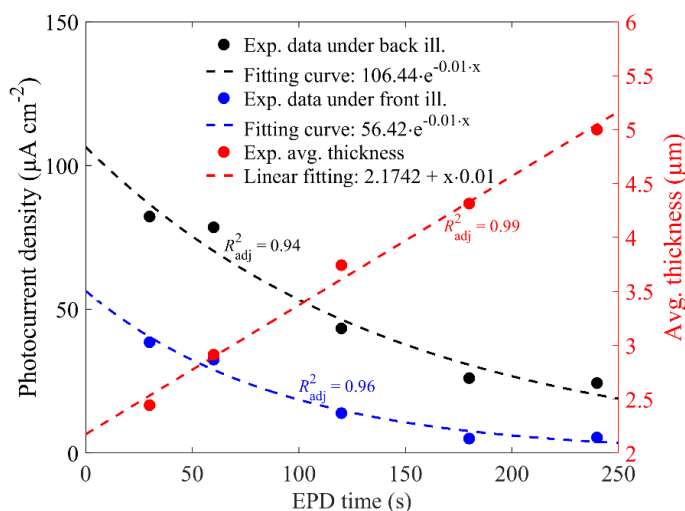


**Fig. 3.2.** Experimental front- and back-side illumination photocurrent densities at 1.23 V<sub>RHE</sub> and averaged thicknesses of the PBPE depending on the electrophoretic deposition time for bare-LTON PBPEs. Dashed curves indicate the numerical fit curves with their corresponding goodness of fit ( $R^2$ ).

The numerical generation rates (obtained by Beer-Lambert law) and photogenerated current densities (obtained by integrating the generation rates, eqns (3.2) and (3.3)) under front- and back-side illumination for case 1 and case 2 are depicted in Fig. 3.3. Case 1, with only the first layer of particles contributing to the photogenerated current ( $\lambda_{\text{lim}}=1.42 \mu\text{m}$ ), is depicted in Fig. 3.3 in opaque colors. Case 2, with the entire particulate film thickness contributing to the photogenerated current is depicted in Fig. 3.3 with semitransparent colors. The front to back photogenerated current ratio is 0.26 for case 1 and 1.11 for case 2 for the thickest PBPE of  $5 \mu\text{m}$ .

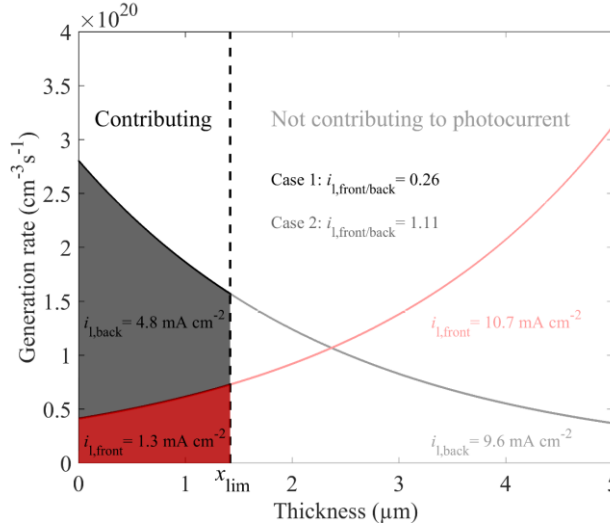


**Fig. 3.3.** Thickness-dependent generation rate and photogenerated current of a LTON PBPE with a thickness of 5  $\mu\text{m}$ , calculated by eqns (3.2) and (3.3) (Beer-Lambert law). The opaque colors are for case 1 considering a single layer of particles (1.42  $\mu\text{m}$ ) contributing to the photogenerated current (Fig. 3.1). The semitransparent colors are for case 2 with the full thickness of the PBPE (5  $\mu\text{m}$ ) contributing to the photogenerated current (Fig. 3.1). Red color indicate front-side illumination and black colors back-side illumination.

The thickness-dependent front to back numerical photogenerated current ratios of cases 1 to 3 are depicted in Fig. 3.4 along with the experimental front to back photocurrent ratio. The numerical photogenerated current ratio of case 1 follows an asymptotic decrease,  $1.97 \cdot e^{-0.405 \cdot d}$  ( $R^2=1$ ), similar to the experimental photocurrent ratio decrease,  $1.13 \cdot e^{-0.352 \cdot d}$  ( $R^2=0.91$ ). The numerical asymptotical decrease,  $e^{-x}$ , is caused by the generation rate that follows a Beer-Lambert law, as presented in eqns (3.2) and (3.3). For case 2 with the entire film thickness contributing to the photocurrent, the photogenerated current ratio is constant at 1.11 over the thickness. The ratio is higher than one because the FTO glass substrate absorbs some light under back-side illumination and none under front-side illumination (eqns (3.2) and (3.3)). Case 3 also shows a front to back photogenerated current ratio with an asymptotic decrease, although the ratio is above one for film thickness below 3  $\mu\text{m}$ . By optimizing the fitting of the numerical photogenerated current ratio to the experimental photocurrent ratio, the contributing thickness,  $x_{\text{lim}}$ , was found to be 450 nm, smaller than a single layer of particles. Only case 1 with  $x_{\text{lim}}=1.42 \mu\text{m}$  or  $x_{\text{lim}}=450 \text{ nm}$  exhibit a similar thickness-dependence as the experimental

### 3: Majority charge carrier transport in particle-based photoelectrodes

---

photocurrent ratio. Cases 2 shows a fundamentally different behavior than the experiment. Case 3 shows a similar thickness dependence, however at larger ratios.

The experimental data and numerical case 1 show a stronger decrease of the photogenerated current under front-side illumination ( $i_{l,front}/i_{l,back} < 1$ ), in accordance with an explanation that particles close to the FTO contribute more or exclusively to the photocurrent. Photogenerated current ratios greater than 1, as observed for our case 2, is similar to particles directly connected to the FTO. Such a situation was experimentally measured for LTON PBPE with a network of carbon nanotubes (CNTs) [148], showing a ratio greater than 1 as predicted by our numerical model.

The contributing thickness is calculated to be 450 nm with a solid phase density of 0.28, based on the best fit between the experimental photocurrent ratio and the numerical photogenerated ratio. However, this thickness is only an estimation as explained in 3.2.1 and thus provides some uncertainty in concluding that exclusively particles in direct contact with FTO are contributing to the photocurrent. However, we claim that the contribution of the upper particles to the photocurrent are most likely negligible as the front to back photogenerated current ratio of case 3 is in disagreement with the experimental data (experimental ratio of 0.47 at 2.5  $\mu\text{m}$  and numerical ratio of 1.15 for case 3 at 2.5  $\mu\text{m}$ ) or do not follow the same thickness-dependence (case 2). The solid phase density was assumed constant at 0.28. However, lowering the solid phase density ( $<0.28$ ) would reduce the absorption coefficient and would result in a thinner contributing thickness ( $<450$  nm). In contrast, increasing the solid phase density would result in a thicker contributing thickness ( $>450$  nm).

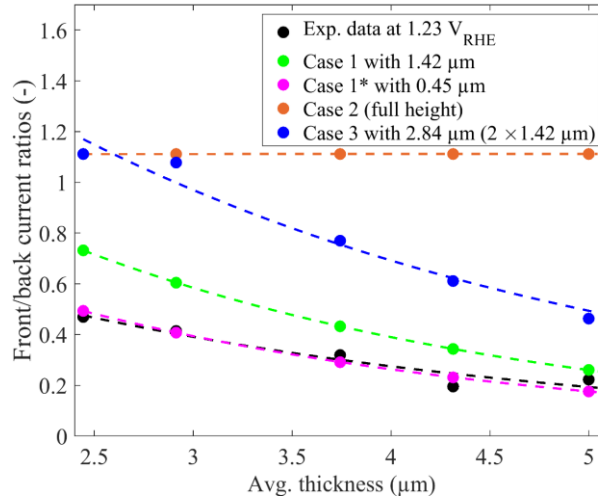


**Fig. 3.4.** Experimental photocurrent ratio 1.23 V<sub>RHE</sub> and numerical photogenerated current ratio ( $i_{\text{front/back}} < 1$ ) depending on the total averaged thickness of bare-LTON PBPEs. The fitting exponential curves are depicted with dashed lines. The fitting curve for the experimental ratio is given by  $1.13 \cdot e^{-0.352 \cdot d}$  ( $R^2=0.91$ ). Case 1, with a current-contributing thickness of 1.42 μm out of the total averaged thickness, has a fitting curve given by  $1.97 \cdot e^{-0.405 \cdot d}$  ( $R^2=1$ ). Case 1, with only a current-contributing thickness of 0.45 μm, has a fitting curve given by  $1.32 \cdot e^{-0.403 \cdot d}$  ( $R^2=1$ ). Case 2, with the full height contributing to the photogenerated current, has a constant fitting curve of 1.11 ( $R^2=1$ ). Case 3, with only a contributing thickness of 2.82 μm (two times an averaged particle height), has a fitting curve given by  $2.67 \cdot e^{-0.338 \cdot d}$  ( $R^2=0.95$ ).

#### 3.3.2. Numerical inter-particle charge transfer mechanisms

We estimated in the previous section—supported by experimental results as well as numerical results based on photogenerated current model—that the active thickness in LTON PBPEs contributing to the photocurrent is likely equal or even below the thickness of the first layer of particles. In order to provide more support for this conclusion, we show results of the more realistic 2D multi-physics PBPE model incorporating the majority carrier transport and the inter-particle transport mechanisms.

The front and back  $I$ - $V$  curves of case 1 (double Schottky contact with an impassable potential barrier for charge carriers) are depicted in Fig. 3.5.a. The numerical  $I$ - $V$  curves are within the experimental  $I$ - $V$  curves variation under front- and back-side



### 3: Majority charge carrier transport in particle-based photoelectrodes

---

illumination. The front and back  $I$ - $V$  curves of case 2 (potential drop at each inter-particle contacts) with a linear potential drop (eqn (3.7)) and an unaffected electron mobility (situation  $i$ ) are depicted in Fig. 3.5.b. The numerical front and back  $I$ - $V$  curves are similar, in contrast to the experimental  $I$ - $V$  curves for which the back photocurrent was found to be higher than the front one. The numerical front  $I$ - $V$  curve could only be smaller than the back one when applying a significantly stronger potential drop. However, applying a stronger potential drop led to a similar transport situation as in case 1, i.e. only the first layer of particles significantly contributed to the photocurrent. Fig. 3.5.c depicts case 2 without any potential drop with unaffected electron mobility (situation  $i$ ). In this case, the photocurrent density reached up to 5 mA cm<sup>-2</sup> at 1.23 V<sub>RHE</sub> and 8 mA cm<sup>-2</sup> at 1.5 V<sub>RHE</sub> under front-side illumination. This case is expected to occur if the LTON particles were in the form of a monocrystalline pillar or if the particles were perfectly connected to an external wire (similar to the CNT network connection approach by Dilger et al.[148]). The  $I$ - $V$  curves of case 2 with the two types of electron mobility drops (situation  $ii$ ) with electron mobility of types I and II and without any potential drop are depicted in Fig. 3.5.d. In this case, the front and back photocurrents are very similar as for case 2 with the linear potential drop and with unaffected electron mobility (Fig. 3.5.b). Only a much stronger mobility drop could significantly reduce the front photocurrent without affecting much the back photocurrent. However, this case would effectively lead to a photocurrent as in case 1.

### 3: Majority charge carrier transport in particle-based photoelectrodes

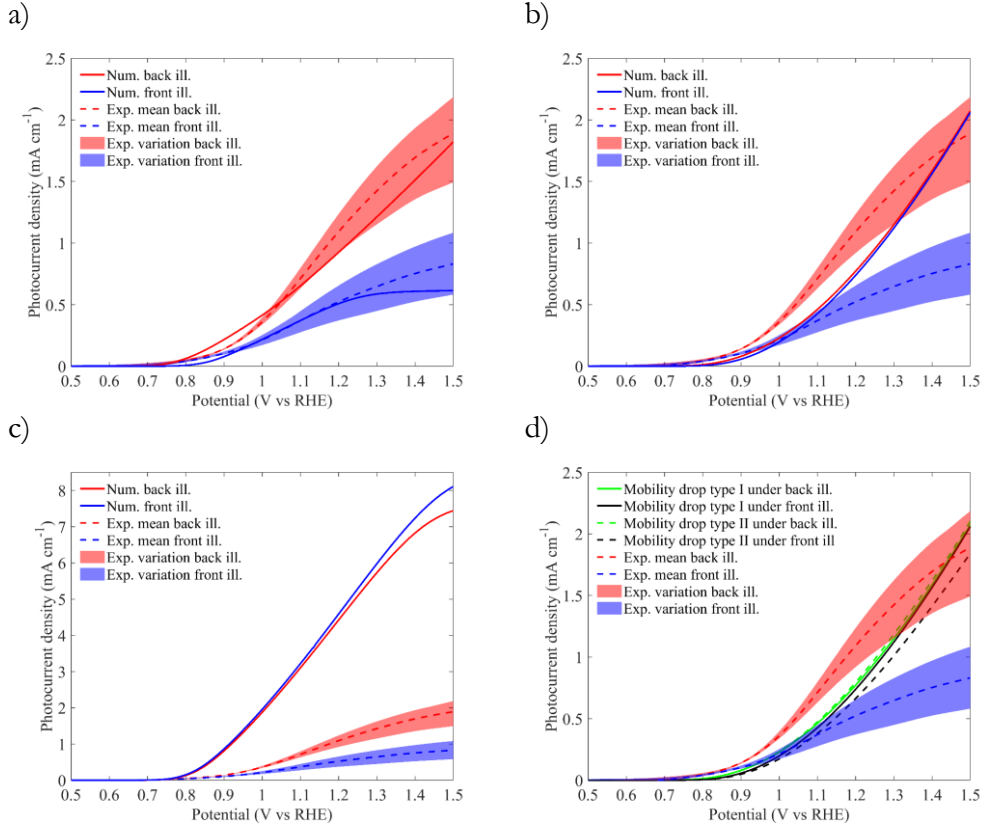


**Fig. 3.5.** Experimental  $I$ - $V$  curves of best-LTON PBPEs with an average film thickness of 8.43  $\mu\text{m}$  taken from Gaudy et al.[161]. The corresponding numerical  $I$ - $V$  curves obtained with the advanced 2D multi-physics PBPE model with assumed inter-particle charge transfer of a) case 1, b) case 2 with linear potential drop and infinite inter-particle mobility (situation  $i$ ), c) case 2 without potential drop and infinite inter-particle mobility (situation  $ii$ ), and d) case 2 without potential drop but mobility drops (type I and II).

The numerical  $I$ - $V$  curves of case 3 (first two layers of particles in *pseudo-series*) for varying inter-particle hole transfer velocities are depicted in Fig. 3.6. The numerical  $I$ - $V$  curves for varying inter-particle electron transfer velocities are depicted in Fig. A3.1. The inter-particle potential barrier was fixed to 0.0762 V to ensure flatband condition at the inter-particle contact, allowing the presence of electrons and holes at the inter-particle contacts. The contributions of the second particle below 0.8 V<sub>RHE</sub> were not relevant since the onset potential is at  $\sim 0.8$  V<sub>RHE</sub>, as visible in Fig. 3.6.a and b. As depicted in Fig. 3.6, the contribution of the second particle reached up to 59 % under front-side illumination and up to 48 % under back-side illumination.

### 3: Majority charge carrier transport in particle-based photoelectrodes

---

Indeed, the integrated generation rate in the second particle was higher than in the first particle under front-side illumination but the situation was inverted under back-illumination with a higher integrated generation rate in the first particle. The smaller the inter-particle velocity, the smaller the contribution of the second particle at higher potential because fewer holes in the first particle are available to recombine with electrons of the second particle. The numerical  $I-V$  curves were only within the experimental variation when the contribution of the second particle was below 10 % at  $1.23 V_{\text{RHE}}$  under back-side illumination and below 5 % under front-side illumination for a numerical photocurrent within the experimental errors bars from  $0.94 V_{\text{RHE}}$  to  $1.5 V_{\text{RHE}}$ , i.e. the inter-particle hole velocity was below or equal to  $10^{-4} \text{ m s}^{-1}$ . In other words, this inter-particle charge transfer mechanism provided numerical  $I-V$  curves similar to the experimental ones only when the contribution of the second particle was minor ( $<20\%$ ). Moreover, it is unlikely that the potential barrier at the inter-particle is negligible in order to allow for the presence of holes in the first particle and electrons in the second particle. A significant potential barrier would reduce even further the chance of having this inter-particle charge transfer mechanism occurring. This observation also supports our observation that inter-particle charge transfer does not play a major role in our LTON PBPEs and that only particles in direct contact with the FTO are significantly contributing to the photocurrent (case 1).

### 3: Majority charge carrier transport in particle-based photoelectrodes

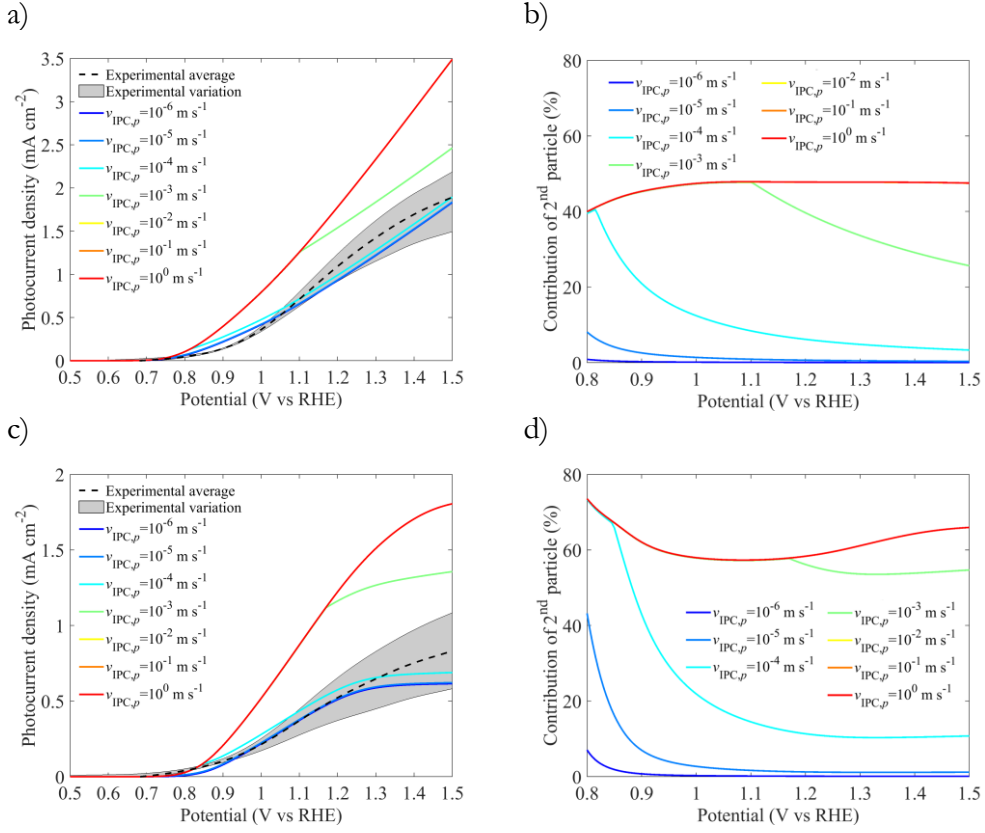


**Fig. 3.6.** Experimental  $I$ - $V$  curves of best-LTON PBPE with an average film thickness of 8.43  $\mu\text{m}$  taken from Gaudy et al.[161]. The corresponding numerical  $I$ - $V$  curves of case 3) for varying inter-particle contact hole velocities under a) back-side illumination and c) front-side illumination, and the corresponding contribution of the 2<sup>nd</sup> particle on the right side in b) and d).

#### 3.3.3. Impact of particle size on the photocurrent

In literature, mainly two particle sizes have been studied experimentally: the particles of bare-LTON, SS-LTON (see section 3.2.4), with sizes in the range of 1.79 and 0.27  $\mu\text{m}$  (longest direction and shortest direction of rectangular particles) [125] and the particle synthesized by polymerized-complex reaction (PC-LTON) with a size of 50 to 300 nm (roughly spherically shaped particles)[140], [168]. The PBPE made of the smaller size PC-LTON particles led to a photocurrent density much smaller, 0.06 mA cm<sup>-2</sup> at 1.8 V<sub>RHE</sub>, than the one of the PBPEs made of the larger SS-LTON

### 3: Majority charge carrier transport in particle-based photoelectrodes

---

particles,  $2.34 \text{ mA cm}^{-2}$  at  $1.8 \text{ V}_{\text{RHE}}$ [140]. The particle must be of a certain size to see a fully developed band bending such as verified by open circuit measurements for SS-LTON[161], which could explain at a first glance the poor performance of smaller PC-LTON PBPEs. However, the doping concentration in LTON is  $7 \cdot 10^{17} \text{ cm}^{-3}$  and the permittivity is 15, which induces a SCR of few nanometers only[161]. The PC-LTON particles are around 50-300 nm[140], [168], a size sufficient to have a fully developed band bending at the SC-EL interface. Thus, the poor performance of PC-LTON PBPE cannot be attributed to the absence of a band bending at the SC-EL interface. Feng et al. [140] attributed the poor performance of PC-LTON PBPE to insufficient penetration of  $\text{TiCl}_4$  necking agent. However, our nanotomography study of the LTON PBPEs[125] indicated that the necking was nicely distributed within the electrode and present at almost all inter-particle locations. It seems that the limited contribution of particles not in direct contact with FTO is more likely the reason for the worse performance of PC-LTON PBPE. Indeed, the smaller the size of the particle is, the less light is absorbed in the first particle layer and the smaller is the resulting photocurrent. We computed the generation rate and the photogenerated current density of PC-LTON and SS-LTON PBPEs to support our hypothesis by using the same EMW propagation model than Gaudy et al.[161]. The same solid phase density profile and optical properties[161] were assumed for PC-LTON and for SS-LTON. A total film thickness of  $8.43 \mu\text{m}$  was assumed for both types of LTON and a first particle thickness of 200 nm was assumed for PC-LTON and  $1.42 \mu\text{m}$  for SS-LTON. As depicted in Fig. 3.7, the back photogenerated current density of PC-LTON was ten times smaller than the one for SS-LTON. This result is in accordance with the work of Feng et al.[140] in which they observed a constant increase of the photocurrent with the size of the particles.

Moreover, Feng et al. observed that PBPEs made of multiple layers of smaller particles (LTON PC 1000) led to higher back than front photocurrent, while PBPEs made of a single layer of larger particles (LTON SSR 1250) led to similar front and back photocurrent. This observation suggests that additional layers only reduce the radiation arriving at the first layer of particles, leading to a lower front than back photocurrent. In contrast, the PBPEs made of larger particles are composed of one or, maximally, two layers of particles, reducing less the light arriving at the particles in direct contact with the FTO for front-side illumination[151].

By explaining higher photocurrents by better inter-particle contacts through necking[140], [149], [153] and neglecting the likely minor contribution of charge carriers from particles away from the FTO, the community might have focused on

### 3: Majority charge carrier transport in particle-based photoelectrodes

increasing the inter-particle conductivity rather than improved contacts between the FTO and the first layer of particles. Based on our modeling results, we hypothesize that the central effect of necking consists in increasing the conductivity between the first layer of particles and the FTO.

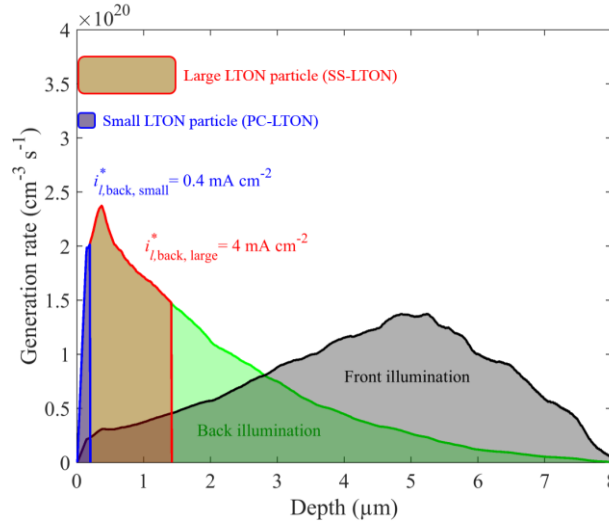


**Fig. 3.7.** Generation rate and photogenerated current density under back-side illumination for small LTON (PC-LTON) and large LTON (SS-LTON) PBPEs.

#### 3.3.4. Design guidelines for particle-based photoelectrodes

We hypothesize that there is a hole quasi-Fermi level discontinuity (Fig. 3.1.d) between particles with inter-particle necking since the contact area between particles is only of few square nanometers. Moreover, the presence of interfacial states between particles is likely to create a double Schottky junction between particles, similar to what has been observed in polycrystalline silicon with a potential barrier that hinders the transfer of electrons between particles[119], [120]. Whereas the contact between the FTO and the first layer of particles allows the transfer of electrons thanks to the TiO<sub>2</sub> necking as discussed in section 3.2.2. Connecting particles by necking, however, remains very challenging and has not been successfully achieved even with TiO<sub>2</sub> as the best necking material[102]. Simpler approaches could be undertaken to improve the efficiency of PBPEs since mostly the first layer of particles is contributing to the photocurrent. We predict an

### 3: Majority charge carrier transport in particle-based photoelectrodes

---

efficiency improve of PBPEs by increasing the solid phase density of the first layer of particle, currently being only 0.28. Indeed, a single layer of particles with a solid phase density close to 1 and with electrolyte-connected nano-pores to maintain a large surface area would be enough to absorb all the incoming light based on the complex refractive index of LTON[161]. This was achieved by Akiyama et al.[103] by a single particle layered PBPE, where the particles were etched to enhance the internal network of nano-pores of LTON particles, obtaining a photocurrent density increase of a factor of 7.4, i.e.  $1.2 \text{ mA cm}^{-2}$  here compared to  $8.9 \text{ mA cm}^{-2}$  in the work of Akiyama et al. at  $1.23 \text{ V}_{\text{RHE}}$ . The active surface area of the PBPEs was increased by creating nano-pores [103] but, more importantly, by doing so the path of holes generated inside the particle was significantly reduced due to additional nano-pores in contact with the electrolyte enabling the potential for high performing PBPEs. In contrast, thin LTON films without an enhanced diffusion length showed only poor performance[116]. In Akiyama et al., the electrons were extracted by depositing Ti on the LTON particles, in contrast to here, where  $\text{TiO}_2$  necking was used. But also for the LTON-Ti contact, a built-in field promotes the electron transfer since the conduction band of LTON is at  $-4.2 \pm 0.1 \text{ V}_{\text{vac}}$ [152], well aligned with the one of Ti at  $-4.3 \text{ V}_{\text{vac}}$ [171]. Thus, the electrons can transfer also efficiently from the LTON particles to the Ti conductive substrate.

Adding a conductive network, as in the work of Dilger et al.[148], radically changes the mechanism of the majority charge carrier transport since the inter-particle charge transfer is replaced by external “wires” that transport the majority charge carriers from the particle directly to the FTO substrate. Therefore, upper particles can also

contribute to the photocurrent (Fig. 3.8.b) and the front photocurrent can be higher than the back one.

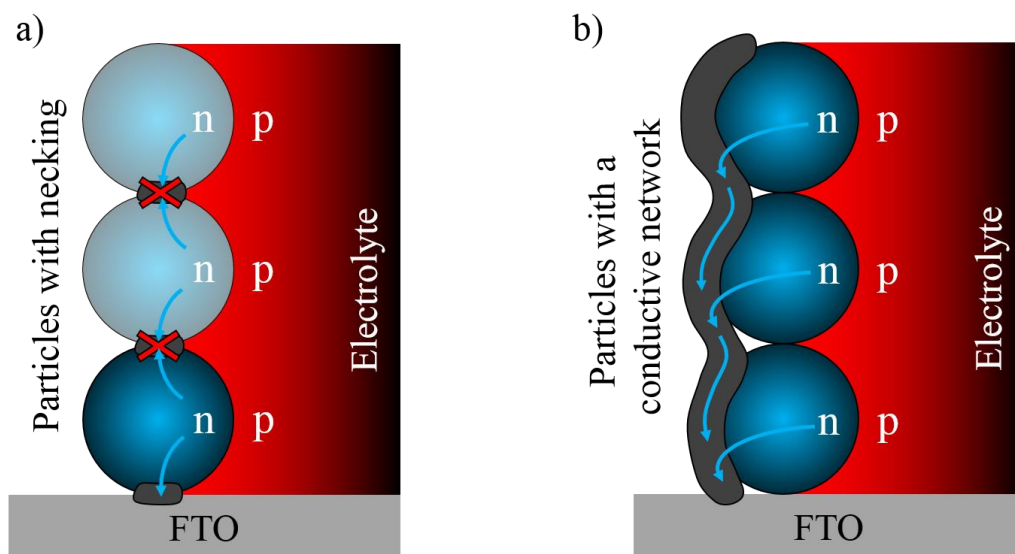


**Fig. 3.8.** Schemes of particulate photoabsorber water-splitting systems: a) PBPE with inter-particle contacts and b) PBPE with a conductive network.

Having a conductive network will result in similar charge transport situation as our modeling case 2, considering a potential drop depending on the effectiveness of the network conductivity. For a perfectly conductive network, the photocurrent density in LTON PBPEs can reach  $5 \text{ mA cm}^{-2}$  at  $1.23 V_{\text{RHE}}$ , i.e. a photocurrent density increase of  $3.8 \text{ mA cm}^{-2}$  at  $1.23 V_{\text{RHE}}$  (Fig. 3.5.c).

The photocurrent can even be further increased by improving the water oxidation reaction kinetics, as predicted by simulations[161]. We carried out experiments and deposited 50 nm layer  $\text{IrO}_x$  (Fig. A3.2)—one of the best oxygen evolution cocatalyst[36]—onto our PBPEs. We found strongly increased photocurrents, i.e. a relative increase of 67 % at  $1.23 V_{\text{RHE}}$  (section A3.2). However,  $\text{IrO}_x$  might not only improve the reaction kinetics but potentially connect upper particles with the FTO glass substrate since  $\text{IrO}_x$  can exhibit high conductivity (in the range of  $2.56 \times 10^6 \text{ S m}^{-1}$ [172]). However, adding a 50 nm layer of  $\text{IrO}_x$  did not allow measuring front to back photocurrent ratios since the  $\text{IrO}_x$  completely blocks the light under front-side



### 3: Majority charge carrier transport in particle-based photoelectrodes

---

illumination. Therefore, we were unable to determine if the deposition of a 50 nm layer  $\text{IrO}_x$  contributes to connect upper particles with the FTO glass substrate. Nevertheless, the deposition of a layer of conductive transparent co-catalyst over all the particles might be an interesting approach to connect upper particles with the FTO glass substrate, similarly to CNT while improving the oxygen evolution reaction kinetic.

#### 3.4. Conclusion

We investigated the inter-particle charge transfer in particle-based photoelectrodes (PBPEs) using LTON particles as model system. Based on the new understanding of this charge transfer, we provided mesostructural guidelines for high performing PBPEs.

Experimental measurements of the thickness-dependence of the front and back photocurrent were undertaken to provide qualitative information about majority charge carrier transport limitation. A simple numerical model, allowing calculating front to back photogenerated current ratios, was developed and compared to the experimental front to back photocurrent ratio. The results suggested that only a limited part of the overall PBPE thickness contributed to the photocurrent. The best fit between the experimental and the numerical front to back current ratio was obtained for a contributing thickness of 450 nm with a solid phase density of 0.28. Different possible inter-particle charge transfer mechanisms were then described and implemented in a more advanced 2D multi-physics PBPE model. The numerical  $I$ - $V$  curves were predicted and subsequently compared to experimental  $I$ - $V$  curves. The results showed that matching was obtained only when the first layer of particles in direct contact with the FTO dominated the photocurrent, i.e. the inter-particle contact can be approximated by a double Schottky barrier too high to allow any electron transfer. We also showed that considering an ohmic contact between particles with a high resistance—a large inter-particle potential drop—could fit reasonably well experimental  $I$ - $V$  curves. If considering only a small inter-particle resistance, the numerical front photocurrent was higher than the back photocurrent, contradicting the experimentally measured photocurrents. Moreover, the numerical front photocurrent was  $5 \text{ mA cm}^{-2}$  when assuming no inter-particle resistance, much higher than the experimental front photocurrent that lied within  $0.4$  to  $0.7 \text{ mA cm}^{-2}$ . Similarly, a low inter-particle resistivity with a low inter-particle electron mobility resulted in a good match between numerical and measured  $I$ - $V$  curves. Considering two particles in pseudo-series, the numerical front photocurrent was within the

### 3: Majority charge carrier transport in particle-based photoelectrodes

---

experimental error bars (from 0.94  $V_{\text{RHE}}$  to 1.5  $V_{\text{RHE}}$ ) but only when the photocurrent contribution of the second particle was below 5 %. Thus, these alternatives (ohmic contact with large inter-particle resistance, or pseudo-series with low inter-particle charge carrier velocities) predicted insignificant inter-particle transport and therefore also that only the first layer of particles significantly contributed to the photocurrent.

The impact of particle size of the PBPE on the photocurrent performance and on the front to back photocurrent ratio was investigated based on published experimental studies with different LTON particle sizes. The photoelectrodes with smaller particles (50 to 300 nm) provided a significantly smaller photocurrent density ( $0.06 \text{ mA cm}^{-2}$  at 1.8  $V_{\text{RHE}}$ ) than the ones with large particles (1.79 and  $0.27 \mu\text{m}$ , photocurrent of  $2.34 \text{ mA cm}^{-2}$  at 1.8  $V_{\text{RHE}}$ )[140]. The back photocurrent was higher than the front photocurrent for photoelectrodes with multiple layer of small particles while for 1-2 layers of larger particles the back and front photocurrent was similar[140]. These observations further supported that only the first layer of particles in direct contact with the FTO glass substrate significantly contributes to the photocurrent.

We recommend that experimental approaches for necking or conductive network design in PBPE focus on particle-substrate connection and not on inter-particle connection. Inter-particle mobility and/or charge carrier velocity would need improvements of multiple orders of magnitude. On the other hand, adding a conductive network to connect the LTON particles to the FTO glass substrate could-according to our model-improve the photocurrent density from  $1.2 \text{ mA cm}^{-2}$  to  $5 \text{ mA cm}^{-2}$  at 1.23  $V_{\text{RHE}}$  under front-side illumination. Generally, attention should be put on the first layer of particles and increasing the solid phase density of this layer in direct contact with the FTO glass substrate should be prioritized. New conductive network designs with different conductive materials to connect particles directly with the FTO should be developed such as the deposition of a transparent co-catalyst layer over all particles joining the function of a cocatalyst and a conductive network. Using co-catalysts transparent to the visible light would allow measuring front-side illumination and front to back photocurrent ratios. Furthermore, the influence of the co-catalyst layer thickness on the performance under front- and back-side illumination could determine if this layer only improves the reaction kinetic or actually provides a conductive network to connect upper particles to the FTO glass substrate.

# Rapid performance optimization method for photoelectrodes<sup>1</sup>

## 4.1. Introduction

Photoelectrochemical (PEC) water-splitting can provide an economically viable solution for large-scale solar fuel production but the photoabsorbers are required to be inexpensive, efficient, and stable for many operating years[16]. Up to now, no photoelectrode can satisfactorily meet all these requirements and therefore new synthesis methods, nanostructures, or materials need to be discovered[173]. The determination and quantification of a photoelectrode's main limitations such as bulk and surface recombination often require investigations that are time consuming and involve multiple experiments, which are destructive and/or not under realistic operating conditions. Indeed, some photoelectrodes such as hematite photoelectrodes have been investigated for many decades before realizing that even with state-of-the-art nanostructuring methods they are not reaching satisfactory performance. Although the research on such candidates has significantly enhanced the knowledge in the field, we now urgently need rapid and non-destructive techniques to access objectively the performance of actual or emerging photoelectrodes. Such a method allows determining if the synthesis method of the material should be modified or if nanostructuring could be sufficient to reach high performance. The challenges to develop a fast method capable of determining the potential of nanostructuring are manifold. The approach must be capable to separate and quantify losses in the bulk, in the space charge region (SCR), and at the surface. The analysis must be able to extract the diffusion length and the surface recombination loss of the photoelectrodes. Moreover, a criterion that can objectively

---

<sup>1</sup> The material from this chapter is in press, 'Y. K. Gaudy and S. Haussener, Rapid Performance Optimization Method for Photoelectrodes, *Journal of Physical Chemistry C*, 2019, in press'.

determine the performance of photoelectrode materials must be established. Finally, the method must be fast, robust and versatile to enable the investigation of various photoelectrode materials and nanostructures. Moreover, the method must be able to quantify the impact of the performance by varying the synthesis methods, by modifying the doping concentration, by passivating the surface, and by nanostructuring, potentially in pristine and at aged conditions. Such a method is currently missing.

Most often, the experimental method to evaluate the potential performance of a photoelectrode is to suppress any surface recombination by using an artificial hole or an electron scavenger. This method is very practical but allows only for a qualitative estimation of the surface and bulk recombination losses. Segev et al.[174] developed a combined experimental-numerical method that provides indications about main material limitations of photoelectrodes. Their method determines the spatial charge collection efficiency and recombination losses of photoelectrodes (exemplified with  $\text{Cu}_2\text{V}_8\text{O}_3$  photoanodes) based on optical modeling and incident photon-to-current efficiency (IPCE) measurements[174]. Although their method allows for the determination of the collection length, which accounts for diffusion and drift transport mechanisms, it does not determine the diffusion length, a parameter particularly important for the characterization of photoelectrodes[175] and for quantitative comparison between different photoelectrodes. The determination of the spatial collection efficiency in the work of Segev et al. was originally developed by Tuominen et al.[176] for solar cells. Tuominen et al. used the spectral response of c-Si solar cells to determine the spatial collection efficiency along with the diffusion length and the surface recombination velocity by additionally using the solution of a simplified minority charge carrier conservation equation. More recently, Nakane et al.[177] determined the optical and recombination losses for numerous thin-film photovoltaic devices by fitting the carrier conservation equation of Gärtner[56] to the IPCE. The Gärtner model, initially developed for Schottky junctions, has often been used to determine the diffusion length of photoelectrode materials, i.e. for  $\text{Fe}_2\text{O}_3$  (ref. [178]),  $\text{BiVO}_4$  (ref. [179]), and  $\text{Cu}_2\text{O}$  (ref. [180]). This model does neither account for recombination in the SCR nor at the semiconductor-electrolyte interface. Thus, the diffusion length for high permittivity or low doping concentration materials (i.e. conditions resulting in a thick SCR) cannot be determined with this model. Moreover, it cannot separate bulk recombination from surface recombination. We have recently reported on a numerical model solving charge transport and conservation equations by finite volume method (FVM), which has allowed to provided key performing parameters

#### 4: Rapid performance optimization method for photoelectrodes

---

of particle-based (p.-b.)  $\text{LaTiO}_2\text{N}$  photoelectrodes[161]. The use of a 2-dimensional (2D) FVM allowed studying the impact of the morphology on p.-b. photoelectrodes' performance, which is not accessible with a 1-dimensional (1D) model. However, this model combined bulk and surface lifetimes by the use of a single effective lifetime, which prevented the separation of bulk and surface recombination losses. Moreover, this method required the knowledge of various material parameters (such as electron and hole mobilities and lifetimes) which are unknown for many recently investigated materials and are very challenging and time-consuming to determine.

So far,  $\text{Fe}_2\text{O}_3$  has been one of the most investigated photoelectrode materials because it is extremely cheap, abundant, stable, and has a suitable bandgap for a well-performing water-splitting tandem device. However,  $\text{Fe}_2\text{O}_3$  has a low diffusion length that leads to poor efficiency. Early on, optimized meso- and nano-structuring was proposed to reduce the hole path and to overcome the low diffusion length of  $\text{Fe}_2\text{O}_3$  (ref. [178]). Various other approaches to increase the diffusion length of  $\text{Fe}_2\text{O}_3$  have been explored and included co-catalyst depositions and doping concentration optimization. None of these techniques succeeded in providing highly efficient photoelectrodes.

Here, we introduce a simple and rapid method to calculate the different losses in photoelectrodes and to determine a dimensionless optical and transport parameter, the diffusion optical number. We apply the method to water-splitting photoelectrodes, given by the abundant data available. Our method uses an IPCE model that includes charge carrier conservation equation, continuous states surface recombination at the semiconductor-electrolyte interface[60], SCR recombination, and finite photoelectrode thickness. The IPCE model allows for simple quantification of bulk, SCR, surface and optical losses. The IPCE model is validated by comparing our determined diffusion length of  $\text{Cu}_2\text{O}$  water-splitting photoelectrodes to reported values. We establish a benchmark—based on the diffusion optical number of nanostructured hematite—that sets an objective criterion for the nanostructuring opportunity of a photoelectrode. Our screening method together with the definition of the benchmark is then used to assess nanostructuring opportunity and to suggest performance improvements of numerous photoelectrode materials and nanostructures: planar  $\text{Cu}_2\text{O}$ , Si,  $\text{Fe}_2\text{O}_3$ ,  $\text{Fe}_2\text{O}_3$ ,  $\text{BiVO}_4$ ,  $\text{Cu}_2\text{V}_8\text{O}_3$ , and  $\text{CuFeO}_2$ , and nanostructured  $\text{Fe}_2\text{O}_3$  and p.-b.  $\text{LaTiO}_2\text{N}$ .

### 4.2. Methodology

#### 4.2.1. Definition of metrics

The main limitations of a photoelectrode result from internal and surface losses. The internal losses account for bulk and SCR recombination losses. These losses can be described by the diffusion optical number,  $\alpha_{500}L$ , defined as the product of the absorption coefficient at 500 nm and the diffusion length

$$\alpha_{500}L = \alpha(\lambda = 500 \text{ nm}) \cdot L. \quad (4.1)$$

$\alpha_{500}L$  is a simple parameter that describes the capability of the photoelectrode to convert light at 500 nm—the wavelength of maximum irradiance of the standard solar spectrum irradiance (AM1.5G)—to exploitable photocurrent. This parameter accounts for the mobility of the charge carrier, the recombination rate of electron/hole pairs, and the absorption coefficient. The diffusion optical number is a practical parameter since it is derived from the approximation of the optimal thickness of a photoelectrode,  $d^*$ , given by[21]:  $d^* \approx \alpha_{500}^{-1} < W + L$ , where  $W$  is the SCR thickness. Thus, a high performing photoelectrode must ensure

$$\alpha_{500}(W + L) > 1. \quad (4.2)$$

If this is not the case, the photoelectrode will not be able to bring enough photoexcited charges to the semiconductor-electrolyte interface. Eqn (4.2) is dependent of the applied potential because  $W$  depends on the applied potential (see eqn (17)). When removing  $W$  from eqn (4.2),  $\alpha_{500}L$  remains, a factor independent of the applied potential and more convenient for comparison between photoelectrodes.  $\alpha_{500}L > 1$  is required for a high performing photoelectrode. The surface losses account for the optical reflection loss and the surface recombination loss. The latter can be described through the ratio of water splitting current and the total current or through the ratio of the surface charge transfer velocity that contributes to the water-splitting reaction,  $S_T$ , and the sum of the surface recombination velocity,  $S_R$ , and  $S_T$ ,

#### 4: Rapid performance optimization method for photoelectrodes

---

$$R_{S,V_{IPCE}} = \frac{S_T}{S_T + S_R}. \quad (4.3)$$

The ratio of currents is determined at a fixed potential at which the IPCE is measured,  $V_{IPCE}$ . This parameter allows evaluating the ratio between surface recombination and charge transfer.  $R_{S,V_{IPCE}} = 1$  indicates no surface recombination at the semiconductor-electrolyte interface.  $R_{S,V_{IPCE}} = 0$  implies no photocurrent since charge carriers are fully recombining at the interface.

The limiting performance of a photoelectrode can be determined if the diffusion optical number and the ratio of currents are identified. The diffusion optical number accounts for all internal losses and the ratio of currents accounts for the surface recombination loss.

$\text{Fe}_2\text{O}_3$  is a good example of a well-studied photoelectrode material having a very low hole diffusion length, in the range of 2-10 nm (ref. [178]). Thus, its diffusion optical number is much lower than one,  $\alpha_{500}L=0.03$  (Table 4.2), which limits the efficiency of this material as a water-splitting photoanode. The nanostructuring of a thin film of the material can be used to overcome minority charge carrier transport limitations, i.e. the high surface area decreases the minority charge carrier transport length. Moreover, nanostructuring often increases the optical scattering providing additional opportunities for absorption to occur and can theoretically overcome a low  $\alpha_{500}L$ . Nevertheless, this approach has been intensively applied to hematite photoelectrodes over the last decades without leading to a breakthrough performing photoelectrode[181]. Hematite photoelectrodes, as an example, highlight the challenges to overcome the limitations of photoelectrodes with low diffusion optical number. On the other hand, surface recombination limitation such as low reaction kinetic or high surface recombination loss have been successfully overcome by the discovery and incorporation of co-catalysts[10] and passivation layers[182]. Thus, the nanostructuring opportunity of a photoelectrode can be based on the diffusion optical number only.

To objectively quantify the nanostructuring opportunity of photoelectrodes, we compared the diffusion optical number of the photoelectrode to a second parameter, the diffusion optical number at an internal quantum efficiency (IQE) above 95 %,  $\alpha_{500}L_{0.95}$ .  $\alpha_{500}L_{0.95}$  is defined as the product of the absorption coefficient at 500 nm and the diffusion length,  $L_{0.95}$ , that provides  $\text{IQE} \geq 95 \%$  at 500 nm, while fixing the surface recombination to zero

$$\alpha_{500}L_{0.95} = \alpha(\lambda = 500 \text{ nm}) \cdot L_{0.95}. \quad (4.4)$$

$L_{0.95}$  is obtained by solving iteratively  $\text{IQE}(L) \geq 95\%$  at 500 nm using eqn (4.6) with  $S_R=0$ , for an infinite electrode thickness. The latter ensures that  $L_{0.95}$  is not overestimated because of photons that would be transmitted through thin photoelectrodes.

When reviewing the literature, we observed that nanostructuring could only provide an improvement of the diffusion optical number of up to one order of magnitude (see  $\text{Fe}_2\text{O}_3$  in Fig. 4.6). Thus, it will be very challenging for a photoelectrode with a diffusion optical number more than two orders of magnitude below  $\alpha_{500}L_{0.95}$  to perform well when nanostructured. Accordingly, we defined the nanostructuring opportunity factor,  $f_{\text{nano}}$ , based on the following conditions

$$f_{\text{nano}} = \log_{10} \left( \frac{\alpha_{500}L_{0.95}}{\alpha_{500}L} \right) \begin{cases} > 2 \rightarrow \text{low performance with nanostructuring} \\ \leq 2 \rightarrow \text{high performance with nanostructuring} \\ < 0 \rightarrow \text{high performance without nanostructuring} \end{cases} \quad (4.5)$$

Fig. 4.1 summarizes the method developed to extract the diffusion optical number and the ratio of currents of photoelectrodes. Firstly, we calculate the numerical IPCE, followed by optimizing the fitting of the numerical IPCE to the experimental IPCE through variation of the diffusion length and the surface recombination velocity. The optimization of the IPCE fitting allows for the determination of the diffusion length and the surface recombination velocity and, thus, the diffusion optical number that determines the nanostructuring opportunity of a photoelectrode.

#### 4.2.2. Numerical determination of the IPCE

The numerical IPCE of a photoelectrode is calculated by solving the minority charge carrier conservation equation, including i) continuous surface states recombination at the semiconductor-electrolyte interface, ii) recombination in the SCR, and iii) finite photoelectrode thickness. The generation rate in the numerical IPCE model is based on Beer-Lambert law limiting the model to photoabsorption without considering wave interferences or resonant light trapping effects (section 4.2.6). The full



#### 4: Rapid performance optimization method for photoelectrodes

---

derivation of the following equations—partially based on the work of Wilson[60]—is presented in the supporting information. The IQE of a photoelectrode in function of the photon wavelength (indicated by the subscript  $\lambda$ ) is given by

$$\text{IQE}_\lambda = \underbrace{\frac{S_T}{S_T + S_R}}_{\text{surface}} \left[ \underbrace{\eta(1 - e^{-\alpha_\lambda W})}_{\text{SCR}} + \underbrace{\xi \left( e^{-\alpha_\lambda W} \frac{L}{L + D/S} \frac{\alpha_\lambda L}{\alpha_\lambda L + 1} \right)}_{\text{bulk}} \right], \quad (4.6)$$

where  $\eta$  is a correction term for the SCR recombination,  $D$  is the diffusion coefficient,  $\xi$  is a correction term accounting for the finite thickness of the photoelectrode, and  $S$  is a surface parameter related to the minority charge carrier surface reactions determined by eqn (4.10). The term  $L/(L + D/S)$  can be removed from eqn (4.6) at a SCR potential larger than 0.23 V (see section 4.2.4). The diffusion coefficient is related to the mobility of a charge carrier,  $\mu$ , given by the Einstein relation.  $\eta$  is the ratio between the photocurrent generated in the SCR reaching the semiconductor-electrolyte interface and the recombination current in the SCR, given by

$$\eta = \frac{i_{\text{SCR}}}{i_{\text{rec}} + i_{\text{SCR}}} = \frac{L^2 \phi_{\text{SC}}}{W^2 V_{\text{th}} + L^2 \phi_{\text{SC}}}, \quad (4.7)$$

$\xi$ , accounting for the finite photoelectrode thickness,  $d$ , is given by

$$\xi = 1 - e^{-\frac{(d-W)(\alpha_\lambda L + 1)}{L}}. \quad (4.8)$$

The surface recombination velocity for continuous surface states is given by integrating the surface states energy levels over the bandgap energy[60]

$$S_R = \int_0^{E_{\text{gap}}} \frac{S_{R,0} \cdot e^{-\beta E}}{1 + e^{(\phi_{\text{SC}}/q - E)/k_B T}} dE, \quad (4.9)$$

where  $S_{R,0}$  is a surface recombination velocity factor and  $\beta$  is a surface states distribution factor.  $S$  is given by

$$S = \left[ (S_T + S_R) e^{\frac{\phi_{SC}}{V_{th}}} - \frac{1 - e^{-\alpha_\lambda W}}{e^{-\alpha_\lambda W} [\alpha_\lambda L / (\alpha_\lambda L + 1)]} \frac{D}{L} \frac{\eta}{\xi} \right] \left[ 1 + \frac{1 - e^{-\alpha_\lambda W}}{e^{-\alpha_\lambda W} [\alpha_\lambda L / (\alpha_\lambda L + 1)]} \frac{\eta}{\xi} \right]^{-1} \quad (4.10)$$

The SCR thickness for a n-type material is given by eqn (17). Finally, the IPCE or the external quantum efficiency (EQE), is given by adding the reflection loss at the semiconductor-electrolyte interface,  $R$ , to the IQE,

$$IPCE_\lambda = EQE_\lambda = IQE_\lambda \cdot (1 - R_\lambda). \quad (4.11)$$

The reflection loss at the semiconductor-electrolyte interface in function of the wavelength—if not experimentally measured—is given by assuming the imaginary part of the refractive index of the electrolyte being equivalent to water ( $k_{water} \ll k_{SC}$ ) and using the Fresnel equation for normally incident and unpolarized light[66],

$$R_\lambda = \frac{[(n(\lambda) - n_{water}(\lambda))^2 + k(\lambda)^2]}{[(n(\lambda) + n_{water}(\lambda))^2 + k(\lambda)^2]}, \quad (4.12)$$

#### 4.2.3. Determination of the diffusion optical number and the ratio of currents

The diffusion optical number,  $\alpha_{500}L$ , and the ratio of currents,  $R_{S,V_{IPCE}}$ , are calculated from the diffusion length and the surface recombination velocity (eqns (4.1) and (4.3)), respectively. The diffusion length and the surface recombination velocity are determined by the IPCE analysis. The IPCE analysis consists of optimizing the fitting of the numerical IPCE given by eqn (4.11) to an experimental IPCE by varying the diffusion length and the surface recombination velocity (Fig. 4.1). Both parameters were varied with a resolution of 50 points per decade for all our investigated photoelectrodes. This procedure requires that the numerical and the

#### 4: Rapid performance optimization method for photoelectrodes

---

experimental IPCEs are taken at the same applied potential,  $V_{\text{IPCE}}$ . We investigated most of the photoelectrodes at a single applied potential. This restriction resulted from a lack of experimental IPCE data at different potentials. The numerical method can be applied at any potential without affecting the determination of the diffusion length. However, the surface recombination loss will vary depending on the applied potential (section 4.2.4). The optimal fitting is determined by maximizing the coefficient of determination,  $R^2$ , between the numerical IPCE and the experimental IPCE, given by

$$R^2 = 1 - \frac{\sum_i (\text{IPCE}_{\text{exp}, \lambda_i} - \text{IPCE}_{\text{num}, \lambda_i})^2}{\sum_i (\text{IPCE}_{\text{exp}, \lambda_i} - \overline{\text{IPCE}_{\text{exp}}})^2}, \quad (4.13)$$

where the subscript  $i$  is the number of wavelengths,  $\lambda_i$ , at which the experimental IPCE,  $\text{IPCE}_{\text{exp}, \lambda_i}$ , was measured.  $\text{IPCE}_{\text{num}, \lambda_i}$  is the numerical IPCE at the corresponding wavelength,  $\lambda_i$ , and  $\overline{\text{IPCE}_{\text{exp}}}$  is the average experimental IPCE over all  $\lambda_i$  from the lowest measured wavelength up to the wavelength corresponding to the bandgap of the investigated photoelectrode. In minimum, two different wavelengths are needed and the smaller the smallest wavelength measured the better. If a photoabsorbing material is present on top of the photoelectrode material, the lowest wavelength must be large enough to ensure that the absorption of the top photoabsorbing material is negligible (higher than the bandgap of a semiconductor material).

Since the diffusion length has a spectral effect on the IPCE and, by contrast, the surface recombination velocity is wavelength independent (following the assumption by Tuominen et al.[176]), we have a unique solution to the IPCE curve fitting problem.

#### 4: Rapid performance optimization method for photoelectrodes

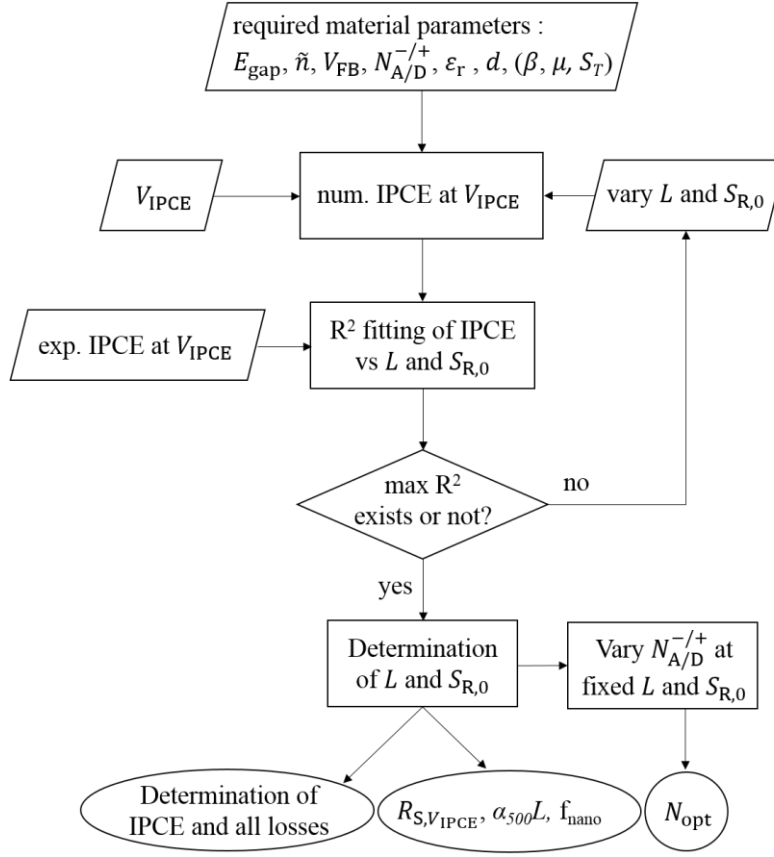


**Fig. 4.1.** Flowchart of the numerical IPCE analysis used to determine the diffusion length and the surface recombination velocity from which reflection, bulk and surface recombination losses are determined. The ratio of currents, the diffusion optical numbers, the nanostructuring opportunity factor, and the doping concentration that maximize the IPCE are also determined. The inputs are the measured IPCE (at least at two wavelengths, for a given applied potential), the bandgap, the spectral complex refractive index, the flatband potential, the fully ionized acceptor/donor doping concentration, the permittivity, and the electrode thickness. The surface state distribution factor, the minority charge carrier mobility, and the surface charge transfer coefficient were assumed (section 4.2.4).

The impact of the diffusion length and the surface recombination velocity on the IQE is illustrated numerically in Fig. 4.2 for a planar p-Si photoelectrode of 1 mm thickness at  $V_{\text{IPCE}} = 1 \text{ V}_{\text{RHE}}$ . Fig. 4.2.a depicts the spectral effect of the diffusion length on the IQE without surface recombination loss. Fig. 4.2.b depicts the wavelength-independence of the surface recombination velocity factor (eqn (4.9)) on the IQE at an infinite diffusion length. The IPCE remains constant for varying

#### 4: Rapid performance optimization method for photoelectrodes

wavelengths up to 1000 nm. The decrease of the absorption coefficient of Si close to 1000 nm (bandgap of 1.12 eV=1107 nm) combined with a finite photoelectrode thickness of 1 mm results in an increase of transmitted photons (not absorbed by the photoelectrode), i.e. a decrease of the IQE above 1000 nm as depicted in Fig. 4.2, even with an infinite diffusion length.

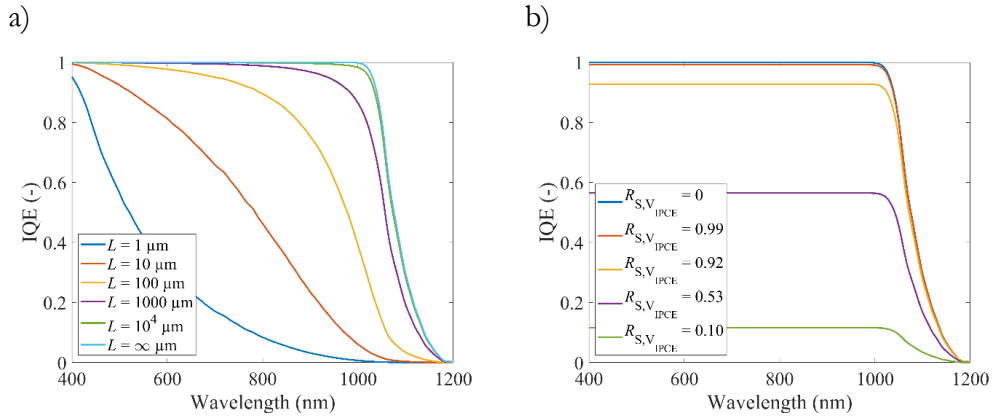


**Fig. 4.2.** Numerical IQE of a planar p-Si photoelectrode of 1 mm thickness at 1 V<sub>RHE</sub> for varying a) diffusion lengths and b) ratios of currents. In a), the surface recombination velocity is fixed to zero and in b) the diffusion length is fixed to infinite and the surface charge transfer to  $10^{-2} \text{ cm s}^{-1}$ . The ratios of currents at 1 V<sub>RHE</sub> in b) were obtained by varying  $S_{R,0}$  from 0, 10, 100, 1000, and  $10^4 \text{ cm s}^{-1}$ .

The internal and surface losses can be easily separated with the numerical IPCE model. The optical reflection loss is determined by eqn (4.12). The surface recombination loss is determined by the difference between the numerical IPCE with all losses (eqn (4.11)) and the numerical IPCE without surface recombination loss. The IPCE without surface recombination loss is determined by setting the surface recombination velocity,  $S_R$ , in eqns (4.6) and (4.10) to zero. The internal loss (bulk and SCR losses) is the IPCE without surface losses (the optical reflection loss and the surface recombination loss). Furthermore, the optimal doping concentration,  $N_{\text{opt}}$ , can be extracted by finding the doping concentration that maximizes the IPCE at 500 nm (Fig. 4.8).

### 4.2.4. Required material parameters

As depicted in Fig. 4.1, numerous material parameters, namely the spectral complex refractive index, the bandgap, the flatband potential, the doping concentration, the permittivity, and the thickness of the photoelectrode must be known to determine the diffusion length and the ratio of currents. Even a rough estimate of these parameters still allows for the determination of the diffusion length within the right order of magnitude and thus allows estimating the diffusion optical number and the nanostructuring opportunity factor of the photoelectrode. The impact of the complex refractive index on the determination of the diffusion length was investigated with n-Fe<sub>2</sub>O<sub>3</sub> photoanodes[23]. Although the R<sup>2</sup> of the IPCE fitting was greatly affected by using two different complex refractive indexes—R<sup>2</sup>=0.96 using the index of Longtin et al.[183] and R<sup>2</sup>=0.57 with Query[184]—the extracted diffusion length was similar with a value of 8.3 nm with the data of Query and 9.1 nm with the data of Longtin et al.  $R_{S,V_{IPCE}}$  also remained close with  $R_{S,V_{IPCE}} = 0.17$  using the index of Query and 0.23 using the index of Longtin et al. (more details in S2.1). The flatband potential did not significantly impact the determination of the diffusion length of the p-Cu<sub>2</sub>O photocathode[169]. The diffusion length changed from 1 μm to 1.8 μm using, respectively, a flatband potential of 1.05 V<sub>RHE</sub> and 0.73 V<sub>RHE</sub>. The  $R_{S,V_{IPCE}}$  showed larger sensitivity, i.e.  $R_{S,V_{IPCE}}$  varied from 0.97 to 0.84 with respect to a flatband potential of 1.05 V<sub>RHE</sub> and 0.73 V<sub>RHE</sub>, respectively (more details in S2.2). The doping concentration showed less significance with respect to the diffusion length. A variation of the diffusion length from 1 μm to 5.5 μm was observed when varying the doping concentration between  $7.1 \times 10^{13} \text{ cm}^{-3}$  to  $10^{18} \text{ cm}^{-3}$ , respectively. The  $R_{S,V_{IPCE}}$  varied from 0.99 to 0.89 with increasing doping concentration from  $7.1 \times 10^{13} \text{ cm}^{-3}$  to  $10^{18} \text{ cm}^{-3}$  (more details in S2.3). The impact of the permittivity on the determination of the diffusion length was investigated using the p-Cu<sub>2</sub>O photocathode[169] at a doping concentration of  $7.1 \times 10^{13} \text{ cm}^{-3}$ . A variation in the diffusion length from 4.2 μm and 2.4 μm was obtained when the permittivity varied from 1 to 80. The surface recombination loss was reduced from 15 % at a permittivity of 1 to 0.5 % at a permittivity of 80 (more detail in S2.4). The thickness of the photoelectrode did not impact the determination of the diffusion length nor  $R_{S,V_{IPCE}}$ , as long as the thickness of the photoelectrode was larger than the SCR width (more details in S2.5). The surface state distribution factor, the minority charge carrier mobility, and the surface charge transfer coefficient are inputs parameters with relatively small effect on the results (Fig. 4.1). Indeed, the minority charge carrier mobility could vary between  $10^{-3} \text{ cm}^2 \text{ V}^{-1} \text{ s}^{-1}$  to  $10^3 \text{ cm}^2 \text{ V}^{-1} \text{ s}^{-1}$  without affecting the determination of the diffusion optical number or the ratio of

## 4: Rapid performance optimization method for photoelectrodes

---

currents as long as the IPCE was measured at a potential region where the SCR potential was above 0.23 V (more details in S2.6). That was the case for all the photoelectrodes investigated in this work and is generally the case since the SCR potential is the main driving force for water-splitting photoelectrodes. Thus, we could remove the term  $L/(L+D/S)$  from eqn (4.6) and ignore the diffusion coefficient and the surface parameter,  $S$ , given by eqn (4.10). The reference minority charge carrier mobility chosen for all photoelectrodes was  $\mu=1 \text{ cm}^2 \text{ V}^{-1} \text{ s}^{-1}$ . The surface states distribution factor,  $\beta$ , (eqn (4.9)) influenced the shape of the  $I$ - $V$  curves but did not influence the determination of the diffusion length. However, this factor affected the ratio of currents resulting in a surface recombination loss difference of 1 % at 500 nm for  $20 \leq \beta \leq 1 \text{ eV}^{-1}$ , using p-Cu<sub>2</sub>O photocathode as an example (more details in S2.7).  $\beta=7 \text{ eV}^{-1}$  was selected for all the photoelectrodes since it best approximated the experimental  $I$ - $V$  curve of p-Cu<sub>2</sub>O photocathode (Fig. A4.3). We determined the value of the ratio of currents (eqn (4.3)) only and not the surface recombination velocity. The surface recombination velocity could only be obtained when assuming a surface charge transfer velocity of  $S_T=10^{-2} \text{ cm s}^{-1}$ . This value provided  $S_{R,0}$  within 1 to 100  $\text{cm s}^{-1}$  for all the photoelectrodes investigated in this work, similar to the work of Wilson[60]. We observed that the determination of the diffusion length was not influenced by the choice of the applied potential,  $V_{\text{IPCE}}$ . Indeed, the diffusion length of the Cu<sub>3</sub>V<sub>2</sub>O<sub>8</sub> photoanode[174] was found to be 1.7 nm at the two different potentials, 1.21 V<sub>RHE</sub> and 1.71 V<sub>RHE</sub>. The surface recombination loss decreased from 9.4 % at 1.21 V<sub>RHE</sub> to 5.1 % at 1.71 V<sub>RHE</sub>, as expected (more details in S2.8).

### 4.2.5. Investigated photoelectrode materials

Numerous photoelectrode materials and nanostructures were investigated: a planar p-Cu<sub>2</sub>O photocathode covered by a Ga<sub>2</sub>O<sub>3</sub>/TiO<sub>2</sub>/RuO<sub>x</sub> layer[169], a planar p-Si photocathode covered by a ~80 nm mesoporous hematite layer[185], a planar non-intentionally doped (nid) Fe<sub>2</sub>O<sub>3</sub> and n-Fe<sub>2</sub>O<sub>3</sub> photoanode[23], a planar n-BiVO<sub>4</sub> photoanode[186], a planar n-Cu<sub>3</sub>V<sub>2</sub>O<sub>8</sub> photoanode[174], a planar p-CuFeO<sub>2</sub> photocathode[187], nanorods n-Fe<sub>2</sub>O<sub>3</sub> photoelectrodes with and without deposited CoBi co-catalyst[188], and a p.-b. n-LaTiO<sub>2</sub>N photoanode[161]. The p.-b. LaTiO<sub>2</sub>N photoanode was composed of TiO<sub>2</sub> inter-particle connections, NiO<sub>x</sub>/CoO<sub>x</sub>/Co(OH)<sub>2</sub> co-catalysts, and a Ta<sub>2</sub>O<sub>5</sub> passivation layer, as used in our previous work[161]. The generation rate under back illumination (illuminated from the side of the fluorine doped tin oxide glass substrate) followed an exponential decrease along the thickness of the photoelectrode. In contrast, the generation rate

under front illumination (illuminated from the LaTiO<sub>2</sub>N's side) shows a more uniform generation rate, given by the particle density, that follows the exponential absorption behavior[161]. Since our numerical model work for photoelectrodes having a generation rate that follows an exponential decay (as in a homogeneous film), only the IPCE of LaTiO<sub>2</sub>N photoanodes under back illumination were used to determine the diffusion length and the surface recombination velocity.

Our IPCE measurements of the p.-b. LaTiO<sub>2</sub>N photoanode is detailed in the supporting information, section A4.3.1. The IPCE of LaTiO<sub>2</sub>N at 1.23 V<sub>RHE</sub> is the average IPCE under back illumination of four fresh photoelectrodes (Fig. A4.5). The complex refractive index of p.-b. LaTiO<sub>2</sub>N was taken from Gaudy et al.[161] based on reflectance and transmittance measurements. Additionally, we used a complex refractive index calculated by density functional theory (DFT), detailed in the supporting information and Fig. A4.6. The imaginary part of the complex refractive index was reduced according to the average electrode volume fraction of 0.28 within the first 1.42 μm of the active photoelectrode's thickness[161]. The required material parameters for all the photoelectrodes are summarized in Table 4.1.



#### 4: Rapid performance optimization method for photoelectrodes

**Table 4.1.** Material parameters used for the IPCE analysis with references in bracket. n/p-type, is a material doped negatively or positively.  $\lambda_{\text{investigate}}$  is the investigated wavelength range,  $R_{\lambda, \text{m}}$ , indicates if the reflection loss are experimentally measured ('yes') or numerically calculated according to eqn (4.12) ('no'). The first value of each parameter is the nominal value, the second or third values are estimated variations.

Material	n/p-type	$E_{\text{gap}}$ (eV)	$V_{\text{FB}}$ ( $V_{\text{RHE}}$ )	$N_{\text{A/D}}^{-/+}$ ( $\text{cm}^{-3}$ )*	$\epsilon_r$ (-)	$V_{\text{IPCE}}$ ( $V_{\text{RHE}}$ )	$d$ (nm)	$\tilde{n}$ [ref.]	$\lambda_{\text{investigate}}$ (nm)	$R_{\lambda, \text{m}}$ (yes/no)
Cu <sub>2</sub> O	p	2.0[189]	1.05[169], [190]** or 0.73[190]	$7.1 \times 10^{13}$ [169]	7.5[190]	0[169]	50 $\mu\text{m}$ [169]	[191]	500-700	no
Si	p	1.12[185]	0.20[192]† or 0.13[185]**	$2.5 \times 10^{17}$ [185], [193], [194]	11.7[10 8]	-1[185]	500 $\mu\text{m}^\ddagger$	[195]	600-1000	yes
Fe <sub>2</sub> O <sub>3</sub>	n (nid)	2.0[23]	0.34[23]	$4.0 \times 10^{18}$ [23]	32[22]	1.46[23]	25[23]	[183] or [184]	300-700	no
Fe <sub>2</sub> O <sub>3</sub>	n	2.0[23]	0.54[23]	$2.6 \times 10^{18}$ [23]	32[22]	1.46[23]	25[23]	[183] or [184]	300-700	no
BiVO <sub>4</sub>	n	2.4[196]	0.08[186] or 0.1[142]	$5 \times 10^{17}$ [186] $10^{18}$ - $10^{17}$	68[197], [198]	1[186]†	~200[186]	[199]	320-575	no
Cu <sub>2</sub> V <sub>8</sub> O <sub>3</sub>	n	2.0[200]	~0.5[174]	$10^{19}$ [174] $10^{20}$ - $10^{18}$	20[174] *	1.5[174]	283[174]	[174]	320-575	no
CuFeO <sub>2</sub>	p	1.55[201]	1.01[187]	$10^{18}$ [187]	20[202] *	0.4[187]	290[187]	[187]	350-850	yes
nano-Fe <sub>2</sub> O <sub>3</sub>	n	2.0[23]	0.54[23]	$2.5 \times 10^{18}$ [203] $10^{19}$ - $10^{18}$	32[22]	1.23[188]	~500	[183]	350-702	no
nano-Fe <sub>2</sub> O <sub>3</sub> -CoB <sub>1</sub>	n	2.0[23]	0.54[23]	$2.5 \times 10^{18}$ [203] $10^{19}$ - $10^{18}$	32[22]	1.23[188]	~500	[183]	350-702	no
LaTiO <sub>2</sub> N	n	2.1[161]	0.1[161]	$7.4 \times 10^{17}$ [161]	15[161]	1.23 $^\S$	1420[161]	[SI] $^\Theta$ and [161] $^\Theta$	420-710	yes

\*The variations of the doping concentration were estimated based on the frequency dispersion of the Mott-Schottky plot present in the referenced publication. \*\*The flatband potential was calculated using eqn (A4.13) and the difference between the doping concentration of the investigated photoelectrode material and the one of the reference with the published flatband potential value. †The flatband potential was estimated using the method of the inversion of photocurrents[27] to determine the flatband potential. ‡The thickness was assumed to make sure that photons are fully absorbed by the photoelectrode. §The IPCE of p.-b. LaTiO<sub>2</sub>N photoanode was measured in this work under back illumination (Fig. A4.5).  $^\Theta$ The absorption coefficient from Gaudy et al.[161] and the one given in the supporting information (SI) were reduced according to the averaged particle density of 0.28 within the first 1.42  $\mu\text{m}$  of the photoelectrode's thickness.

### 4.2.6. Model limitations

The IPCE model does not account for majority carrier charge transport or reaction and therefore any limitation due to the majority charge carriers was not considered. The model is limited to photoelectrodes having a thickness equal or larger than the SCR thickness. If this condition is not fulfilled, as for example for n-Fe<sub>2</sub>O<sub>3</sub> photoelectrodes with a doping concentration of  $2.6 \times 10^{18} \text{ cm}^{-3}$  (ref. [23]) leading to a SCR thickness of 35 nm (eqn (17)), the photoelectrode thickness was set to a value equal or larger than the SCR thickness. The diffusion length was assumed to be independent of the doping concentration. However, this assumption could be modified by using an empirical relation for the diffusion length as a function of the doping concentration as discussed in section A4.4. The IPCE must be measured at a potential region where the SCR potential is above 0.23 V so that the charge carrier mobility is not a required parameter (see section A4.2.6). The model assumes perfectly planar photoelectrodes. With this method, the actual diffusion length is not accessible for a structured photoelectrode and can only be extracted for flat photoelectrodes. However, a projected diffusion length and projected diffusion optical number can be determined for structured photoelectrodes. The projected diffusion length corresponds to the diffusion length obtained by assuming an equivalent perfectly flat photoelectrode providing the same IPCE as for the structured photoelectrode. Thus, the projected diffusion length has to be greater than the actual diffusion length for nanostructured photoelectrodes. If the photoelectrode is perfectly flat, the projected and the actual diffusion length are equivalent and we use the term diffusion length. The generation of electron/hole pairs follows the Beer-Lambert law, thus wave interferences, resonant light trapping, or plasmonic effect were not considered. If these optical effects are significant and induce a generation rate radically different from Beer-Lambert's law, the applicability of the presented method is compromised. Plasmonic effects might be considered by using an effective absorption coefficient if plasmons are introduced homogeneously in the material. Low excitonic binding energy of materials was assumed. Thus, free photogenerated charge carriers are assumed to be related to the absorption coefficient by considering a quantum yield of one. The electric field present in the SCR is assumed to be unperturbed by the photon flux. The doping concentration is constant throughout the entire photoelectrode. The surface recombination velocity and the charge carrier dynamics are wavelength-independent as assumed by Tuominen et al.[176]. All the equations derived to determine the IPCE are at steady-state conditions.

### 4.3. Results and discussions

#### 4.3.1. Model validation

The numerical IPCE model was validated by comparing the diffusion length of p-Cu<sub>2</sub>O obtained by our IPCE analysis using the experimental IPCE of p-Cu<sub>2</sub>O photocathode from Niu et al.[169] with the diffusion length reported by Dimitriadis et al[180]. The experimental IPCE of p-Cu<sub>2</sub>O below 500 nm was not considered for the IPCE fitting because of discrepancies in the photoelectrodes with different Cu<sub>2</sub>O thicknesses of Niu et al.'s data below 500 nm and to reduce the impact of absorption from the Ga<sub>2</sub>O<sub>3</sub>/TiO<sub>2</sub>/RuO<sub>x</sub> layer deposited on Cu<sub>2</sub>O (section 4.2.5). The R<sup>2</sup> of the IPCE fitting was above 0.99 for diffusion lengths varying from 0.9 μm to 2 μm and a ratio of currents of 0.79 to 1 with a maximum R<sup>2</sup> of 0.998 at a diffusion length of 1 μm and a ratio of currents of 0.99 (Fig. 4.3). The determined diffusion length is in agreement with the value of 1 μm found in the work of Dimitriadis et al. for a doping concentration of 9×10<sup>13</sup> cm<sup>-3</sup>, close to the doping concentration of 7.1×10<sup>13</sup> cm<sup>-3</sup> from Niu et al.

For the maximum IPCE fitting of the p-Cu<sub>2</sub>O photocathode, an R<sup>2</sup>=0.998 was calculated, indicating a nearly perfect fit between our numerical IPCE and the experimental IPCE of Niu et al. (Fig. 4.4). Hence, our numerical method can also precisely reproduce the experimental IPCE spectra. This is due to the accuracy of our numerical IPCE model but also to the quality of the complex refractive index data from Malerba et al[191]. Indeed, low quality complex refractive index data can lead to poor IPCE fitting (R<sup>2</sup>=0.57) as shown for Fe<sub>2</sub>O<sub>3</sub> photoanode (Fig. A4.2).

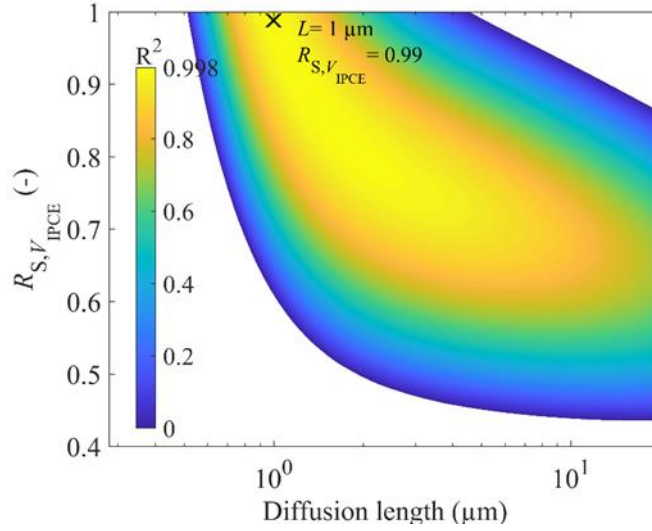


**Fig. 4.3.**  $R^2$  of the numerical-experimental IPCE fitting at 0  $V_{RHE}$  depending on diffusion length and the ratio of currents for p-Cu<sub>2</sub>O photocathode covered by Ga<sub>2</sub>O<sub>3</sub>/TiO<sub>2</sub>/RuO<sub>x</sub> [169].  $L$  and  $S_{R,0}$  were varied with 50 points per decade from  $10^{-0.5}$  to  $10^{1.5}$   $\mu\text{m}$  for  $L$  and  $10^{-2}$  to  $10^3$   $\text{cm s}^{-1}$  for  $S_{R,0}$ .

The surface recombination loss represents only 1 % loss in the IPCE at 500 nm (Fig. 4.4), indicating that the combination of a passivation layer and a co-catalyst layer made of Ga<sub>2</sub>O<sub>3</sub>/TiO<sub>2</sub>/RuO<sub>x</sub> reduces surface recombination loss ( $R_{S,V_{IPCE}}$  increases). Surface recombination loss are usually experimentally determined by comparing the photocurrent obtained in a standard electrolyte to the one in a charge scavenger electrolyte. A charge scavenger can increase the surface charge transfer velocity but does not necessarily completely suppress surface recombination. In contrast, our numerical model can fully separate surface recombination loss from the photocurrent and precisely predict the photocurrent without any surface recombination loss.

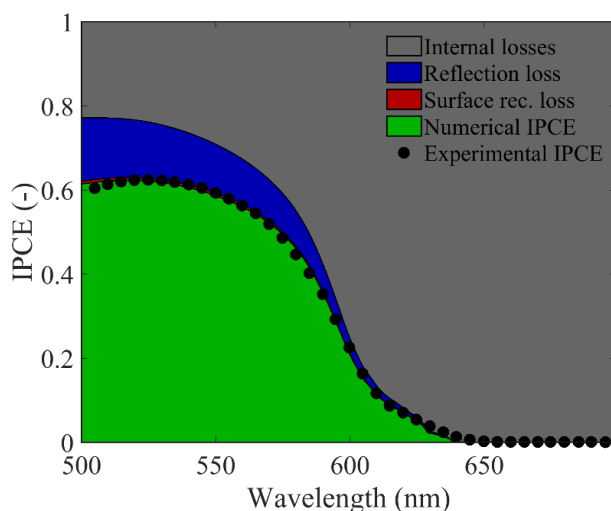


**Fig. 4.4.** Numerical and experimental IPCE at 0  $V_{\text{RHE}}$  for a planar p-Cu<sub>2</sub>O photocathode covered by a Ga<sub>2</sub>O<sub>3</sub>/TiO<sub>2</sub>/RuO<sub>x</sub> layer with the internal losses (grey), the reflection loss (blue), the surface recombination loss (red), and the numerical IPCE (green). The numerical IPCE was fitted to the experimental IPCE from Niu et al.[169] (black dots).

### 4.3.2. Diffusion lengths and diffusion optical numbers

The diffusion lengths of planar p-Cu<sub>2</sub>O, p-Si, n-d- and n-Fe<sub>2</sub>O<sub>3</sub>, and BiVO<sub>4</sub> photoelectrodes were determined using our IPCE analysis and were compared to reported values in the literature (Fig. 4.5). All the determined diffusion lengths were within the range of reported values except the one of CuFeO<sub>2</sub> with a mismatch of nearly two orders of magnitude. The diffusion length of a planar Cu<sub>3</sub>V<sub>2</sub>O<sub>8</sub> photoelectrode for which, to our knowledge, no diffusion length is currently reported was also determined. The IPCE analysis was additionally applied to determine projected diffusion lengths of nanostructured Fe<sub>2</sub>O<sub>3</sub> and p-b. LaTiO<sub>2</sub>N photoanodes (Fig. 4.5). Most of  $L_{0.95}$  were within 1-6  $\mu\text{m}$ , except for Si, BiVO<sub>4</sub>, and LaTiO<sub>2</sub>N with values of 15.8  $\mu\text{m}$ , 112  $\mu\text{m}$ , and 3-42.6  $\mu\text{m}$ , respectively (Table 4.2). Si is an indirect bandgap semiconductor and thus the probability to capture a photon to generate an electron-hole pair is reduced. This low probability results in a poor absorption coefficient and thus must be compensated by a large diffusion length to reach high efficiency. BiVO<sub>4</sub> is also an indirect bandgap semiconductor[204] but has a comparatively larger bandgap (2.5 eV or 496 nm compared to 1.12 eV or 1107 nm for Si) that is close to 500 nm at which  $L_{0.95}$  is calculated. Therefore, similarly as for

Si, the absorption coefficient of BiVO<sub>4</sub> at 500 nm is very low and a large diffusion length is also required to reach high efficiency.  $L_{0.95}$  of LaTiO<sub>2</sub>N varies from 3 to 42.6  $\mu\text{m}$  when using the DFT (section A4.3.2) or experimental[161] complex refractive index data, respectively. The imaginary part of the experimental complex refractive index,  $k$ , of LaTiO<sub>2</sub>N was low, which induces a high  $L_{0.95}$ . We think that the experimental  $k$  extracted from p.-b. LaTiO<sub>2</sub>N photoelectrodes with a highly complex morphology might be underestimated while the DFT-based  $k$  is for a monocrystalline planar LaTiO<sub>2</sub>N film, probably providing more realistic  $k$  values.

As depicted in Fig. 4.5, Si is the only photoelectrode for which  $L_{0.95}$  is smaller than the diffusion length. The diffusion length of Cu<sub>2</sub>O is 1-1.8  $\mu\text{m}$ , slightly below the  $L_{0.95}$  of 2.4  $\mu\text{m}$ . All the other photoelectrodes have a diffusion length two or three orders of magnitude lower than  $L_{0.95}$ , except the nanostructured Fe<sub>2</sub>O<sub>3</sub>-CoB<sub>i</sub> and p.-b. LaTiO<sub>2</sub>N photoelectrode with a projected diffusion length only one order of magnitude below  $L_{0.95}$ .

The relatively large variation in the determined diffusion length and  $L_{0.95}$  of LaTiO<sub>2</sub>N is a result of the different complex refractive index used for the IPCE analysis, one coming from Gaudy et al.[161] and the other one determined by DFT calculations done in this work (Fig. A4.6). The determined projected diffusion length of the p.-b. LaTiO<sub>2</sub>N photoelectrode and its variation straddles the determined diffusion length of Gaudy et al.[161] of 280 nm (with a hole lifetime of 0.5 ns and a hole mobility of 61 cm<sup>2</sup> V<sup>-1</sup> s<sup>-1</sup>).

The diffusion length of CuFeO<sub>2</sub> was found to be 6.3 nm, much below the value of 225 nm determined by time-resolved microwave conductivity measurement (TRMC)[205]. This discrepancy might be due to the fact that TRMC is a technique that cannot discriminate between the mobilities of majority or minority charge carriers while here only the minority charge carrier's diffusion length is determined. Moreover, TRMC determines a local bulk diffusion length while here the diffusion length is not a bulk diffusion length but a projected diffusion length that includes the defects present in the entire photoelectrode. Thus, we believe that TRMC is a technique that potentially overestimates the actual diffusion length. However, a different synthesis technique of CuFeO<sub>2</sub>, such as physical vapor deposition or chemical vapor deposition, could reduce the defects present in the material and increase the diffusion length.

The calculated projected diffusion length of the nanostructured Fe<sub>2</sub>O<sub>3</sub> photoanode covered by CoB<sub>i</sub> from Xi et al.[188] was 39.5-119.4 nm, one order of magnitude

#### 4: Rapid performance optimization method for photoelectrodes

---

below  $L_{0.95}$  of 3.6  $\mu\text{m}$  (Table 4.2). The calculated diffusion length of planar  $\text{Fe}_2\text{O}_3$  was 4.6-9.1 nm, i.e. three orders of magnitude below  $L_{0.95}$  (Fig. 4.5).

The Si photoelectrode was the only photoelectrode for which the diffusion optical number,  $\alpha_{500}L$ , was larger than  $\alpha_{500}L_{0.95}$ , indicating high performance (Fig. 4.6). The  $\text{Cu}_2\text{O}$  photoelectrode is a photoelectrode with  $\alpha_{500}L=3-5$  close to  $\alpha_{500}L_{0.95}=7$  (Table 4.2). Thus,  $\text{Cu}_2\text{O}$  photoelectrode is a well performing photoelectrode[169] but can currently not outperform an IQE of 95 % without surface recombination loss at 500 nm (below  $\alpha_{500}L_{0.95}$ ).  $\alpha_{500}L$  of  $\text{Fe}_2\text{O}_3$  photoelectrodes is increased from 0.02-0.04 to 0.187-0.564 by nanostructuring. Thus, nanostructuring improves the projected diffusion length by about two orders of magnitude but only by one order of magnitude for  $\alpha_{500}L$ , which is not enough to reach  $\alpha_{500}L_{0.95}$  (Fig. 4.6).

The diffusion length of p.-b.  $\text{LaTiO}_2\text{N}$  photoanodes is about two orders of magnitude below  $\alpha_{500}L_{0.95}$ . However, the nanostructure of the investigated p.-b.  $\text{LaTiO}_2\text{N}$  photoanodes[161] is not optimized and a more recent report from Akiyama et al.[103] of p.-b.  $\text{LaTiO}_2\text{N}$  photoanodes with significantly higher specific surface area at reduced electrode thickness shows a photocurrent density at 1.23  $\text{V}_{\text{RHE}}$ , 7.4 times higher than our photocurrent density, which translates in significantly larger projected diffusion length. Unfortunately, no IPCE data is available in the work of Akiyama et al. and therefore the corresponding diffusion length could not be quantified.

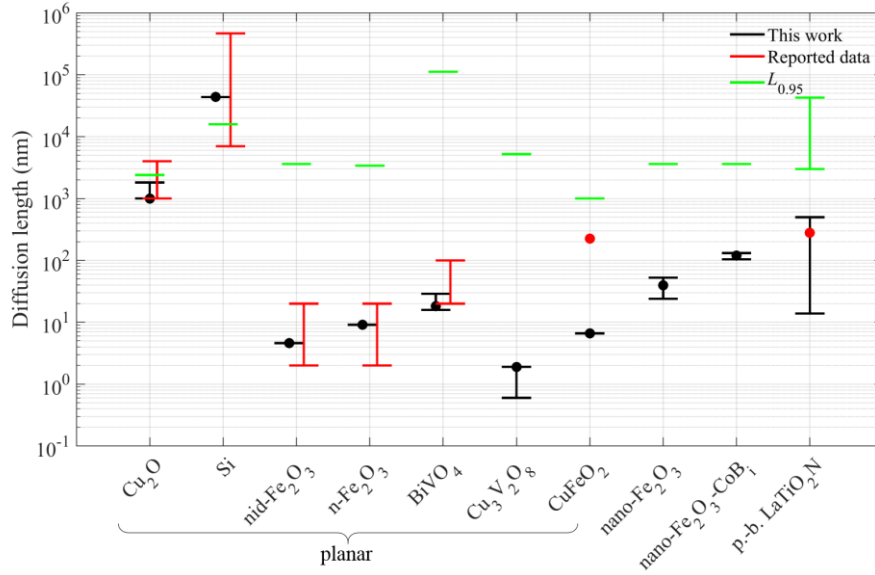


**Fig. 4.5.** Diffusion lengths of all water-splitting photoelectrode materials investigated in this work. The black error bars are the variation in the diffusion length due to variations in the input material parameters (see Table 4.1) and the black dots are the nominal values. The red error bars are the variation in the diffusion lengths reported in literature. The green lines indicate the diffusion lengths for which the IQE without surface recombination is above 95 % at 500 nm,  $L_{0.95}$  (eqn (4.4)). The diffusion lengths of Cu<sub>2</sub>O reported from literature vary from 1  $\mu\text{m}$  to 4  $\mu\text{m}$ [180]. The calculated diffusion length of Si varies from 7  $\mu\text{m}$  to 467  $\mu\text{m}$ [194] using a p-Si photoelectrode with a resistivity of 0.01-1  $\Omega\text{ cm}$ [185] and a doping concentration of  $8 \times 10^{18}$ - $1.5 \times 10^{16}\text{ cm}^{-3}$ [193]. The diffusion lengths of Fe<sub>2</sub>O<sub>3</sub> reported from literature are 2, 3, 4, 10 nm[178], and 20 nm[206]. The diffusion lengths of BiVO<sub>4</sub> reported from literature are 20 nm[179], 45 nm[207], 70 nm[208], and 100 nm[209]. The reported diffusion length of CuFeO<sub>2</sub> is 225 nm[205]. The diffusion length of p-b. LaTiO<sub>2</sub>N photoelectrode is 280 nm[161].



#### 4: Rapid performance optimization method for photoelectrodes

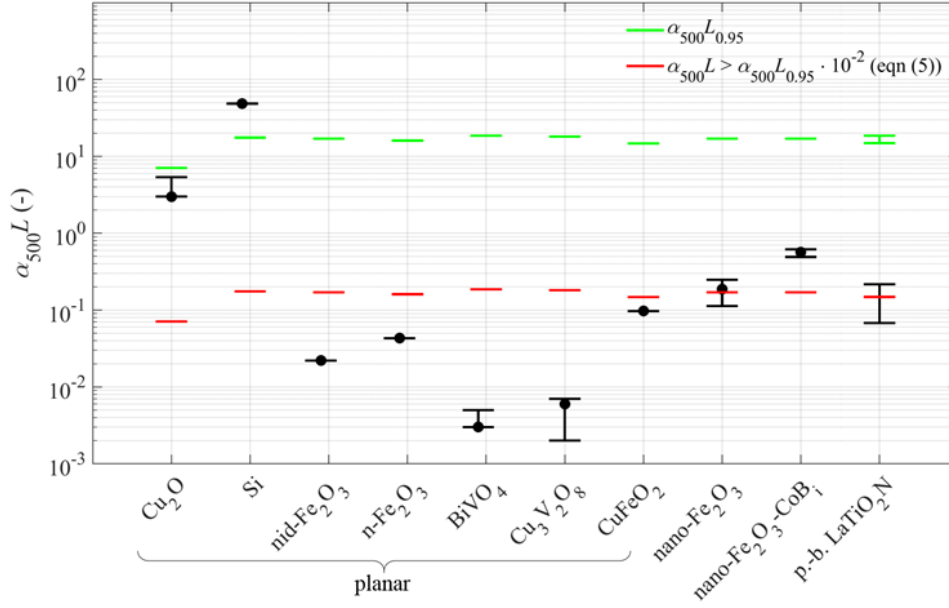


**Fig. 4.6.** Diffusion optical numbers,  $\alpha_{500}L$ , of various photoelectrode materials and nanostructures. The green lines indicate the  $\alpha_{500}L_{0.95}$  for which the IQE without surface recombination is above 95 % at 500 nm (eqn (4.4)). The red lines indicate the minimum  $\alpha_{500}L$  for which a photoelectrode can perform very well when nanostructured (eqn (4.5)), i.e. an  $\alpha_{500}L$  (black lines) below the red line indicates a photoelectrode with low performance even when nanostructured. The black dots are the determined nominal values, the error bars are due to the variations in the input parameters (according to Table 4.1).

#### 4.3.3. Pathways to photoelectrode improvements

**Improvement by nanostructuring.** According to the nanostructuring criterion (eqn (4.5)),  $\text{Fe}_2\text{O}_3$ ,  $\text{BiVO}_4$ ,  $\text{Cu}_3\text{V}_2\text{O}_8$ , and  $\text{CuFeO}_2$  photoelectrodes are not expected to perform very well, even if nanostructured. Their diffusion optical number,  $\alpha_{500}L$ , was more than two orders of magnitude below  $\alpha_{500}L_{0.95}$  (Table 4.2). Accordingly, the projected diffusion length of these photoelectrodes should not be improved by nanostructuring but rather by modifying their synthesis method, by reducing the bulk defects and by optimizing the doping concentration. Si and  $\text{Cu}_2\text{O}$  photoelectrodes showed to be good performing candidates since their  $\alpha_{500}L$  were in the same order of magnitude as  $\alpha_{500}L_{0.95}$ . However,  $\text{Cu}_2\text{O}$  photoelectrodes should be nanostructured to achieve an IQE above 95 % at 500 nm.  $\text{LaTiO}_2\text{N}$  is considered potentially good performing since  $\alpha_{500}L$  was about two orders of magnitude below

$\alpha_{500}L_{0.95}$ . Thus, if  $\alpha_{500}L$  of particle-based  $\text{LaTiO}_2\text{N}$  photoelectrode could be further improved by nanostructuring, p.-b.  $\text{LaTiO}_2\text{N}$  photoelectrode could become an interesting candidate for high performing water-splitting. Indeed, nanostructuring of p.-b.  $\text{LaTiO}_2\text{N}$  photoelectrodes by increasing the internal nano-pores in contact to the electrolyte using an acidic treatment has been recently achieved and has shown higher performance with a photocurrent density of  $8.9 \text{ mA cm}^{-2}$  at  $1.23 \text{ V}_{\text{RHE}}$  (ref. [103]). We estimate that this increase in the current density translates in an increase of around 50 times the projected diffusion length, i.e. a diffusion length of 694 nm (13.8 nm with our photoelectrodes) calculated with an estimated IPCE of 0.8 at 500 nm for ref. [103], the DFT complex refractive index (see section A4.3.2) and the material properties of  $\text{LaTiO}_2\text{N}$  (Table 4.1). Thus,  $\text{LaTiO}_2\text{N}$  photoelectrodes made of mesoscopic particles with optimized, internal nano-pores seem viable photoelectrodes.

**Reduction of surface losses.** In addition to the assessment of the nanostructuring opportunity factor of a photoelectrode, our experimental-numerical method can provide guidance on performance improvements of the photoelectrode. We can calculate the potential improvement by reducing surface recombination and reflection losses. The internal, reflection and surface recombination losses for planar photoelectrodes of  $\text{Cu}_2\text{O}$ , Si,  $\text{Fe}_2\text{O}_3$ ,  $\text{BiVO}_4$ ,  $\text{Cu}_3\text{V}_2\text{O}_8$ , and  $\text{CuFeO}_2$ , nanostructured  $\text{Fe}_2\text{O}_3$ , and p.-b.  $\text{LaTiO}_2\text{N}$  photoelectrodes are depicted in Fig. 4.7 (Fig. 4.4 for  $\text{Cu}_2\text{O}$ ).

For example, the p- $\text{Cu}_2\text{O}$  photocathode covered by a  $\text{Ga}_2\text{O}_3/\text{TiO}_2/\text{RuO}_x$  layer showed only a surface recombination loss of 1 % at 500 nm but a reflection loss of 15 % (Fig. 4.4). Thus, an improvement up to 15 % in the IPCE at 500 nm could be obtained by reducing the reflection loss with an antireflection coating[210]. Nanostructuring the p- $\text{Cu}_2\text{O}$  photocathode could further improve the performance to an IPCE over 95 % by increasing the projected diffusion length from 1  $\mu\text{m}$  to up to 2.4  $\mu\text{m}$ .

The IPCE of p-Si photocathode covered by a layer of mesoporous hematite[185] was very high, i.e. over 60 % at 600 nm. The reflection loss at the semiconductor-electrolyte interface was taken from the measured reflectance of Li et al.[185] and was minor (1.4 % at 600 nm) according to Fig. 4.7.a. However, the IPCE can be increased up to 26 % at 600 nm by fully suppressing the surface recombination loss (Fig. 4.7.a). The numerical IPCE for this photoelectrode was only investigated for the wavelength range from 600 nm to 1100 nm since the layer of hematite deposited

#### 4: Rapid performance optimization method for photoelectrodes

---

on the Si layer absorbs light until 600 nm, and therefore greatly influences the IPCE below 600 nm.

The IPCE of planar  $\text{Fe}_2\text{O}_3$  photoanodes could be improved to nearly 30 % at 300 nm when completely suppressing surface recombination loss (Fig. 4.7.c). Nevertheless, the internal losses related to the short diffusion length of planar  $\text{Fe}_2\text{O}_3$  limited the performance to up to an IPCE of 63 % at 300 nm and of 14 % at 500 nm.

The best IPCE fitting of  $\text{BiVO}_4$  had an  $R^2=0.66$  only. This poor fitting was observed in Fig. 4.7.d, i.e. the numerical IPCE was 5 % below the experimental IPCE in the wavelength range from 325 nm to 390 nm and 5 % above it in the wavelength range from 400 nm to 470 nm. The poor fitting of the IPCE was a result of the poor refractive index data of  $\text{BiVO}_4$ . Indeed, the complex refractive index giving the best IPCE fit was calculated by DFT of polycrystalline  $\text{BiVO}_4$  (ref. [199]) and not by experimental measurements[204]. Nevertheless, the determined diffusion length of 16-29 nm was within reported data in the literature[179], [207]–[209].  $\text{BiVO}_4$  appears to have only a potential IPCE improvement of ~5 % to up to an IPCE of 28 % at 320 nm when fully suppressing surface recombination and reflection losses.

$\text{Cu}_2\text{V}_3\text{O}_8$  and  $\text{CuFeO}_2$  were both poorly performing photoelectrodes with very limited potential for improvements as planar photoelectrodes, i.e. a maximum IPCE of 16 % at 320 nm for  $\text{Cu}_2\text{V}_3\text{O}_8$  and 35 % at 352 nm for  $\text{CuFeO}_2$  when fully suppressing surface recombination and reflection losses (Fig. 4.7.e and f).

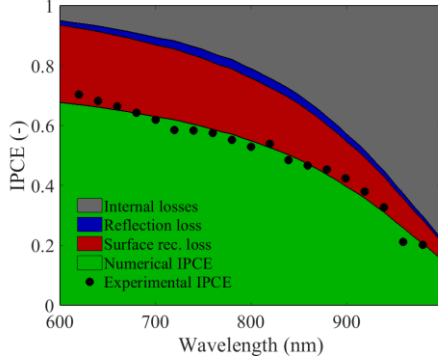
The  $\text{Fe}_2\text{O}_3$  nanorods photoanode showed greatly reduced internal losses (Fig. 4.7.h) with a projected diffusion length of up to 131 nm. The actual diffusion length of  $\text{Fe}_2\text{O}_3$  remains within 4.6-9.1 nm (Table 4.2) while the projected diffusion length of 131 nm for  $\text{Fe}_2\text{O}_3$  nanorods photoanode is nearly two orders of magnitude (14 times) higher than the actual diffusion length. As mentioned in section A4.2.6, our method only determines a projected diffusion length for structured photoelectrodes. However, Fig. 4.7.g and Fig. 4.7.h also highlight the challenge raised by nanostructured photoelectrodes, which is the increase of the active surface area and thus an increased surface recombination. Indeed, the surface recombination loss reached 53 % for a nano- $\text{Fe}_2\text{O}_3$  photoanode at 350 nm (Fig. 4.7.g) compared to 10 % for  $\text{Fe}_2\text{O}_3$  at 350 nm (Fig. 4.7.b) or 30 % for  $\text{Fe}_2\text{O}_3$  (Fig. 4.7.c). Nano- $\text{Fe}_2\text{O}_3$ - $\text{CoBi}$  photoanodes could reach an IPCE of 94 % at 350 nm if the surface recombination and the reflection losses could be fully suppressed. Thus, the deposition of a passivation layer, such as  $\text{Ga}_2\text{O}_3$  (ref. [169]) should be prioritized to increase the efficiency of these nanostructured  $\text{Fe}_2\text{O}_3$  photoelectrodes. However,

even by completely suppressing surface recombination and reflection loss, the IPCE at 500 nm could only reach 45 % because of the low diffusion optical number  $\alpha_{500}L=0.564$  (Table 4.2).

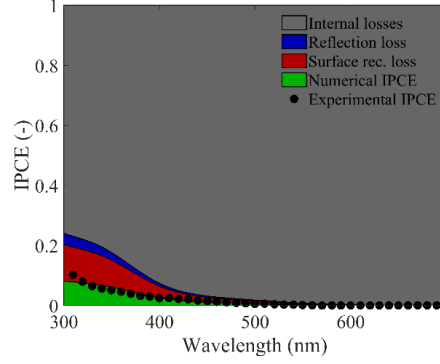
The numerical IPCE of p.-b LaTiO<sub>2</sub>N photoanodes did not fit well to the measured IPCE with  $R^2=0.65$  using the index determined in this work by DFT calculation and  $R^2=0.55$  using the complex refractive index of Gaudy et al.[161] (Fig. 4.7.i and j). Reasons for the discrepancy between the numerical and experimental IPCE could lie in inaccurate complex refractive index data of LaTiO<sub>2</sub>N. As depicted in Fig. 4.7.i and j, the surface recombination loss was independent of the complex refractive index data used (Fig. A4.6 or Gaudy et al.[161]), i.e. there was no surface recombination loss in both cases. Thus, the main internal losses was due to the low projected diffusion length. This result differs from our former conclusion identifying the low surface charge transfer velocity as limiting[161] (interfacial hole transfer velocity). This previous model resolved numerically the electromagnetic wave propagation and the charge transport and conservation in a 2D computational domain representing a typical particle of the film, however neglecting continuous surface state recombination. Here, continuous surface states were considered but the 2D nature of the porous film came into play through the effective properties only, with the minority charge path length limited by our 1D modeling domain. Consequently, the different modeling assumptions favor or punish certain transport mechanism. Most probably, the diffusion length as well as the surface losses are limiting and experiments support this conclusion: increasing the projected diffusion length using nanostructuring and improving the reaction kinetic through the deposition of co-catalysts has shown to improve the performance of p.-b. LaTiO<sub>2</sub>N photoelectrodes[103].

#### 4: Rapid performance optimization method for photoelectrodes

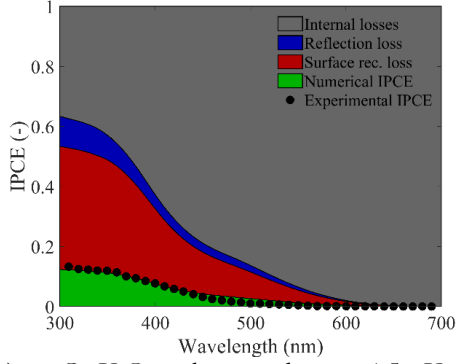
a) p-Si photocathode at -1 V<sub>RHE</sub>, R<sup>2</sup>=0.978



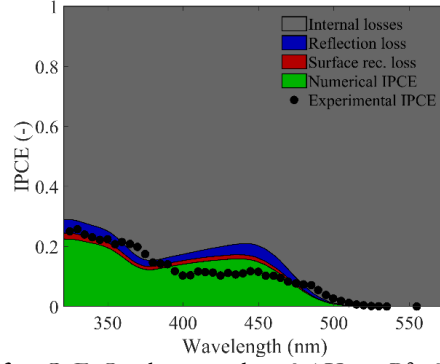
b) n<sub>i</sub>d-Fe<sub>2</sub>O<sub>3</sub> photoanode at 1.46 V<sub>RHE</sub>, R<sup>2</sup>=0.843



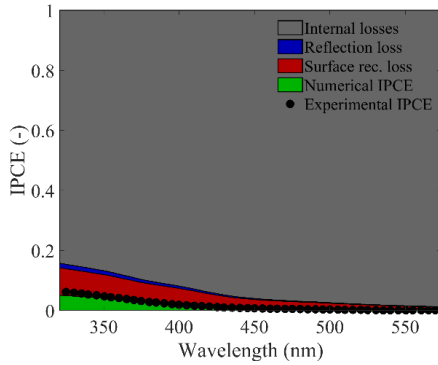
c) n-Fe<sub>2</sub>O<sub>3</sub> photoanode at 1.46 V<sub>RHE</sub>, R<sup>2</sup>=0.966



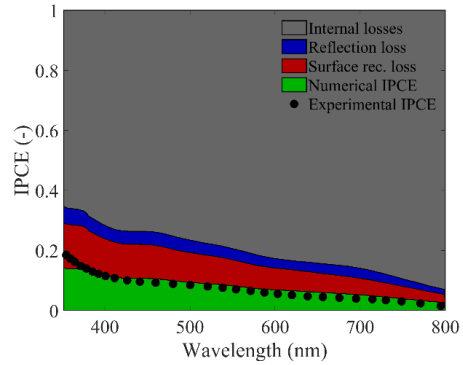
d) n-BiVO<sub>4</sub> photoanode at 1 V<sub>RHE</sub>, R<sup>2</sup>=0.758



e) n-Cu<sub>3</sub>V<sub>2</sub>O<sub>8</sub> photoanode at 1.5 V<sub>RHE</sub>, R<sup>2</sup>=0.901

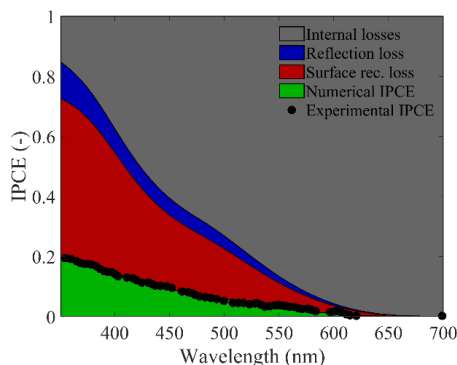


f) p-CuFeO<sub>2</sub> photoanode at 0.4 V<sub>RHE</sub>, R<sup>2</sup>=0.892

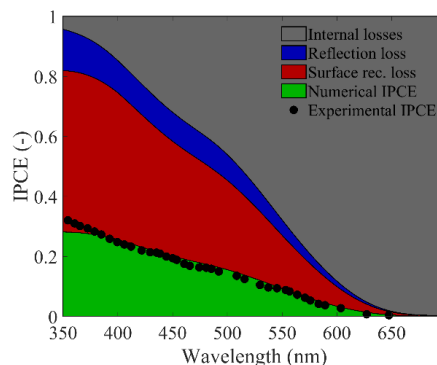


#### 4: Rapid performance optimization method for photoelectrodes

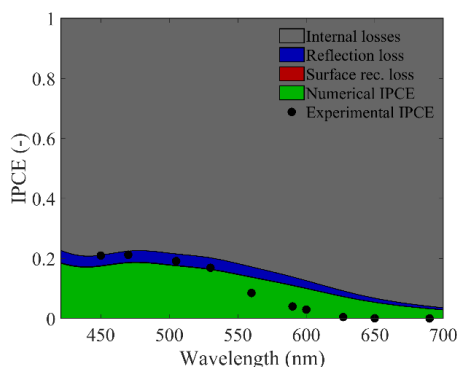
g) nano-Fe<sub>2</sub>O<sub>3</sub> photoanode at 1.23 V<sub>RHE</sub>, R<sup>2</sup>=0.991



h) nano-Fe<sub>2</sub>O<sub>3</sub>-CoB<sub>i</sub> photoanode at 1.23 V<sub>RHE</sub>, R<sup>2</sup>=0.992



i) p.-b. LaTiO<sub>2</sub>N photoanode with refractive index from this work (Fig. A4.6) at 1.23 V<sub>RHE</sub>, R<sup>2</sup>=0.545



j) p.-b. LaTiO<sub>2</sub>N photoanode with refractive index at 1.23 V<sub>RHE</sub>, R<sup>2</sup>=0.619 from Gaudy et al.[161]

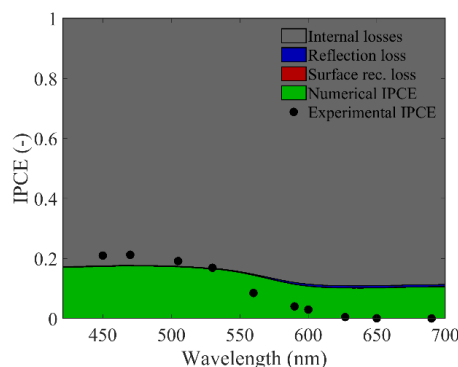


**Fig. 4.7.** Numerical and experimental IPCE for water splitting a) planar p-Si photocathode covered by a mesoporous layer of hematite[185], b) planar n-d-Fe<sub>2</sub>O<sub>3</sub> photoanode[23], c) planar n-Fe<sub>2</sub>O<sub>3</sub> photoanode[23], d) planar n-BiVO<sub>4</sub> photoanode[186], e) planar n-Cu<sub>3</sub>V<sub>2</sub>O<sub>8</sub> photoanode[174], f) planar n-CuFeO<sub>2</sub> photoanode[201], g) nanorods n-Fe<sub>2</sub>O<sub>3</sub> photoanode without co-catalyst, h) nanorods n-Fe<sub>2</sub>O<sub>3</sub> photoanode with CoB<sub>i</sub> co-catalyst [188], and p.-b. LaTiO<sub>2</sub>N photoanodes using complex refractive index from i) DFT calculations (Fig. A4.6) and from j) Gaudy et al.[161] and our experimental IPCE measurements (Fig. A4.5). The applied potential of the IPCE,  $V_{\text{IPCE}}$ , and the R<sup>2</sup> of the IPCE fitting are also indicated.

**Optimization of the photoelectrode's thickness.** The photoelectrode thickness can be optimized for maximal performance. Niu et al.[169] reported that the thickness of their photoelectrode was influencing the IPCE, with the thinnest photoelectrode of 50  $\mu\text{m}$  having the highest efficiency. Since our IPCE model, based only on minority charges, was insensitive to changes in the photoelectrode thickness

#### 4: Rapid performance optimization method for photoelectrodes

---

(down to the SCR width of 3.47  $\mu\text{m}$ , see section A4.2.5), we can attribute this result to a limitation of the majority charge carrier diffusion length. Thus, our IPCE model can be used to find the minimum thickness for which the IPCE remains unchanged. This minimum thickness will automatically correspond to the smallest, and thus, the optimized thickness for limiting majority carrier diffusion length.

**Optimization of the doping concentration.** An optimal doping concentration—or an optimal SCR width according to eqn (I7)—can be obtained by varying the doping concentration without changing the diffusion length nor the ratio of currents. A maximum IPCE at 500 nm and at 0  $V_{\text{RHE}}$  was found with a doping concentration of  $10^{15} \text{ cm}^{-3}$  for the p- $\text{Cu}_2\text{O}$  photocathode of Niu et al.[169] (Fig. 4.8).

The calculated IPCE does not tend to zero with increasing doping concentration (Fig. 4.8) although in reality a semiconductor with high doping concentration becomes degenerated (degeneracy starts at  $\sim 10^{20} \text{ cm}^{-3}$  for Si) and behaves like a metal, unable to generate any photocurrent and thus the IPCE drops to zero. The numerical IPCE model could account for an IPCE drop to zero for high doping concentration by including the decrease of the diffusion length with increasing doping concentration (see S4 with Si as an example). However, the empirical relation for the diffusion length as a function of the doping concentration is required and is only known for well-established semiconductor materials such as Si, GaN, InP, GaAs, Ge, etc.[111] but not for most photoelectrode materials.

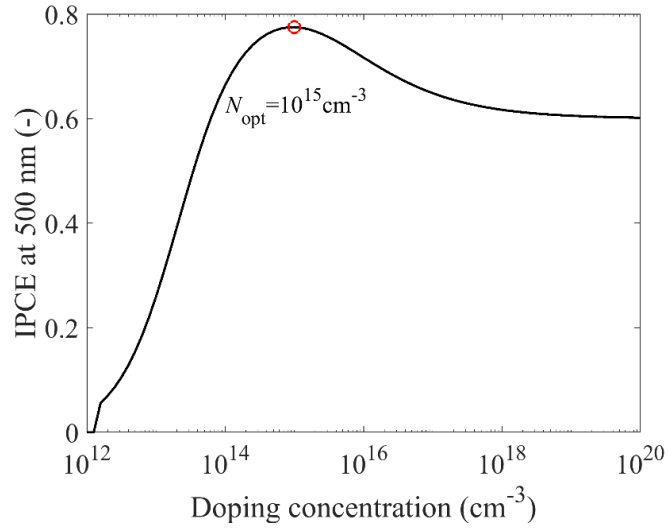


**Fig. 4.8.** Calculated IPCE at 500 nm as a function of the doping concentration for the p-Cu<sub>2</sub>O photocathode covered by Ga<sub>2</sub>O<sub>3</sub>/TiO<sub>2</sub>/RuO<sub>x</sub>[169] with a fixed diffusion length of 1  $\mu\text{m}$  (Table 4.2). A maximum IPCE at 500 nm of 0.78 is obtained at an acceptor doping concentration of  $1.0 \times 10^{15} \text{ cm}^{-3}$ .

The optimal doping concentrations that maximized the IPCE for all investigated photoelectrodes are presented in Table 4.2. The predicted optimal doping concentrations are all within experimentally achievable values. However, the synthesis routes of metal oxides do often not offer a precise control of the doping concentration[17]. Table 4.2 summarizes also the  $R^2$  of the IPCE fitting, the diffusion length,  $L$ , the diffusion length that provides an IQE without surface losses higher than 95 %,  $L_{0.95}$ , the ratio of currents,  $R_{S,IPCE}$ , the diffusion optical number,  $\alpha_{500}L$ , the nanostructuring opportunity factor,  $f_{\text{nano}}$ , obtained for all the photoelectrodes investigated in this work.



#### 4: Rapid performance optimization method for photoelectrodes

**Table 4.2.** Summary of the determined material parameters and factors for all the photoelectrode materials investigated in this work. Only nominal values are depicted according to Table 4.1.

Material	$R^2$ (-)	$L$ (nm)	$L_{0.95}$ ( $\mu\text{m}$ )	$R_{S,V_{IPC}}$ (-)	$\alpha_{500}L$ (-)	$\alpha_{500}L_{0.95}$ (-)	$f_{\text{viability}}$ (-)	$N_{\text{opt}}$ ( $\text{cm}^{-3}$ )
p-Cu <sub>2</sub> O	0.998	1000	2.4	0.99	3.0	7.1	0.4	$1.0 \times 10^{15}$
p-Si	0.978	$43.7 \times 10^3$	15.8	0.72	48.5	17.5	-0.4	$6.3 \times 10^{13}$
nid-Fe <sub>2</sub> O <sub>3</sub>	0.843	4.6	3.6	0.18	0.022	17.0	2.9	$5.0 \times 10^{18}$
n-Fe <sub>2</sub> O <sub>3</sub>	0.966	9.1	3.4	0.23	0.043	16.1	2.6	$2.5 \times 10^{18}$
n-BiVO <sub>4</sub>	0.758	18.2	112	0.92	0.003	18.6	3.8	$6.3 \times 10^{17}$
n-Cu <sub>3</sub> V <sub>8</sub> O <sub>3</sub>	0.901	1.9	5.2	0.36	0.007	18.1	3.4	$1.6 \times 10^{19}$
p-CuFeO <sub>2</sub>	0.892	6.6	1.0	0.49	0.097	14.8	2.2	$2.5 \times 10^{18}$
nano-Fe <sub>2</sub> O <sub>3</sub>	0.991	39.5	3.6	0.27	0.187	17.0	2	$1.6 \times 10^{17}$
nano-Fe <sub>2</sub> O <sub>3</sub> -CoBi	0.992	119.4	3.6	0.38	0.564	17.0	1.5	$4.0 \times 10^{16}$
LaTiO <sub>2</sub> N	0.545	497.9	3.0	1.00	0.217	18.6	1.9	$1.3 \times 10^{15}$

#### 4.4. Conclusion

Decades of research dedicated to the discovery of novel photoelectrode materials have led to a large amount of semiconductor materials with suitable bandgaps for high-performing tandem water-splitting cells. However, none of these materials could provide solutions for efficient, cheap and stable water-splitting photoelectrodes highlighting that the bandgap is not the only criterion for the viability of a photoelectrode. Indeed, charge carrier transport (in the bulk, in the SCR, and across interfaces) has appeared to be as important as the bandgap. Unfortunately, transport properties are much more difficult to evaluate and density functional theory, which is efficient and reasonably accurate in predicting the bandgap of a material, has not yet reached the maturity to accurately predict transport properties. Thus, efforts have been made towards developing rapid techniques to determine the transport properties of photoelectrodes. However, these efforts remain mostly qualitative and have not defined any objective benchmark to evaluate the viability of photoelectrodes or of synthesis method. Here, we have developed a versatile method and coupled it to the nanostructuring opportunity factor in order to objectively investigate if nanostructuring provide a path to reach high performance for a photoelectrode. Furthermore, the method provides an evaluation of the photoelectrode viability by determining if the transport limitation of a photoelectrode can be overcome by nanostructuring and if not, an alternative synthesis method should be developed. Thus, our method could be coupled to experimental high-throughput efforts[211] in order to provide a rapid screening of the viability of novel photoelectrode materials and synthesis methods. The method

#### 4: Rapid performance optimization method for photoelectrodes

---

requires wavelength-dependent IPCE measurements and estimation of the spectral complex refractive index, the bandgap, the flatband potential, the doping concentration, the permittivity and the photoelectrode thickness as inputs and determines in turn the actual or projected diffusion length, the actual or projected diffusion optical number, and the ratio of currents of a photoelectrode. The detailed knowledge of the surface state distribution factor, the minority charge carrier mobility, and the surface charge transfer coefficient is not required since these properties are neither affecting the determination of the diffusion optical number nor the nanostructuring opportunity factor of photoelectrodes. The method was validated with a p-Cu<sub>2</sub>O photocathode<sup>[169]</sup> and then used with an objective benchmark to determine the nanostructuring opportunity of water-splitting photoelectrodes. Specifically, a photoelectrode was considered to have a good nanostructuring opportunity if its diffusion optical number was less than two orders of magnitude below the theoretical diffusion optical number ( $\alpha_{500}L_{0.95}$ ), which resulted in an IQE without surface recombination loss above 95 %. This benchmark was established based on the observed increase in the diffusion optical number of one order of magnitude only of Fe<sub>2</sub>O<sub>3</sub> photoanode using state-of-the-art nanostructuring techniques.

We investigated different materials and nanostructures to highlight the versatility of our method. Although only PEC water-splitting photoelectrodes were investigated in this work, there is no restriction to applying our method for any other PEC reactions, including CO<sub>2</sub> reduction. The candidates investigated in this work include planar Cu<sub>2</sub>O, Si, Fe<sub>2</sub>O<sub>3</sub>, BiVO<sub>4</sub>, Cu<sub>3</sub>V<sub>2</sub>O<sub>8</sub>, and CuFeO<sub>2</sub> photoelectrodes, and nanostructured Fe<sub>2</sub>O<sub>3</sub> and p.-b. LaTiO<sub>2</sub>N photoelectrodes. We also presented guidelines for improving the performance of these photoelectrodes by nanostructuring and by evaluating the surface recombination and reflection losses. Furthermore, the doping concentration that maximized the ICPE at 500 nm was calculated for all the photoelectrode materials and nanostructures investigated in this work.

Our IPCE analysis predicted that Fe<sub>2</sub>O<sub>3</sub>, BiVO<sub>4</sub>, CuFeO<sub>2</sub>, and Cu<sub>3</sub>V<sub>2</sub>O<sub>8</sub> have a low nanostructuring opportunity factor ( $f_{\text{nano}} > 2$ ) due to their low diffusion optical number and thus are difficult to improve with nanostructuring since their internal losses are very high. The nanostructuring opportunity factor of Si was (as the only candidate of all the investigated photoelectrodes) below zero and, thus, could perform without nanostructuring. The use of better catalysts could further improve the performance and at the same time help addressing the stability challenge of Si, a problem still not solved. Since the nanostructuring opportunity factor of Cu<sub>2</sub>O was

#### 4: Rapid performance optimization method for photoelectrodes

---

0.4, we estimate that only a small effort in nanostructuring  $\text{Cu}_2\text{O}$  photocathodes would be required to achieve highly performing photocathodes with an IQE above 95 % at 500 nm. Moreover, a small increase in the doping concentration of up to  $10^{15} \text{ cm}^{-3}$  could theoretically increase the IPCE at 500 nm by 15 % (from 62.3 % to 77.5 %). P.-b.  $\text{LaTiO}_2\text{N}$  photoanodes could potentially have a high performance as the projected diffusion optical number of the nanostructured p.-b.  $\text{LaTiO}_2\text{N}$  photoelectrode investigated here lied at the limit of our nanostructuring opportunity factor benchmark. Indeed, a report in literature[103] indicates that improved nanostructures of p.-b. photoelectrode have the potential for further improvements in the diffusion length. A similar approach for nanostructured  $\text{Fe}_2\text{O}_3$  photoelectrodes might be interesting to undertake as these photoelectrodes lied also at the limit of our nanostructuring opportunity factor benchmark. However, since we observed that nanostructuring also increased the surface recombination loss, the deposition of a surface passivation layer or a co-catalyst to suppress surface recombination should be conjointly considered.

The durability of photoelectrodes has not been considered in this work although it is a key factor for cost-effective and industrial scale hydrogen production[41]. Nevertheless, our method could be used in combination with IPCE measurements at different operating times (for example *in-operando*) to evaluate the chronological change (i.e. increase) in surface recombination, internal or reflection losses. The ability to capture the chronological increase of each loss could greatly enhance the understanding of degradation phenomena and their effects on photoelectrode properties. Moreover, the durability could be quantified and used as an additional criterion for the performance of photoelectrodes.

Finally, the ability of our method to provide an estimation of the diffusion length in the right order of magnitude, even if some required material parameters are not precisely known or even unknown, gives an indication that our method can be used as a rapid and facile tool to quickly estimate the viability and the nanostructuring opportunity factor of new photoelectrodes. A user-friendly executable of the developed method is available in the supporting files and on our laboratory webpage[212], software POPe[213].

# Theoretical maximum efficiency and performance characterization of $\text{In}_x\text{Ga}_{1-x}\text{N}/\text{Si}$ tandem water-splitting photoelectrodes<sup>1</sup>

## 5.1. Introduction

Compositionally graded  $\text{In}_x\text{Ga}_{1-x}\text{N}$  layers of high structural and optical quality grown on Si has been achieved in the last years[214], [215] opening new perspective for cheap and efficient solar harvesting systems. Theoretical maximum efficiency for tandem photoelectrochemical (PEC) water-splitting systems could reach over 22.5% with Si as bottom cell and  $\text{In}_x\text{Ga}_{1-x}\text{N}$  as top cell with a bandgap between 1.6-1.8 eV[216], an indium content of 37-44 % respectively[215]. An efficiency over 20% could theoretically lead to a hydrogen prize below 3 \$  $\text{kg}^{-1}$  for PEC water-splitting devices under concentrated solar irradiation which would be approximatively equivalent to the price of gasoline for the same amount of energy[6], [16].

Notwithstanding the high theoretical efficiency of  $\text{In}_x\text{Ga}_{1-x}\text{N}$  for solar hydrogen production, previous attempts of  $\text{In}_x\text{Ga}_{1-x}\text{N}$  water-splitting photoelectrodes has only lead to very poor performance with photocurrent below 0.1  $\text{mA cm}^{-2}$  under AM1.5G irradiation, i.e. a performance even below pure n-GaN with a bandgap of 3.4 eV[217]. This low performance was attributed to the low crystalline quality of  $\text{In}_x\text{Ga}_{1-x}\text{N}$  without further investigations to explain the gap between theoretical and experimental efficiency. In-depth investigations on  $\text{In}_x\text{Ga}_{1-x}\text{N}$  were performed based

---

<sup>1</sup> A manuscript of this chapter is in preparation, 'Y. K. Gaudy and S. Haussener, Theoretical maximum efficiency and performance characterization of  $\text{In}_x\text{Ga}_{1-x}\text{N}/\text{Si}$  tandem water-splitting photoelectrodes, 2019, in preparation'.

## 5: Theoretical maximum efficiency and performance characterization of $\text{In}_x\text{Ga}_{1-x}\text{N}/\text{Si}$ tandem water-splitting photoelectrodes

---

on finite element simulations of  $\text{p-GaN}/\text{n-In}_x\text{Ga}_{1-x}\text{N}/\text{n-In}_{0.5}\text{Ga}_{0.5}\text{N}/\text{p-Si}/\text{n-Si}$  tandem structure solar cells. These simulations predict 28.9 % efficiency and showed that the thickness and the doping concentration of the graded region substantially affected the performance of the solar cell[218]. Modeling of  $\text{InGa}\text{N}/\text{Si}$  tandem solar cells ignoring space charge recombination showed a theoretical maximum efficiency of 31 % [219]. These models are based on  $\text{In}_x\text{Ga}_{1-x}\text{N}$  solar cells and not on  $\text{In}_x\text{Ga}_{1-x}\text{N}$  water-splitting photoelectrodes, which has a complete different physics due to the semiconductor-electrolyte interface, an interface at the core of PEC water-splitting devices performance[54]. Experimental and numerical studies of  $\text{In}_x\text{Ga}_{1-x}\text{N}/\text{Si}$  tandem water-splitting photoelectrodes are missing and would be greatly useful to identify and quantify the main losses in these photoelectrodes.

In this work, we evaluated the effect on the efficiency of compositionally graded  $\text{In}_x\text{Ga}_{1-x}\text{N}$  water-splitting photoelectrodes. First, we calculated a maximum theoretical photogeneration efficiency of  $\text{In}_x\text{Ga}_{1-x}\text{N}/\text{Si}$  tandem photoelectrodes. Then, we measured the photocurrent-voltage ( $I$ - $V$ ) curves and the incident photon-to-current efficiency (IPCE) of  $\text{In}_x\text{Ga}_{1-x}\text{N}$  photoelectrodes with indium content of  $x=9.5$  %, 16.5 %, 23.5 %, 33.3 %, and 41.4 %. Finally, the diffusion length, the diffusion optical number (section 4.2.1), the internal and surface losses, and the nanostructuring opportunity factor of the  $\text{In}_x\text{Ga}_{1-x}\text{N}$  water-splitting photoelectrodes were calculated with the measured IPCE and the software POPe[213].

### 5.2. Methodology

#### 5.2.1. Theoretical photogeneration efficiency of $\text{In}_x\text{Ga}_{1-x}\text{N}/\text{Si}$ photoelectrodes

Electromagnetic wave (EMW) propagation in thin  $\text{In}_x\text{Ga}_{1-x}\text{N}$  semiconductor film on a Si layer give rise to interferences between the forward and backward-propagating waves due to reflection on the Si layer. These interferences can lead to wavy generation rate inside the  $\text{In}_x\text{Ga}_{1-x}\text{N}$  semiconductor film that can be predicted by solving Maxwell's equation[220] whereas Beer-Lambert's law[55], [61], [63] or ray-tracing methods[66] fail in this prediction. Thus, the generation rate and the photogeneration current density in the  $\text{In}_x\text{Ga}_{1-x}\text{N}$  and Si semiconductors were calculated by solving the Maxwell's curl equations for each frequency,  $\omega$ , considered, given by eqn (1.1). The optical power absorbed per unit volume is given by eqn (1.2). The generation rate along the film thickness is calculated by integrating the spectral generation rate over the considered spectrum (eqn (1.3)). Finally, the

## 5: Theoretical maximum efficiency and performance characterization of $\text{In}_x\text{Ga}_{1-x}\text{N}/\text{Si}$ tandem water-splitting photoelectrodes

photogeneration current is calculated by integrating the generation rate over the thickness of the semiconductor, given by

$$i_l = q \int_0^d G(z) dz. \quad (5.1)$$

The EMW propagation was calculated in the electrolyte and in the semiconductors assuming AM1.5G front illumination with an incident angle of  $0^\circ$  as depicted in Fig. 5.1. The reflection loss at the semiconductor-electrolyte interface can greatly influence the photogeneration efficiency and was included using  $2 \mu\text{m}$  of water in front of the  $\text{In}_x\text{Ga}_{1-x}\text{N}$  layer (Fig. 5.1). The absorption loss due to the electrolyte is negligible since the water extinction coefficient is below the order of  $10^{-5}$  ( $k < 4 \cdot 10^{-6}$ ) in the visible range[83]. Indeed, the same photogenerated current density was observed using a layer of  $1 \text{ cm}$  or  $2 \mu\text{m}$  of electrolyte but the latter could save computational time.

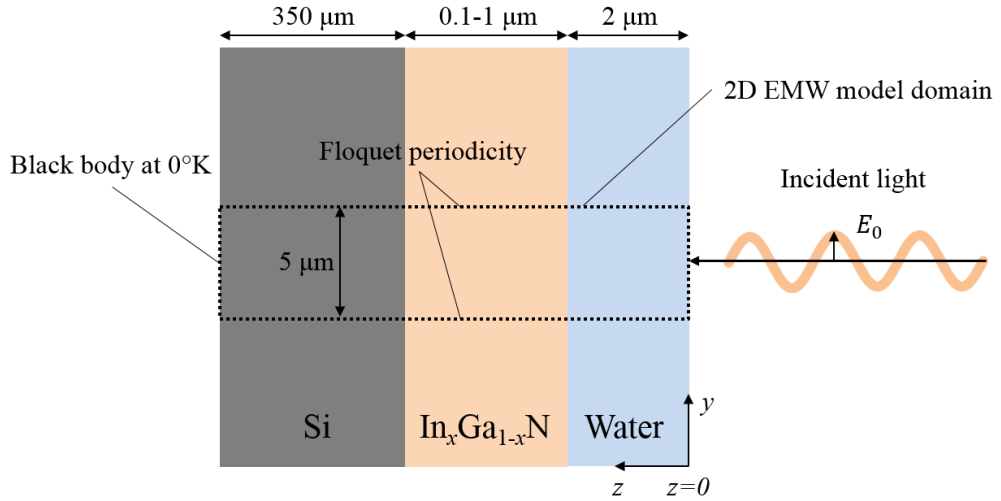


**Fig. 5.1.** Scheme of the numerical 2D EMW propagation model domain for an  $\text{In}_x\text{Ga}_{1-x}\text{N}/\text{Si}$  tandem water-splitting photoelectrode (not to scale).

## 5: Theoretical maximum efficiency and performance characterization of $\text{In}_x\text{Ga}_{1-x}\text{N}/\text{Si}$ tandem water-splitting photoelectrodes

---

The current in series tandem cell such as  $\text{In}_x\text{Ga}_{1-x}\text{N}/\text{Si}$  photoelectrode is limited by the lowest subcell current. Thus, the highest photogeneration efficiency of a tandem cell is obtained with an equal photogenerated current in all subcells and is given by

$$\eta = \min(i_{l,\text{In}_x\text{Ga}_{1-x}\text{N}}, i_{l,\text{Si}})/i_0, \quad (5.2)$$

where  $i_{l,\text{In}_x\text{Ga}_{1-x}\text{N}}$  is the photogenerated current density in the  $\text{In}_x\text{Ga}_{1-x}\text{N}$  subcell,  $i_{l,\text{Si}}$  is the photogenerated current density in the Si subcell. The incident photocurrent density of AM1.5G was considered without UV light ( $\lambda_{\text{ph}} > 400 \text{ nm}$ ) being  $59.7 \text{ mA cm}^{-2}$ . The photogeneration efficiency of  $\text{In}_x\text{Ga}_{1-x}\text{N}/\text{Si}$  tandem photoelectrodes was investigated by varying the thickness and the indium content, consequently the bandgap, of  $\text{In}_x\text{Ga}_{1-x}\text{N}$ . The thickness of  $\text{In}_x\text{Ga}_{1-x}\text{N}$  was varied from 10 nm to 1000 nm with an indium content varying from 17 % to 59 % that corresponds to an optical bandgap of 2.6 eV and 1.2 eV (Table 5.1), a region with a theoretical solar-to-hydrogen (STH) efficiency above 5 % for tandem water-splitting cells[16]. Films below 50 nm were investigated to determine if  $\text{In}_x\text{Ga}_{1-x}\text{N}$  ultrathin film could benefit from resonant light trapping effect. Indeed,  $\text{In}_x\text{Ga}_{1-x}\text{N}$  ultrathin film would greatly reduce the amount of indium and gallium, two relatively expensive and rare material, and reduce loss due to poor minority charge conductivity or high bulk recombination[221]. The theoretical photogeneration efficiency was also calculated without any reflection loss at the  $\text{In}_x\text{Ga}_{1-x}\text{N}/\text{electrolyte}$  interface—by simply removing the electrolyte layer in front of the  $\text{In}_x\text{Ga}_{1-x}\text{N}$  film (Fig. 5.1)—to account for an anti-reflective coating.

The complex refractive index of  $\text{In}_x\text{Ga}_{1-x}\text{N}$  required in the EMW propagation model was linearly interpolated from Hazari et al.[222]. The complex refractive indexes of  $\text{In}_x\text{Ga}_{1-x}\text{N}$  with the indium content of the photoelectrodes made in this work,  $x=9.5 \%$ ,  $16.5 \%$ ,  $23.5 \%$ ,  $33.3 \%$ , and  $41.4 \%$ , are depicted in Fig. 5.2. The data of the complex refractive index of single crystalline silicon were taken from Edwards[223].

## 5: Theoretical maximum efficiency and performance characterization of $\text{In}_x\text{Ga}_{1-x}\text{N}/\text{Si}$ tandem water-splitting photoelectrodes

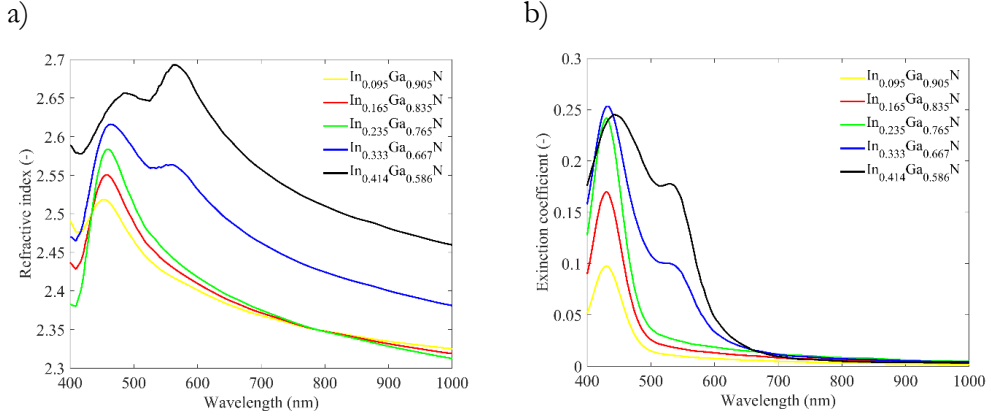


**Fig. 5.2.** a) Spectral refractive index and b) extinction coefficient of  $\text{In}_x\text{Ga}_{1-x}\text{N}$  interpolated from the data of Hazari et al.[222].

**Computational details.** The wavelengths used for the EMW model were varied from 400 nm to 1116 nm that corresponds respectively to the first visible wavelength and the bandgap of Si (1.11 eV=1116 nm). The light below 400 nm was not considered in this work because the complex refractive index of  $\text{In}_x\text{Ga}_{1-x}\text{N}$  was only available between 400 nm to 1687 nm[222]. The light was considered as transverse electric and therefore only the out-of-plane electric field was calculated. Bloch-Floquet theory was assumed for the periodicity on both side of the computational domain (Fig. 5.1) which is typically used for infinite slab models where no boundary effects appear and where the phase shift is determined by a wave vector and the distance between the source and the destination[80], [81]. The Maxwell's curl equations and the generation rate given by eqns (1.1) and (1.2) were solved with a commercial software[77]. Convergence was obtained with a direct MUMPS solver. A relative tolerance of  $10^{-4}$  in the electric field was used as convergence criteria. Mesh convergence was obtained for linear mesh discretization, i.e. a piecewise linear finite element basis functions, with size ratio of 4 and element numbers,  $n_{\text{el}}$ , depending on the irradiation wavelength,  $\lambda$ , and the layer thickness,  $d$ :  $n_{\text{el}} = d \cdot \beta / \lambda$  with  $\beta = 150$  for Si,  $\beta = 200$  for  $\text{In}_x\text{Ga}_{1-x}\text{N}$  and  $\beta = 30$  for water. The number of mesh elements perpendicularly to the direction of light propagation was fixed to 5 with a width of 5  $\mu\text{m}$ . We observed that for planar problems, the solver was less robust using cubic or quadratic discretization order, leading to fluctuations of the electric field in the perpendicular direction of propagation. On the other hand, linear



## 5: Theoretical maximum efficiency and performance characterization of $\text{In}_x\text{Ga}_{1-x}\text{N}/\text{Si}$ tandem water-splitting photoelectrodes

---

discretization needed finer mesh but the calculation time was still reduced compared to quadratic or cubic discretization with a coarser mesh.

### 5.2.2. Performance and characteristics of $\text{In}_x\text{Ga}_{1-x}\text{N}$ photoelectrodes

We investigated in this work only the performance and characteristics of  $\text{In}_x\text{Ga}_{1-x}\text{N}$  photoanode since Si water-splitting photocathodes has been already highly studied[185], [192], [224]–[227]. Linear sweep voltammetry with chopped light was undertaken under 1 M  $\text{H}_2\text{SO}_4$  and 1 M  $\text{Na}_2\text{SO}_3$  as hole scavenger. The hole scavenger is used to provide a photocurrent to highly increase the reaction kinetic at the  $\text{In}_x\text{Ga}_{1-x}\text{N}/\text{electrolyte}$  interface. The diffusion length,  $L$ , the diffusion optical number,  $\alpha_{500}L$ , the ratio of current,  $R_{S,V_{\text{IPCE}}}$ , the nanostructuring opportunity factor,  $f_{\text{nano}}$ , the surface recombination loss, the reflection loss, and the bulk loss of  $\text{In}_x\text{Ga}_{1-x}\text{N}$  photocathodes were determined by using the software POPE[213]. However, POPE requires measuring the IPCE spectra of the photoelectrode as well as the following parameters: the complex refractive index, the bandgap, the flatband potential, the doping concentration, the relative permittivity, and the thickness of the photoelectrode. The complex refractive index of  $\text{In}_x\text{Ga}_{1-x}\text{N}$  was linearly interpolated from the data of Hazari et al.[222] and are presented in Fig. 5.2. The bandgap of  $\text{In}_x\text{Ga}_{1-x}\text{N}$  was calculated by Vegard's law with a bowing parameter of 2.5 eV and bandgaps of 0.7 eV and 3.4 eV for InN and GaN[215], respectively, given by

$$E_{\text{gap}, \text{In}_x\text{Ga}_{1-x}\text{N}} = 0.7x + 3.4(1 - x) - 2.5x(1 - x). \quad (5.3)$$

The flatband potential and the doping concentration were obtained from Mott-Schottky analysis. The equivalent circuit depicted in Fig. 5.7 was used to fit the measured impedance spectra.  $R_s$  in the equivalent circuit is the series resistance of the electrolyte and the semiconductor.  $R_{sc}$  and  $C_{sc}$  are the resistance and the capacitance in the space charge region (SCR).  $R_{ss}$  and  $C_{ss}$  are the resistance and the capacitance caused by interface states at the semiconductor–electrolyte interface. This equivalent circuit is usually used for photoelectrodes with species adsorption at the semiconductor-electrolyte interface and was previously used for n-type GaN[94], only the Warburg diffusion element,  $W$ , was added as for pyrite photoelectrodes[228]. The Warburg diffusion element is typically used for the diffusion of charges to a large planar electrode as for  $\text{In}_x\text{Ga}_{1-x}\text{N}$  photoelectrodes[9]. Indeed, the presence of very high doping concentration in  $\text{In}_x\text{Ga}_{1-x}\text{N}$

## 5: Theoretical maximum efficiency and performance characterization of $\text{In}_x\text{Ga}_{1-x}\text{N}/\text{Si}$ tandem water-splitting photoelectrodes

---

photoelectrodes[229] reduce the SCR to only few nanometers—below 1 nm for  $\text{In}_x\text{Ga}_{1-x}\text{N}$  and an applied potential of 1.23  $\text{V}_{\text{RHE}}$ —and therefore most of the photogenerated charges are transported by diffusion. The relative permittivity of  $\text{In}_x\text{Ga}_{1-x}\text{N}$  depending on the indium content was linearly interpolated from the relative permittivity of GaN and InN, given by[218]

$$\varepsilon_r(x) = 8.9(1 - x) + 10.5x. \quad (5.4)$$

The thickness of the  $\text{In}_x\text{Ga}_{1-x}\text{N}$  photoelectrodes were measured by scanning electron microscopy (SEM).

Here, we briefly introduce the parameters obtained by POPE and used to characterize the performance of  $\text{In}_x\text{Ga}_{1-x}\text{N}$  photoelectrodes. The diffusion optical number is given by eqn (4.1). The ratio of current,  $\alpha_{500}L$ , is the ratio of the surface charge transfer velocity that contributes to the water-splitting reaction,  $S_T$ , and the sum of the surface recombination velocity,  $S_R$ , and  $S_T$ , given by eqn (4.3). The ratio of currents,  $R_{S,V_{\text{IPCE}}}$ , is given for a fixed potential at which the IPCE is measured,  $V_{\text{IPCE}}$ . This parameter evaluates the ratio between surface recombination and charge transfer. For  $R_{S,V_{\text{IPCE}}} = 1$ , no surface recombination is occurring at the semiconductor-electrolyte interface and for  $R_{S,V_{\text{IPCE}}} = 0$  there is no photocurrent and electron-hole pairs are fully recombining at the interface. The nanostructuring opportunity factor is only valid for flat photoelectrodes (not nanostructured photoelectrodes) and is given by eqn (4.5). More details on these parameters can be found in section 4.2.1.

### 5.2.3. Experimental details

***$\text{In}_x\text{Ga}_{1-x}\text{N}$  sample preparation.***  $\text{In}_x\text{Ga}_{1-x}\text{N}$  was deposited on a sapphire (0001) substrate by plasma-assisted molecular beam epitaxy[215] with a highly doped layer of GaN as buffer. The ohmic contacts were made with indium in contact with the highly doped layer of GaN beneath the  $\text{In}_x\text{Ga}_{1-x}\text{N}$  layer. Copper wire were fixed to the indium with conductive silver paint. Photoelectrode's edges and ohmic contacts were then covered by white opaque epoxy (Fig. 5.3). The ohmic contacts were tested by measuring the resistance between two ohmic contacts separated by a distance of 3 mm. The resistance was always below 16  $\Omega$  ensuring a negligible contact resistance (Table A5.1).

## 5: Theoretical maximum efficiency and performance characterization of $\text{In}_x\text{Ga}_{1-x}\text{N}/\text{Si}$ tandem water-splitting photoelectrodes

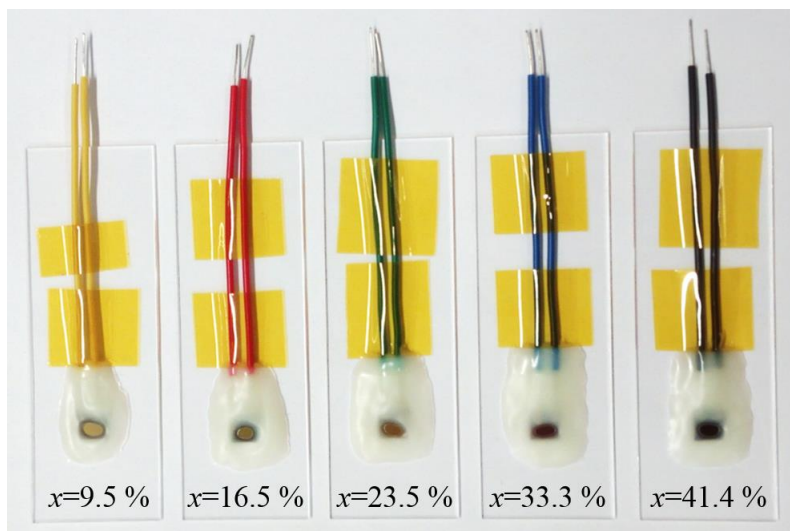


**Fig. 5.3.** Image of the prepared  $\text{In}_x\text{Ga}_{1-x}\text{N}$  photoelectrodes. The different copper wire colors corresponds to the different indium content: yellow for  $x=9.5\%$ , red for  $x=16.5\%$ , green for  $x=23.5\%$ , blue for  $x=33.3\%$ , and black for  $x=41.4\%$  as given in [Table 5.1](#).

**Indium content and thickness measurements.** The indium content of  $\text{In}_x\text{Ga}_{1-x}\text{N}$  was measured by X-ray diffraction (XRD) ([Fig. A5.1](#)). The thickness of the  $\text{In}_x\text{Ga}_{1-x}\text{N}$  photoelectrode is the average of three thicknesses measured using the cross-sectional view of SEM images ([Fig. 5.4](#)).

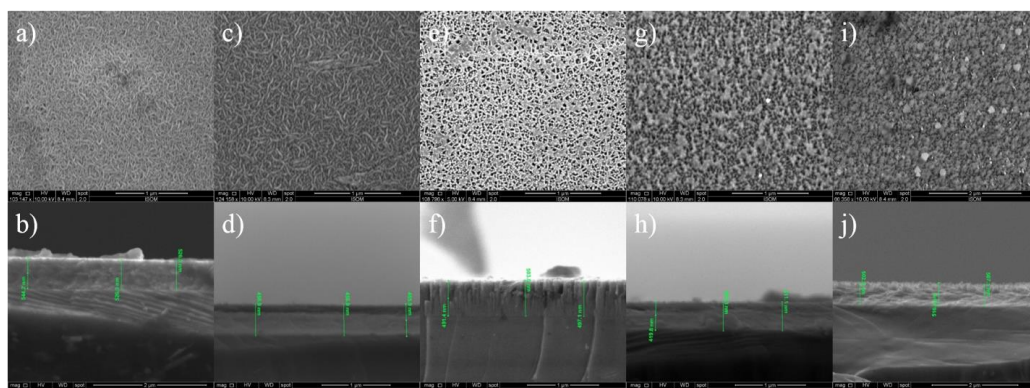


**Fig. 5.4.** Top and cross-sectional view scanning electron microscopy images of: (a), b)  $\text{In}_x\text{Ga}_{1-x}\text{N}$  with  $x=9.5\%$ ; (c), d)  $\text{In}_x\text{Ga}_{1-x}\text{N}$  with  $x=16.5\%$ ; (e), f)  $\text{In}_x\text{Ga}_{1-x}\text{N}$  with  $x=23.5\%$ ; (g), h)  $\text{In}_x\text{Ga}_{1-x}\text{N}$  with  $x=33.3\%$ ; (i), j)  $\text{In}_x\text{Ga}_{1-x}\text{N}$  with  $x=41.4\%$ .

## 5: Theoretical maximum efficiency and performance characterization of $\text{In}_x\text{Ga}_{1-x}\text{N}/\text{Si}$ tandem water-splitting photoelectrodes

---

**PEC experimental setup and measurements.** Electrochemical experiments were carried out in a three-electrode setup to refer the potential of our measurements to the reversible hydrogen electrode. The reference electrode was Ag/AgCl (sat. KCl) and the counter electrode was Pt. The aqueous electrolyte solution was 1 M  $\text{H}_2\text{SO}_4$  and 1 M  $\text{Na}_2\text{SO}_4$ . The  $I$ - $V$  curves were obtained using linear sweep voltammetry with a varying voltage rate of  $10 \text{ mV s}^{-1}$  in the range of 0.5 to 1.5  $\text{V}_{\text{RHE}}$ . The voltage rate of  $10 \text{ mV s}^{-1}$  gave a stable steady-state current without any photocurrent hysteresis. To ensure that  $\text{In}_x\text{Ga}_{1-x}\text{N}$  photoelectrodes were stable within the time of our measurements (below 5 min), chronoamperometry of GaN photoelectrode at 1.23  $\text{V}_{\text{RHE}}$  under AM1.5G was undertaken. The photocurrent dropped only after 4 h ensuring that stability was not an issue for our measurements (section A5.2). The electrochemical impedance spectra were measured under dark conditions in 1 M  $\text{H}_2\text{SO}_4$  at potentials varying from 0.4 to -0.6  $\text{V}_{\text{RHE}}$  with a potential step of 50 mV and covering a frequency from 10 Hz to 20 kHz with 10 measures per frequency decade.

IPCE spectra were measured at 1.23  $\text{V}_{\text{RHE}}$  from 300 nm to 900 nm in 1 M  $\text{Na}_2\text{SO}_4$  as a hole scavenger to achieve measurable photocurrents. However, the lowest wavelength used by the POPE software was 420 nm because it provided better R-square values of the numerical and experimental IPCEs fitting. Indeed, the R-square was 0.9 starting from a wavelength of 420 nm apart for  $x=9.5 \%$  with a R-square of 0.5 compared to R-square values below 0 for  $x=9.5 \%$  starting from 400 nm (the limit of the available refractive index data depicted in Fig. 5.2).

### 5.3. Results and discussion

#### 5.3.1. Photogeneration efficiency of $\text{In}_x\text{Ga}_{1-x}\text{N}/\text{Si}$ tandem photoelectrodes

The photogeneration efficiencies for varying  $\text{In}_x\text{Ga}_{1-x}\text{N}$  film thicknesses and bandgaps are depicted in Fig. 5.5. The photogeneration efficiencies for varying  $\text{In}_x\text{Ga}_{1-x}\text{N}$  film thicknesses and indium contents are depicted in Fig. A5.1. The theoretical maximum efficiency of 27 % is slightly lower than the previous prediction of 31 % for  $\text{InGaN}/\text{Si}$  solar cells[219]. This difference is caused by the reflection loss at the  $\text{In}_x\text{Ga}_{1-x}\text{N}/\text{electrolyte}$  interface that is not present for  $\text{In}_x\text{Ga}_{1-x}\text{N}/\text{Si}$  solar cells. The photogenerated current density at the maximum efficiency of 27 % is  $16.8 \text{ mA cm}^{-2}$  (compared to  $59.7 \text{ mA cm}^{-2}$  at 100 %). Two regions with maximum efficiency can be observed, a region with low bandgap 1.2-1.4 eV (indium content of 59-51 %) and low film thickness 300-550 nm, and a second region with a bandgap

## 5: Theoretical maximum efficiency and performance characterization of $\text{In}_x\text{Ga}_{1-x}\text{N}/\text{Si}$ tandem water-splitting photoelectrodes

of 1.5 eV ( $x=47\%$ ) and film thickness of 700-900 nm. The low bandgap region corresponds to a photogeneration efficiency limited to the photogenerated current in the Si subcell. Indeed, a top cell bandgap of 1.2-1.4 eV can absorb most of the light and its thickness must be reduced to let enough light reaching the bottom Si subcell. By contrast, the efficiency of the 1.5 eV bandgap region is limited by  $\text{In}_x\text{Ga}_{1-x}\text{N}$  subcell and therefore its thickness must be increased up to 700 nm. The maximum theoretical efficiency can only be obtained for  $\text{In}_x\text{Ga}_{1-x}\text{N}$  bandgaps between 1.2 eV and 1.5 eV, out of the optimal range of 1.6-1.8 eV (indium content of 37-44 %) for top cells in tandem photoelectrochemical device[216] with Si as bottom cell. The maximum photogeneration efficiency of  $\text{In}_x\text{Ga}_{1-x}\text{N}$  bandgaps between 1.6-1.8 eV can reach 23.5 % with a bandgap of 1.6 eV and a thickness of 1  $\mu\text{m}$ . The photogeneration efficiency is between 19.5 % to 23.5 % for  $\text{In}_x\text{Ga}_{1-x}\text{N}$  bandgaps between 1.6-1.8 eV with a thickness of at least 1000 nm (Fig. 5.5.a). Reducing the thickness will reduce the efficiency down to an efficiency of 6 % at a bandgap of 1.8 eV and a thickness of 100 nm. At a thickness of 500 nm, the photogeneration efficiency is between 16-19.5% for bandgaps between 1.6-1.8 eV.

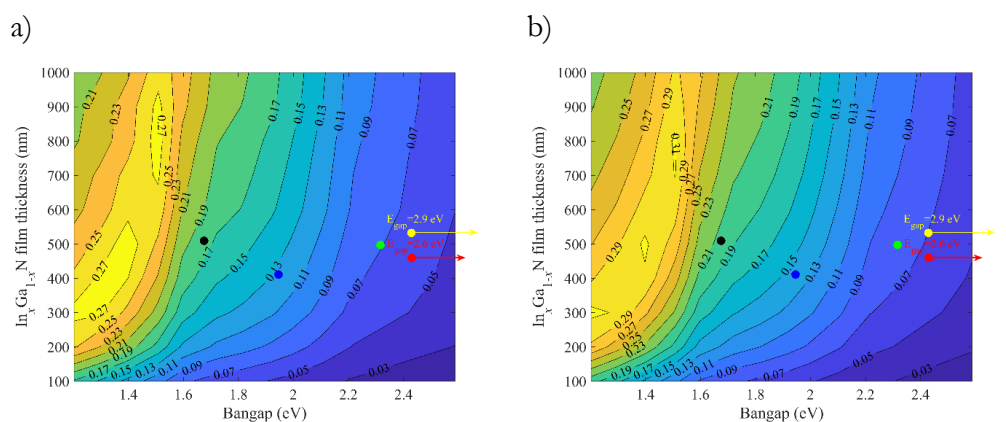


**Fig. 5.5.** Photogeneration efficiency of  $\text{In}_x\text{Ga}_{1-x}\text{N}/\text{Si}$  tandem water-splitting photoelectrode depending on film thickness and bandgap a) with and b) without reflection loss at the  $\text{In}_x\text{Ga}_{1-x}\text{N}/\text{water}$  interface.

The photogeneration efficiency considering a perfect anti-reflective coating without any reflection loss at the  $\text{In}_x\text{Ga}_{1-x}\text{N}/\text{electrolyte}$  interface is depicted in Fig. 5.5.b. The maximum efficiency goes up to 31 % with a current density of  $18.7 \text{ mA cm}^{-2}$ , 3 % more than the efficiency including the reflection loss. Two maximum efficiency

## 5: Theoretical maximum efficiency and performance characterization of $\text{In}_x\text{Ga}_{1-x}\text{N}/\text{Si}$ tandem water-splitting photoelectrodes

---

regions can be observed as for Fig. 5.5.a, a first region with low bandgaps between 1.2-1.4 eV and low film thicknesses of 300-550 nm, and a second region with a bandgap of 1.5 eV and film thicknesses between 700-900 nm.

The generation rates of ultrathin  $\text{In}_x\text{Ga}_{1-x}\text{N}$  film on Si film showed clear interference between forward and backward EMW propagating waves (Fig. A5.5) but no resonant light trapping effect were observed since the photogeneration efficiency was only decreasing by reducing the thickness (Fig. A5.6). Indeed, resonant light trapping effect occurs for ultrathin film deposited on a highly reflective material such as gold or silver. The refractive index of Si is  $n=3.55\text{-}5.59$  for visible light that is too high to enhance resonant light trapping in contrast to gold with  $n=0.04\text{-}0.09$  or silver with  $n=0.1\text{-}1.67$ .

### 5.3.2. Performance characteristics of $\text{In}_x\text{Ga}_{1-x}\text{N}$ photoelectrodes

***I-V curves of  $\text{In}_x\text{Ga}_{1-x}\text{N}$  photoanodes.*** The  $I-V$  curves of  $\text{In}_x\text{Ga}_{1-x}\text{N}$  photoanodes with chopped light in 1 M  $\text{H}_2\text{SO}_4$  and 1 M  $\text{Na}_2\text{SO}_4$  are depicted in Fig. 5.6. The fact that the photocurrent density at 1.23  $V_{\text{RHE}}$  1 M  $\text{H}_2\text{SO}_4$  decreases under higher indium content is in conflict with the generated charge carriers that increases with higher indium content since the bandgap decreases (Fig. 5.6.a). In contrast, the photocurrent density at 1.23  $V_{\text{RHE}}$  in 1 M  $\text{Na}_2\text{SO}_4$  does not decrease with the indium content but neither does it follow a continuous increase. Indeed, the photocurrent density increases from  $x=9.5\%$  to 16.5 %, then decreases at  $x=23.5\%$  and increases again with a maximum photocurrent density at  $x=41.4\%$ , i.e. a photocurrent density of 1.9  $\text{mA cm}^{-2}$  at 1.23  $V_{\text{RHE}}$ . The photocurrent drops from 1.1  $\text{mA cm}^{-2}$  to 0.6  $\text{mA cm}^{-2}$  at 1.23  $V_{\text{RHE}}$  with the indium content varying from 16.5 % to 23.5 % in conflict with the doping concentration decreasing, i.e. the doping concentration decreases from  $1.4 \cdot 10^{22} \text{ cm}^{-3}$  to  $9.8 \cdot 10^{20} \text{ cm}^{-3}$  with respect to the indium content varying from 16.5 % to 23.5 % (Fig. 5.7 and Table 5.1).

A lower doping concentration leads usually to a reduction of the bulk[155] and surface[230] recombinations, as well as a higher minority charge mobility[154] and a larger SCR width, all factors supposed to affect positively the photocurrent[70] in contradiction with the current observation. The decrease of the photocurrent in 1 M  $\text{H}_2\text{SO}_4$  with increasing indium content and the irregular variation of the photocurrent depending on the indium content in 1 M  $\text{Na}_2\text{SO}_4$  appears to be correlated to the surface roughness of the photoelectrode. The surface roughness of  $\text{In}_x\text{Ga}_{1-x}\text{N}$  films appears to increase continuously with the indium content as depicted in top view



## 5: Theoretical maximum efficiency and performance characterization of $\text{In}_x\text{Ga}_{1-x}\text{N}/\text{Si}$ tandem water-splitting photoelectrodes

SEM images (Fig. 5.4). Thus, we think that the photocurrent decreases in 1 M  $\text{H}_2\text{SO}_4$  electrolyte because of increasing effective surface area causing higher surface recombination. The situation is different using a hole scavenger since the surface recombination is decreased by boosting the charge transfer kinetic and thus the surface roughness might play a smaller role. However, we can observe a correlation between the surface structure and the photocurrent in 1 M  $\text{Na}_2\text{SO}_4$ . A worm-like surface structure is present for indium contents of 9.5 % and 16.5 % with a coarser surface for  $x=16.5$  % (Fig. 5.4.a, b, c, and d). Since the surface is similar for both indium contents, the photocurrent is mostly driven by the indium content, i.e. a higher indium content provides a smaller bandgap and thus a larger photocurrent as observed in Fig. 5.6.b. The surface structure at  $x=23.5$  % is different from all the other ones. This surface structure is composed of holes covering the entire surface with a depth of around one third of the  $\text{In}_x\text{Ga}_{1-x}\text{N}$  film thickness (Fig. 5.4.e and f). This surface structure might be causing the low photocurrent in 1 M  $\text{Na}_2\text{SO}_4$ , a photocurrent similar to the one at  $x=9.5$  % (Fig. 5.6.b) even if the bandgap is 2.3 eV for  $x=23.5$  % and 2.9 eV for  $x=9.5$  % (Table 5.1). This hypothesis is later confirmed by the determination of the ratio of currents. A grain-like surface structure is present for  $x=33.3$  % and  $x=41.4$  %. Since the surface is similar, the photocurrent increases with the indium content as for  $x=9.5$  % and 16.5 %.

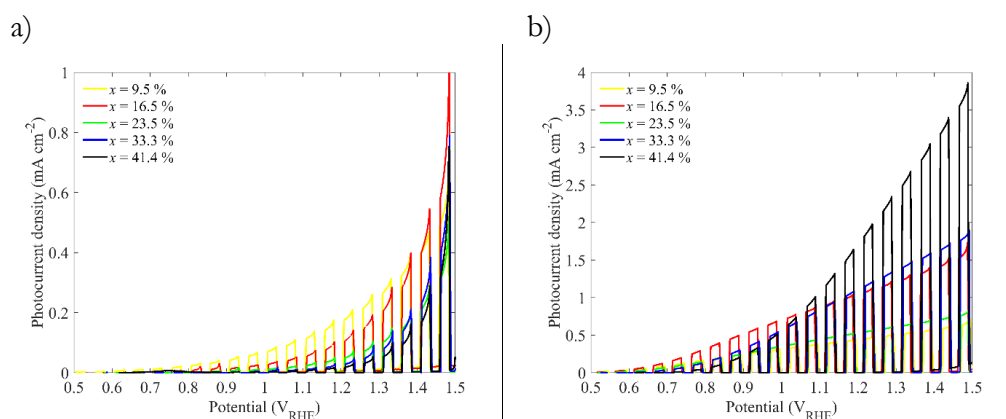


**Fig. 5.6.** Photocurrent–voltage curves of  $\text{In}_x\text{Ga}_{1-x}\text{N}$  photoelectrodes with chopped light in a) 1 M  $\text{H}_2\text{SO}_4$  and b) 1 M  $\text{Na}_2\text{SO}_4$ .

**Flatband and doping concentration of  $\text{In}_x\text{Ga}_{1-x}\text{N}$  photoanodes.** The flatband potential and the doping concentration for varying indium content is depicted in

## 5: Theoretical maximum efficiency and performance characterization of $\text{In}_x\text{Ga}_{1-x}\text{N}/\text{Si}$ tandem water-splitting photoelectrodes

**Fig. 5.7.** More details on the Mott-Schottky analysis can be found in the supporting information. The lowest flatband potential is  $-0.33 \text{ V}_{\text{RHE}}$  and is obtained at an indium content of 9.5 %. The doping concentration are very high for all indium contents, between  $8.1 \cdot 10^{20} \text{ cm}^{-3}$  ( $x=33.3 \%$ ) and  $1.9 \cdot 10^{22} \text{ cm}^{-3}$  ( $x=9.5 \%$ ). The high doping concentration of  $\text{In}_x\text{Ga}_{1-x}\text{N}$  is probably the main cause for the low efficiency of these photoelectrodes. As previously mentioned, a high doping concentration causes a reduction of the minority charge mobility[154] and an increase of the bulk[155] and surface recombinations[230]. Moreover, the SCR width being below 1 nm at doping concentration  $\geq 8.1 \cdot 10^{20} \text{ cm}^{-3}$ , the charge carriers are driven by diffusion and not by migration, which further reduces the performance of the photoelectrodes. Thus, the high doping concentration should be addressed in priority to increase the efficiency of  $\text{In}_x\text{Ga}_{1-x}\text{N}$  photoelectrodes. Lowering the doping concentration could also prolong the charge carriers lifetime as observed for GaN in the work of Kumano et al.[231]. However, Kumano et al. used indium as a dopant material for GaN. Thus, indium atoms are either present to produce  $\text{In}_x\text{Ga}_{1-x}\text{N}$  either present as dopants. It becomes obvious that controlling or reducing the doping concentration of  $\text{In}_x\text{Ga}_{1-x}\text{N}$  is very challenging.

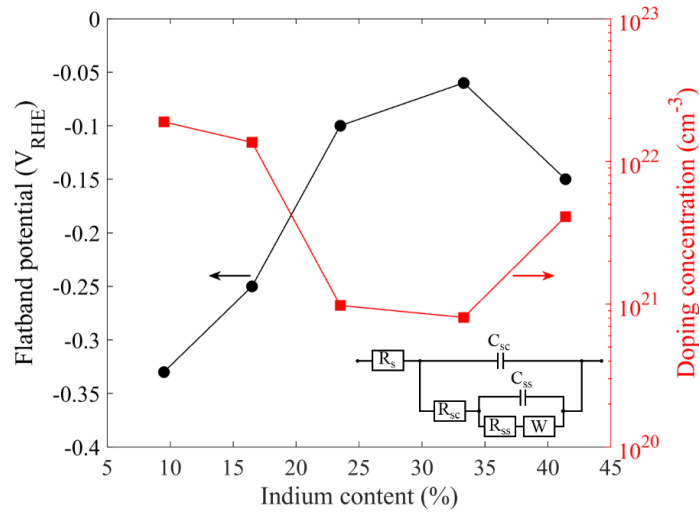


**Fig. 5.7.** Flatband potential and doping concentration of  $\text{In}_x\text{Ga}_{1-x}\text{N}$  water-splitting photoelectrodes determined by Mott-Schottky plots (A5.4). The equivalent circuit for the electrochemical impedance spectra fit is also indicated.



## 5: Theoretical maximum efficiency and performance characterization of $\text{In}_x\text{Ga}_{1-x}\text{N}/\text{Si}$ tandem water-splitting photoelectrodes

**Diffusion lengths, diffusion optical numbers, ratio of currents, and nanostructuring opportunity factors.** Table 5.1 summarizes the different material parameters required for the software POPE to determine the diffusion length, the diffusion optical number, the ratio of currents and the nanostructuring opportunity factor (eqns (4.1)-(4.5)).

The different parameters to characterize the performance of  $\text{In}_x\text{Ga}_{1-x}\text{N}$  photoelectrodes calculated by POPE are given in Table 5.2. The highest diffusion length, 262 nm, is obtained for an indium content of 23.5 %, then comes  $x=33.3$  % with a diffusion length of 158 nm, 32 nm for  $x=9.5$  %, 16 nm for  $x=41.4$  %, and finally 11 nm for  $x=16.5$  %. Since the  $\text{In}_x\text{Ga}_{1-x}\text{N}$  photoelectrode at  $x=23.5$  % presents surface nanostructures, the diffusion length is not the actual diffusion length but a projected diffusion length as well as for  $x=33.3$  % and  $x=41.4$  % (Fig. 5.4). However, the doping concentration at  $x=41.4$  % is higher than for  $x=23.5$  % and  $x=33.3$  % that might cause a reduction of the diffusion length.

**Table 5.1.** Numerical values of the material parameters of  $\text{In}_x\text{Ga}_{1-x}\text{N}$  water-splitting photoelectrodes used as inputs for POPE[213].

Parameters	$x=9.5$ %	$x=16.5$ %	$x=23.5$ %	$x=33.3$ %	$x=41.4$ %	Unit
Attributed color	yellow	red	green	blue	black	-
Relative permittivity, $\epsilon_r$	9.1	9.2	9.3	9.4	9.6	-
Band gap, $E_{\text{gap}}$	2.9	2.6	2.3	1.9	1.7	eV
Flatband potential, $V_{\text{FB}}$	-0.33	-0.25	-0.1	-0.06	-0.15	$V_{\text{RHE}}$
Donor concentration, $N_D^+$	$1.9 \cdot 10^{22}$	$1.4 \cdot 10^{22}$	$9.8 \cdot 10^{20}$	$8.1 \cdot 10^{20}$	$4.1 \cdot 10^{21}$	$\text{cm}^{-3}$
Thickness, $d$	532	460	497	411	509	nm
Wavelength's range	420-460	420-477	400-539	400-653	400-729	

## 5: Theoretical maximum efficiency and performance characterization of $\text{In}_x\text{Ga}_{1-x}\text{N}/\text{Si}$ tandem water-splitting photoelectrodes

**Table 5.2.** Calculated diffusion length, diffusion optical number, nanostructuring opportunity factor, and ratio of currents of  $\text{In}_x\text{Ga}_{1-x}\text{N}$  photoelectrodes.

Parameters	$x=9.5\%$	$x=16.5\%$	$x=23.5\%$	$x=33.3\%$	$x=41.4\%$
$L$ (nm)	32	11	262	158	16
$\alpha_{500}L$ (-)	0.012	0.007	0.244	0.431	0.074
$R_{S,V_{\text{IPCE}}}$ (-)	1	0.96	0.07	0.16	0.93
$f_{\text{nano}}$ (-)	3.2	3.4	1.9	1.6	2.4

The experimental and numerical IPCE spectra with internal, reflection, and surface recombination losses are given in Fig. A5.9. The diffusion optical number and the ratio of currents are key parameters to understand the performance of  $\text{In}_x\text{Ga}_{1-x}\text{N}$  photoelectrodes in 1 M  $\text{Na}_2\text{SO}_4$  (Fig. 5.6.b). The diffusion optical number is maximized at  $x=23.5\%$  in accordance with the diffusion length (Fig. 5.8 and Table 5.2). However, the ratio of current is highly decreased at  $x=23.5\%$  to reach a value of 0.07, i.e. the surface recombination is significantly reducing the photocurrent and the IPCE. Indeed, the presence of surface nanostructures at  $x=23.5\%$  increases the effective diffusion optical number but also increases the semiconductor-electrolyte interface area and thus the surface recombination. Moreover, it appears that the hole scavenger ( $\text{Na}_2\text{SO}_4$ ) is unable to cancel the surface recombination probably because of the high doping concentration and the high surface roughness. Thus, the increase of the surface recombination,  $R_{S,V_{\text{IPCE}}}=0.07$ , at  $x=23.5\%$  ( $E_{\text{gap}}=2.3$  eV) leads to an overall reduction of the photocurrent density compared to  $x=16.5\%$  with  $R_{S,V_{\text{IPCE}}}=0.96$  even if the photogeneration current and the diffusion length is increased compared to  $x=16.5\%$  ( $E_{\text{gap}}=2.6$  eV) in accordance with the  $I$ - $V$  curves (Fig. 5.6). High surface recombinations are only significantly present for  $x=23.5\%$  and  $x=33.3\%$  (Fig. 5.8 and Fig. A5.9) in accordance with the surface roughness, observable on the SEM images (Fig. 5.4). Aside of the special case of  $\text{In}_x\text{Ga}_{1-x}\text{N}$  photoelectrodes at  $x=23.5\%$ , the photocurrent current in 1 M  $\text{Na}_2\text{SO}_4$  increases with the bandgap decreasing, i.e. a photocurrent increasing from  $E_{\text{gap}}=2.9$  eV ( $x=9.5\%$ ) to  $E_{\text{gap}}=2.6$  eV ( $x=16.5\%$ ), and from  $E_{\text{gap}}=1.9$  eV ( $x=33.3\%$ ) to  $E_{\text{gap}}=1.7$  eV ( $x=41.4\%$ ).

Finally, the nanostructuring opportunity factors of  $\text{In}_x\text{Ga}_{1-x}\text{N}$  photoelectrodes were investigated and showed that only  $\text{In}_x\text{Ga}_{1-x}\text{N}$  photoelectrodes at  $x=23.5\%$  and  $x=33.3\%$  were below two (Table 5.2) and could perform with an internal quantum efficiency higher than 95 % by nanostructuring (eqn (4.5)). However, these photoelectrodes are already partially nanostructured—presence of wells at the surface reaching one third of the thickness of  $\text{In}_x\text{Ga}_{1-x}\text{N}$  photoelectrodes with

## 5: Theoretical maximum efficiency and performance characterization of $\text{In}_x\text{Ga}_{1-x}\text{N}/\text{Si}$ tandem water-splitting photoelectrodes

$x=23.5\%$  (Fig. 5.4)—and thus does not strictly follow the nanostructuring opportunity factor that is only valid for flat photoelectrodes. Thus, none of the  $\text{In}_x\text{Ga}_{1-x}\text{N}$  photoelectrodes can perform well even with nanostructuring as long as the synthesis method is not modified to reduce the doping concentration. Indeed, only a maximum photocurrent density of  $1.9\text{ mA cm}^{-2}$  at  $1.23\text{ V}_{\text{RHE}}$  in  $1\text{ M Na}_2\text{SO}_4$  (Fig. 5.6) was obtained at a bandgap of  $1.7\text{ eV}$  ( $x=41.4\%$ ) with negligible surface recombination ( $R_{\text{S},V_{\text{IPCE}}}=0.93$ , see Table 5.2 and Fig. A5.9), much below the theoretical maximum of  $23.8\text{ mA cm}^{-2}$  for a semiconductor with a bandgap of  $1.7\text{ eV}$ .

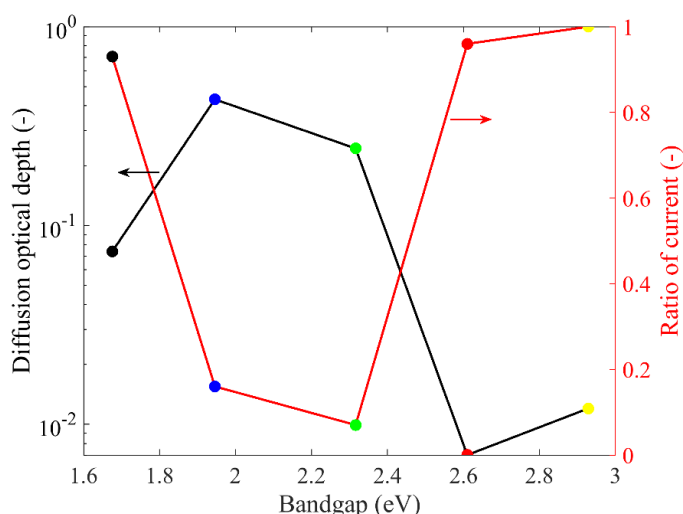


**Fig. 5.8.** Diffusion optical number ( $y_1$ -axis) and the ratio of current ( $y_2$ -axis) of  $\text{In}_x\text{Ga}_{1-x}\text{N}$  photoelectrodes in function of the bandgap (indium content). The dot colors corresponds to the indium content according to Table 5.1 and Fig. 5.3.

### 5.4. Conclusion

Tunable bandgap photoelectrode materials can be a route to highly efficient and cheap PEC water-splitting devices. A theoretical maximum efficiency of  $27\%$  was calculated for  $\text{In}_x\text{Ga}_{1-x}\text{N}/\text{Si}$  tandem photoelectrodes with reflection loss at the semiconductor-electrolyte interface for an indium content between  $50\%$  and  $60\%$  (bandgap between  $1.2\text{ eV}$  and  $1.4\text{ eV}$ ) and a film thickness between  $280\text{ nm}$  and  $560$

## 5: Theoretical maximum efficiency and performance characterization of $\text{In}_x\text{Ga}_{1-x}\text{N}/\text{Si}$ tandem water-splitting photoelectrodes

---

nm. A maximum efficiency of 31 % was obtained without any surface reflection loss. Despite the high theoretical efficiency of  $\text{In}_x\text{Ga}_{1-x}\text{N}/\text{Si}$  tandem photoelectrode, our fabricated  $\text{In}_x\text{Ga}_{1-x}\text{N}$  photoelectrodes with an indium content varying from 9.5 % to 41.4 % led to a maximum photocurrent density of only  $1.9 \text{ mA cm}^{-2}$  at  $1.23 \text{ V}_{\text{RHE}}$  with a hole scavenger as electrolyte for  $x=41.4$  %. This photocurrent density represents only 8 % of the maximum theoretical photocurrent density of  $23.8 \text{ mA cm}^{-2}$  for a semiconductor with a bandgap of 1.7 eV. Furthermore, we observed that the surface morphology plays a key role for the performance of  $\text{In}_x\text{Ga}_{1-x}\text{N}$  photoanode. Indeed,  $\text{In}_x\text{Ga}_{1-x}\text{N}$  with  $x=23.5$  % presented a higher nanostructured surface than  $x=16.5$  % causing a higher surface recombination loss and an overall lower photocurrent density in 1 M  $\text{Na}_2\text{SO}_4$  even if the diffusion length for  $x=23.5$  % was 262 nm and the bandgap 2.3 eV and the diffusion length for  $x=16.5$  % was 11 nm and the bandgap 2.6 eV. These results were obtained by using the software POPE combined with SEM images, experimental IPCE, and Mott-Schottky analysis. This combination proved to be a powerful approach to investigate the performance of  $\text{In}_x\text{Ga}_{1-x}\text{N}$  photoelectrodes and can be applied in the future to any emerging water-splitting photoelectrodes presenting surface nanostructures.

Finally, we calculated that  $\text{In}_x\text{Ga}_{1-x}\text{N}$  photoelectrodes with the actual synthesis method is not efficient even if nanostructured. We attributed the low performance of  $\text{In}_x\text{Ga}_{1-x}\text{N}$  photoelectrodes to the extremely high doping concentration, i.e. a doping concentration of  $4.1 \cdot 10^{21} \text{ cm}^{-3}$  for  $x=41.4$  % that led to a diffusion length of only 16 nm and a diffusion optical number of 0.074, more than two orders of magnitude below  $\alpha_{500} L_{0.95}$ . Therefore, the doping concentration must be reduced in priority to increase the efficiency of  $\text{In}_x\text{Ga}_{1-x}\text{N}$  photoanodes. This reduction might be achieved by optimizing the synthesis method to reduce indium donor dopants or by using another synthesis method such as physical vapor deposition. Furthermore, the diffusion length (or the diffusion optical number) should be further increased by nanostructuring the entire film thickness and not only one third of the thickness as for  $x=23.5$  % to achieve high performance. However, the increase of surface recombination caused by the nanostructuring should be addressed by the deposition of a passivation layer and co-catalysts.

## Conclusion

This work provides material and mesostructural design guidelines for more efficient morphologically complex photoelectrodes and a method to optimize rapidly the performance of photoelectrodes. The developed numerical models are at the core of this work and covers atomistic-scale calculation with DFT calculations to determine bulk material properties, continuum meso- and macro-scale simulation by FVM numerical model and analytical IPCE model. Their applicability to any redox reaction such as water splitting or CO<sub>2</sub> reduction and their ability to integrate atomistic and macro-scale opens a new range of questions that can be investigated. Detailed 3D modeling of the exact mesoscale morphology with bulk material parameters can be tackled applying the FVM model presented in chapter 1 to provide key material parameters and their impact on the performance. Moreover, this model can provide material and mesostructural design guidelines of morphologically complex photoelectrode such as particle-based LTON photoelectrode (chapters 2 and 3). The rapid screening model using effective material parameters presented in chapter 4 allow determining the nanostructuring opportunity of emerging photoelectrodes and their improvement by modifying the doping concentration. All these models focus on the same physical principles, namely light absorption, charge generation, transport, and recombination in the bulk and at the semiconductor-electrolyte interface. A good understanding of these model's limitations is required to orient future research to the appropriate numerical model or extend the developed models. Here, these models and their limitations are briefly summarized.

The electron-hole pairs generation rates in photoelectrodes were calculated by an EMW propagation model solving the Maxwell's curl equation with FVM and by solving analytically the Beer-Lambert law. The EMW propagation model enables the investigation of nanostructured photoelectrodes as well as thin film with interferences between the forward and backward-propagating waves. Its most useful usage in this work was to calculate the photogeneration efficiency of tandem

$\text{In}_x\text{Ga}_{1-x}\text{N}/\text{Si}$  PEC water splitting device with  $\text{In}_x\text{Ga}_{1-x}\text{N}$  film thickness varying from 10 nm to 1000 nm (chapter 5). Indeed, the presence of significant forward and backward-waves interferences in the generation rate of  $\text{In}_x\text{Ga}_{1-x}\text{N}$  could only be calculated by solving the Maxwell's equation. The same model was applied to flat GaN and particle-based LTON photoanodes but the Beer-Lambert law was proven sufficient to determine the generation rate inside these photoanodes and could save significant calculation power. Although the calculation of the generation rate inside the exact morphology of LTON photoanode was not undertaken in this work because of significant additional modeling efforts, this calculation would have been only possible with the EMW propagation model. Indeed, a simplified LTON photoanode morphology was used for which the Beer-Lambert law was sufficient, i.e. a thin film with an absorption coefficient as function of the particle density in chapters 2 and 3. Moreover, the exact reflection loss was determined experimentally by spectrophotometry. Therefore, the Beer-Lambert law should be used for flat thick photoelectrodes or to have a first estimation of the generation in highly morphologically complex photoelectrode. However, the EMW propagation model should be used for thin films, resonant light trapping films, or relatively simple meso- or nano-structured photoelectrodes.

The charge transport for GaN and LTON photoanodes was investigated by solving the drift-diffusion equation combined with the Poisson's equation to account for the influence of the electrostatic potential present in the SCR (chapters 1, 2, and 3). The charge carrier concentration was given by integrating the product of the Fermi–Dirac distribution and the density of states over all possible states. For a non-degenerated semiconductor, the charge carrier concentration could be simplified by using the Maxwell– Boltzmann distribution instead of the Fermi–Dirac distribution (chapter 1). The set of PDEs were solved by FVM using MUMPS for the fully coupled variables (hole concentration, electron concentration, and potential) in 1D for GaN and 2D for LTON photoelectrodes. The highly nonlinear PDEs requires expensive calculations and small potential step of 5 mV to reach convergence for the calculation of the  $I$ - $V$  curves. This modeling framework—developed in chapter 1 and extended in chapters 2 and 3—should be combined ideally with an EMW model to investigate in detail the influence of the exact morphology on the photoelectrode performance (chapters 2 and 3) or to quantify the impact on the performance of a specific parameter such as the minority charge carrier mobility. In contrast, the IPCE model developed in chapter 4 is limited to a 1D morphology since the model is based on a 1D analytical solution of the charge transport and recombination in the photoelectrode. Moreover, the charge transport and recombination is combined in

a single parameter, the diffusion length. Furthermore, the model only accounts for minority charge carriers. Thus, the impact of the morphology, the majority charge carriers, the mobility or the lifetime, cannot be investigated with this model. However, nanostructured photoelectrode can still be investigated using the IPCE model since it determines a projected diffusion length, i.e. a larger diffusion length than the bulk one that accounts for the shorten minority charge carrier path (chapter 4). The IPCE model should be used with priority for the investigation of novel photoelectrode material. If the material shows good performance further investigations could be undertaken with the FVM model to identify the key material parameters and morphological properties and their impact on the photoelectrode performance.

The charge recombination in the FVM model accounted for bulk and surface SRH recombination, direct recombination, and Auger recombination for GaN photoanode (chapter 1). For LTON, only bulk and surface SRH recombination were considered since they are the main recombination process in photoelectrodes (chapters 2 and 3). For both materials, the bulk and surface SRH recombination were combined into a single SRH recombination process by the use of an effective lifetime. This simplification avoided the need to determine surface and bulk lifetimes but also prevented separation of the two recombination processes. Moreover, the bulk and the surface recombinations were assumed to follow a recombination through a single discrete surface state energy level, which might not be the case for most photoelectrodes. Indeed, a single surface state provides a photocurrent increasing from the offset potential to the saturation current potential within 0.2 V. Whereas, the presence of continuous surface state energy level provides usually a slower increase of  $\sim 1$  V [60]. In contrast, our IPCE model presented in chapter 4 considers continuous surface state energy level recombination. This model allows separating the surface recombination loss and the internal loss. Indeed, the surface recombination is calculated by the ratio of currents (section 4.2.1) while the internal loss by the diffusion length that accounts for carrier mobility and lifetime. Since the method based on this model determines the ratio of currents and the diffusion length, the losses caused by surface recombination or internal recombination can be separately calculated. This separation is only possible using the effective lifetime if the bulk lifetime is known as for example GaN (chapter 1). The FVM model using effective lifetime should be used to investigate for example the impact of the photoelectrode morphology but the effective lifetime should be modified according to the change in the surface area of the photoelectrode. In contrast, the IPCE model cannot do such investigation since it is 1D model. However, a detail investigation of

surface recombination with continuous surface states recombination can only be undertaken using the IPCE model but must be applied to a flat photoelectrode. A strategy to include continuous surface states recombination in the FVM model is presented in the next section.

The charge transfer at the semiconductor-electrolyte interface (or semiconductor-catalyst-electrolyte interface) was modeled by using an adaptive Schottky contact (chapter 1) with the flatband potential and the interfacial hole transfer velocity as relevant material parameter. Thus, this model is limited to an applied potential dropping only in the SCR. In contrast, a potential drop occurring in the HL (Fermi level pinning) has been observed for photoelectrode with continuous surface states energy level[127] and cannot be modelled with the adaptive Schottky contact used in this work. However, by artificially reducing the interfacial hole transfer velocity, holes accumulate and recombine in the SCR and the impact on the  $I$ - $V$  curves becomes similar as the one observed for photoelectrode with Fermi level pinning, i.e. a photocurrent reaching saturation within  $\sim 1$  V and not 0.2 V as previously mentioned. Similarly, the model presented in chapter 4 does not account for Fermi level pinning but the  $I$ - $V$  curves can follow the one of a photoelectrode with Fermi level pinning by accounting for continuous surface states energy level recombination. The following section provides strategies to account for Fermi-level pinning and continuous surface states recombination in future modeling work.

### Prospects

***Modelling of semiconductor-surface states-catalyst-electrolyte system.*** The charge transfer at a semiconductor-electrolyte interface can follow different paths as mentioned in chapter 1. These paths are depicted in Fig. C1: i) direct charge transfer from the semiconductor surface to the electrolyte ii) surface state mediated charge transfer and iii) tunneling charge transfer from the SCR to the electrolyte. Tunneling charge transfer might only occur under high doping concentration where the SCR thickness becomes so thin that bulk photogenerated charge carriers can directly tunnel through the potential barrier. Currently, the numerical model developed in chapter 1 only considers a direct charge transfer without considering any species concentration or mass transport limitation in the electrolyte (path 3 and 4 to the SS energy level only, Fig. C1). Basically, the charge transfer follows a Schottky contact with an experimentally determined band bending[104]. The combination of surface state current between the bands and the surface state, and a Butler-Volmer current between the surface state and the electrolyte has only been implemented at this stage



## Conclusion and prospects

for majority current with a simplified analytical solution (section 1.2.3). A similar approach could be undertaken by converting the minority current at the semiconductor-electrolyte interface to a majority current as long as the Fermi level remains within the surface states energy level (Fig. C1). Thus, the dark current used in eqn (1.32) would be proportional to the surface states density and the applied potential drop in the HL could be determined. Furthermore, the interface current could account for redox species concentration through a modified Butler-Volmer equation containing redox species concentration dependencies[67]. The governing equations of chemical species transport and reactions in the electrolyte are well known[8], [9], [67] and have been previously studied[68]. The surface state mediated charge transfer process is more complex than the direct charge transfer process since the change in the HL potential depends on the photocurrent[51], [52].

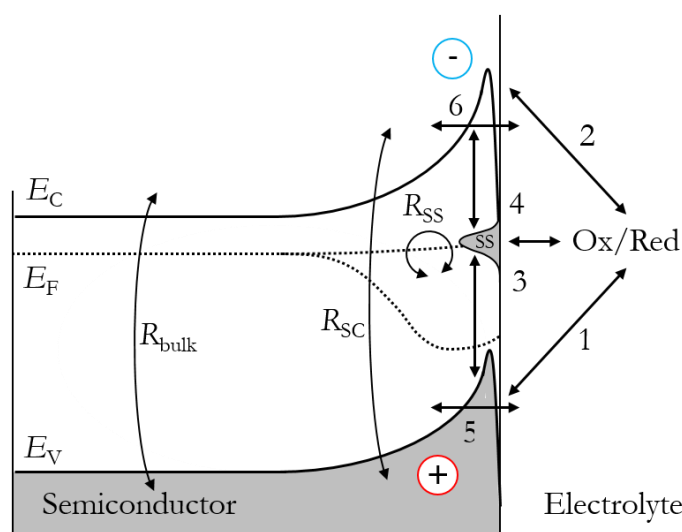


**Fig. C1.** Energy band diagram of a n-type semiconductor with p-type surface states including the different current paths at the semiconductor-electrolyte interface: 1) direct hole transfer 2) direct electron transfer 3) surface state mediated hole transfer 4) surface state mediated electron transfer 5) space charge tunneling hole transfer 6) space charge tunneling electron transfer.  $R_{\text{bulk}}$  stands for bulk recombination,  $R_{\text{sc}}$  for SCR recombination, and  $R_{\text{ss}}$  for surface states recombination.

The tunneling currents from the SCR to the electrolyte and their effect on the overall photocurrent could be implemented[232]. Furthermore, surface recombination at the semiconductor-electrolyte interface separated from the bulk and SCR

recombination could be implemented by either a single surface trap level [73] either continuous or distributed surface traps levels. The combination of these different charge transfer paths to determine the effect of surface states, ionized chemical species concentration and doping concentration on the photocurrent density is still missing and could bring additional fundamental understanding of the semiconductor-electrolyte interface.

***Diffusion and migration contribution dependency of the photoelectrode thickness and particle size.*** In conventional photoelectrode—a photoelectrode thicker than the Debye length (see **Conventional photoelectrodes**)—the band bending is fully developed and the main contribution to the photocurrent results from migration of the minority charge carriers. The majority charge carriers only compensate minority charge carriers leaving the semiconductor at the semiconductor-electrolyte interface but are not limiting the photocurrent (chapter 2). However, the band bending cannot fully develop for photoelectrode or particle size below the Debye length. In this case, the diffusion transport influence significantly the photocurrent as well as the majority charge transport mobility. This situation is similar to a photoelectrode with a low doping concentration ( $\leq 10^{16} \text{ cm}^{-3}$ ). Indeed, the SCR width becomes sufficiently large to observe the influence of the majority carrier mobility, i.e. a low mobility will significantly reduce the photocurrent in contrast to photoelectrode with higher doping concentration (chapter 2). The numerical model presented in chapter 1 already accounts for the diffusion and migration of charge carriers. Therefore, the influence of the photoelectrode thickness or particle size on the contribution of the diffusion and migration charge transport could be investigated. Moreover, the size limit of the nanostructured photoelectrode at which the front-side illumination becomes higher than the back-side illumination because of majority charge transport limitation could be determined. Such investigation could clarify or even fully elucidate the front to back photocurrent ratio above 1 for nanostructured  $\text{BiVO}_4$  photoelectrode that is currently attributed to a region of trap free transport close to the FTO glass substrate[170].

***Charge transport mechanism under varying light concentration.*** Under concentrated irradiance, traps in metal oxides could be filled by the photoexcited charges. The charge transport mechanism would shift from an electron hopping transport to a transport of electrons of the valence band. This shift could be observed by an increase of the diffusion length under higher light concentration. The IPCE of a metal oxide photoelectrode such as hematite could be measured under varying light concentration[16]. Then, this IPCE combined with the free software

POPe presented in chapter 4 could be used to determine the diffusion length under varying light concentration. Such an investigation could be beneficial for further understanding of the charge transport mechanism in metal oxide and could potentially lead to cheap and stable photoelectrode such as hematite highly performing under concentrated irradiance.

**Improvement of LTON photoelectrode.** Further investigations should be undertaken to improve the efficiency by increasing the particle density of particle-based LTON photoelectrode in contact with the FTO glass substrate (chapters 3 and 4). New conductive network design with different conductive material to connect particles directly with the FTO should be developed such as the deposition of co-catalyst layer over all the particles. Using co-catalysts transparent to the visible light would allow measuring front-side illumination and front to back photocurrent ratio. Furthermore, the influence of the co-catalyst layer thickness on the performance under front- and back-side illumination could determine if this layer only improves the reaction kinetic or actually provides a conductive network to connect upper particles to the FTO glass substrate.

**Photoelectrode stability.** The durability of photoelectrode materials has not been considered in this work although it is a key factor for cost-effective and industrial scale hydrogen production[41]. Nevertheless, the method developed in chapter 4 could be used in combination with IPCE measurements at different operating times (for example *in-operando*) to evaluate the chronological change in surface recombination, internal or reflection losses. The ability to capture the chronological change of each loss could greatly enhance the understanding of degradation phenomena and their effects on material properties. Moreover, the durability could be quantified and used as an additional criterion to evaluate the performance of a photoelectrode material.

**Improvement of  $\text{In}_x\text{Ga}_{1-x}\text{N}$  photoanodes.** The poor efficiency of  $\text{In}_x\text{Ga}_{1-x}\text{N}$  photoanodes was attributed to the high doping concentration that highly limits the diffusion length (chapter 5.3.2). Thus, the doping concentration must be reduced in priority. This reduction might be achieved by adding an acceptor dopant during the material synthesis to compensate the indium donor dopant. Furthermore, the diffusion length (or the diffusion optical number) should be further increased by nanostructuring the entire film thickness and not only one third of the thickness as for  $x=23.5\%$  to achieve high performance. However, the increase of surface recombination caused by nanostructuring should be addressed by the deposition of a passivation layer and a co-catalyst. Furthermore, a protective layer should be

deposited for the stability of  $\text{In}_x\text{Ga}_{1-x}\text{N}$ . Indeed, nitride semiconductors immersed in an electrolyte corrode under illumination.

Overall, essential material and mesostructural design guidelines for morphologically complex photoelectrodes with enhanced performance have been proposed. A method to determine the nanostructuring opportunity of emerging photoelectrodes was developed and applied to a large variety of water-splitting photoelectrodes. The different numerical models and experimental approaches presented in this thesis can serve as a platform for further understanding of the multi-physical mechanisms occurring in photoelectrodes and more specifically at the beautifully complex semiconductor-electrolyte interface. The full understanding of these mechanisms are the path to highly efficient and stable PEC water-splitting devices.

# Appendix of chapter 1

## A1.1. Numerical model boundary conditions

### A1.1.1. Majority current

For a majority current, i.e an electron current in the case of a n-type material, the applied potential dropped in the SCR and HL, and, consequently,  $\Delta\phi_H$  is not equal zero. We developed a simple analytical solution presented below to determine  $\Delta\phi_H$  depending on the applied potential.

A constant difference between conduction band and Fermi level over the applied potential is assumed. The current densities in eqns (1.20) and (1.21) are rewritten in terms of the potential difference in the SCR,  $\Delta\phi_{sc}$ :

$$\mathbf{i}_n \cdot \hat{\mathbf{n}} = -qv_{s,n}n_{eq}(e^{-\Delta\phi_{sc}/V_{th}} - 1) = -i_n^0(e^{-\Delta\phi_{sc}/V_{th}} - 1), \quad (A1.1)$$

$$\mathbf{i}_p \cdot \hat{\mathbf{n}} = qv_{s,p}p_{eq}(e^{\Delta\phi_{sc}/V_{th}} - 1) = i_p^0(e^{\Delta\phi_{sc}/V_{th}} - 1), \quad (A1.2)$$

where the electron and hole dark current densities are defined as  $i_n^0 = qv_{s,n}n_{eq}$  and  $i_p^0 = qv_{s,p}p_{eq}$ . Note that the current densities shown in eqns (A1.1) and (A1.2) are similar to valence and conduction band currents derived from Marcus theory or quantum mechanical theory for weak interactions[53].

In the case of majority current in a n-type semiconductor material, the band bending is negative ( $\Delta\phi_{sc} < 0$ ) and the hole current negligible. If we assume  $\Delta\phi_{sc} < -0.12V$ , the total current given by the electron current density in eqn (A1.1) can be rewritten by:

$$\mathbf{i}_n \cdot \hat{\mathbf{n}} = i_{sc} = -i_n^0 e^{-\Delta\phi_{sc}/V_{th}}. \quad (A1.3)$$

Less than 1% error in the current appears when using this equation at  $\Delta\phi_{sc} = -0.12V$  and the error decreases exponentially for smaller potentials (<0.05% error at  $\Delta\phi_{sc} = -0.2V$ ).

With the current conservation presented in eqn (1.22), the current in the electrolyte must be equal to the current in the semiconductor at steady-state operation. The corresponding current in the electrolyte follows a Butler-Volmer equation and in terms of an HL potential difference,  $\Delta\phi_H$ , is given by[8], [9]:

$$i_H = i_{H_2}^0 \left( e^{\frac{(1-\alpha)\Delta\phi_H}{V_{th}}} - e^{-\frac{\alpha\Delta\phi_H}{V_{th}}} \right). \quad (A1.4)$$

In the case of n-type GaN and downward band bending, the exchange current density is the hydrogen evolution reaction exchange current density,  $i_{H_2}^0$ . The charge transfer coefficient,  $\alpha$ , is typically around  $\alpha \approx 0.5$ [9]. It should be noted that eqn (A1.4) does not take redox species concentration into account as we consider an electrolyte with high conductivity and without mass transport limitation. For downward band bending, the HL potential drop is negative and the anodic current becomes quickly negligible (<1% error on the current density at  $\Delta\phi_H = -0.06V$ ) and eqn (A1.4) can be rewritten as a Tafel equation[9]:

$$i_H = -i_{H_2}^0 e^{-\frac{\alpha\Delta\phi_H}{V_{th}}}. \quad (A1.5)$$

With the current conservation (eqn (1.22)) and the potential drop equality (eqn (1.29)), the HL potential difference in case of downward band bending was given in terms of an applied potential by:

$$\Delta\phi_H(V_a) = \frac{v_{th} \ln\left(\frac{i_{H_2}^0}{i_n^0}\right) + V_a}{1+\alpha} < 0. \quad (A1.6)$$

The applied potential has to be at least below -0.18 V according to eqn (1.29) and with  $\Delta\phi_{sc} < -0.12$  V and  $\Delta\phi_H < -0.06$  V.

### A1.2. Experimental details

All measured potentials against Ag/AgCl sat. KCl were converted to the reversible hydrogen electrode (RHE) according to the Nernst equation[233]:

$$E_{RHE} = E_{Ag/AgCl} + 0.059\text{pH} + E_{Ag/AgCl}^0 \quad (A1.7)$$

where  $E_{RHE}$  is the converted potentials vs. RHE,  $E_{Ag/AgCl}$  is the experimentally measured potential of Ag/AgCl sat. KCl and  $E_{Ag/AgCl}^0$  is the potential of Ag/AgCl vs the standard hydrogen electrode (SHE) and equals +0.197 V at 25°C[234]. An aqueous electrolyte of 1 M H<sub>2</sub>SO<sub>4</sub> (pH=0) was used as the electrolyte.

The spectral irradiance of the UV LED used as a light source is depicted in Fig. A1.1.

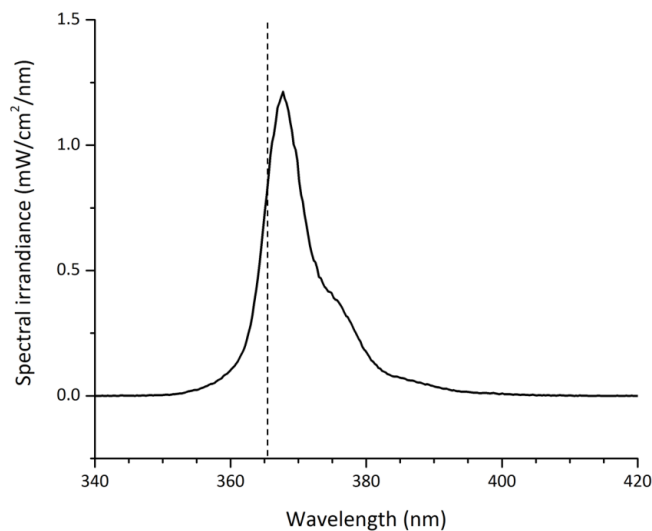


**Fig. A1.1.** Spectral irradiance of the UV LED used for the experimental measurements. Only the part of the LED spectrum below 365.6 nm is absorbed by GaN (dashed line).

The photocurrents were stable for the first few runs of cyclic voltammetry (6 min) as depicted in Fig. A1.2 before seeing the effect of photocorrosion.

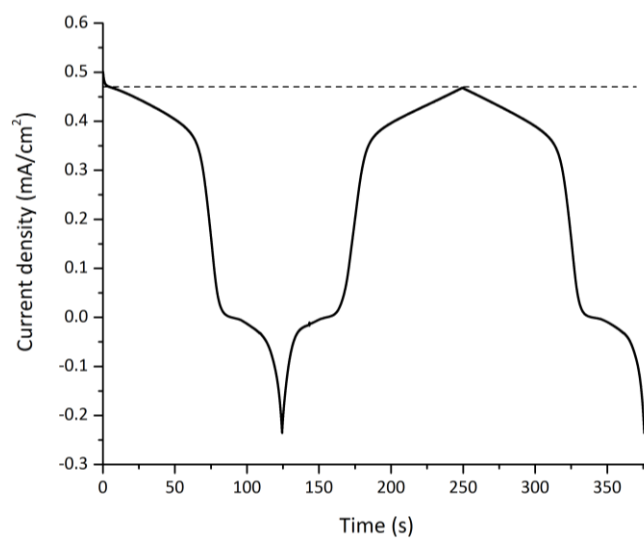


**Fig. A1.2.** Current density versus time during linear sweep voltammetry. Potential sweep from  $1.7 V_{RHE}$  to  $-0.8 V_{RHE}$ . The dashed line indicates the current density at  $t = 0$ .



### A1.3. Numerical model – detailed results

For the reference cases (parameters indicated in Table 1.1 and Table 1.2), the electron-hole pair generation rate in the semiconductor is depicted in Fig. A1.3. The generation rate profile follows an exponential decrease similarly to the Beer-Lambert's law.

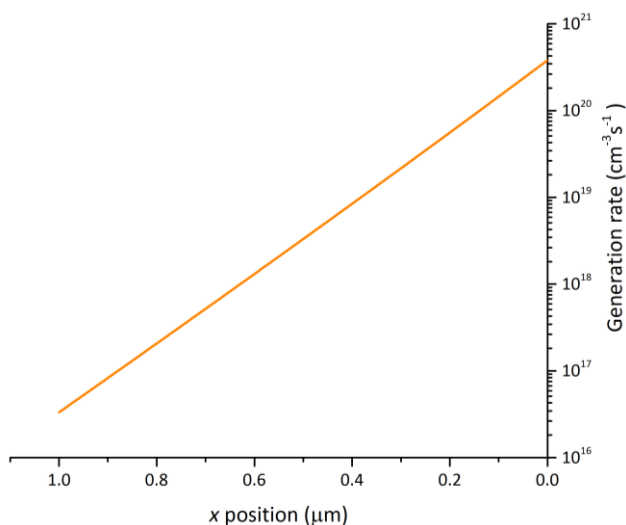


**Fig. A1.3.** Numerical results of the electron-hole pair generation rate inside the semiconductor. The right side at 0  $\mu\text{m}$  is the illuminated side with the semiconductor-electrolyte interface and the left side at 1  $\mu\text{m}$  is the ohmic back contact (according to Fig. 1.1).

The depth-dependent electron and hole concentration in the semiconductor at a potential of 0  $V_{\text{RHE}}$  is depicted in Fig. A1.4. At the ohmic contact ( $x=1 \mu\text{m}$ ), the hole concentration is zero because GaN is naturally n-doped and the ohmic contact assumes local thermodynamic equilibrium. The electron concentration equals the doping concentration  $4 \cdot 10^{16} \text{ cm}^{-3}$  in the bulk of the semiconductor according to Poisson's equation (see eqn (1.4)) since the charge density is zero and the hole concentration is negligible as depicted in Fig. A1.4. In the space charge region, the electron concentration drops while the hole concentration increases as depicted in Fig. A1.5. The hole concentration is higher than the electron concentration at the semiconductor-electrolyte interface ( $x=0$ ) and therefore the minority current dominates at the interface.

The band potential diagram at a potential of 0  $V_{\text{RHE}}$  is depicted in Fig. A1.5. The quasi-Fermi potentials are split inside the entire semiconductor due to the generation rate profile inside the semiconductor (see Fig. A1.3) and because n-d-GaN does not contain any acceptors. The quasi-Fermi potentials only unite at the ohmic contact where there is thermodynamic equilibrium.

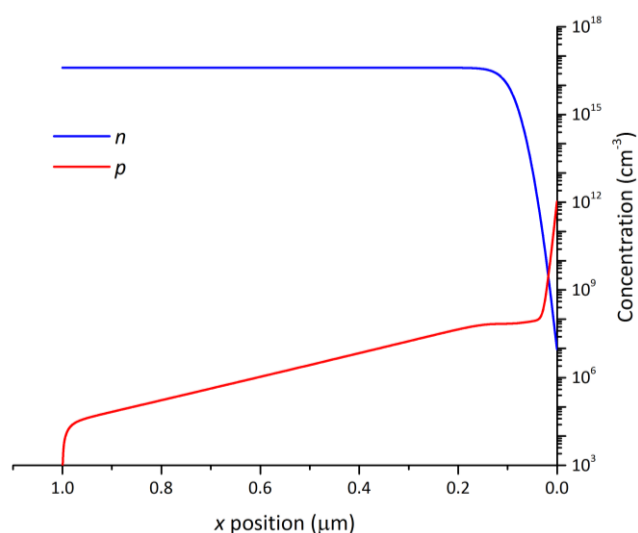


**Fig. A1.4.** Numerical results of the electron (blue line) and hole (red line) concentration at 0  $V_{\text{RHE}}$  inside the semiconductor. The right side at 0  $\mu\text{m}$  is the illuminated side with the semiconductor-electrolyte interface and the left side at 1  $\mu\text{m}$  is the back ohmic contact (according to Fig. 1.1).

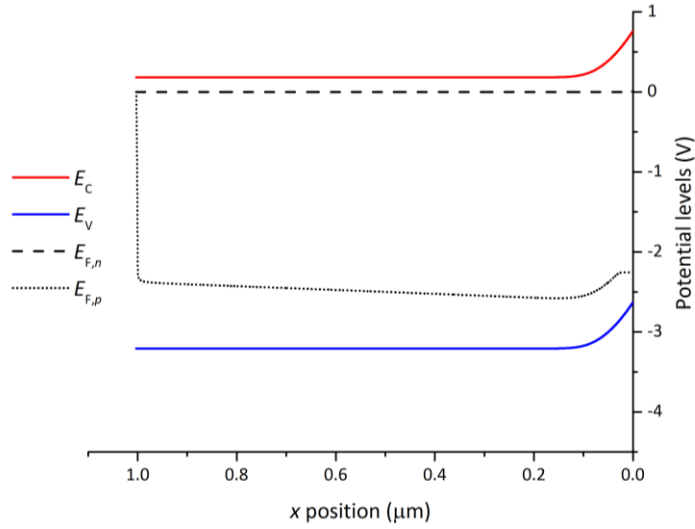


**Fig. A1.5.** Numerical results of the band potential diagram at 0 V<sub>RHE</sub> with conduction band (red line), valence band (blue line), electron and hole quasi-Fermi potential (dashed and dotted lines respectively) inside the semiconductor. The right side at 0 μm is the illuminated side with the semiconductor-electrolyte interface and the left side at 1 μm is the back ohmic contact (according to Fig. 1.1).

# A1.4. Parametric analysis on key factors

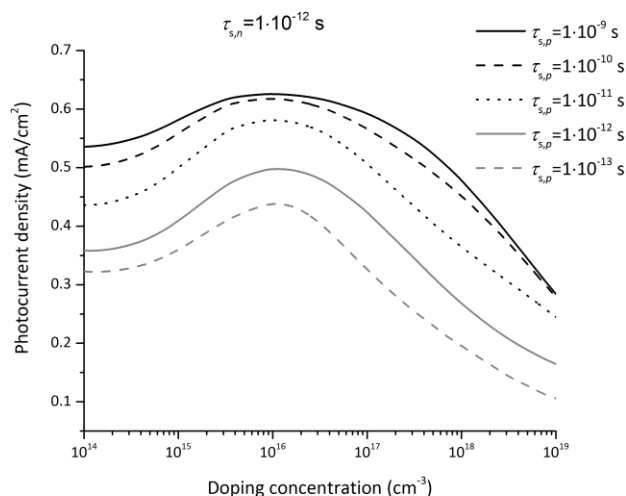


**Fig. A1.6.** Photocurrent density at 1.23 V<sub>RHE</sub> as a function of the doping concentration for various hole surface lifetimes ( $\tau_{s,p} = 10^{-9}$ ,  $10^{-10}$ ,  $10^{-11}$ ,  $10^{-12}$ ,  $10^{-13}$  s) and an electron surface lifetime of 1 ps. An optimum doping concentration appeared at  $1 \cdot 10^{16}$  cm<sup>-3</sup>.

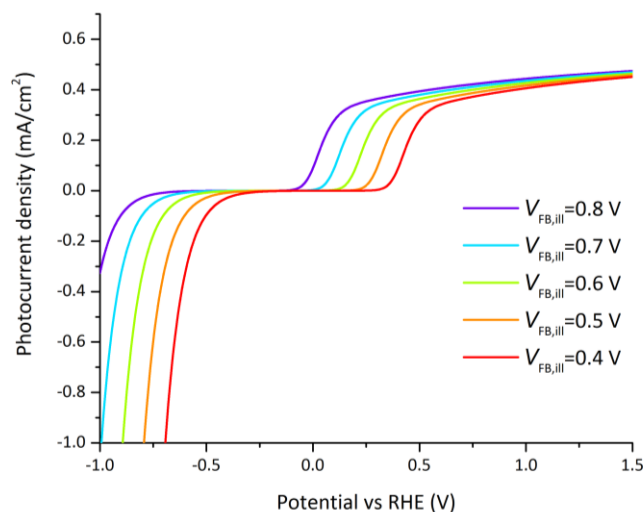


**Fig. A1.7.** Photocurrent-voltage curves for varying flatband potentials for the reference case (parameters indicated in Table 1.1 and Table 1.2).

## Appendix of chapter 2

## A2

### A2.1. Quantitative structural analysis of LTON particle-based PEs

Nominal sizes of particles were determined by using digitalized meso-structure information obtained by focused ion beam scanning electron microscopy data. Ellipse were fitted into the individual particles and the main axis dimensions were recorded to obtain their frequency distributions[125] (Fig. A2.1). A log-normal distribution was fit to the three particle dimensions' frequency distribution curves.

The extracted particle orientations of LTON particle-based PEs are depicted in Fig. A2.2. The orientation was determined based on the vector of the longest axis of the fitted ellipse with respect to the FTO substrate's surface normal. The calculated averaged angle is  $37.4^\circ$  for all particles with center point within the bottom  $1\text{ }\mu\text{m}$  of the film's thickness.

The density of LTON photoelectrodes deposited on FTO by electrophoretic deposition was determined by integrating the volumes of the different phases (Fig. A2.3).[125]

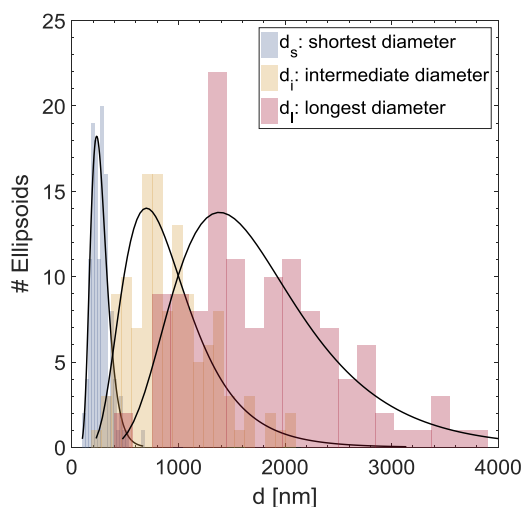


**Fig. A2.1.** Size distribution of the three ellipsoid diameters based on lognormal distributions:  $d_{s,\text{mean}}=272$  nm,  $d_{s,\text{SD}}=88$  nm;  $d_{i,\text{mean}}=932$  nm,  $d_{i,\text{SD}}=427$  nm;  $d_{l,\text{mean}}=1789$  nm,  $d_{l,\text{SD}}=773$  nm.

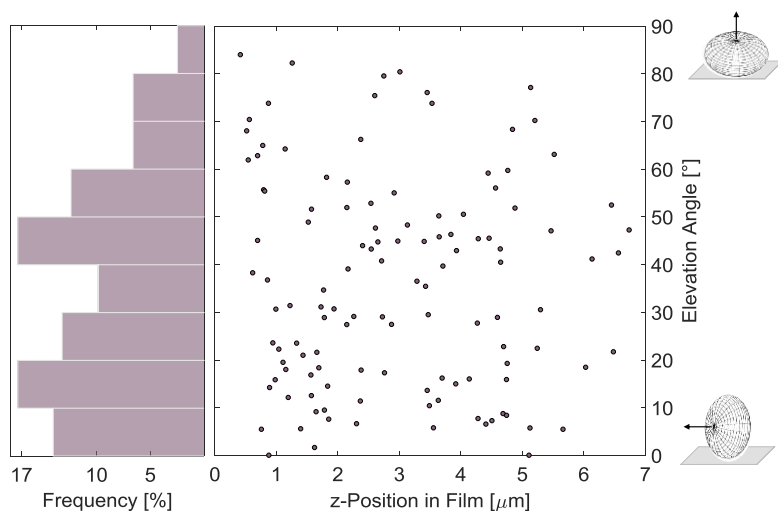


**Fig. A2.2.** Particle orientation determined by the direction of the longest diameter. Elevation angle=90°: particle lies flat relative to the FTO, and elevation angle=0°: particle stands upright relative to the FTO. The scatter plot demonstrates no trend of particle orientation as a function of z-position; however, normal vectors of the particles were elevated most frequently by 10° or 45°, as shown in the frequency distribution.

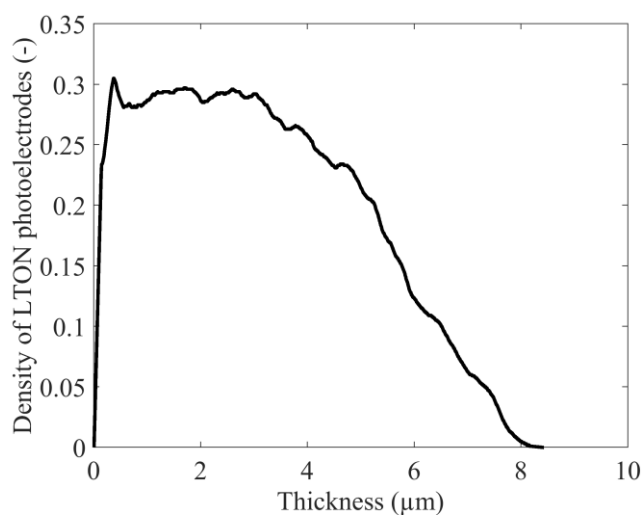


**Fig. A2.3.** Normalized density profile of LTON photoelectrodes electrophoretically deposited on a FTO substrate.

### A2.2. Solar simulator characterisitscs

The spectral irradiance of the Verasol-2 LED class AAA solar simulator from Oriel is depicted in [Fig. A2.4](#). The solar simulator was calibrated using the UV-Vis spectrometer HR4000CG-UV-NIR from Ocean Optics to measure each LED's spectrum with a spectral-stepping of 0.27 nm. The total irradiance of each LED was measured with a calibrated Si diode (FDS1010 from Thorlabs).

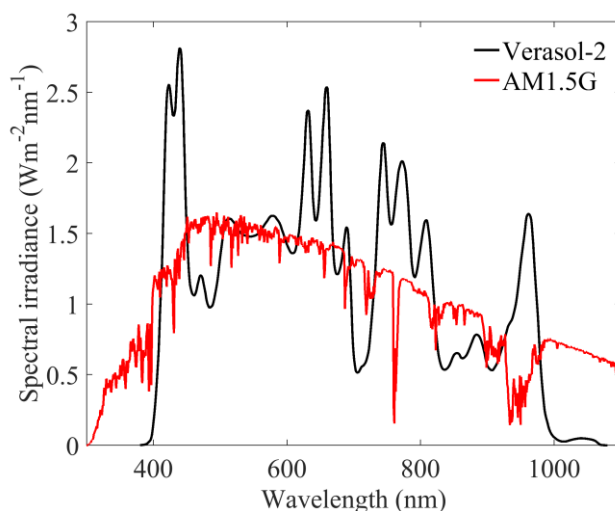


**Fig. A2.4.** Spectral irradiance of the Verasol-2 LED class AAA solar simulator from Newport and the reference spectral irradiance AM1.5G.

### A2.3. Solar Open-circuit voltage

The open-circuit voltage (OCV) measurements were conducted in 0.1 M  $\text{Na}_2\text{SO}_4$  and NaOH at  $\text{pH}=13.2\pm0.2$  and under AM1.5G with a periodic light chopping every 10s. The OCV was measured after 200s of stabilization and the OCV was determined by taking the potential difference between on and off light, after the 10s transients.

We confirmed the presence of band bending at the semiconductor-electrolyte interface with OCV greater than zero (Fig. A2.5). The OCVs of bare-LTON PEs was smaller (0.01 V under back-side illumination and 0.15 V under front-side illumination) than the ones of best-LTON (0.25 V under back-side illumination and 0.35 V under front-side illumination). This difference was explained by less recombination at the semiconductor-electrolyte interface for best-LTON. Less recombination increased the concentration of holes at the surface and therefore the quasi-Fermi level of holes, in other words the photovoltage measured by OCV measurements.

For both types of PEs, the front-side illumination led to higher OCVs than the back-side illumination although the relative difference was smaller for best-LTON PEs (29% for best-LTON and 93% for bare-LTON). The photocurrent is fixed to zero



for the OCV measurements and therefore there is no inter-particle charge transfer. In this case, the upper particles can contribute to the OCV. Upper particles are less in contact with surrounding particles. Thus, a larger surface is exposed to the semiconductor-electrolyte interface, which increases the OCV, compared to lower particles. The side of light illumination must also be considered, and since under back-side illumination most of the light is absorbed by the lower particles, the upper particles cannot contribute significantly to the OCV. In contrast, the upper particles are mostly contributing to the OCV under front-side illumination. Both effects explain the larger OCV under front-side illumination than under back-side illumination.

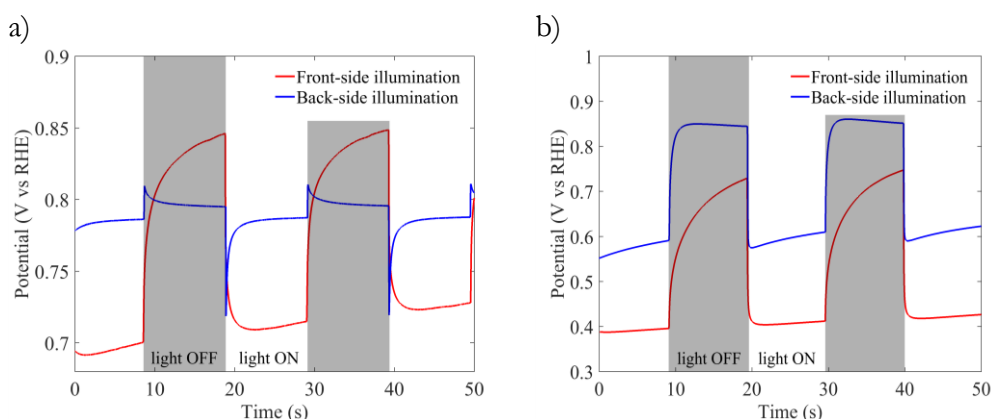


**Fig. A2.5.** Variation of the open-circuit potential under periodic light chopping of 10s for a) bare-LTON and b) best-LTON photoelectrodes immersed in 0.1 M NaSO<sub>4</sub> and NaOH (pH=13.2) under back- (blue) and front-side (red) illumination. The OCV increased by adding a co-catalyst, i.e. the OCV of bare-LTON was 0.01 V under back-side illumination while it was 0.25 V for best-LTON.

### A2.4. Electrochemical impedance spectroscopy

The Mott-Schottky plot with frequency dispersion is depicted in Fig. A2.6. The experimental and simulated impedance spectra of best-LTON at 0.12 V<sub>RHE</sub> is presented in Fig. A2.7.

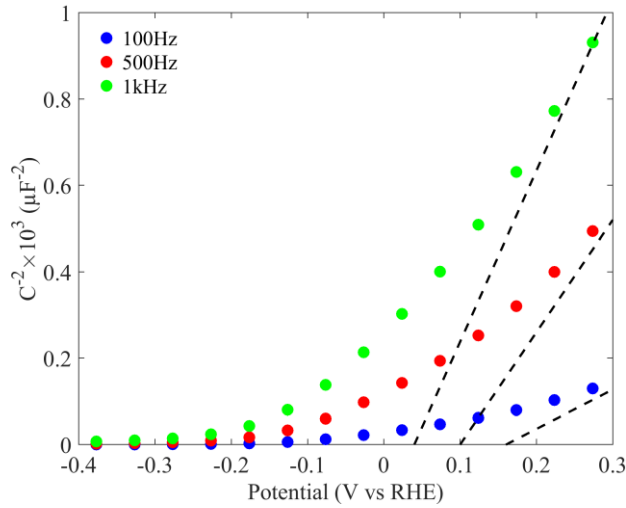


**Fig. A2.6.** Mott-Schottky plot for three frequencies (100Hz, 500Hz, 1kHz) of best-LTON electrodes immersed in 0.1 M NaSO<sub>4</sub> and NaOH (pH=13.2) under dark conditions.

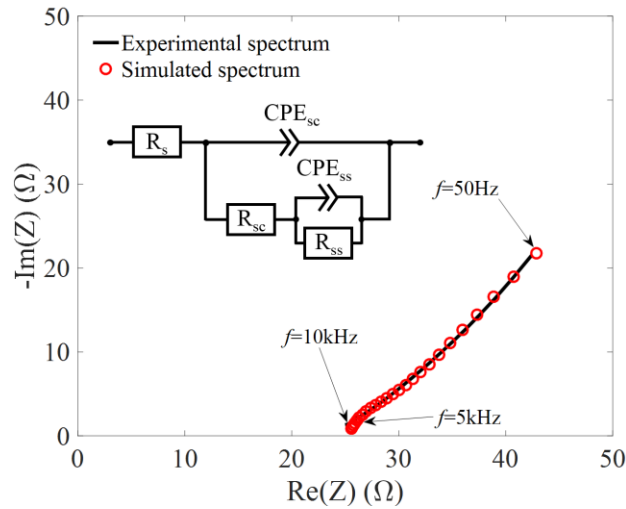


**Fig. A2.7.** Experimental and simulated impedance spectra of best-LTON photoelectrodes at 0.12 V<sub>RHE</sub> immersed in 0.1 M NaSO<sub>4</sub> and NaOH (pH=13.2) under dark conditions. The electrical impedances at 0.12 V<sub>RHE</sub> are  $R_s=25.43 \Omega$ ,  $R_{sc}=6.228 \Omega$ ,  $Y_{0,sc}=2.221 \cdot 10^{-5} \text{ F s}^{-\alpha}$  with  $\alpha_{sc}=0.96$ ,  $R_{ss}=347.7 \Omega$  and  $Y_{0,ss}=8.182 \cdot 10^{-4} \text{ F s}^{-\alpha}$  with  $\alpha_{ss}=0.65$ .

### A2.5. Optical parameters

The calculated Tauc plot is depicted in Fig. A2.8. The linear extrapolation (dashed black lines) indicates a bandgap of 1.9 eV, below the well-known value of 2.1 eV [19], [102], [148], [150]–[153]. This underestimation of the bandgap might be due to absorption of scattered photons. If we assume a constant scattering absorption, we can remove the scattering part by shifting the zero of the  $y$ -axis in the Tauc plot (red dashed line in Fig. A2.8) and estimate a bandgap of 2.08 eV, closer to the actual value of 2.1 eV.

The Kubelka-Munk (K-M) transform:  $F(\rho) = (1 - \rho)^2 / \rho$  from total reflectance measurements (diffuse and direct) can be used to evaluate the absorbance of inhomogeneous media with light scattering such as particle-based PE. The Tauc plot based on the K-M transform of LTON particle-based PE is depicted in Fig. A2.9 and shows a bandgap of 2.1 eV, in accordance with the known value of 2.1 eV and confirming the role of light scattering in these PEs.

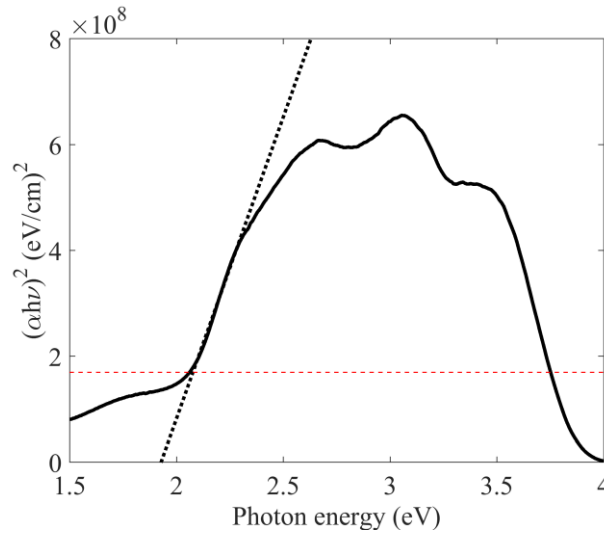


**Fig. A2.8.** Direct bandgap Tauc plot of LTON particle-based PEs based on the calculated absorption coefficient, eqn (2.5). The direct bandgap is found to be 1.9 eV according to the linear interpolation (dashed black line). If the plot is corrected for the constant absorption of light scattering, the estimated bandgap is 2.1 eV (crossing of red and black dashed lines).

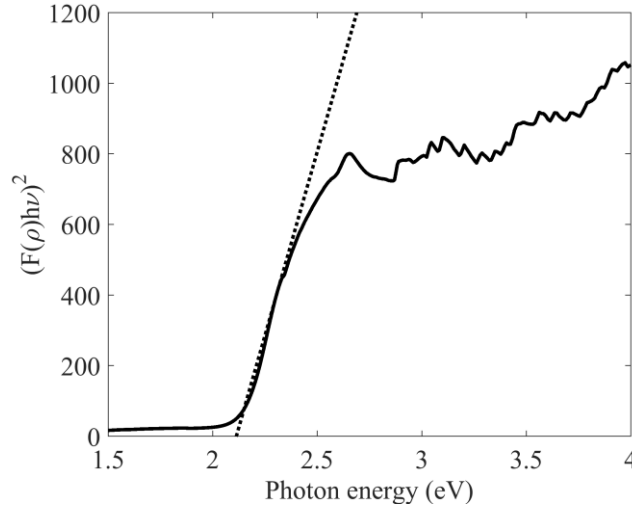


**Fig. A2.9.** Direct bandgap Tauc plot of LTON particle-based PEs based on K-M transform. The direct bandgap is found to be 2.1 eV according to the linear interpolation (dashed black line).

## A2.6. Optical simulations

### A2.6.1. Computational details for photoabsorption model

Convergence was obtained with a direct MUMPS solver. A relative tolerance of  $10^{-4}$  in the electric field was used as convergence criteria. Mesh convergence was obtained for linear mesh discretization with size ratio of 4, and element numbers,  $n_{el}$ , depending on the irradiation wavelength,  $\lambda$ , and the layer thickness,  $d$ :  $n_{el} = d \cdot \beta / \lambda$  with  $\beta = 200$  for  $\text{SnO}_2$ ,  $\beta = 150$  for  $\text{LaTiO}_2\text{N}$ ,  $\beta = 50$  for glass, and  $\beta = 30$  for water. The number of mesh elements perpendicularly to the direction of light propagation was fixed to 5 in the domain with a width of  $5 \mu\text{m}$ .

### A2.6.2. Model validation by transmittance

The EMW model has the same dimension as the PEs: a slab of  $2 \mu\text{m}$  of air to account for reflection at the air-LTON interface, followed by  $8.433 \mu\text{m}$  of LTON,  $360 \text{ nm}$  of  $\text{SnO}_2$ ,  $2.2 \text{ mm}$  of glass and again  $2 \mu\text{m}$  of air. Complex refractive index for bare glass (glass TCO22-15) and  $\text{SnO}_2$  were provided by Solaronix (Fig. A2.10 and Fig.

A2.11). The complex refractive index of air was taken from Ciddor.[235] The calculated transmittance under back- and front-side illumination using EMW propagation model are depicted in Fig. A2.12.

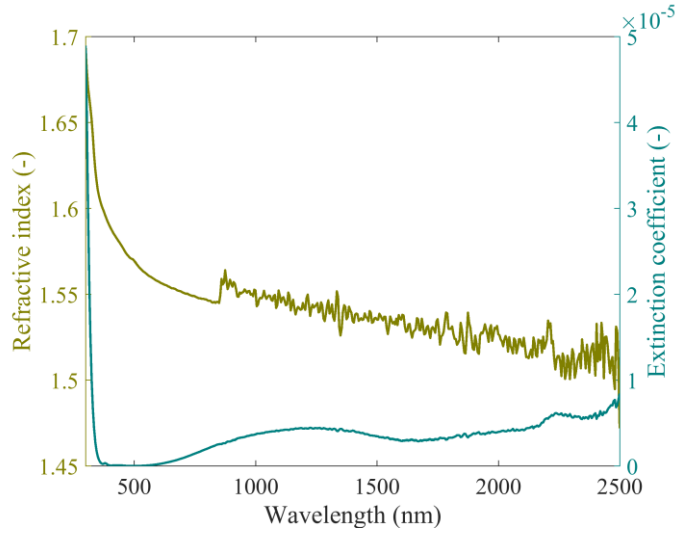


**Fig. A2.10.** Complex refractive index of bare glass of 2.2  $\mu\text{m}$  for TCO22-15 transparent conductive layer of Solaronix.

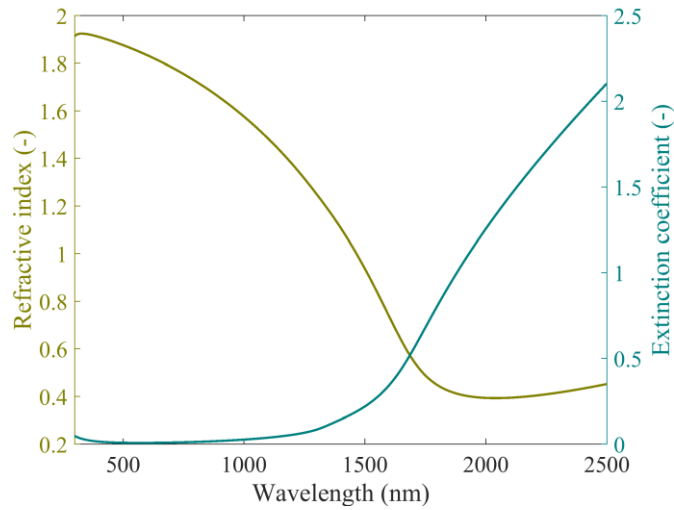


**Fig. A2.11.** Complex refractive index of  $\text{SnO}_2$  layer of 360 nm for TCO22-15 transparent conductive layer of Solaronix.

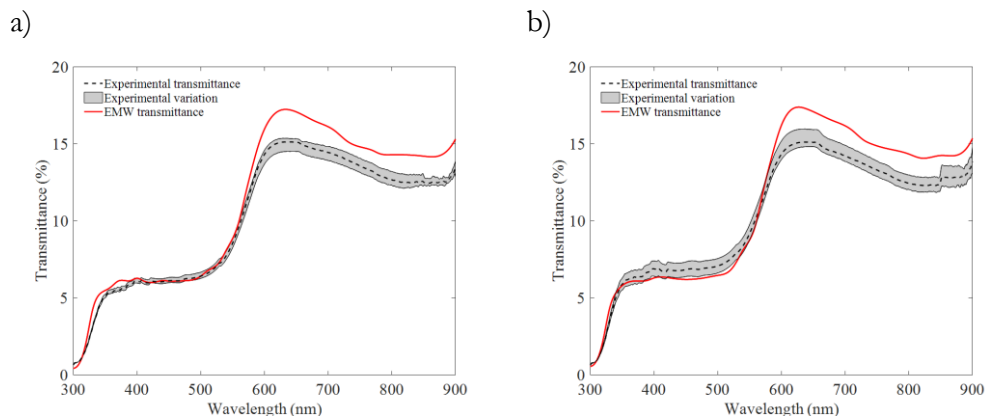


**Fig. A2.12.** Measured and calculated transmittance of LTON particle-based photoelectrode under a) back- and b) front-side illumination. Transmittance is calculated with an EMW propagation model each 10 nm and a cubic spline interpolation is used for smoothing. The numerical transmittance is below 2 % error compared to the measured transmittance from 400 nm to 590 nm (2.1 eV, band gap of LTON). The experimental variation is obtained by measuring four different LTON photoelectrodes.

The calculated transmittance under back- and front-side illumination using Beer-Lambert's law are depicted in Fig. A2.13. The calculated transmittance for both methods is below 2% error from 400 nm to 590 nm, corresponding respectively to the lowest photon's wavelength emitted by the Verasol-2 solar simulator and the bandgap of LTON. The calculation of the generation rate using one of these methods would lead to a photogenerated current error of  $0.005 \text{ mA cm}^{-2}$  under front-side illumination and  $0.124 \text{ mA cm}^{-2}$  under back-side illumination, both using AM1.5G spectral irradiance. These errors are below the experimental photocurrent density variation of  $0.167 \text{ mA cm}^{-2}$  under back-side illumination and  $0.204 \text{ mA cm}^{-2}$  under front-side illumination at  $1.23 \text{ V}_{\text{RHE}}$  (Fig. 2.5).

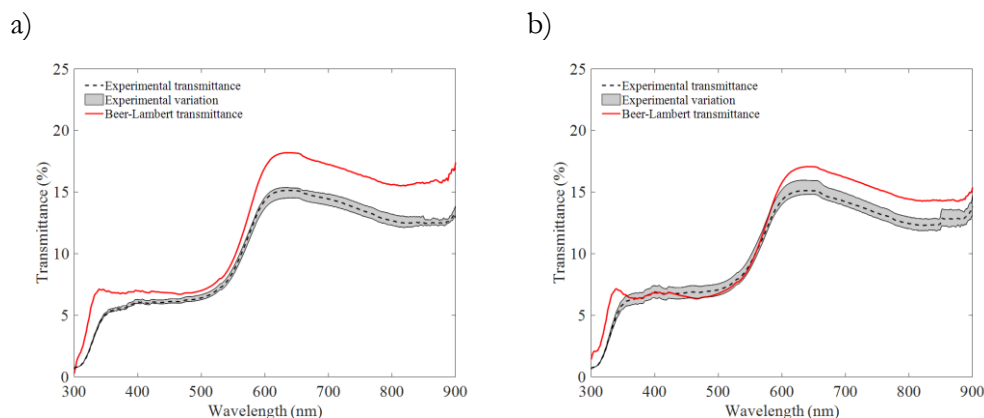


**Fig. A2.13.** Measured and calculated transmittance of LTON particle-based photoelectrodes under a) back- and b) front-side illumination. Transmittance is calculated using Beer-Lambert's law and is below 2% error compared to the measured transmittance in the spectral range of 400 nm to 590 nm (2.1 eV, band gap of LTON). The experimental variation is obtained by measuring four different LTON photoelectrodes.

## A2.7. DFT calculations

### A2.7.1. DFT computational details

Our DFT calculations were performed with a kinetic energy cutoff of 40 Ry for the wavefunctions and a cutoff of 320 Ry for the augmented density. Electron-core interactions are described by ultrasoft pseudopotentials with La(5s, 5p, 5d, 6s, 6p), Ti(3s, 3d, 3p, 4s), O(2s, 2p) and N(2s, 2p) valence electrons, where the O and N potentials were combined into a virtual crystal potential at  $2/3$  and  $1/3$  weight respectively, describing a complete disorder on the anion site. For the 20-atom orthorhombic cell, reciprocal space was sampled using a  $6 \times 6 \times 6$  mesh. Atoms were relaxed until forces converged below 0.05 eV/Å. Due to a code limitation, the dielectric constant was computed using DFPT without inclusion of the Hubbard U correction.

### A2.7.2. Electronic band structure

In Fig. A2.14, we show the band structure of orthorhombic LTON within the virtual crystal approximation to describe disorder on the anion site. Within this description, the material exhibits a direct bandgap of 1.96 eV at the  $\Gamma$ -point of the Brillouin zone

which agrees reasonably well - given the use of a semilocal functional - with the experimentally measured 2.1 eV[19] but is larger than calculations using explicit disorder models on the anion site.[137]

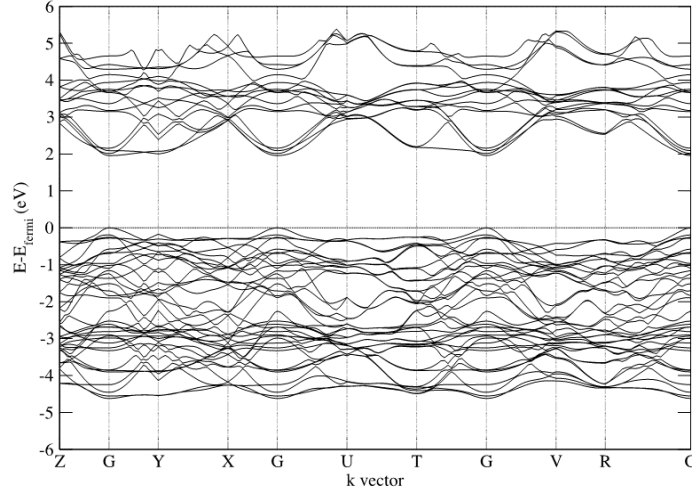


**Fig. A2.14.** Electronic band structure of orthorhombic  $\text{LaTiO}_2\text{N}$  along high-symmetry lines of the Brillouin zone.

### A2.7.3. Full dielectric tensor

Considering both electronic and ionic contributions, we obtain the following dielectric permittivity tensor for orthorhombic  $\text{LaTiO}_2\text{N}$ :

$$\begin{pmatrix} 19.458105 & 0.057050 & -0.466666 \\ 0.057050 & 11.451939 & -0.632479 \\ -0.466666 & -0.632479 & 13.897091 \end{pmatrix}$$



### A2.8. Semiconductor physics simulations

#### A2.8.1. Computational details for charge transport and conservation

Convergence was obtained with a direct MUMPS solver fully coupled for the corresponding variables, i.e. electron and hole concentrations and electric potential. A relative tolerance in the hole and electron concentrations and the electric potential of  $10^{-3}$  was used as a convergence criterion. For the 2D model, the mesh convergence was obtained for mesh element number,  $n_{\text{mesh}} = d/5$  nm along the height and width with symmetric mesh distributions and an element ratio of 15. The symmetric distribution ensured a highly resolved mesh at each boundary in the model.

#### A2.8.2. I-V curves for varying light intensity

Numerical and experimental photocurrent-voltage curves of best-LTON photoelectrode under back-side illumination for varying light intensities are depicted [Fig. A2.15](#).

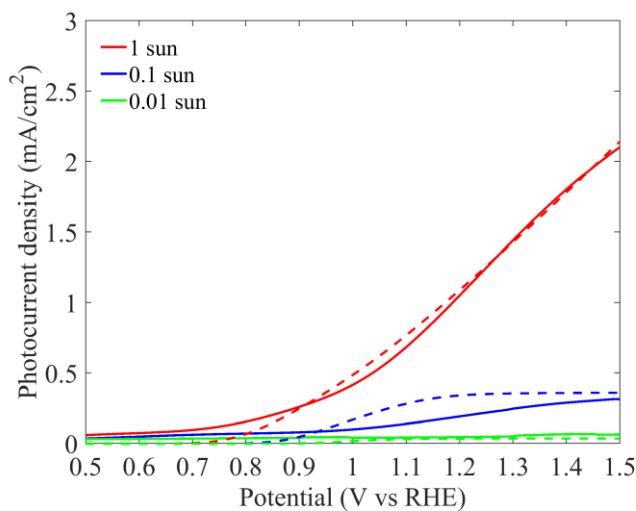


**Fig. A2.15.** Numerical (dashed lines) and experimental (solid lines) photocurrent-voltage curves of best-LTON photoelectrode under back-side illumination for varying light intensities (1, 0.1, and 0.01 sun).

### A2.8.3. Photoelectrode with the entire thickness being active

I-V curves of LTON particle-based PE with the entire thickness of the photoelectrode being active, i.e. without any potential loss along the thickness of the PEs, are depicted in Fig. A2.16.

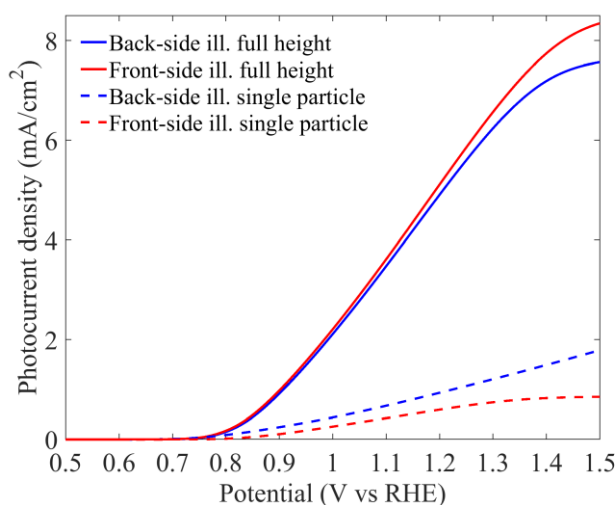


**Fig. A2.16.** Numerical and experimental photocurrent-voltage curves of best-LTON PEs with entire thickness ( $8.43\ \mu\text{m}$ ) being active (no potential loss along the thickness of the PE) and only the first single particle's layer ( $1.42\ \mu\text{m}$ ) being active under back- and front-side illumination.

### A2.8.4. Electron mobility

The impact of electron mobility on the photocurrent under back- and front-side illumination is depicted in Fig. A2.17. There is no effect of electron mobility on the photocurrent under back-side illumination. Under front-side illumination, the photocurrent is also independent of the electron mobility although below a mobility of  $0.1\ \text{cm}^2\ \text{V}^{-1}\ \text{s}^{-1}$ , there is suddenly no photocurrent. The electron transport is only relevant to maintain charge conservation to have holes leaving the semiconductor to make the oxygen evolution reaction. Nevertheless, the charge conservation cannot be maintained if the mobility of electron becomes too small. Then, the electron cannot be collected anymore and will recombine with holes leading to the loss of the photocurrent as depicted in Fig. A2.17.

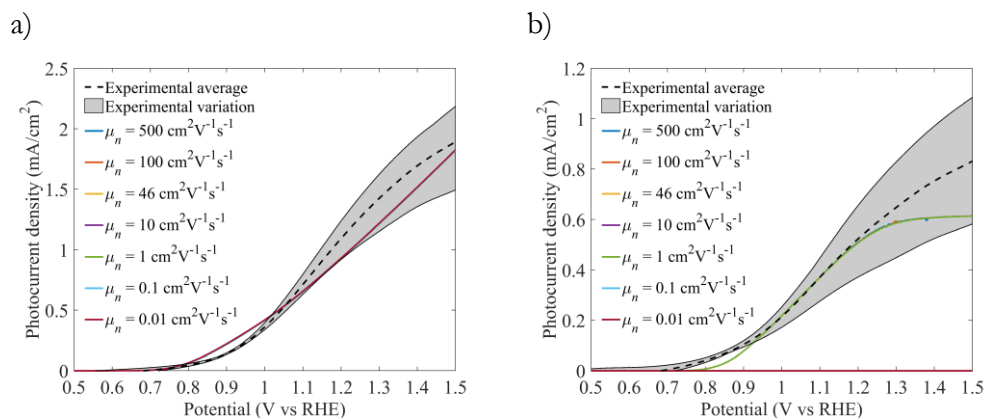


**Fig. A2.17.** Numerical and experimental photocurrent-voltage curves of best-LTON PEs under a) back- and b) front-side illumination for varying electron mobilities.

### A2.8.5. Doping concentration

The impact of doping concentration on the calculated photocurrents under back- and front-side illumination is depicted in Fig. A2.18, together with the experimentally measured ones. The doping concentration has a variety of opposing effects on the performance. First, increasing the doping concentration increases the electron density of the particle in the bulk ( $n \approx N_D^+$ ) but also in the SCL, which increases the recombination rate and thus decreases the photocurrent. Second, the SCL is thinned, reducing the drift current. On the other hand, since the SCL is reduced, the electric field (gradient of the potential) is locally increased, providing a stronger charge separation force.

Under back-side illumination, it appeared that a change in the doping concentration did not affect the photocurrent (Fig. A2.18.a). We conclude that the doping concentration and the recombination rate related to the change in the doping concentration are not limiting under back-side illumination. Indeed, both electron and hole paths are short under back-side illumination and the good transport and recombination properties of LTON prevent charges to recombine. In contrast, the photocurrent under front-side was more affected by the doping concentration because the electron transport followed a longer path in which recombination and doping concentration started to play a role (Fig. A2.18.b). Nevertheless, the doping concentration did not appear as a key parameter for the photocurrent. Indeed, the photocurrent density is only slightly reduced from  $0.59 \text{ mA cm}^{-2}$  to  $0.50 \text{ mA cm}^{-2}$  at

1.23 V<sub>RHE</sub> when reducing the doping concentration from  $10^{16} \text{ cm}^{-3}$  to  $10^{19} \text{ cm}^{-3}$ . Thus, a large range of doping concentration (from  $1 \cdot 10^{16} \text{ cm}^{-3}$  to  $1 \cdot 10^{18} \text{ cm}^{-3}$ ) satisfied the calculated photocurrents within experimental variation.

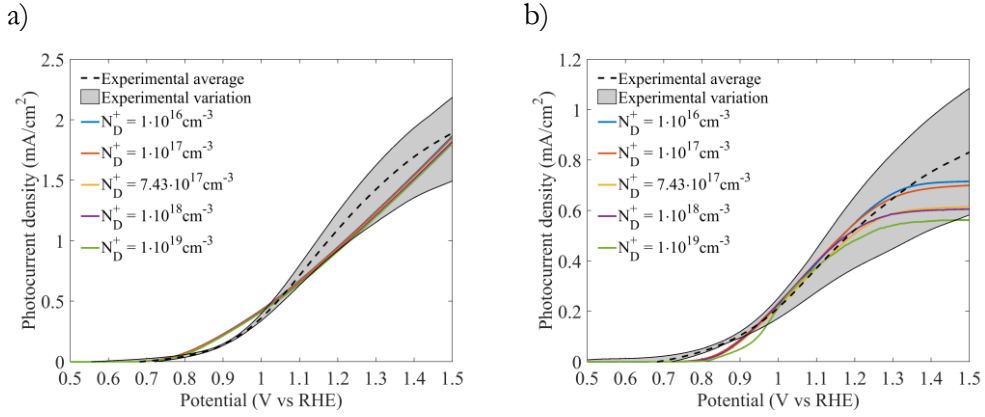


**Fig. A2.18.** Numerical photocurrent-voltage curves of best-LTON PEs under a) back- and b) front-side illumination for varying doping concentration.

#### A2.8.6. Numerical I-V curves for bare-LTON

The numerical I-V curves for bare-LTON is presented in Fig. A2.19. The numerical photocurrent is well inside the experimental error bars for potential above 1.2 V<sub>RHE</sub> but the numerical onset potential is higher than the experimental one. The effective lifetimes of electron and holes are 0.01 ns and the interfacial hole velocity is  $8.2 \cdot 10^{-9} \text{ cm s}^{-1}$ . This experimental photocurrent in the potential range of 0.6 V to 1 V<sub>RHE</sub> can be attributed to a photocorrosion current present in LTON. It might also be attributed to a transient current attributed to high transient effects in this potential region.<sup>[102]</sup>

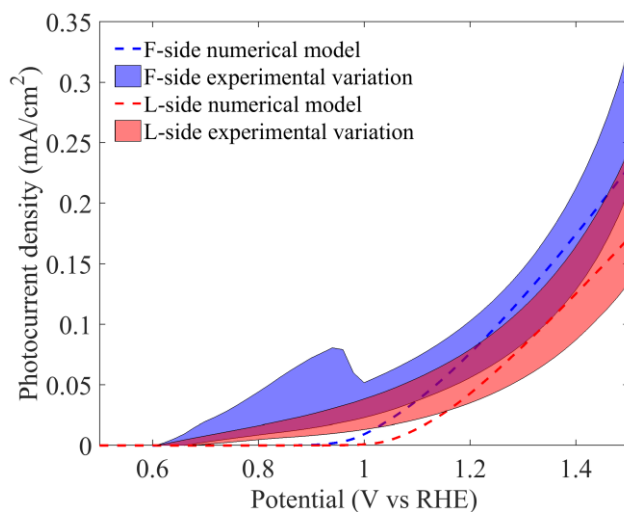


**Fig. A2.19.** Numerical and experimental photocurrent-voltage curves of bare-LTON under back- and front-side illumination.

## Appendix of chapter 3

### A3.1. Numerical inter-particle charge transfer mechanisms

The numerical  $I$ - $V$  curves of case 3 for varying inter-particle electron transfer velocities are depicted in Fig. A3.1. The inter-particle potential barrier was fixed to 0.0762 V to ensure flat bands at the inter-particle contact. The contributions of the second particle below 0.8  $V_{\text{RHE}}$  are not relevant since the onset potential is at  $\sim 0.8$   $V_{\text{RHE}}$  as depicted in Fig. A3.1. a) and b).

### A3.2. Best-LTON photoelectrodes with 50 nm $\text{IrO}_x$

50 nm of  $\text{IrO}_x$  were deposited on a best-LTON PE[161] by sputtering at ambient temperature (Alliance-Concept DP 650). The LTON PE with 50 nm  $\text{IrO}_x$  on top were tested under back illumination only since the  $\text{IrO}_x$  blocks almost completely the light. Fig. A3.2 compares the photocurrent of the same LTON PE before and after  $\text{IrO}_x$  deposition. As it can be seen, the photocurrent is highly improved, i.e. a relative increase of 67 % at 1.23  $V_{\text{RHE}}$ . The LTON PE without  $\text{IrO}_x$  was freshly prepared when measured. The same LTON PE was then modified with  $\text{IrO}_x$  to enable direct comparison. However, the performance of LTON PE with  $\text{IrO}_x$  might be underestimated, since aging effects between the two measurements cannot be excluded. The onset potential is also slightly lowered with  $\text{IrO}_x$  similar to the numerical prediction[161].

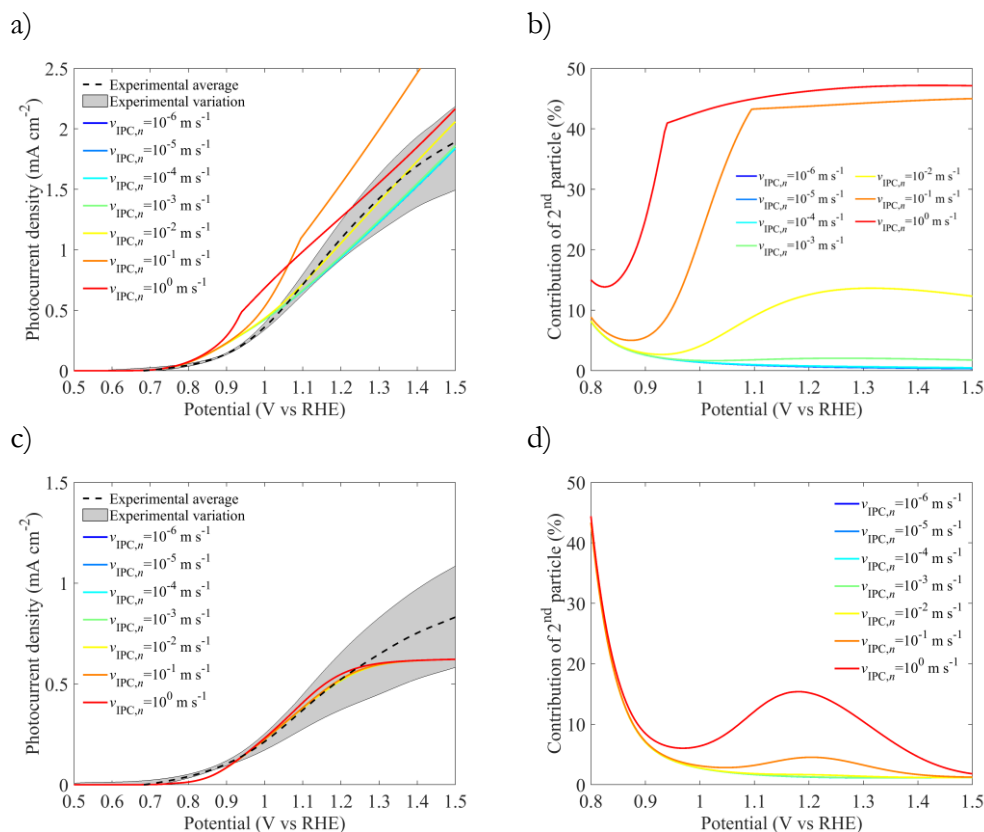


**Fig. A3.1.** Experimental  $I$ - $V$  curves of best-LTON PBPE with an average film thickness of 8.43  $\mu\text{m}$  taken from Gaudy et al.[161]. The corresponding numerical  $I$ - $V$  curves of case 3) for varying inter-particle contact electron velocities under a) back-side illumination and c) front-side illumination, and the corresponding contribution of the 2<sup>nd</sup> particle on the right side in b) and d).

The photoelectrochemical measurements were conducted in a three electrode setup with the LTON PE as working electrode, a Ag/AgCl reference electrode (sat. KCl) and Pt as counter electrode. The electrolytes used was 0.1 M Na<sub>2</sub>SO<sub>4</sub> as a buffer solution with pH=13.0 $\pm$ 0.2 by adding NaOH. The potential was controlled with a potentiostat (Bio-Logic VSP-300) controlled by EC-lab software and the scan rate for the cyclic voltammetry was 10 mV s<sup>-1</sup> from 0 V<sub>RHE</sub> to 1.5 V<sub>RHE</sub>. The sample was illuminated by the solar simulator VeraSol-2 from Oriel corresponding to AM1.5G[161]. The current density was averaged between forward and backward swept voltage because of the presence of a hysteresis.

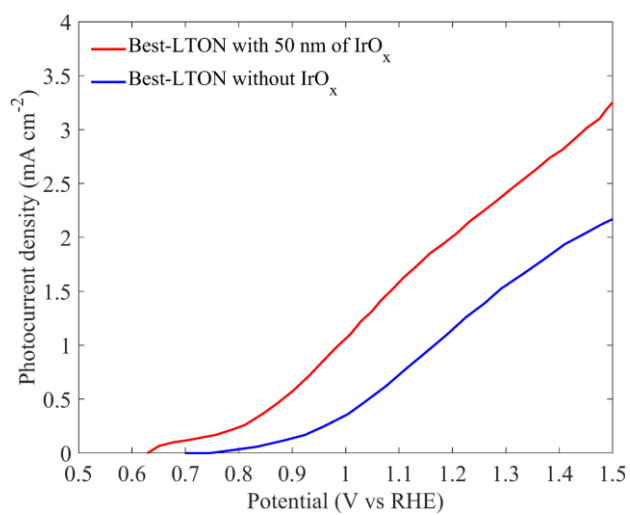


**Fig. A3.2.** Experimental I-V curves of best-LTON PE with and without a 50 nm layer of IrO<sub>x</sub> in 0.1 M Na<sub>2</sub>SO<sub>4</sub> at pH=13.0±0.2 by adding NaOH.



# Appendix of chapter 4

## A4

### A4.1. Development of the internal quantum efficiency equation

The full mathematical development of the internal quantum efficiency (IQE) of a photoelectrode is based on the work of Wilson[60]. The IQE is determined by accounting for the contribution of the bulk and the space charge region (SCR).

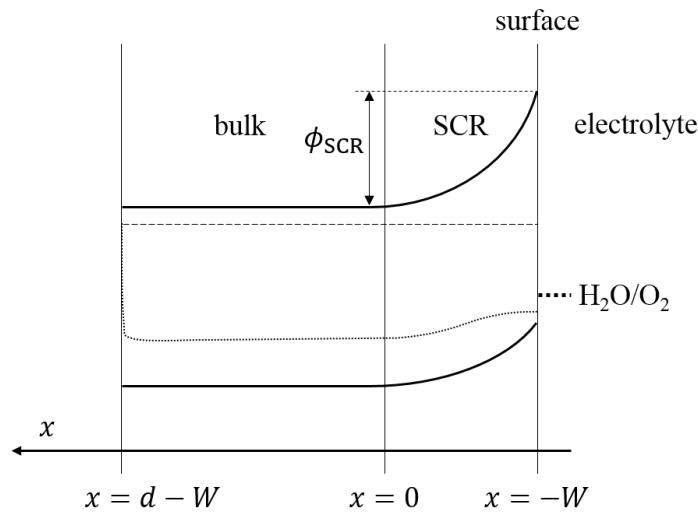


**Fig. A4.1.** Schematic of the band diagram for an n-type semiconductor photoanode in contact with an electrolyte.

The IQE of a photoelectrode for a specific photon wavelength (indicated by the subscript  $\lambda$ ) is given by the integration of the probability of a charge carrier to reach

the semiconductor surface,  $U^*(x)$ , times the generation rate,  $G(x)$ , over the entire photoelectrode thickness,  $d$ , divided by the photon flux entering at the semiconductor surface,  $\Phi(x = -W)$  (Fig. A4.1). Additionally, the ratio of charges being transfer for the water oxidation reaction and the charges recombining at the surface must be included in the IQE equation, which leads to

$$\begin{aligned}
 \text{IQE}_\lambda &= \frac{S_T}{S_T + S_R} \left( \frac{1}{\Phi(-W)} \int_{-W}^{d-W} U^*(x) G(x) dx \right) \\
 &= \frac{S_T}{S_T + S_R} \left( -\frac{\eta}{\Phi(-W)} \int_{-W}^0 \alpha_\lambda \Phi(-W) e^{-\alpha_\lambda x} dx \right. \\
 &\quad \left. + \frac{1}{\Phi(-W)} \int_0^{d-W} U \Phi(0) \alpha_\lambda e^{-\alpha_\lambda x} dx \right) \\
 &= \frac{S_T}{S_T + S_R} \left( \eta(1 - e^{-\alpha_\lambda W}) + \frac{\Phi(0)}{\Phi(-W)} \int_0^{d-W} \frac{L e^{-x/L}}{L + D/S} \alpha_\lambda e^{-\alpha_\lambda x} dx \right) \\
 &= \frac{S_T}{S_T + S_R} \left( \eta(1 - e^{-\alpha_\lambda W}) \right. \\
 &\quad \left. + \frac{\Phi(-W) e^{-\alpha_\lambda W}}{\Phi(-W)} \int_0^{d-W} \frac{L}{L + D/S} \alpha_\lambda e^{-x \frac{1+\alpha_\lambda L}{L}} dx \right) \\
 &= \frac{S_T}{S_T + S_R} \left[ \eta(1 - e^{-\alpha_\lambda W}) \right. \\
 &\quad \left. + e^{-\alpha_\lambda W} \frac{L}{L + D/S} \frac{\alpha_\lambda L}{\alpha_\lambda L + 1} \left( 1 - e^{-\frac{(d-W)(1+\alpha_\lambda L)}{L}} \right) \right] \\
 &= \frac{S_T}{S_T + S_R} \left[ \eta(1 - e^{-\alpha_\lambda W}) + \xi \left( e^{-\alpha_\lambda W} \frac{L}{L + D/S} \frac{\alpha_\lambda L}{\alpha_\lambda L + 1} \right) \right],
 \end{aligned} \tag{A4.1}$$

where  $\Phi(0)$  is the photon flux entering at the edge of the of the bulk region,  $U$  is the probability of charge generated in the bulk to reach the SCR and is given by  $\frac{L e^{-x/L}}{L + D/S}$  [60],  $D$  is the diffusion coefficient related to the mobility by the Einstein

relation, and  $L$  is the diffusion length.  $\xi = 1 - e^{-\frac{(d-W)(1+\alpha_\lambda L)}{L}}$  is a factor representing the transmitted photons due to the finite thickness of the photoelectrode,  $S$  is a parameter related to minority charge carrier surface reactions which is determined by eqn (4.10), and  $\eta$  is the ratio of the charges generated in the SCR that are reaching the semiconductor-electrolyte interface without recombining (eqn (A4.5)). The IQE equation assumes that all the charges generated in the bulk that reach the SCR are contributing to the photocurrent, i.e. no  $\eta$  correction is applied to them.

$\eta$  is determined by assuming that the photocurrent density in the SCR is only driven by the electric field,  $\phi(x)$ . Here, we assume that the material is n-type with holes being the minority charge carriers but the same can be applied with p-type material and electrons as minority charge carriers. The photocurrent density resulting from the generated charge carriers in the SCR is given by

$$i_{\text{SCR}} = q\mu\Delta p(x) \frac{d\phi(x)}{dx}, \quad (\text{A4.2})$$

where  $\Delta p$  is the photogenerated hole concentration in the SCR. By simplifying the SCR with a linear band bending, the derivative of the potential can be rewritten with the space charge layer potential,  $\phi_{\text{SC}}$ , and the SCR thickness, given by

$$i_{\text{SCR}} \approx q\mu\overline{\Delta p} \frac{\phi_{\text{SC}}}{W}. \quad (\text{A4.3})$$

where  $\overline{\Delta p}$  is the averaged photogenerated hole concentration in the SCR. The band bending potential is given by  $\phi_{\text{SC}} = V_a - V_{\text{FB}}$  with  $V_a$  the applied potential and  $V_{\text{FB}}$  the flatband potential. By simplifying the system with an averaged constant photogenerated hole density over the entire SCR,  $\overline{\Delta p}$ , the recombination current density in the SCR is given by

$$i_{\text{rec}} \approx q \frac{\overline{\Delta p}}{\tau} W, \quad (\text{A4.4})$$

where  $\tau$  is the lifetime of minority charge carriers. By using the definition of the diffusion length,  $L = \sqrt{D\tau}$  with  $D = \mu \cdot V_{\text{th}}$  along with eqns (A4.3) and (A4.4),  $\eta$ , i.e. the ratio between the photocurrent reaching the semiconductor-electrolyte interface and the recombination is given by

$$\eta = \frac{i_{\text{SCR}}}{i_{\text{rec}} + i_{\text{SCR}}} = \frac{L^2 \phi_{\text{SC}}}{W^2 V_{\text{th}} + L^2 \phi_{\text{SC}}}. \quad (\text{A4.5})$$

This term is added to the SCR photocurrent contribution in eqn (A4.1) to take into account SCR recombination. We can observe that with this equation increasing  $W$  by, for example, increasing the doping concentration (eqn (17)) increases the recombination and therefore reduces the SCR photocurrent contribution. This effect is due to a decrease of the electric field in the SCR by increasing  $W$ . This term will enable an optimum between increasing  $W$  that increases the SCR contribution and decrease bulk contribution but also increases SCR recombination depending on the value of the diffusion length.

$S$  is determined similarly as in the work of Wilson[60]. Here, we assumed holes as minority charge carriers. The flux of holes at the bulk and SCR interface,  $F_b$ , corresponds to the second integration term in the second line of eqn (A4.1), given by

$$F_b = \phi(0) \int_0^{d-W} U \alpha_\lambda e^{-\alpha_\lambda x} dx = \phi(-W) e^{-\alpha_\lambda W} \xi \left( \frac{L}{L+D/S} \frac{\alpha_\lambda L}{\alpha_\lambda L+1} \right) = S p_0, \quad (\text{A4.6})$$

where  $p_0$  is the hole concentration at the bulk and SCR interface ( $x=0$ ).  $p_0$  can be extracted from eqn (A4.6), given by

$$p_0 = \phi(-W) e^{-\alpha_\lambda W} \xi \left( \frac{L}{SL+D} \frac{\alpha_\lambda L}{\alpha_\lambda L+1} \right). \quad (\text{A4.7})$$

The hole concentration at the surface ( $x=-W$ ) is approximated by[21]

$$p_s = p_0 e^{\frac{\phi_{sc}}{V_{th}}}. \quad (\text{A4.8})$$

The total flux of holes reaching the surface is the sum of the recombination flux and the charge transfer flux times the hole concentration at the surface (eqn (A4.8)), given by

$$F_p = (S_T + S_R)p_0 e^{\frac{\phi_{SC}}{V_{th}}} \quad (A4.9)$$

We can substitute  $p_0$  from eqn (A4.7) into eqn (A4.9) which leads to

$$F_p = (S_T + S_R)\phi(-W)e^{-\alpha_\lambda W} \xi \left( \frac{L}{S_L+D} \frac{\alpha_\lambda L}{\alpha_\lambda L+1} \right) e^{\frac{\phi_{SC}}{V_{th}}} \quad (A4.10)$$

The total flux of holes can also be calculated by using eqn (A4.1)

$$F_p = \phi(-W) \cdot IQE_\lambda \cdot \frac{S_T+S_R}{S_T} = \phi(-W) \left[ \eta(1 - e^{-\alpha_\lambda W}) + \xi \left( e^{-\alpha_\lambda W} \frac{L}{L+D/S} \frac{\alpha_\lambda L}{\alpha_\lambda L+1} \right) \right] \quad (A4.11)$$

$S$  can be extracted by resolving for  $S$  the equality of the total hole flux given by eqns (A4.10) and (A4.11) for  $S$ :

$$S = \left[ (S_T + S_R)e^{\frac{\phi_{SC}}{V_{th}}} - \frac{1-e^{-\alpha_\lambda W}}{e^{-\alpha_\lambda W}[\alpha_\lambda L/(\alpha_\lambda L+1)]} \frac{D}{L} \frac{\eta}{\xi} \right] \left[ 1 + \frac{1-e^{-\alpha_\lambda W}}{e^{-\alpha_\lambda W}[\alpha_\lambda L/(\alpha_\lambda L+1)]} \frac{\eta}{\xi} \right]^{-1} \quad (A4.12)$$

## A4.2. Sensitivity analysis

Prior to the determination of diffusion length and the ratio of current, numerous material parameters must be known, namely the complex refractive index, the bandgap, the flatband potential, the doping concentration, the permittivity, the thickness of the photoelectrode, the minority charge carrier mobility, and the surface state distribution factor. The thickness of the photoelectrode determines the part of the light not absorbed by the photoelectrode, given by eqn (4.8). The sensitivity study presented here predicts that these parameters do not have to be known accurately and already an estimation of these parameters allows for the calculation of the diffusion length within the right order of magnitude.

### A4.2.1. Complex refractive index

The impact of different complex refractive index data on the numerical IPCE spectra and, therefore, on the determination of the diffusion length was investigated for n-Fe<sub>2</sub>O<sub>3</sub> photoanodes[23]. The complex refractive indexes from Querry[184] and Longtin et al.[183] were used. The R<sup>2</sup> value of the IPCE fitting (Fig. A4.2) was 0.572 when using the complex refractive index data of Querry, and 0.96 when using the data of Longtin et al. Although the data of Querry led to a poor IPCE fitting compared to Longtin et al., the calculated diffusion lengths remained very similar, i.e. 8.3 nm with the data based on Querry and 9.1 nm with Longtin et al..  $R_{S,V_{IPCE}}$  was also not very sensitive to the complex refractive index data difference, with  $R_{S,V_{IPCE}} = 0.17$  using the data of Querry and 0.23 using the data of Longtin et al., inducing an estimated surface loss of 42% with the data based on Querry and 40% with Longtin et al. at 300 nm. Thus, a good estimation of the diffusion length and the surface recombination loss using our IPCE model can be obtained with any reasonable complex refractive index data that provides an R<sup>2</sup> >0.5.

No sensitivity analysis was done on the optical bandgap of the material because it is strongly related to the complex refractive index, more specifically to the absorption coefficient. The bandgap of the material can be estimated from the absorption coefficient by using a Tauc plot. Our numerical IPCE model is anyway based on the complex refractive index and not on the bandgap of the material. The bandgap is only used as upper boundary to determine the R<sup>2</sup> of the IPCE fitting and to calculate the diffusion optical number (eqn (4.13)).

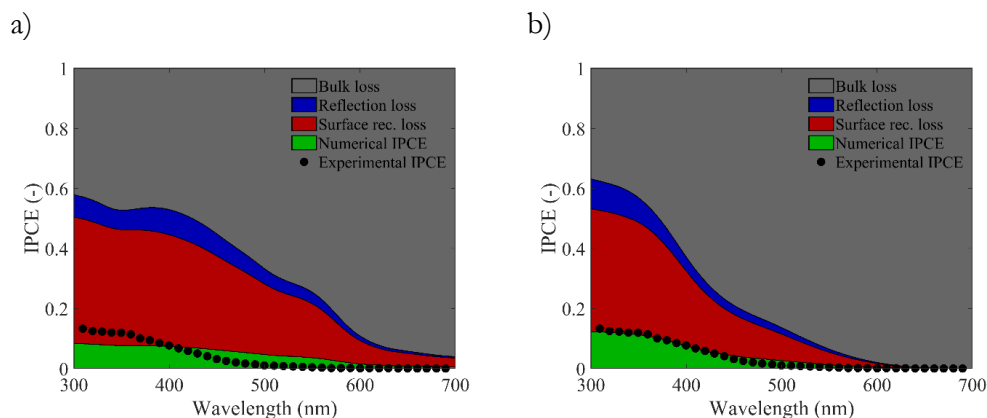


**Fig. A4.2.** Experimental spectral IPCE at 1.46 VRHE (black dotted) and numerical IPCE (green), surface recombination loss (red), reflection loss (blue) and bulk loss (grey), for planar n-Fe<sub>2</sub>O<sub>3</sub> photoanodes[23] with the complex refractive index from a) Query[184] and b) Longtin et al.[183]. The numerical IPCE was fitted to the experimental IPCE from Yan et al.[23] and the optimized fitting resulted in R2 of a) 0.567 and b) 0.964. The determined diffusion lengths are a) 8.3 nm and b) 9.1 nm.

### A4.2.2. Flatband potential

The flatband potential is a key parameter since it dictates the band bending at the semiconductor-electrolyte interface, i.e. the driving force of the water-splitting photoelectrodes. The flatband potential can be obtained directly by a Mott-Schottky analysis[53]. Sometimes however the Mott-Schottky plot shows a high frequency dispersion, requiring the use of more advanced equivalent circuits in order to fit the impedance spectra. The proper choice of the equivalent circuit can be highly complicated due to various physicochemical phenomena taking place[133]. We quantified the impact of the flatband potential on the determination of the diffusion length of p-Cu<sub>2</sub>O photocathode with a doping concentration of  $7.1 \times 10^{13} \text{ cm}^{-3}$ [169]. Since the flatband potential for this photocathode was not reported, the flatband potential was taken from the work of Luo et al.[190] as 0.73 V<sub>RHE</sub> and a doping concentration of  $2 \times 10^{18} \text{ cm}^{-3}$ . In a doped material such as a p-type material, the majority charge carrier in the bulk is approximately equal to the doping concentration, given by  $p \approx N_A^-$ . The Fermi level potential in a p-type semiconductor is therefore related to the doping concentration, following[70]

$$V_F = V_{th} \ln \left( \frac{N_V}{N_A} \right) + V_{VB}, \quad (A4.13)$$

where  $N_V$  and  $V_{VB}$  are the density of states and the potential of the valence band, respectively. If we assume that the band edge position remains constant with the doping concentration and neglect any Fermi level pinning to surface states, the difference of the flatband potential for the same p-type material but with a different doping concentration is given by

$$\Delta V_{FB} = \Delta V_F = V_{F,2} - V_{F,1} = V_{th} \ln \left( \frac{N_{A,1}^-}{N_{A,2}^-} \right). \quad (A4.14)$$

In the case of the p-Cu<sub>2</sub>O photocathode with a doping concentration of  $7.1 \times 10^{13} \text{ cm}^{-3}$ , the calculated flatband potential was  $1.05 \text{ V}_{RHE}$ . The numerical IPCE reproduced well the experimental IPCE spectra as depicted in Fig. 4.4, with a  $R^2$  value of 0.998. Using a flatband potential of  $0.73 \text{ V}_{RHE}$ , the IPCE analysis led to the same  $R^2$  value of 0.998. Thus, the flatband potential did not affect the goodness of the IPCE fit. Indeed, the IPCE measurements were conducted at  $0 \text{ V}_{RHE}$ , a potential region far from the onset potential (of ca.  $0.9 \text{ V}_{RHE}$ ) where the flatband potential does not affect much the photocurrent[104]. However, the diffusion length slightly varied from 1 to  $1.8 \text{ }\mu\text{m}$  and  $R_{S,V_{IPCE}}$  from 0.97 to 0.84 with respect to a flatband potential of  $1.05 \text{ V}_{RHE}$  and  $0.73 \text{ V}_{RHE}$ , respectively. The variation in  $R_{S,V_{IPCE}}$  represented, respectively, a surface recombination loss of 2% to 11% at 500 nm. We conclude that the flatband potential does not affect significantly the diffusion length in a potential region far from the onset potential. However, the estimation of the surface recombination loss should be carefully evaluated keeping in mind its sensitivity towards the flat band potential.

### A4.2.3. Doping concentration

The impact on the determination of the diffusion length using different doping concentration was investigated using the p-Cu<sub>2</sub>O photocathode[169]. A diffusion length of  $7.9 \text{ }\mu\text{m}$  was obtained for a doping concentration of  $10^{10} \text{ cm}^{-3}$ , a diffusion length of  $1 \text{ }\mu\text{m}$  obtained at a doping concentration of  $7.1 \times 10^{13} \text{ cm}^{-3}$ , and a diffusion length of  $5.5 \text{ }\mu\text{m}$  for a doping concentration of  $10^{18} \text{ cm}^{-3}$ . A variation in the doping concentration of eight orders of magnitude induced a variation of the diffusion



length within the same order of magnitude. The variation was reduced for smaller doping concentration variations, i.e. the diffusion length varied between 4.8  $\mu\text{m}$  to 5.5  $\mu\text{m}$  with respect to a doping concentration variation of  $10^{15} \text{ cm}^{-3}$  to  $10^{18} \text{ cm}^{-3}$ . The fitting quality of the IPCE was significantly impacted by the doping concentration with a  $R^2=0.3$  at a doping concentration of  $10^{12} \text{ cm}^{-3}$  to a  $R^2=0.8$  at a doping concentration of  $10^{13} \text{ cm}^{-3}$ . The  $R^2$  value was above 0.98 for a doping concentration above  $10^{15} \text{ cm}^{-3}$ . The surface recombination loss was also significantly impacted by the doping concentration with a loss of 2% at doping concentration of  $10^{12} \text{ cm}^{-3}$ , a loss of 15% at  $10^{15} \text{ cm}^{-3}$ , and a loss of 8% at  $10^{18} \text{ cm}^{-3}$ .

Thus, a diffusion length in the right order of magnitude can be predicted even when using a rough estimation of the doping concentration. However, the surface recombination loss is more affected by the doping concentration and needs to be precisely known to have an accurate estimation of the surface recombination loss.

### A4.2.4. Relative permittivity

The relative permittivity affects the SCR width (eqn (17)) and, thus, can influence the determination of the diffusion length. Since the doping concentration is also affecting the SCR width (eqn (17)), one material with low doping concentration and one with high doping concentration was investigated using, respectively, the p-Cu<sub>2</sub>O photocathode[169] and the n-Fe<sub>2</sub>O<sub>3</sub> photoanode[23]. The permittivity was varied from 1 to 80, an interval which includes the permittivity of all the materials investigated in this work and of most semiconductor materials such as III-V semiconductors[236] (7.1 for BN to 16.2 for Ge) and metal oxides[237] (2.25 for SiO<sub>2</sub> to 7.8 for TiO<sub>2</sub>). Although, the value of the relative permittivity of a material can vary in a larger range, the relative permittivity of most semiconductors stays within 1 to 80—1 for LiF[237] to 80 for TiO<sub>2</sub>[238]. A permittivity of 1 and 80 with a doping concentration of  $7.1 \times 10^{13} \text{ cm}^{-3}$  for the p-Cu<sub>2</sub>O photocathode[169] gave a diffusion length of 4.2  $\mu\text{m}$  and 2.4  $\mu\text{m}$ , respectively, with a non-linear relation between permittivity and diffusion length. A diffusion length of 1  $\mu\text{m}$  was found for the actual permittivity of Cu<sub>2</sub>O, which is 7.5[190]. The surface recombination loss varied significantly with the permittivity, namely from 15% with a permittivity of 1 to 0.5% with a permittivity of 80. For the same material but with a doping concentration of  $10^{18} \text{ cm}^{-3}$ , the diffusion length remained constant at 5.5  $\mu\text{m}$  for the permittivity varying between 1 and 80. The  $R^2$  of the IPCE fitting remained at 0.98 for all permittivities, slightly lower than 0.998 obtained with a doping concentration

of  $7.1 \times 10^{13} \text{ cm}^{-3}$  and a permittivity of 7.5. The surface recombination loss remained also constant at 9% for varying permittivity at a doping concentration of  $10^{18} \text{ cm}^{-3}$ .

The diffusion length varied from 9.8 nm to 10 nm when varying the permittivity from 1 to 80 for the n- $\text{Fe}_2\text{O}_3$  photoanode with a doping concentration of  $2.6 \times 10^{18} \text{ cm}^{-3}$  [23]. A lower diffusion length of 5.5 nm was obtained by using the actual permittivity of  $\text{Fe}_2\text{O}_3$ , which is 32 [22].  $R^2$  decreased from 0.98 to 0.91 with a permittivity of 1 to 80, respectively. The surface recombination losses were 27%, 23%, and 33% with a relative permittivity of 1, 32, and 80, respectively.

The calculated diffusion length remained within the same order of magnitude when varying the relative permittivity from 1 to 80. The permittivity has a more significant impact on the surface recombination loss, although dependent on the material, i.e. the variation was 10% with  $\text{Fe}_2\text{O}_3$  and 14% with  $\text{Cu}_2\text{O}$ . An accurate value of the relative permittivity should be a priority for the estimation of the surface recombination loss.

#### A4.2.5. Photoelectrode thickness

The thickness of the photoelectrode does neither influence the IPCE fitting nor the diffusion length nor the surface recombination loss, as long as the thickness of the photoelectrode is larger than the SCR width (a limitation of our model, see section 4.2.6) and the diffusion length. The latter might be problematic since the IPCE analysis is supposed to determine the diffusion length by knowing the photoelectrode thickness. However, in reality the diffusion length is usually smaller than the thickness of the photoelectrode or even the SCR. For example, the SCR width at 0  $V_{\text{RHE}}$  in the p- $\text{Cu}_2\text{O}$  photoelectrode with a doping concentration of  $7.1 \times 10^{13} \text{ cm}^{-3}$  was  $3.47 \text{ }\mu\text{m}$  and the photoelectrode thickness was  $50 \text{ }\mu\text{m}$  [169], both larger than the determined diffusion length of  $1 \text{ }\mu\text{m}$ . Thus, varying the thickness from  $3.47 \text{ }\mu\text{m}$  and above did neither influence the IPCE fitting nor the diffusion length nor the surface recombination loss. The diffusion lengths of most materials investigated in this work are few nanometers only, much smaller than the typical thickness of the electrode and the SCR. In the case of p-Si photocathode with an estimated diffusion length of  $50 \text{ }\mu\text{m}$  (Table 4.2), no impact on the results was observed when reducing the photoelectrode thickness down to  $50 \text{ }\mu\text{m}$ . However below that thickness, the model was not able to follow the experimental IPCE spectra and instead tried to compensate for the lack of absorbed light by infinitely increasing the diffusion length. Thus, an overestimation of the thickness is better than an underestimation, if the photoelectrode thickness is unknown.

### A4.2.6. Minority charge carrier mobility

The charge carrier mobility was varied within  $10^{-3} \text{ cm}^2 \text{ V}^{-1} \text{ s}^{-1}$  to  $10^3 \text{ cm}^2 \text{ V}^{-1} \text{ s}^{-1}$  without affecting the IPCE nor the determination of the diffusion length for any of the materials investigated in this work. The charge carrier mobility—related to the diffusion coefficient by the Einstein relation—influences the photocurrent through the bulk contribution only by the term  $\frac{L}{L+D/S}$  (eqn (A4.1)). Therefore, if  $D/S \ll L$ , the mobility does not influence the photocurrent and neither does the surface parameter,  $S$ , given by eqn (A4.12). In the case of the diffusion length being large (i.e. for a mobility  $> 10^3 \text{ cm}^2 \text{ V}^{-1} \text{ s}^{-1}$ ), the diffusion length is divided by the surface velocity factor given by eqn (A4.1). This factor increases exponentially with the applied potential and is always much larger than the diffusion coefficient even at low applied potential, i.e. fourteen orders of magnitude larger than the diffusion coefficient for p-Cu<sub>2</sub>O at 0 V<sub>RHE</sub>. Thus, the surface velocity factor appears to cancel any influence of the mobility (or diffusion coefficient) on the photocurrent. In other words, the mobility can be set to any values between  $10^{-3} \text{ cm}^2 \text{ V}^{-1} \text{ s}^{-1}$  to  $10^3 \text{ cm}^2 \text{ V}^{-1} \text{ s}^{-1}$  without having any impact on the determination of the diffusion length or surface recombination loss. This observation is very convenient since the minority charge carrier mobility is usually unknown for novel semiconductor materials. Moreover, the determination of the charge mobility involves demanding experiments such as time resolved microwave conductivity measurements (TRCM)[239] that can actually not differentiate minority or majority charge carrier mobility. Simpler experiments are also possible like Hall effect measurements. However, Hall effect measurements require clean ohmic contacts in the semiconductor which is not always possible due to the morphology of the photoelectrode or because it creates a Schottky contact instead of an ohmic contact.

The mobility can play a role if the IPCE is measured in a potential region where the space charge region potential is below 0.23V, corresponding to the exponential term  $e^{\Delta\phi_{sc}/V_{th}}$  in eqn (4.10) being below  $10^4$ . In that case,  $S$  might not be large enough to cancel the influence of the charge mobility on the photocurrent. However, such a case is not likely to happen since photoelectrodes are not performing well under low applied potentials because of the electric field in the SCR being not sufficient to drive the water-splitting reaction.

#### A4.2.7. Surface states distribution factor

The surface states distribution factor is a parameter specific to the numerical IPCE model used here (eqn (4.9)). This parameter is not generally mentioned in the literature, except for the work of Wilson[60] on which our model is based. Thus, its impact on the determination of the diffusion length must be carefully investigated. The sensitivity of the diffusion length on  $\beta$  was investigated with the p-Cu<sub>2</sub>O photocathode[169]. Although the shape of the  $I$ - $V$  curves is affected by  $\beta$  (Fig. A4.3), the diffusion length of p-Cu<sub>2</sub>O remains constant at 1  $\mu\text{m}$  with  $1 < \beta < 20 \text{ eV}^{-1}$ , a range of values similar to the work of Wilson[60]. The normalized experimental  $I$ - $V$  curve in Fig. A4.3 is the  $I$ - $V$  curve measured by Niu et al.[169] under standard solar irradiance AM1.5G divided by a photocurrent of  $-6.63 \text{ mA cm}^{-2}$  obtained at  $0.2 V_{\text{RHE}}$ . Similarly, the normalized numerical  $I$ - $V$  curves were obtained by dividing the  $I$ - $V$  curves under standard solar irradiance AM1.5G by the photocurrent obtained at  $-0.2 V_{\text{RHE}}$ . An infinite surface states distribution factor indicates a single discrete surface state recombination process.  $R_{\text{S},V_{\text{IPCE}}}$  varied from 0.967 with  $\beta=1 \text{ eV}^{-1}$  to 0.987 with  $\beta=20 \text{ eV}^{-1}$ . This variation in  $\beta$  resulted in a surface recombination loss difference of only 1% at 500nm (2% surface recombination loss at 500nm with  $\beta=1 \text{ eV}^{-1}$  and 1% with  $\beta=20 \text{ eV}^{-1}$ ). Thus, the determination of the diffusion length and the ratio of currents does not significantly dependent on  $\beta$  and any values between 1 and  $20 \text{ eV}^{-1}$  could be selected. Even though here we do not aim at optimizing the fitting of experimental  $I$ - $V$  curves, the normalized experimental  $I$ - $V$  curve were best fitted with  $\beta=7 \text{ eV}^{-1}$  for Cu<sub>2</sub>O photocathode (Fig. A4.3). Moreover, the shape of the numerical  $I$ - $V$  curve with  $\beta=7 \text{ eV}^{-1}$  was similar to usual experimental ones. Thus,  $\beta=7 \text{ eV}^{-1}$  was selected for all photoelectrode materials used in this work.

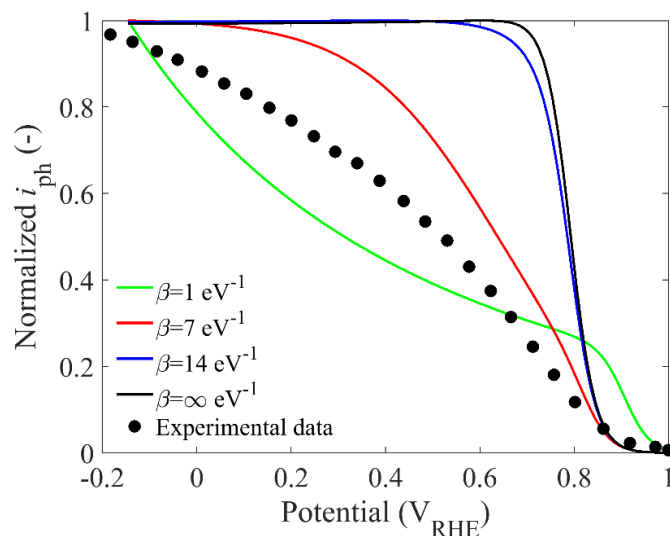


**Fig. A4.3.** Normalized numerical  $I$ - $V$  curves of p-Cu<sub>2</sub>O photocathode for varying surface states distribution factor (eqn (4.9)). The numerical normalization is the  $I$ - $V$  curves under AM1.5G divided by the photocurrent at -0.2 V<sub>RHE</sub>. The experimental  $I$ - $V$  curve of p-Cu<sub>2</sub>O photocathode was taken from Niu et al.[169] under AM1.5G and normalized by the photocurrent density of -6.63 mA cm<sup>-2</sup> obtained at -0.2 V<sub>RHE</sub>.

#### A4.2.8. Applied potential of the IPCE

Our numerical IPCE model is developed to work at any applied potential. However, an IPCE is measured at a fixed potential,  $V_{\text{IPCE}}$ , and often it is reported at a single applied potential only. Thus, we need to ensure that the diffusion length obtained by our screening method is independent of the choice of  $V_{\text{IPCE}}$ . In contrast, the surface recombination loss depends on  $V_{\text{IPCE}}$ , as depicted in Fig. A4.4. The impact of  $V_{\text{IPCE}}$  on the determination of the surface recombination loss and the diffusion length was investigated using Cu<sub>2</sub>V<sub>8</sub>O<sub>3</sub> photoanode with experimental IPCEs measured at 1.21 V<sub>RHE</sub> and 1.71 V<sub>RHE</sub>[174]. As depicted in Fig. A4.4, the surface recombination was higher at 1.21 V<sub>RHE</sub> with a surface recombination loss of 9.4% compared to a loss of 5.1% at 1.71 V<sub>RHE</sub>. The diffusion length remained constant at 1.7 nm under both applied potentials, as expected. The IPCE at 320 nm without any surface recombination loss or reflection loss remained at 11.6% at both potentials, as expected. Thus, our method determined the surface recombination loss dependent on  $V_{\text{IPCE}}$  while the diffusion length was independent of  $V_{\text{IPCE}}$ .

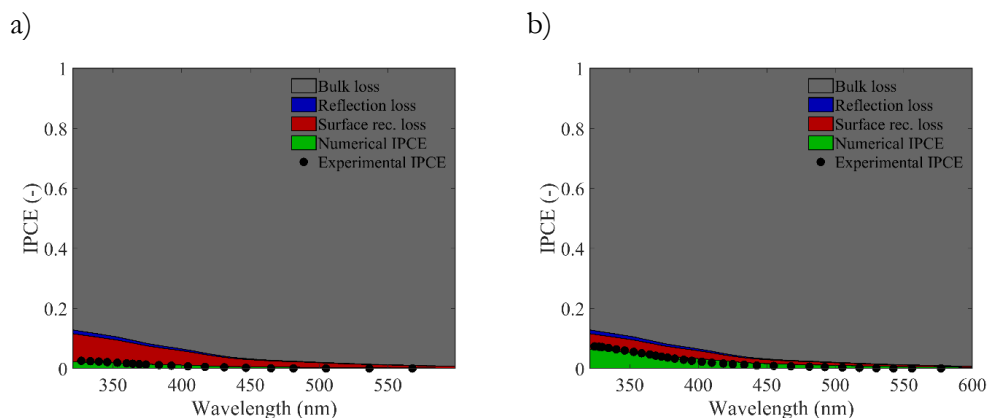


**Fig. A4.4.** Numerical and experimental IPCE at a) 1.21  $V_{\text{RHE}}$  and b) 1.71  $V_{\text{RHE}}$  for a planar n-  $\text{Cu}_2\text{V}_8\text{O}_3$  photoanode with the bulk loss (grey), the reflection loss (blue), the surface recombination loss (red), and the numerical IPCE (green). The numerical IPCE was fitted to the experimental IPCE from Segev et al.[174] (black dots).

In conclusion, a rough estimation of unknown material parameters does not prevent an accurate determination of the diffusion length or the diffusion optical number within the right order of magnitude. Therefore, the nanostructuring opportunity factor of a photoelectrode material can still be estimated. The determination of the surface recombination loss is more sensitive to inaccuracies in the material parameters and should be treated with attentions.

### A4.3. Particle-based $\text{LaTiO}_2\text{N}$ photoelectrode

#### A4.3.1. IPCE measurements

The IPCE measurements of p.-b.  $\text{LaTiO}_2\text{N}$  photoanodes were carried out in a three-electrode setup. The photoanodes were connected to a potentiostat (Bio-Logic VSP-300 controlled by the EC-lab software). The reference electrode was  $\text{Ag}/\text{AgCl}$  (sat.  $\text{KCl}$ ) and the counter electrode was Pt. The aqueous electrolyte solution was 0.1 M  $\text{Na}_2\text{SO}_4$  ( $\text{pH}=13$  by adding  $\text{NaOH}$ ). The applied potential was  $\Phi_{\text{RHE}}=1.23V_{\text{RHE}}$  corresponding to an applied potential vs. the reference electrode of  $\Phi_{\text{Ag}/\text{AgCl}}=0.266 V_{\text{Ag}/\text{AgCl}}$  using the equation

$$\Phi_{\text{Ag/AgCl}} = \Phi_{\text{RHE}} - \Phi_{\text{Ag/AgCl vs. SHE}}^0 - 0.059\text{pH}, \quad (\text{A4.15})$$

where  $\Phi_{\text{Ag/AgCl vs. SHE}}^0$  is the Ag/AgCl reference electrode with respect to the standard hydrogen electrode.  $\Phi_{\text{Ag/AgCl vs. SHE}}^0$  is 0.197 V at 25 °C for Ag/AgCl reference electrode filled with sat. KCl. The IPCE of p.-b. LaTiO<sub>2</sub>N photoanodes were measured under back illumination using each light-emitting diode (LED) of a solar simulator Verasol-2 from Oriel (Fig. A4.5). The photon flux of each LED was preliminary measured with a calibrated Si diode (FDS1010-CAL from Thorlabs). The wavelengths at which the IPCE was measured correspond to the maximum of the spectral photon flux of each LED. The spectral photon flux of each LED was measured by an UV-Vis spectrometer (HR4000CG-UV-NIR from Ocean Optics). The IPCE for each wavelength was the average over the last 5 s of a photocurrent measurement of 10 s at a fixed applied potential of 1.23 V<sub>RHE</sub> to avoid any transient effects in the IPCE measurements.

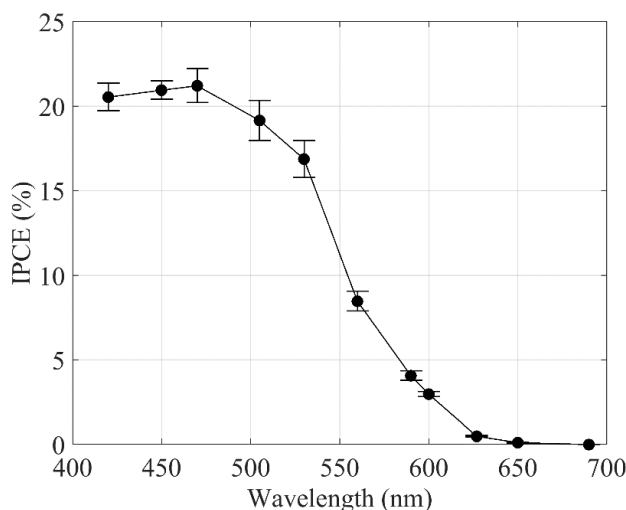


**Fig. A4.5.** IPCE of p.-b. LaTiO<sub>2</sub>N photoanodes at 1.23 V<sub>RHE</sub> under back illumination in 0.1 M Na<sub>2</sub>SO<sub>4</sub> (pH 13 by adding NaOH). The dot points are the average IPCE of four fresh photoelectrodes and the error bars are the IPCE measurement variations.

### A4.3.2. Complex refractive index

The complex refractive index,  $\tilde{n} = n - ik$ , of LaTiO<sub>2</sub>N was calculated by density functional theory (DFT) with the PBEsol functional[240] using the VASP code[241]–[244]. We used the virtual crystal approximation (VCA) to represent anion disorder with PAW potentials[245], [246] with La (5s, 5p, 5d, 6s), Ti (3p, 3d, 4s), O (2s, 2p) and N(2s, 2p) valence shells. Wave functions were expanded in plane-waves with a cutoff of 550 eV and reciprocal space was sampled with a 6x6x4 k-mesh for the 20-atom orthorhombic cell. The complex frequency-dependent dielectric tensor ( $\epsilon$ ) was then calculated within the independent-particle approximation determining the imaginary part by summation over all conduction band states, while the real part was determined via the Kramers-Kronig transformation. Finally, we determined the real part of the complex refractive index ( $n$ ) and imaginary part of the complex refractive index ( $k$ ) along  $x$ ,  $y$  and  $z$  directions as shown in Fig. A4.6 from the diagonal elements via

$$\begin{aligned} n_i &= \sqrt{\frac{1}{2} \left( \sqrt{\epsilon_{i,\text{real}}^2 + \epsilon_{i,\text{im}}^2} + \epsilon_{i,\text{real}} \right)} \text{ and} \\ k_i &= \sqrt{\frac{1}{2} \left( \sqrt{\epsilon_{i,\text{real}}^2 + \epsilon_{i,\text{im}}^2} - \epsilon_{i,\text{real}} \right)}, \end{aligned} \tag{A4.16}$$

where  $i$  is one of the cartesian directions. The absorption coefficient,  $\alpha$ , used in the EQE analysis was calculated based on the mean in all directions of the extinction coefficient and by using  $\alpha = 4\pi k/\lambda$ .



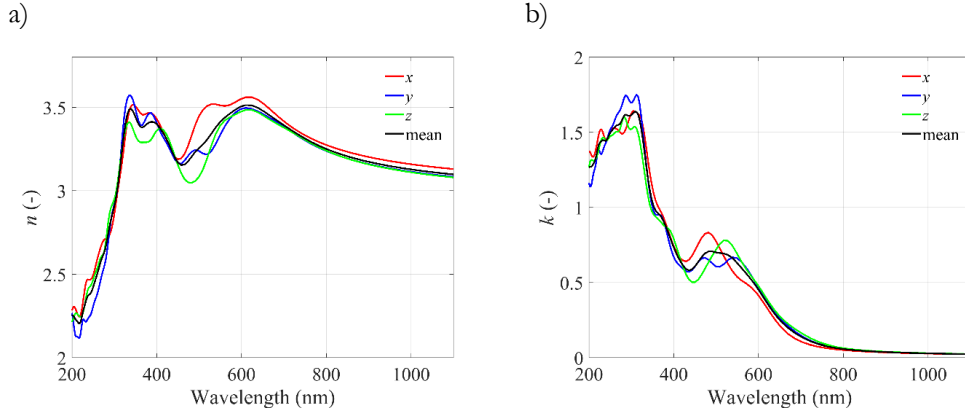


**Fig. A4.6.** Spectral a) real part of the complex refractive index and b) imaginary part of the complex refractive index of LaTiO<sub>2</sub>N in  $x$ ,  $y$  and  $z$  directions and the mean in all directions calculated by DFPT.

#### A4.4. IPCE at 500 nm as a function of doping concentration for Si

The IPCE at 500 nm as a function of doping concentration with a fixed diffusion length of 50  $\mu\text{m}$  and with a diffusion length as a function of the doping concentration were calculated for a planar p-Si photocathode covered by a  $\sim 80\text{nm}$  mesoporous hematite layer[185] (Fig. A4.7). The relation for the diffusion length as a function of the doping concentration was calculated using  $L(N_A^-) = [D(N_A^-) \cdot \tau(N_A^-)]^{1/2}$  where  $D(N_A^-) = \mu(N_A^-) \cdot V_{\text{th}}$  and is depicted in Fig. A4.7. b). The lifetime,  $\tau$ , and the mobility,  $\mu$ , as function of the acceptor doping concentration,  $N_A^-$ , were taken from Tyagi and Van Overstraeten[194]. As expected, the IPCE with a fixed diffusion length does not tend to zero with the doping concentration while the IPCE with the diffusion length as a function of the doping concentration tends to zero under high doping concentration (Fig. A4.7).

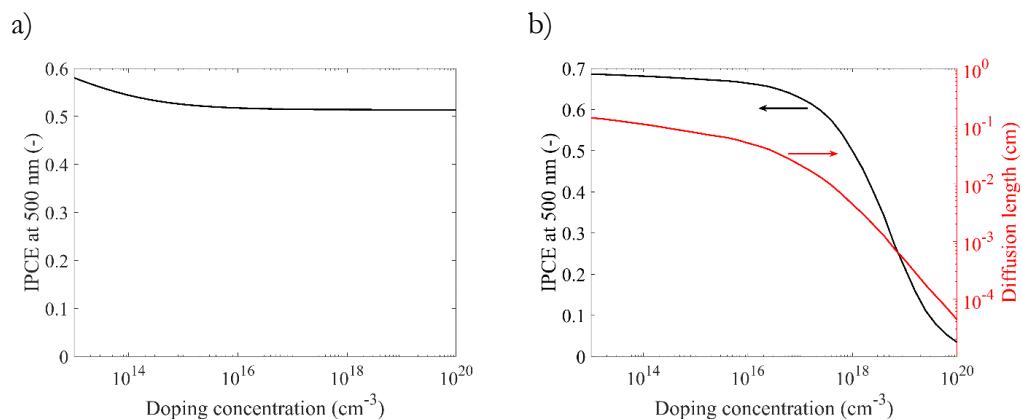


**Fig. A4.7.** Calculated IPCE at 500 nm as a function of the doping concentration for a planar p-Si photocathode covered by a ~80nm mesoporous hematite layer[185] with a) a fixed diffusion length of 50  $\mu\text{m}$  and b) a diffusion length as a function of the doping concentration. The relation of the diffusion length as a function of the doping concentration is given on the right y-axis of figure b).

# Appendix of chapter 5

## A5.1. Indium content measurements of $\text{In}_x\text{Ga}_{1-x}\text{N}$

The indium content of the fabricated  $\text{In}_x\text{Ga}_{1-x}\text{N}$  photoelectrode was measured by X-ray diffraction (XRD) (Fig. A5.1).

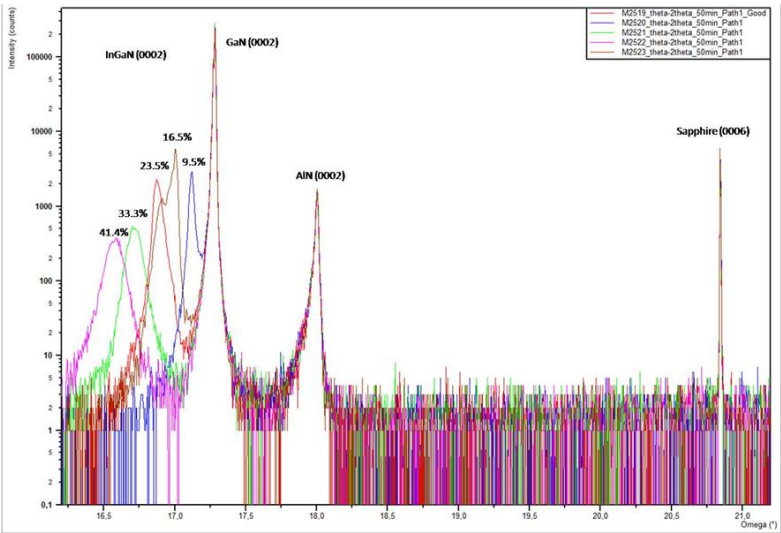


**Fig. A5.1.** X-ray diffraction spectra and indium contents in percentage of the fabricated  $\text{In}_x\text{Ga}_{1-x}\text{N}$  photoelectrodes.

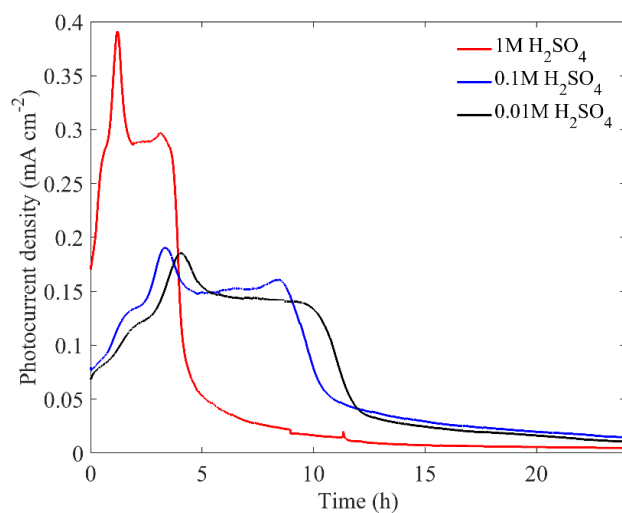
### A5.2. Conductivity and photocorrosion measurements of the prepared $\text{In}_x\text{Ga}_{1-x}\text{N}$ photoelectrodes

The ohmic contacts of the prepared  $\text{In}_x\text{Ga}_{1-x}\text{N}$  photoelectrodes (Fig. 5.3) were tested by measuring the resistance between two contacts separated by a distance of 3 mm (Table A5.1). The resistance was always below 16  $\Omega$ , a negligible resistance since the measured photocurrent was always below 0.25 mA (maximum 4 mA  $\text{cm}^{-2}$  as depicted in Fig. 5.6), which provides a potential shift of only 4 mV.

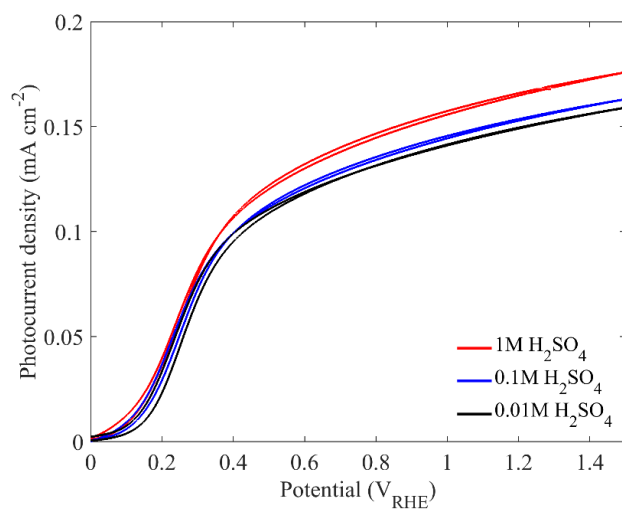
**Table A5.1.** Measured surface area and ohmic resistance between two ohmic contacts separated by a distance of 3 mm of the prepared  $\text{In}_x\text{Ga}_{1-x}\text{N}$  photoelectrodes.

Indium content (%)	Surface area ( $\text{cm}^2$ )	Ohmic resistance ( $\Omega$ )
9.5	0.0860	12
16.5	0.0457	16
23.5	0.0520	11
33.3	0.0530	11
41.4	0.0594	10

The impact of the photocorrosion for different sulfuric acid concentrations was investigated using GaN photoelectrodes. Three different concentration were used: 1 M, 0.1 M and 0.01 M  $\text{H}_2\text{SO}_4$ . An UV light-emitting diode (LED) with a nominal wavelength at 368 nm and an irradiance of 9.9 mW  $\text{cm}^{-2}$  was used as light source. The photocurrent only dropped after 4 h in 1 M  $\text{H}_2\text{SO}_4$  as depicted in Fig. A5.2, a timescale largely sufficient to perform all the measurements required in this work for  $\text{In}_x\text{Ga}_{1-x}\text{N}$  photoelectrodes. We could also observe, independently of the sulfuric acid concentrations, an increase over time of the photocurrent before starting to drop completely. This increase was attributed to an increase of the active surface area caused by the corrosion of the surface that finally leads to a completely damaged photoelectrode. Since the photocurrent was larger under higher concentration as confirmed by cyclic voltammetry (Fig. A5.3) and that the photoelectrodes are sufficiently stable over time, 1 M  $\text{H}_2\text{SO}_4$  was used to perform the  $I$ - $V$  curves measurements of  $\text{In}_x\text{Ga}_{1-x}\text{N}$  photoelectrodes.



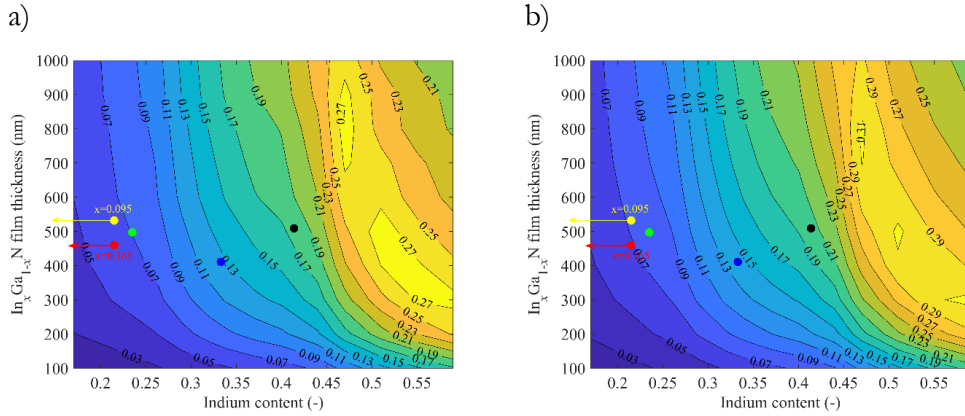
**Fig. A5.2.** Photocurrent density over 24 hours of pure GaN photoelectrodes at 1.23V<sub>RHE</sub> in 1 M, 0.1 M and 0.01 M H<sub>2</sub>SO<sub>4</sub> under UV light with a nominal wavelength at 368 nm and an irradiance of 9.9 mW cm<sup>-2</sup>.



**Fig. A5.3.** Cyclic voltammograms of GaN photoelectrode in 1 M, 0.1 M and 0.01 M H<sub>2</sub>SO<sub>4</sub> under UV light with a nominal wavelength at 368 nm and an irradiance of 9.9 mW cm<sup>-2</sup>.

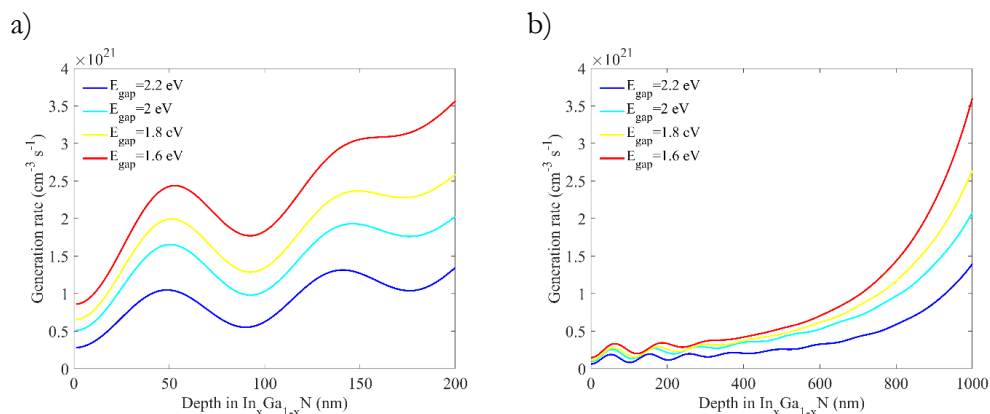
### A5.3. Photogeneration efficiency of $\text{In}_x\text{Ga}_{1-x}\text{N}/\text{Si}$ tandem photoelectrodes

The photogeneration efficiencies for varying thicknesses and indium contents of  $\text{In}_x\text{Ga}_{1-x}\text{N}/\text{Si}$  tandem water-splitting photoelectrode with and without reflection loss are depicted in Fig. A5.4.

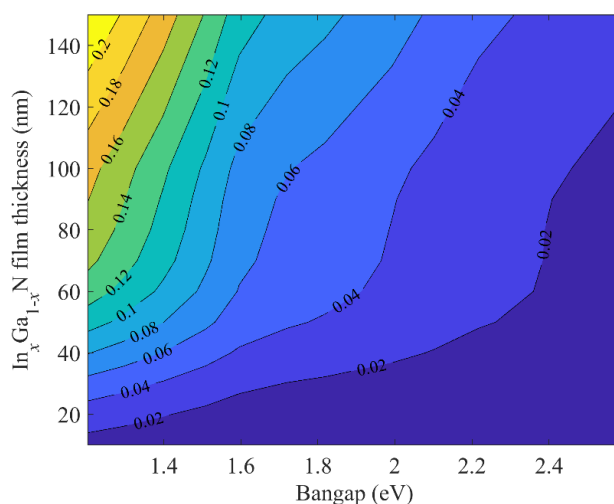


**Fig. A5.4.** Photogeneration efficiency of  $\text{In}_x\text{Ga}_{1-x}\text{N}/\text{Si}$  tandem water-splitting photoelectrode depending on film thickness and indium a) with and b) without reflection loss at the  $\text{In}_x\text{Ga}_{1-x}\text{N}/\text{water}$  interface.

The forward and backward-waves interferences are significant for ultrathin  $\text{In}_x\text{Ga}_{1-x}\text{N}$  layer ( $\leq 200$  nm) as depicted in Fig. A5.5.a. In contrast, the generation rate is less influenced by the wave interferences and follows more a Beer-Lambert's law for thicker layer as depicted in Fig. A5.5.b for an  $\text{In}_x\text{Ga}_{1-x}\text{N}$  layer of 1000 nm.



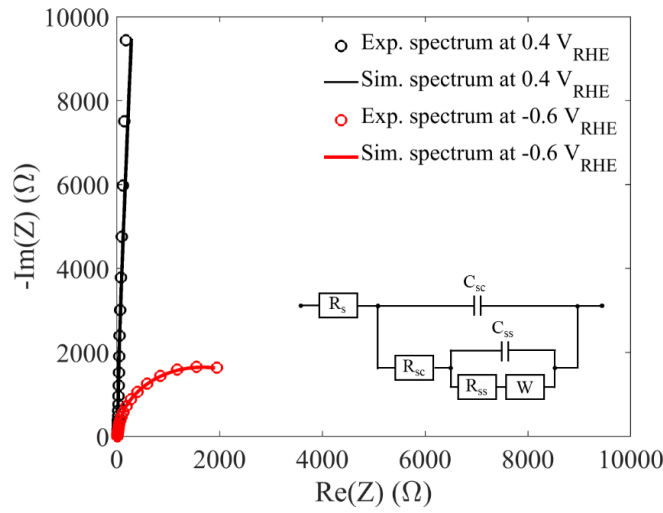
**Fig. A5.5.** Generation rate along the  $\text{In}_x\text{Ga}_{1-x}\text{N}$  thickness of  $\text{In}_x\text{Ga}_{1-x}\text{N}/\text{Si}$  tandem water-splitting photoelectrode for varying bandgap and a thickness of a) 200 nm and b) 1000 nm. The photogeneration efficiency of ultrathin  $\text{In}_x\text{Ga}_{1-x}\text{N}$  film on  $350 \mu\text{m}$  Si layer as water-splitting photoelectrode depending on film thickness and bandgap is depicted in Fig. A5.6. Ultrathin  $\text{In}_x\text{Ga}_{1-x}\text{N}$  does not show any resonant trapping effect. The efficiency is driven by Beer-Lambert's law light absorption, i.e. increasing the thickness and reducing the bandgap increases the efficiency.



**Fig. A5.6.** Photogeneration efficiency of ultrathin  $\text{In}_x\text{Ga}_{1-x}\text{N}$  film on  $350 \mu\text{m}$  Si layer as water-splitting photoelectrode depending on film thickness and bandgap with reflection loss at the  $\text{In}_x\text{Ga}_{1-x}\text{N}/\text{water}$  interface.

#### A5.4. Mott-Schottky analysis

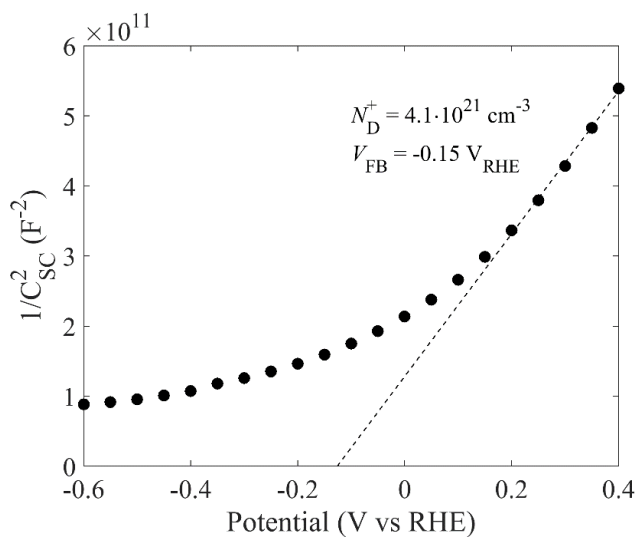
The experimental and simulated impedance spectra of  $\text{In}_{0.414}\text{Ga}_{0.586}\text{N}$  photoelectrodes under dark conditions in 1 M  $\text{H}_2\text{SO}_4$  at 0.4  $V_{\text{RHE}}$  and -0.6  $V_{\text{RHE}}$  are depicted in Fig. A5.7. The value of each electronic circuit component was determined using the Z fit tool available in the EC-Lab software with the randomize and simplex method and 5000 maximum iterations.



**Fig. A5.7.** Experimental and simulated impedance spectra of  $\text{In}_{0.414}\text{Ga}_{0.586}\text{N}$  photoelectrodes under dark conditions in 1 M  $\text{H}_2\text{SO}_4$  at 0.4  $V_{\text{RHE}}$  and -0.6  $V_{\text{RHE}}$ . The equivalent circuit for the electrochemical impedance spectra fit is also indicated. At 0.4  $V_{\text{RHE}}$ , the electrical components values are  $R_s=11.22 \, \Omega$ ,  $R_{sc}=338.7 \, \Omega$ ,  $R_{ss}=9.955 \cdot 10^4 \, \Omega$ ,  $C_{sc}=1.362 \cdot 10^{-6} \, \text{F}$ ,  $C_{ss}=2.801 \cdot 10^{-6} \, \text{F}$ , and  $W=1.239 \cdot 10^6 \, \Omega \, \text{s}^{-0.5}$ . At -0.6  $V_{\text{RHE}}$ , the electrical components values are  $R_s=11.06 \, \Omega$ ,  $R_{sc}=257.4 \, \Omega$ ,  $R_{ss}=304.8 \, \Omega$ ,  $C_{sc}=3.363 \cdot 10^{-6} \, \text{F}$ ,  $C_{ss}=8.713 \cdot 10^{-6} \, \text{F}$ , and  $W=152.8 \, \Omega \, \text{s}^{-0.5}$ .

The space charge layer capacitance,  $C_{sc}$ , at varying potentials of  $\text{In}_{0.414}\text{Ga}_{0.586}\text{N}$  photoelectrodes is depicted in a Mott-Schottky plot (Fig. A5.8) from which the doping concentration and the flatband concentration can be determined[74]. The same equivalent circuit and the same approach was used to provide the doping concentration and flatband potential for all the  $\text{In}_x\text{Ga}_{1-x}\text{N}$  photoelectrodes (Fig. 5.7 and Table 5.1).

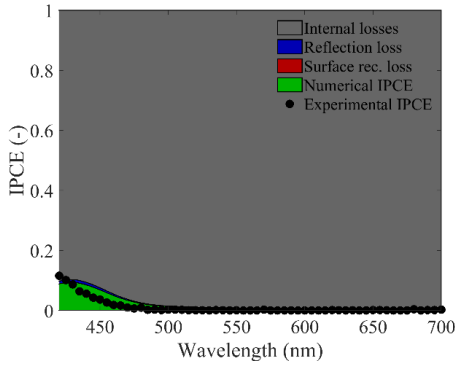
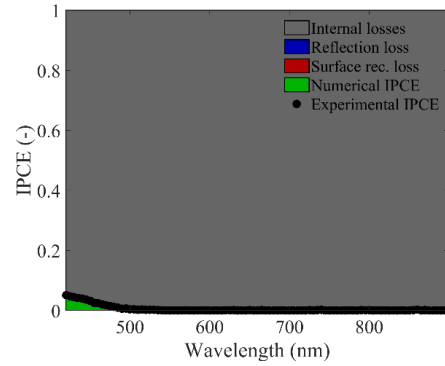
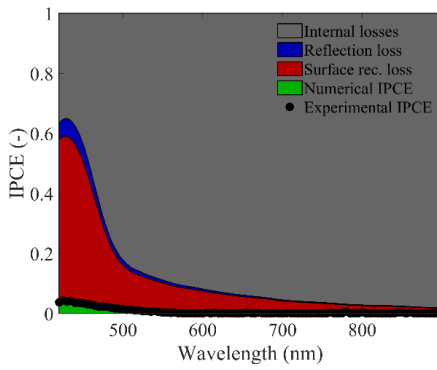
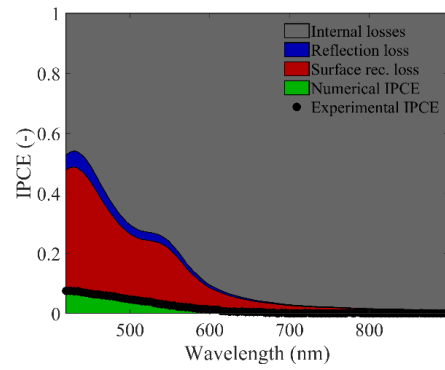
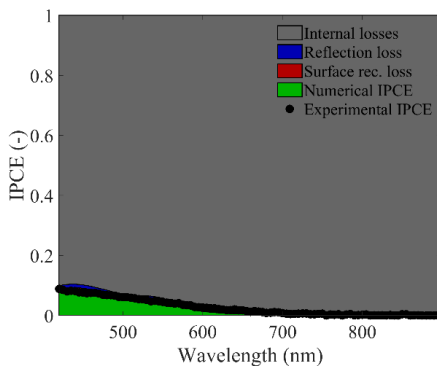




**Fig. A5.8.** Mott-Schottky plot of the space charge layer capacitance,  $C_{SC}$ , of  $\text{In}_{0.414}\text{Ga}_{0.586}\text{N}$  photoelectrodes under dark conditions in 1 M  $\text{H}_2\text{SO}_4$ . The calculated doping concentration and flatband potential are also indicated.

### A5.5. Numerical and experimental IPCE

The numerical and experimental IPCEs of  $\text{In}_x\text{Ga}_{1-x}\text{N}$  with varying indium content and with the internal loss, the reflection loss, and the surface recombination loss are depicted in [Fig. A5.9](#).

a)  $\text{In}_x\text{Ga}_{1-x}\text{N}$  with  $x=0.095$ b)  $\text{In}_x\text{Ga}_{1-x}\text{N}$  with  $x=0.165$ c)  $\text{In}_x\text{Ga}_{1-x}\text{N}$  with  $x=0.235$ d)  $\text{In}_x\text{Ga}_{1-x}\text{N}$  with  $x=0.333$ e)  $\text{In}_x\text{Ga}_{1-x}\text{N}$  with  $x=0.414$ 

**Fig. A5.9.** Numerical and experimental IPCE at 1.23  $V_{\text{RHE}}$  for  $\text{In}_x\text{Ga}_{1-x}\text{N}$  water-splitting photoanodes in 1 M  $\text{Na}_2\text{SO}_4$  and indium content of a)  $x=0.095$ , b)  $x=0.165$ , c)  $x=0.235$ , d)  $x=0.333$ , e)  $x=0.414$ . The internal losses are in grey, the reflection loss in blue, the surface recombination loss in red, the numerical IPCE in green, and the experimental IPCEs are depicted with black dots.

# Appendix: POPe manual

## A6

### A6.1. Instructions

The instructions to use the POPe software can also be found directly in the information tab of POPe (Fig. A6.1).

1. Click select folder.
2. Select the folder containing the IPCE and the complex refractive index data of the investigated PE material with the dialog box (click "select the folder").
3. Data files must be in txt format as the data provided with the software. The name of the folder will automatically appear in the material text box.
4. Setup up all the required parameters such as bandgap, flatband potential, doping concentration, etc. Default parameters are for nano\_Fe<sub>2</sub>O<sub>3</sub>\_CoBi.
5. Choose a range of values for the surface recombination velocity and the diffusion length. If no maximum appears in the R<sub>2</sub> of IPCE fitting plot, click reset and increase the range of values and run the calculation again. Repeat the operation until you find a maximum.
6. Reduce or increase the calculation time by decreasing or increasing the number of points per decades. Higher number of points give higher resolution but longer calculation time. The numerical IPCE with the different losses is automatically saved as a txt file in the folder.
7. Click save to save a print of all the results and graphs. Make sure to minimize all other windows or close all other software before clicking the button save.

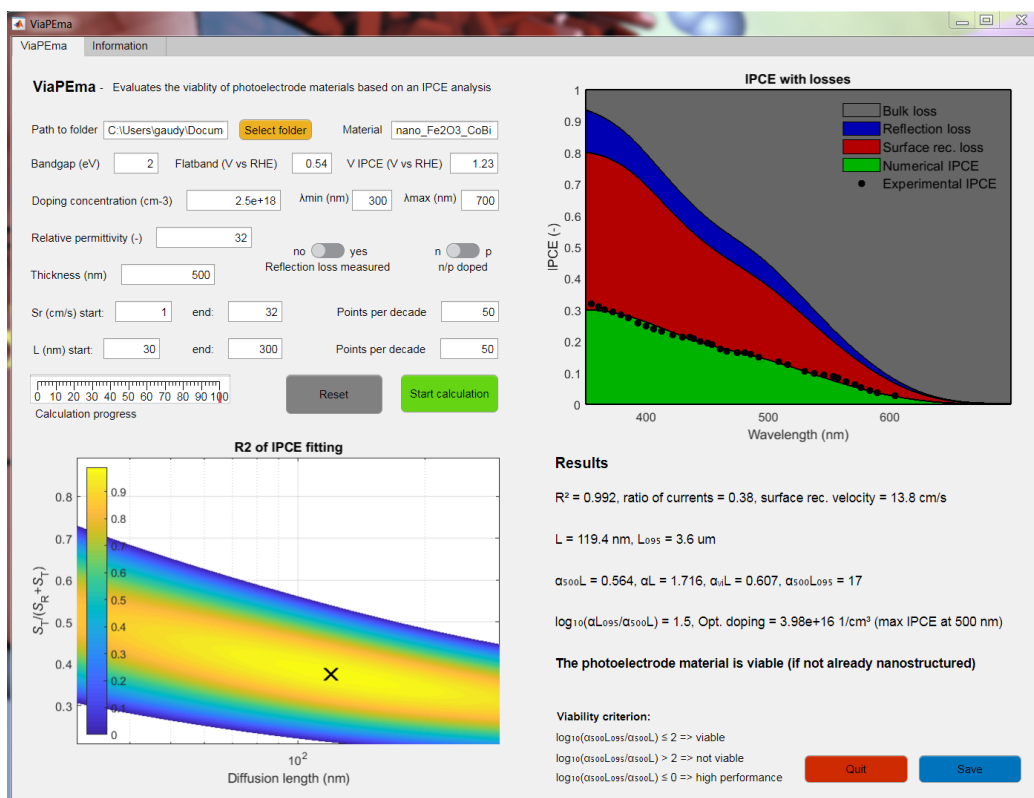


**Fig. A6.1.** Print screen of the software POPe after running the calculation for nanostructured Fe<sub>2</sub>O<sub>3</sub> with CoBi catalysts[188].

## A6.2. Description of the results

The description of the results can also be found directly in the information tab of POPe (Fig. A6.1).

1.  $R^2$  is the R-square value of the IPCE fitting between the experimental and the numerical IPCE.
2. The ratio of currents is the ratio of water splitting current and the total current at the potential at which the IPCE is measured. In other words, the ratio of the surface charge transfer velocity that contributes to the water-splitting reaction,  $S_T$ , and the sum of the surface recombination velocity,  $S_R$ , and  $S_T$
3. The surface rec. velocity is the surface recombination velocity  $S_R$  at the potential at which the IPCE is measured.  $S_T$  is by default 0.01 cm s<sup>-1</sup>.

4.  $L_{095}$  is the diffusion length that provides  $\text{IQE} \geq 95\%$  at 500 nm while fixing the surface recombination to zero.
5.  $\alpha_{500}L$  is the diffusion optical number at 500 nm, the product of the absorption coefficient at 500 nm and the extracted diffusion length.
6.  $\alpha L$  is the averaged diffusion optical number, the product of the absorption coefficient from the minimum wavelength to the maximum one and the extracted diffusion length.
7.  $\alpha_{\text{vis}}L$  is the visible diffusion optical number, the product of the absorption coefficient from 400 nm to the maximum wavelength and the extracted diffusion length.
8.  $\alpha_{500}L_{095}$  is the diffusion optical number that provides  $\text{IQE} \geq 95\%$  at 500 nm, the product of the absorption coefficient at 500 nm and  $L_{095}$ .
9.  $\log_{10}(\alpha_{500}L_{095}/\alpha_{500}L)$  is the nanostructuring opportunity factor. If greater than two the material cannot perform well even if nanostructured. If smaller than two the material can highly perform if nanostructured. If smaller than 0 the material is highly performing without nanostructuring.
10. Opt. doping is the optimal doping concentration that optimize the IPCE at 500 nm using the extracted diffusion length of the material.

# Bibliography

- [1] M. R. Allen *et al.*, “Warming caused by cumulative carbon emissions towards the trillionth tonne,” *Nature*, vol. 458, no. 7242, pp. 1163–1166, 2009.
- [2] International Energy Agency, “Key world energy statistics,” 2017.
- [3] J. G. Speth, “The transition to a sustainable society,” *Proc. Natl. Acad. Sci. USA*, vol. 89, no. 3, pp. 870–872, 1992.
- [4] N. S. Lewis and D. G. Nocera, “Powering the planet: Chemical challenges in solar energy utilization,” *PNAS*, vol. 103, no. 42, pp. 15729–15735, 2006.
- [5] M. A. Pellow, C. J. M. Emmott, C. J. Barnhart, and S. M. Benson, “Hydrogen or batteries for grid storage? A net energy analysis,” *Energy Environ. Sci.*, vol. 8, no. 7, pp. 1938–1952, 2015.
- [6] M. Dumortier, S. Tembhurne, and S. Haussener, “Holistic design guidelines for solar hydrogen production by photo-electrochemical routes,” *Energy Environ. Sci.*, pp. 3614–3628, 2015.
- [7] Y. Cheng and S. P. Jiang, “Advances in electrocatalysts for oxygen evolution reaction of water electrolysis-from metal oxides to carbon nanotubes,” *Prog. Nat. Sci. Mater. Int.*, vol. 25, no. 6, pp. 545–553, 2015.
- [8] J. Newman and K. E. Thomas-Alyea, *Electrochemical Systems*, 3rd editio. John Wiley & Sons, Inc., 2001.
- [9] A. J. Bard and L. R. Faulkner, *Electrochemical Methods: Fundamentals and Application*, Second edi. John Wiley & Sons, Inc., 2001.
- [10] C. C. L. McCrory, S. Jung, I. M. Ferrer, S. Chatman, J. C. Peters, and T. F.

## Bibliography

---

- Jaramillo, "Benchmarking HER and OER Electrocatalysts for Solar Water Splitting Devices," *J. Am. Chem. Soc.*, vol. 137, pp. 4347–4357, 2015.
- [11] Z. Xing, X. Zong, J. Pan, and L. Wang, "On the engineering part of solar hydrogen production from water splitting: Photoreactor design," *Chem. Eng. Sci.*, vol. 104, pp. 125–146, 2013.
- [12] M. A. Modestino and S. Haussener, "An Integrated Device View on Photo-Electrochemical Solar-Hydrogen Generation," *Annu. Rev. Chem. Biomol. Eng.*, vol. 6, no. 1, pp. 13–34, 2014.
- [13] A. C. Nielander, M. R. Shaner, K. M. Papadantonakis, S. a. Francis, and N. S. Lewis, "A taxonomy for solar fuels generators," *Energy Environ. Sci.*, vol. 8, no. 1, pp. 16–25, 2015.
- [14] S. Haussener, S. Hu, C. Xiang, A. Z. Weber, and N. S. Lewis, "Simulations of the irradiation and temperature dependence of the efficiency of tandem photoelectrochemical water-splitting systems," *Energy Environ. Sci.*, vol. 6, no. 12, p. 3605, 2013.
- [15] D. M. Fabian *et al.*, "Particle suspension reactors and materials for solar-driven water splitting," *Energy Environ. Sci.*, vol. 8, no. 10, pp. 2825–2850, 2015.
- [16] B. a. Pinaud *et al.*, "Technical and economic feasibility of centralized facilities for solar hydrogen production via photocatalysis and photoelectrochemistry," *Energy Environ. Sci.*, vol. 6, no. 7, pp. 1983–2002, 2013.
- [17] A. R. Puigdollers, P. Schlexer, S. Tosoni, and G. Pacchioni, "Increasing Oxide Reducibility: The Role of Metal / Oxide Interfaces in the Formation of Oxygen Vacancies," *ACS Catal.*, vol. 7, p. 6493–6513, 2017.
- [18] J. Liu *et al.*, "Metal-free efficient photocatalyst for stable visible water splitting via a two-electron pathway," *Science (80-. )*, vol. 347, no. 6225, pp. 970–974, 2015.
- [19] A. Kasahara *et al.*, "Photoreactions on LaTiO<sub>2</sub>N under Visible Light Irradiation," *J. Phys. Chem. A*, vol. 106, no. 29, pp. 6750–6753, 2002.
- [20] H.-J. Lewerenz and L. Peter, Eds., *Photoelectrochemical Water Splitting: Materials, Processes and Architectures*, RSC Energy. Cambridge: RSC Publishing, 2013.

- 
- [21] R. van de Krol and M. Grätzel, *Photoelectrochemical Hydrogen Production*. Boston: Springer, 2012.
- [22] B. Klahr, S. Gimenez, F. Fabregat-Santiago, T. Hamann, and J. Bisquert, “Water Oxidation at Hematite Photoelectrodes : The Role of Surface States,” *J. Am. Chem. Soc.*, vol. 134, no. 9, pp. 4294–4302, 2012.
- [23] D. Yan *et al.*, “The role of the domain size and titanium dopant in nanocrystalline hematite thin films for water photolysis,” *Nanoscale*, vol. 7, no. 44, pp. 18515–18523, 2015.
- [24] D. Favrat and L. Borel, *Thermodynamique et Énergétique (Volume 1) - De l'énergie à l'exergie*, 2ème édit. Lausanne: PPUR, 2011.
- [25] R. Memming, *Semiconductor Electrolyte*, Wiley-VCH. 1999.
- [26] Andrzej Lasia, *Electrochemical Impedance Spectroscopy and its Applications*. 2014.
- [27] S. M. Wilhelm, K. S. Yun, L. W. Ballenger, and N. Hackerman, “Semiconductor Properties of Iron Oxide Electrodes,” *J. Electrochem. Soc.*, vol. 126, no. 3, pp. 419–424, 1979.
- [28] A. Hagfeldt, U. Björkstén, and M. Grätzel, “Photocapacitance of Nanocrystalline Oxide Semiconductor Films : Band-Edge Movement in Mesoporous TiO<sub>2</sub> Electrodes during UV Illumination,” *J. Phys. Chem.*, vol. 100, no. 20, pp. 8045–8048, 1996.
- [29] K. Rajeshwar, “Fundamentals of Semiconductor Electrochemistry and Photoelectrochemistry,” in *Encyclopedia of Electrochemistry*, WILEY-VCH Verlag, 2007.
- [30] O. Khaselev and J. a Turner, “A Monolithic Photovoltaic-Photoelectrochemical Device for Hydrogen Production via Water Splitting,” *Science (80-. )*, vol. 280, pp. 425–427, 1998.
- [31] W. H. Cheng *et al.*, “Monolithic Photoelectrochemical Device for Direct Water Splitting with 19% Efficiency,” *ACS Energy Lett.*, vol. 3, no. 8, pp. 1795–1800, 2018.
- [32] J. H. Kim, D. Hansora, P. Sharma, J. W. Jang, and J. S. Lee, “Toward practical solar hydrogen production-an artificial photosynthetic leaf-to-farm challenge,” *Chem. Soc. Rev.*, vol. 48, no. 7, pp. 1908–1971, 2019.



## Bibliography

---

- [33] S. Rühle, “Tabulated values of the Shockley-Queisser limit for single junction solar cells,” *Sol. Energy*, vol. 130, pp. 139–147, 2016.
- [34] W. a. Smith, I. D. Sharp, N. C. Strandwitz, and J. Bisquert, “Interfacial band-edge energetics for solar fuels production,” *Energy Environ. Sci.*, vol. 8, pp. 2851–2862, 2015.
- [35] A. Zakutayev *et al.*, “Defect tolerant semiconductors for solar energy conversion,” *J. Phys. Chem. Lett.*, vol. 5, no. 7, pp. 1117–1125, 2014.
- [36] C. C. L. McCrory, S. Jung, J. C. Peters, and T. F. Jaramillo, “Benchmarking heterogeneous electrocatalysts for the oxygen evolution reaction,” *J. Am. Chem. Soc.*, vol. 135, no. 45, pp. 16977–87, 2013.
- [37] A. Maljusch, O. Conradi, S. Hoch, M. Blug, and W. Schuhmann, “Advanced Evaluation of the Long-Term Stability of Oxygen Evolution Electrocatalysts,” *Anal. Chem.*, vol. 88, no. 15, pp. 7597–7602, 2016.
- [38] F. Nandjou and S. Haussener, “Kinetic Competition between Water-Splitting and Photocorrosion Reactions in Photoelectrochemical Devices,” *ChemSusChem*, vol. 12, no. 9, pp. 1984–1994, 2019.
- [39] M. R. Shaner, S. Hu, K. Sun, and N. S. Lewis, “Stabilization of Si microwire arrays for solar-driven H<sub>2</sub>O oxidation to O<sub>2</sub>(g) in 1.0 M KOH(aq) using conformal coatings of amorphous TiO<sub>2</sub>,” *Energy Environ. Sci.*, vol. 8, no. 1, pp. 203–207, 2015.
- [40] C. U. Maier, M. Specht, and G. Bilger, “Hydrogen evolution on platinum-coated p-silicon photocathodes,” *Int. J. Hydrog. Energy*, vol. 21, pp. 859–864, 1996.
- [41] F. Nandjou and S. Haussener, “Degradation in photoelectrochemical devices: Degradation in photoelectrochemical devices: review with an illustrative case study,” *J. Phys. D. Appl. Phys.*, vol. 50, pp. 1–23, 2017.
- [42] D. Bae, B. Seger, P. C. K. Vesborg, O. Hansen, and I. Chorkendorff, “Strategies for stable water splitting: Via protected photoelectrodes,” *Chem. Soc. Rev.*, vol. 46, no. 7, pp. 1933–1954, 2017.
- [43] S. Hu, N. S. Lewis, J. W. Ager, J. Yang, J. R. Mckone, and N. C. Strandwitz, “Thin-Film Materials for the Protection of Semiconducting Photoelectrodes in Solar-Fuel Generators,” 2015.

- 
- [44] F. Freytag, G. Corradi, and M. Imlau, "Atomic insight to lattice distortions caused by carrier self-trapping in oxide materials," *Sci. Rep.*, vol. 6, no. November, pp. 1–7, 2016.
- [45] L. M. Carneiro *et al.*, "Excitation-wavelength-dependent small polaron trapping of photoexcited carriers in  $\alpha$ -Fe<sub>2</sub>O<sub>3</sub>," *Nat. Mater.*, vol. 16, no. 8, pp. 819–825, 2017.
- [46] N. Guijarro, M. S. Prévot, and K. Sivula, "Surface modification of semiconductor photoelectrodes," *Phys. Chem. Chem. Phys.*, vol. 17, no. 24, pp. 15655–74, 2015.
- [47] Fraunhofer Institute for Solar Energy Systems, "Photovoltaics report," 2019.
- [48] J. Y. Kim, J.-W. Jang, D. H. Youn, G. Magesh, and J. S. Lee, "A Stable and Efficient Hematite Photoanode in a Neutral Electrolyte for Solar Water Splitting: Towards Stability Engineering," *Adv. Energy Mater.*, vol. 4, no. 13, pp. 1–7, 2014.
- [49] K. Sivula, F. Le Formal, and M. Grätzel, "Solar water splitting: Progress using hematite ( $\alpha$ -Fe<sub>2</sub>O<sub>3</sub>) photoelectrodes," *ChemSusChem*, vol. 4, no. 4, pp. 432–449, 2011.
- [50] Y. W. Phuan, W.-J. Ong, M. N. Chong, and J. D. Ocon, "Prospects of electrochemically synthesized hematite photoanodes for photoelectrochemical water splitting: A review," *J. Photochem. Photobiol. C Photochem. Rev.*, vol. 33, pp. 54–82, 2017.
- [51] D. Vanmaekelbergh, "Direct and surface state mediated electron transfer at semiconductor/electrolyte junctions—II. A comparison of the interfacial admittance," *Electrochim. Acta*, vol. 42, no. 7, pp. 1135–1141, Jan. 1997.
- [52] D. Vanmaekelbergh, "Direct and surface state mediated electron transfer at semiconductor/electrolyte junctions—II. A comparison of the interfacial admittance," *Electrochim. Acta*, vol. 42, no. 7, pp. 1135–1141, 1997.
- [53] R. Memming, *Semiconductor Electrochemistry*. Weinheim: Wiley-VCH, 2001.
- [54] A. J. Nozik and R. Memming, "Physical Chemistry of Semiconductor - Liquid Interfaces," *J. Phys. Chem.*, vol. 100, no. 31, pp. 13061–13078, 1996.
- [55] T. J. Mills, F. Lin, and S. W. Boettcher, "Theory and Simulations of

## Bibliography

---

- Electrocatalyst-Coated Semiconductor Electrodes for Solar Water Splitting,” *Phys. Rev. Lett.*, vol. 112, no. 14, pp. 1–5, 2014.
- [56] W. W. Gärtner, “Depletion-Layer Photoeffects in Semiconductors,” *Phys. Rev.*, vol. 116, no. 1, pp. 84–87, 1959.
- [57] C. Sah, R. N. Noyce, and W. Shockley, “Carrier Generation and Recombination in P-N Junctions and P-N Junction Characteristics,” *Proc. IRE*, vol. 1, pp. 1228–1243, 1956.
- [58] J. Reichman, “The current-voltage characteristics of semiconductor-electrolyte junction photovoltaic cells,” *Appl. Phys. Lett.*, vol. 36, no. 7, pp. 574–577, 1980.
- [59] M. Ono *et al.*, “Photoelectrochemical reaction and H<sub>2</sub> generation at zero bias optimized by carrier concentration of n-type GaN,” *J. Chem. Phys.*, vol. 126, no. 5, p. 054708, Feb. 2007.
- [60] R. H. Wilson, “A model for the current-voltage curve of photoexcited semiconductor electrodes,” *J. Appl. Phys.*, vol. 48, no. 10, pp. 4292–4297, Oct. 1977.
- [61] A. Berger and J. Newman, “An Integrated 1-Dimensional Model of a Photoelectrochemical Cell for Water Splitting,” *J. Electrochem. Soc.*, vol. 161, no. 8, pp. 3328–3340, 2014.
- [62] T. J. Mills, F. Lin, and S. W. Boettcher, “Theory and Simulations of Electrocatalyst-Coated Semiconductor Electrodes for Solar Water Splitting,” *Phys. Rev. Lett.*, vol. 112, no. 14, p. 148304, 2014.
- [63] P. Cendula *et al.*, “Calculation of the Energy Band Diagram of a Photoelectrochemical Water Splitting Cell,” *J. Phys. Chem. C*, vol. 118, pp. 29599–29607, 2014.
- [64] F. E. Osterloh, “Inorganic nanostructures for photoelectrochemical and photocatalytic water splitting,” *Chem. Soc. Rev.*, vol. 42, no. 6, pp. 2294–2320, Mar. 2013.
- [65] T. Lopes, L. Andrade, F. Le Formal, M. Gratzel, K. Sivula, and A. Mendes, “Hematite photoelectrodes for water splitting: evaluation of the role of film thickness by impedance spectroscopy,” *Phys. Chem. Chem. Phys.*, vol. 16, no. 31, pp. 16515–16523, 2014.

- [66] R. Siegel and J. Howell, *Thermal radiation heat transfer*, 4th ed. New York: Taylor & Francis, 2002.
- [67] K. J. Vetter, *Electrochemical Kinetics Theoretical and Experimental Aspects*. Academic Press Inc., 1967.
- [68] S. Haussener, C. Xiang, J. M. Spurgeon, S. Ardo, N. S. Lewis, and A. Z. Weber, “Modeling, simulation, and design criteria for photoelectrochemical water-splitting systems,” *Energy Environ. Sci.*, vol. 5, no. 12, pp. 9922–9935, 2012.
- [69] D. M. Pozar, *Microwave Engineering*, 4th editio. Wiley, 2012.
- [70] S. M. Sze and K. K. Ng, *Physics of semiconductor devices*, 3rd ed. Hoboken: John Wiley & Sons, Inc., 2007.
- [71] K. Gullbinas, V. Grivickas, H. P. Mahabadi, M. Usman, and A. Hallen, “Surface Recombination Investigation in Thin 4H-SiC Layers,” *Mater. Sci.*, vol. 17, no. 2, pp. 119–124, 2011.
- [72] A. B. Sproul, “Dimensionless solution of the equation describing the effect of surface recombination on carrier decay in semiconductors,” *J. Appl. Phys.*, vol. 76, no. 5, pp. 2851–2854, 1994.
- [73] D. J. Michalak, F. Gstrein, and N. S. Lewis, “The role of band bending in affecting the surface recombination velocities for Si(111) in contact with aqueous acidic electrolytes,” *J. Phys. Chem. C*, vol. 112, no. 15, pp. 5911–5921, 2008.
- [74] K. Gelderman, L. Lee, and S. W. Donne, “Flat-Band Potential of a Semiconductor: Using the Mott–Schottky Equation,” *J. Chem. Educ.*, vol. 84, no. 4, pp. 685–688, Apr. 2007.
- [75] L. Ivanova, S. Borisova, H. Eisele, M. Dähne, a. Laubsch, and P. Ebert, “Surface states and origin of the Fermi level pinning on nonpolar GaN (11- $\bar{2}0$ ) surfaces,” *Appl. Phys. Lett.*, vol. 93, no. 2008, pp. 7–10, 2008.
- [76] C. G. Van De Walle and D. Segev, “Microscopic origins of surface states on nitride surfaces,” *J. Appl. Phys.*, vol. 101, no. 8, p. 081704, 2007.
- [77] Comsol Inc, “Comsol Multiphysics.” 2016.

## Bibliography

---

- [78] D. C. Montgomery, *Design and Analysis of Experiments*, Seventh ed. New York: John Wiley & Sons, Inc., 2008.
- [79] State-Ease Design Expert v9, “State-Ease, Design-Expert.” 2015.
- [80] A. Nicolet, S. Guenneau, C. Geuzaine, and F. Zolla, “Modelling of electromagnetic waves in periodic media with finite elements,” *J. Comput. Appl. Math.*, vol. 168, pp. 321–329, 2004.
- [81] E. A. B. Cole, *Mathematical and Numerical Modelling of Heterostructure Semiconductor Devices: From Theory to Programming*, Springer. 2009.
- [82] S. Adachi, *Optical Constants of Crystalline and Amorphous Semiconductors: Numerical Data and Graphical Information*. Norwell, MA: Kluwer Academic Publishers, 1999.
- [83] G. M. Hale and M. R. Querry, “Optical Constants of Water in the 200-nm to 200-um Wavelength Region,” *Appl. Opt.*, vol. 12, no. 3, pp. 555–563, 1973.
- [84] S. Nakamura and M. R. Krames, “History of gallium-nitride-based light-emitting diodes for illumination,” *Proc. IEEE*, vol. 101, no. 10, pp. 2211–2220, 2013.
- [85] J. I. Pankove, S. Bloom, and G. Harbeke, “No Title,” *RCA Rev.*, vol. 36, p. 163, 1975.
- [86] S. Bloom, G. Harbeke, E. Meier, and I. B. Ortenburger, “No Title,” *Phys. Stat. Solidi*, vol. 66, pp. 161–168, 1974.
- [87] J. F. Muth *et al.*, “Absorption coefficient, energy gap, exciton binding energy, and recombination lifetime of GaN obtained from transmission measurements,” *Appl. Phys. Lett.*, vol. 71, no. 18, pp. 2572–2574, 1997.
- [88] J. Piprek, R. Sink, M. A. Hansen, J. E. Bowers, and S. P. DenBaars, “Simulation and Optimization of 420 nm InGaN/GaN Laser Diodes,” *Proc. SPIE*, vol. 3944, pp. 3912–3944, 2000.
- [89] P. Mackowiak and W. Nakwaski, “Threshold currents of nitride vertical-cavity surface-emitting lasers with various active regions,” *MRS Internet J. Nitride Semicond. Res.*, vol. 3, pp. 1–10, 1998.
- [90] V. Bougrov, M. E. Levinshtein, S. L. Rumyantsev, and A. Zubrilov, *Properties*

- of Advanced Semiconductor Materials GaN, AlN, InN, BN, SiC, SiGe*, vol. 1. New York: John Wiley & Sons, 2001.
- [91] T. P. Chow and M. Ghezzo, *SiC Power Devices in III-Nitride, SiC and Diamond Materials for Electronic Devices*, vol. 423. Pittsburg, PA: Material Research Society Symposium Proceedings, 1996.
- [92] M. Ono *et al.*, “Photoelectrochemical reaction and H<sub>2</sub> generation at zero bias optimized by carrier concentration of n-type GaN,” *J. Chem. Phys.*, vol. 126, no. 5, p. 054708, Feb. 2007.
- [93] M. Rubin, N. Newmann, J. S. Chan, T. C. Fu, and J. T. Ross, “p-type gallium nitride by reactive ion-beam molecular beam epitaxy with ion implantation, diffusion, or coevaporation of Mg,” *Appl. Phys. Lett.*, vol. 64, no. 1, 1994.
- [94] M. Ono *et al.*, “Photoelectrochemical reaction and H<sub>2</sub> generation at zero bias optimized by carrier concentration of n-type GaN,” *J. Chem. Phys.*, vol. 126, no. 5, p. 054708, Feb. 2007.
- [95] A. Nakamura, M. Sugiyama, K. Fujii, and Y. Nakano, “Comparison of Semiconductor – Electrolyte and Semiconductor – Metal Schottky Junctions Using AlGa<sub>0.3</sub>N / GaN Photoelectrochemical Electrode Comparison of Semiconductor – Electrolyte and Semiconductor – Metal Schottky Junctions Using AlGa<sub>0.3</sub>N/GaN Photoelectrochem,” *Jpn. J. Appl. Phys.*, vol. 52, p. 08JN20, 2013.
- [96] O. Madelung, U. Rössler, D. Strauch, and S. Adachi, *Group IV elements, IV-IV and III-V compounds*. Springer, 2001.
- [97] P. Stallinga, *Electrical Characterization of Organic Electronic Materials and Devices*. Chichester: John Wiley & Sons, 2009.
- [98] J. J. Kelly and R. Memming, “The Influence of Surface Recombination and Trapping on the Cathodic Photocurrent at p-Type III-V Electrodes,” *J. Electrochem. Soc.*, vol. 129, no. 4, pp. 730–738, 1982.
- [99] C. A. Grimes, O. K. Varghese, and S. Ranjan, *Light , Water , Hydrogen*. New York: Springer, 2008.
- [100] S. S. Kocha, M. W. Peterson, D. J. Arent, J. M. Redwing, M. A. Tischler, and J. A. Turner, “Electrochemical Investigation of the Gallium Nitride-Aqueous Electrolyte Interface,” *J. Electrochem. Soc.*, vol. 142, no. 12, pp. 238–240, 1995.

## Bibliography

---

- [101] L. Jing, J. Zhou, J. R. Durrant, J. Tang, D. Liu, and H. Fu, “Dynamics of photogenerated charges in the phosphate modified TiO<sub>2</sub> and the enhanced activity for photoelectrochemical water splitting,” *Energy Environ. Sci.*, vol. 5, no. 4, pp. 6552–6558, 2012.
- [102] S. Landsmann, A. E. Maegli, M. Trottmann, C. Battaglia, A. Weidenkaff, and S. Pokrant, “Design Guidelines for High-Performance Particle-Based Photoanodes for Water Splitting: Lanthanum Titanium Oxynitride as a Model,” *ChemSusChem*, vol. 8, no. 20, pp. 3451–3458, 2015.
- [103] S. Akiyama *et al.*, “Highly Efficient Water Oxidation Photoanode Made of Surface Modified LaTiO<sub>2</sub>N Particles,” *Small*, vol. 12, no. 39, pp. 1–9, 2016.
- [104] Y. K. Gaudy and S. Haussener, “Utilizing modeling, experiments, and statistics for the analysis of water-splitting photoelectrodes,” *J. Mater. Chem. A*, vol. 4, no. 8, pp. 3100–3114, 2016.
- [105] S. Tembhurne and S. Haussener, “Integrated Photo-Electrochemical Solar Fuel Generators under Concentrated Irradiation - I. 2-D Non-Isothermal Multi-Physics Modeling,” *J. Electrochem. Soc.*, vol. 163, no. 10, pp. H988–H998, 2016.
- [106] S. Tembhurne and S. Haussener, “Integrated Photo-Electrochemical Solar Fuel Generators under Concentrated Irradiation - II. Thermal Management a Crucial Design Consideration,” *J. Electrochem. Soc.*, vol. 163, no. 10, pp. H988–H998, 2016.
- [107] A. Hankin, F. E. Bedoya-Lora, C. K. Ong, J. C. Alexander, F. Petter, and G. H. Kelsall, “From millimetres to metres: the critical role of current density distributions in photo-electrochemical reactor design,” *Energy Environ. Sci.*, vol. 10, no. 1, pp. 346–360, 2017.
- [108] M. Levinshtein, S. Rumyantsev, and M. Shur, Eds., *Handbook series on semiconductor parameters*. Singapore: World Scientific, 1996.
- [109] S. Adachi, *Handbook on Physical Properties of Semiconductors*, vol. 3: II–VI C. Boston: Kluwer Academic Publishers, 2004.
- [110] D. K. Schroder, *Semiconductor Material and Device Characterization: Third Edition*, 3rd ed. Hoboken: John Wiley & Sons, Inc., 2005.
- [111] “New Semiconductor Materials. Characteristics and Properties,” *Ioffe Physico-*

- Technical Institute.* [Online]. Available:  
<http://www.ioffe.rssi.ru/SVA/NSM/Semicond/>. [Accessed: 04-Jul-2016].
- [112] F. F. Abdi, N. Firet, and R. Van de Krol, "Efficient BiVO<sub>4</sub> Thin Film Photoanodes Modified with Cobalt Phosphate Catalyst and W-doping," *ChemCatChem*, vol. 5, no. 2, pp. 490–496, 2013.
- [113] T. W. Kim and K.-S. Choi, "Nanoporous BiVO<sub>4</sub> Photoanodes with Dual-Layer Oxygen Evolution Catalysts for Solar Water Splitting," *Science (80-. )*, vol. 343, pp. 990–994, 2014.
- [114] Y. Ham *et al.*, "Flux-mediated doping of SrTiO<sub>3</sub> photocatalysts for efficient overall water splitting," *J. Mater. Chem. A*, vol. 4, no. 8, pp. 3027–3033, 2016.
- [115] P. Zhang, T. Ochi, M. Fujitsuka, Y. Kobori, T. Majima, and T. Tachikawa, "Topotactic Epitaxy of SrTiO<sub>3</sub> Mesocrystal Superstructures with Anisotropic Construction for Efficient Overall Water Splitting," *Angew. Chemie - Int. Ed.*, vol. 56, no. 19, pp. 5299–5303, 2017.
- [116] M. Pichler *et al.*, "LaTiOxNy Thin Film Model Systems for Photocatalytic Water Splitting: Physicochemical Evolution of the Solid–Liquid Interface and the Role of the Crystallographic Orientation," *Adv. Funct. Mater.*, vol. 27, no. 20, 2017.
- [117] C. Xiang *et al.*, "Modeling, Simulation, and Implementation of Solar-Driven Water-Splitting Devices," *Angew. Chemie Int. Ed.*, vol. 55, no. 42, pp. 12974–12988, 2016.
- [118] S. Pokrant, S. Dilger, and S. Landsmann, "Morphology and mesopores in photoelectrochemically active LaTiO<sub>2</sub>N single crystals," *J. Mater. Res.*, vol. 31, no. 11, pp. 1574–1579, 2016.
- [119] G. Blatter and F. Greuter, "Carrier transport through grain boundaries in semiconductors," *Phys. Rev. B*, vol. 33, no. 6, pp. 3952–3966, 1986.
- [120] F. Greuter and G. Blatter, "Electrical properties of grain boundaries in polycrystalline compound semiconductors," *Semicond. Sci. Technol.*, vol. 5, pp. 111–137, 1990.
- [121] S. C. Warren *et al.*, "Identifying champion nanostructures for solar water-splitting," *Nat. Mater.*, vol. 12, no. 9, pp. 842–9, 2013.



## Bibliography

---

- [122] J. Levinson, F. R. Shepherd, P. J. Scanlon, W. D. Westwood, G. Este, and M. Rider, “Conductivity behavior in polycrystalline semiconductor thin film transistors,” *J. Appl. Phys.*, vol. 53, no. 2, pp. 1193–1202, 1982.
- [123] S. Verlaak, V. Arkhipov, and P. Heremans, “Modeling of transport in polycrystalline organic semiconductor films,” *Appl. Phys. Lett.*, vol. 82, no. 5, pp. 745–747, 2003.
- [124] F. Huang, D. Chen, Y. Chen, R. a. Caruso, and Y.-B. Cheng, “Mesoporous titania beads for flexible dye-sensitized solar cells,” *J. Mater. Chem. C*, vol. 2, no. 7, p. 1284, 2014.
- [125] S. Suter, M. Cantoni, Y. K. Gaudy, S. Pokrant, and S. Haussener, “Linking morphology and multi-physical transport in structured photoelectrodes,” *Sustain. Energy Fuels*, vol. 2, no. 12, pp. 2661–2673, 2018.
- [126] H. Döscher, J. F. Geisz, T. G. Deutsch, and J. A. Turner, “Sunlight absorption in water – efficiency and design implications for photoelectrochemical devices,” *Energy Environ. Sci.*, vol. 7, no. 9, pp. 2951–2956, 2014.
- [127] M. F. Lichterman *et al.*, “Direct Observation of the Energetics at a Semiconductor/Liquid Junction by Operando X-ray Photoelectron Spectroscopy,” *Energy Environ. Sci.*, vol. 8, pp. 2409–2416, 2015.
- [128] P. Giannozzi *et al.*, “QUANTUM ESPRESSO: a modular and open-source software project for quantum simulations of materials,” *J. Phys. Condens. Matter*, vol. 21, no. 39, pp. 1–19, 2009.
- [129] J. P. Perdew, K. Burke, and M. Ernzerhof, “Generalized Gradient Approximation Made Simple,” *Phys. Rev. Lett.*, vol. 77, no. 3, pp. 3865–3868, 1996.
- [130] V. I. Anisimov, J. Zaanen, and O. K. Andersen, “Band theory and Mott insulators: Hubbard U instead of Stoner I,” *Phys. Rev. B*, vol. 44, no. 3, pp. 943–954, 1991.
- [131] A. Fonari and C. Sutton, “Effective Mass Calculator,” 2012.
- [132] L. Kavan, N. Tétreault, T. Moehl, and M. Grätzel, “Electrochemical Characterization of TiO<sub>2</sub> Blocking Layers for Dye- Sensitized Solar Cells,” *J. Phys. Chem. C*, vol. 118, pp. 16408–16418, 2014.

- 
- [133] H. Cesiulis, N. Tsyntsaru, A. Ramanavicius, and G. Ragoisha, "The Study of Thin Films by Electrochemical Impedance Spectroscopy," in *Nanostructures and Thin Films for Multifunctional Applications*, I. Tiginyanu, P. Topala, and V. Ursaki, Eds. Springer, 2016.
- [134] S. P. Harrington and T. M. Devine, "Analysis of Electrodes Displaying Frequency Dispersion in Mott-Schottky Tests," *J. Electrochem. Soc.*, vol. 155, p. C381, 2008.
- [135] P. Zoltowski, "On the electrical capacitance of interfaces exhibiting CPE behavior," *J. Electroanal. Chem.*, vol. 443, no. 1, pp. 149–154, 1998.
- [136] C. H. Hsu and F. Mansfeld, "Technical Note: Concerning the Conversion of the Constant Phase Element Parameter  $Y_0$  into a Capacitance," *Corrosion*, vol. 57, no. 9, pp. 747–748, 2001.
- [137] S. Ninova and U. Aschauer, "Surface structure and anion order of the oxynitride  $\text{LaTiO}_2\text{N}$ ," *J. Mater. Chem. A*, vol. 00, no. 001, pp. 1–7, 2017.
- [138] M. Bouri and U. Aschauer, "Bulk and surface properties of the Ruddlesden–Popper oxynitride  $\text{Sr}_2\text{TaO}_3\text{N}$ ," *Phys. Chem. Chem. Phys.*, vol. 20, no. 4, pp. 2771–2776, 2018.
- [139] D. Stroud and A. Kazaryan, "Optical sum rules and effective-medium theories for a polycrystalline material: Application to a model for polypyrrole," *Phys. Rev. B*, vol. 53, no. 11, pp. 7076–7084, 1996.
- [140] J. Feng *et al.*, "Highly Photo-Responsive  $\text{LaTiO}_2\text{N}$  Photoanodes by Improvement of Charge Carrier Transport among Film Particles," *Adv. Funct. Mater.*, vol. 24, no. 23, pp. 3535–3542, Jun. 2014.
- [141] S. Landsmann, Y. Surace, M. Trottmann, S. Dilger, A. Weidenka, and S. Pokrant, "Controlled Design of Functional Nano-Coatings: Reduction of Loss Mechanisms in Photoelectrochemical Water Splitting," *ACS Appl. Mater. Interfaces*, vol. 8, pp. 12149–12157, 2016.
- [142] Y. Ma, S. R. Pendlebury, A. Reynal, F. le Formal, and J. R. Durrant, "Dynamics of photogenerated holes in undoped  $\text{BiVO}_4$  photoanodes for solar water oxidation," *Chem. Sci.*, vol. 5, no. 8, pp. 2964–2973, 2014.
- [143] M. Xie, Z. Zhang, W. Han, X. Cheng, X. Li, and E. Xie, "Efficient hydrogen evolution under visible light irradiation over  $\text{BiVO}_4$  quantum dot decorated

## Bibliography

---

- screw-like  $\text{SnO}_2$  nanostructures,” *J. Mater. Chem. A*, vol. 5, no. 21, pp. 10338–10346, 2017.
- [144] S. Nandy *et al.*, “Synthesis and Photocatalytic Activity of  $\text{La}_{0.5}\text{Ti}_2\text{Cu}(\text{S}_{1-x}\text{Se}_x)_5\text{O}_7$  Solid Solutions for  $\text{H}_2$  Production under Visible Light Irradiation,” *ChemPhotoChem*, vol. 1, no. 6, pp. 265–272, 2017.
- [145] T. Suzuki, T. Hisatomi, K. Teramura, Y. Shimodaira, H. Kobayashi, and K. Domen, “A titanium-based oxysulfide photocatalyst:  $\text{La}_{0.5}\text{Ti}_2\text{MS}_5\text{O}_7$  ( $\text{M} = \text{Ag, Cu}$ ) for water reduction and oxidation,” *Phys. Chem. Chem. Phys.*, vol. 14, no. 44, p. 15475, 2012.
- [146] E. L. Miller, A. Deangelis, and S. Mallory, *Photoelectrochemical Hydrogen Production*, vol. 102. Boston, MA: Springer US, 2012.
- [147] M. Tomkiewicz, “The Potential Distribution at the  $\text{TiO}_2$  Aqueous Electrolyte Interface,” *J. Electrochem. Soc.*, vol. 126, no. 9, p. 1505, 1979.
- [148] S. Dilger, S. Landsmann, M. Trottmann, and S. Pokrant, “Carbon containing conductive networks in composite particle-based photoanodes for solar water splitting,” *J. Mater. Chem. A*, vol. 4, no. 43, pp. 17087–17095, 2016.
- [149] M. Higashi, K. Domen, and R. Abe, “Fabrication of efficient  $\text{TaON}$  and  $\text{Ta}_3\text{N}_5$  photoanodes for water splitting under visible light irradiation,” *Energy Environ. Sci.*, vol. 4, no. 10, p. 4138, 2011.
- [150] T. Hisatomi, T. Minegishi, and K. Domen, “Kinetic Assessment and Numerical Modeling of Photocatalytic Water Splitting toward Efficient Solar Hydrogen Production,” *Chem. Soc. Japan*, vol. 655, no. 6, pp. 647–655, 2012.
- [151] T. Minegishi, N. Nishimura, J. Kubota, and K. Domen, “Photoelectrochemical properties of  $\text{LaTiO}_2\text{N}$  electrodes prepared by particle transfer for sunlight-driven water splitting,” *Chem. Sci.*, vol. 4, no. 3, p. 1120, 2013.
- [152] C. Le Paven-Thivet *et al.*, “Photoelectrochemical properties of crystalline perovskite lanthanum titanium oxynitride films under visible light,” *J. Phys. Chem. C*, vol. 113, no. 15, pp. 6156–6162, 2009.
- [153] N. Nishimura *et al.*, “Effect of  $\text{TiCl}_4$  treatment on the photoelectrochemical properties of  $\text{LaTiO}_2\text{N}$  electrodes for water splitting under visible light,” *Thin Solid Films*, vol. 518, no. 20, pp. 5855–5859, 2010.

- [154] T. T. Mnatsakanov, M. E. Levinshtein, L. I. Pomortseva, S. N. Yurkov, G. S. Simin, and M. A. Khan, "Carrier mobility model for GaN," *Solid. State. Electron.*, vol. 47, no. 1, pp. 111–115, 2003.
- [155] E. Gaubas and J. Vanhellemont, "Comparative Study of Carrier Lifetime Dependence on Dopant Concentration in Silicon and Germanium," *J. Electrochem. Soc.*, vol. 154, no. 3, p. H231, 2007.
- [156] K. T. Fountaine, H. J. Lewerenz, and H. A. Atwater, "Efficiency limits for photoelectrochemical," *Nat. Commun.*, vol. 7, pp. 1–9, 2016.
- [157] M.-J. Jeng, Y.-L. Wung, L.-B. Chang, and L. Chow, "Particle Size Effects of TiO<sub>2</sub> Layers on the Solar Efficiency of Dye-Sensitized Solar Cells," *Int. J. Photoenergy*, vol. 2013, pp. 1–9, 2013.
- [158] J. Bisquert and R. A. Marcus, "Device Modeling of Dye-Sensitized Solar Cells," in *Multiscale Modelling of Organic and Hybrid Photovoltaics*, D. Beljonne and J. Cornil, Eds. Berlin, 2013, pp. 325–396.
- [159] J. Bisquert, "Theory of the impedance of charge transfer via surface states in dye-sensitized solar cells," *J. Electroanal. Chem.*, vol. 646, no. 1–2, pp. 43–51, 2010.
- [160] L. M. Peter, "Dye-sensitized nanocrystalline solar cells," *Phys. Chem. Chem. Phys.*, vol. 9, no. 21, pp. 2630–2642, 2007.
- [161] Y. K. Gaudy, S. Dilger, S. Landsmann, U. Aschauer, S. Pokrant, and S. Haussener, "Determination and optimization of material parameters of particle-based LaTiO<sub>2</sub>N photoelectrodes," *J. Mater. Chem. A*, vol. 6, no. 36, pp. 17337–17352, 2018.
- [162] H. Dotan, K. Sivula, M. Grätzel, A. Rothschild, and S. C. Warren, "Probing the photoelectrochemical properties of hematite ( $\alpha$ -Fe<sub>2</sub>O<sub>3</sub>) electrodes using hydrogen peroxide as a hole scavenger," *Energy Environ. Sci.*, vol. 4, no. 3, p. 958, 2011.
- [163] F. E. Bedoya Lora, A. Hankin, and G. H. Kelsall, "En route to a unified model for photo-electrochemical reactor optimization. I - Photocurrent and H<sub>2</sub> yield predictions," *J. Mater. Chem. A*, no. 16 mm, pp. 22683–22696, 2017.
- [164] D. O. Scanlon *et al.*, "Band alignment of rutile and anatase TiO<sub>2</sub>," *Nat. Mater.*, vol. 12, no. 9, pp. 798–801, 2013.

## Bibliography

---

- [165] S. Rühle and D. Cahen, “Electron tunneling at the TiO<sub>2</sub>/substrate interface can determine dye-sensitized solar cell performance,” *J. Phys. Chem. B*, vol. 108, no. 46, pp. 17946–17951, 2004.
- [166] A. Goetzberger, C. Hebling, and H.-W. Schock, “Photovoltaic materials, history, status and outlook,” *Mater. Sci. Eng. R*, vol. 40, no. 1, pp. 1–46, 2003.
- [167] C. W. Lan *et al.*, “The emergence of high-performance multi-crystalline silicon in photovoltaics,” *J. Cryst. Growth*, vol. 468, no. October 2016, pp. 17–23, 2017.
- [168] A. E. Maegli, S. Pokrant, T. Hisatomi, M. Trottmann, K. Domen, and A. Weidenka, “Enhancement of Photocatalytic Water Oxidation by the Morphological Control of LaTiO<sub>2</sub>N and Cobalt Oxide Catalysts,” *J. Phys. Chem. C*, vol. 118, pp. 16344–16351, 2014.
- [169] W. Niu, T. Moehl, W. Cui, R. Wick-Joliat, L. Zhu, and S. D. Tilley, “Extended Light Harvesting with Dual Cu<sub>2</sub>O-Based Photocathodes for High Efficiency Water Splitting,” *Adv. Energy Mater.*, vol. 8, no. 10, pp. 1–8, Apr. 2018.
- [170] S. Xiao *et al.*, “Origin of the Different Photoelectrochemical Performance of Mesoporous BiVO<sub>4</sub> Photoanodes between the BiVO<sub>4</sub> and the FTO Side Illumination,” *J. Phys. Chem. C*, vol. 4, p. 151004165821008, 2015.
- [171] D. R. Lide, “CRC Handbook of Chemistry and Physics,” *J. Am. Chem. Soc.*, pp. 1–2661, Sep. 2005.
- [172] M. A. El Khakani, M. Chaker, and E. Gat, “Pulsed laser deposition of highly conductive iridium oxide thin films,” *Appl. Phys. Lett.*, vol. 69, no. 14, pp. 2027–2029, 1996.
- [173] C. Jiang, S. J. A. Moniz, A. Wang, T. Zhang, and J. Tang, “Photoelectrochemical devices for solar water splitting-materials and challenges,” *Chem. Soc. Rev.*, vol. 46, no. 15, pp. 4645–4660, 2017.
- [174] G. Segev, C. Jiang, J. Eichhorn, F. M. Toma, J. K. Cooper, and I. D. Sharp, “Quantification of the loss mechanisms in emerging water splitting photoanodes through empirical extraction of the spatial charge collection efficiency,” *Energy Environ. Sci.*, vol. 11, pp. 904–913, 2018.
- [175] G. Hodes and P. V. Kamat, “Understanding the Implication of Carrier Diffusion Length in Photovoltaic Cells,” *J. Phys. Chem. Lett.*, vol. 6, no. 20, pp.

4090–4092, 2015.

- [176] E. Tuominen, M. Acerbis, A. Hovinen, T. Siirtola, and J. Sinkkonen, “A method extracting solar cell parameters from spectral response by inverse laplace transform,” *Phys. Scr.*, vol. T69, no. T69, pp. 306–309, 1997.
- [177] A. Nakane *et al.*, “Quantitative determination of optical and recombination losses in thin-film photovoltaic devices based on external quantum efficiency analysis,” *J. Appl. Phys.*, vol. 120, no. 6, pp. 1–24, 2016.
- [178] J. H. Kennedy and K. W. Frese, “Photooxidation of water at  $\alpha$ -Fe<sub>2</sub>O<sub>3</sub> electrodes,” *J. Electrochem. Soc.*, vol. 125, no. 5, pp. 709–714, 1978.
- [179] X. Zhao *et al.*, “Quantitative Analysis and Visualized Evidence for High Charge Separation Efficiency in a Solid-Liquid Bulk Heterojunction,” *Adv. Energy Mater.*, vol. 4, no. 9, pp. 1–7, Jun. 2014.
- [180] C. A. Dimitriadis, L. Papadimitriou, and N. A. Economou, “Resistivity dependence of the minority carrier diffusion length in single crystals of Cu<sub>2</sub>O,” *J. Mater. Sci. Lett.*, vol. 2, pp. 691–693, 1983.
- [181] D. A. Wheeler, G. Wang, Y. Ling, Y. Li, and J. Z. Zhang, “Nanostructured hematite: synthesis, characterization, charge carrier dynamics, and photoelectrochemical properties,” *Energy Environ. Sci.*, vol. 5, no. 5, pp. 6682–6702, 2012.
- [182] R. Liu, Z. Zheng, J. Spurgeon, and X. Yang, “Enhanced photoelectrochemical water-splitting performance of semiconductors by surface passivation layers,” *Energy Environ. Sci.*, vol. 7, no. 8, pp. 2504–2517, 2014.
- [183] D. R. Longtin, E. P. Shettle, J. R. Hummel, and J. D. Pryce, “Wind Dependent Desert Aerosol Model: Radiative Properties,” 1988.
- [184] M. R. Querry, “Optical Constants,” 1985.
- [185] S. Li *et al.*, “Enhanced photoelectrochemical performance of planar p-Silicon by APCVD deposition of surface mesoporous hematite coating,” *Appl. Catal. B Environ.*, vol. 200, pp. 372–377, Jan. 2017.
- [186] M. Li, L. Zhao, and L. Guo, “Preparation and photoelectrochemical study of BiVO<sub>4</sub> thin films deposited by ultrasonic spray pyrolysis,” *Int. J. Hydrogen*

## Bibliography

---

- Energy*, vol. 35, no. 13, pp. 7127–7133, Jul. 2010.
- [187] M. S. Prévot, N. Guijarro, and K. Sivula, “Enhancing the performance of a robust sol-gel-processed p-type delafossite CuFeO<sub>2</sub> photocathode for solar water reduction,” *ChemSusChem*, vol. 8, no. 8, pp. 1359–1367, 2015.
- [188] L. Xi, C. Schwanke, D. Zhou, D. Drevon, R. van de Krol, and K. M. Lange, “In Situ XAS Study of CoBi Modified Hematite Photoanodes,” *Dalt. Trans.*, vol. 46, pp. 15719–15726, 2017.
- [189] C. Xiang, G. M. Kimball, R. L. Grimm, B. S. Brunschwig, H. A. Atwater, and N. S. Lewis, “820 mV open-circuit voltages from Cu<sub>2</sub>O/CH<sub>3</sub>CN junctions,” *Energy Environ. Sci.*, vol. 4, no. 4, pp. 1311–1318, 2011.
- [190] J. Luo, L. Steier, M. K. Son, M. Schreier, M. T. Mayer, and M. Grätzel, “Cu<sub>2</sub>O Nanowire Photocathodes for Efficient and Durable Solar Water Splitting,” *Nano Lett.*, vol. 16, no. 3, pp. 1848–1857, 2016.
- [191] C. Malerba, F. Biccari, C. L. A. Ricardo, M. D’Incau, P. Scardi, and A. Mittiga, “Absorption coefficient of bulk and thin film Cu<sub>2</sub>O,” *Sol. Energy Mater. Sol. Cells*, vol. 95, pp. 2848–2854, 2011.
- [192] Y. Hou *et al.*, “Bioinspired molecular co-catalysts bonded to a silicon photocathode for solar hydrogen evolution,” *Nat. Mater.*, vol. 10, no. 6, pp. 434–438, 2011.
- [193] B. Van Zeghbroeck, *Principles of Semiconductor Devices*. University of Colorado, 2002.
- [194] M. S. Tyagi and R. Van Overstraeten, “Minority carrier recombination in heavily doped silicon,” *Solid-State Electron.*, vol. 26, no. 6, pp. 577–597, 1983.
- [195] M. A. Green, “Self-consistent optical parameters of intrinsic silicon at 300 K including temperature coefficients,” *Sol. Energy Mater. Sol. Cells*, vol. 92, no. 11, pp. 1305–1310, 2008.
- [196] S. Tokunaga, H. Kato, and A. Kudo, “Selective preparation of monoclinic and tetragonal BiVO<sub>4</sub> with scheelite structure and their photocatalytic properties,” *Chem. Mater.*, vol. 13, no. 12, pp. 4624–4628, 2001.
- [197] M. Valant and D. Suvorov, “Chemical Compatibility between Silver Electrodes and Low-Firing Binary-Oxide Compounds: Conceptual Study,” *J.*

- Am. Ceram. Soc.*, vol. 83, no. 188846, pp. 2721–2729, 2000.
- [198] S.-H. Wee, D.-W. Kim, and S.-I. Yoo, “Microwave Dielectric Properties of Low-Fired ZnNb<sub>2</sub>O<sub>6</sub> Ceramics with BiVO<sub>4</sub> Addition,” *J. Am. Ceram. Soc.*, vol. 40, no. 87, pp. 871–874 (2004), 2004.
- [199] Z. Zhao, Z. Li, and Z. Zou, “Electronic structure and optical properties of monoclinic clinobisvanite BiVO<sub>4</sub>,” *Phys. Chem. Chem. Phys.*, vol. 13, no. 10, pp. 4746–4753, 2011.
- [200] J. A. Seabold and N. R. Neale, “All First Row Transition Metal Oxide Photoanode for Water Splitting Based on Cu<sub>3</sub>V<sub>2</sub>O<sub>8</sub>,” *Chem. Mater.*, vol. 27, no. 3, pp. 1005–1013, Feb. 2015.
- [201] C. G. Read, Y. Park, and K.-S. Choi, “Electrochemical Synthesis of p-Type CuFeO<sub>2</sub> Electrodes for Use in a Photoelectrochemical Cell,” *J. Phys. Chem. Lett.*, vol. 3, no. 14, pp. 1872–1876, Jul. 2012.
- [202] T. Kimura, J. C. Lashley, and A. P. Ramirez, “Inversion-symmetry breaking in the noncollinear magnetic phase of the triangular-lattice antiferromagnet CuFeO<sub>2</sub>,” *Phys. Rev. B - Condens. Matter Mater. Phys.*, vol. 73, no. 22, pp. 1–4, 2006.
- [203] B. Iandolo, H. Zhang, B. Wickman, I. Zorić, G. Conibeer, and A. Hellman, “Correlating flat band and onset potentials for solar water splitting on model hematite photoanodes,” *RSC Adv.*, vol. 5, no. 75, pp. 61021–61030, 2015.
- [204] J. K. Cooper *et al.*, “Indirect bandgap and optical properties of monoclinic bismuth vanadate,” *J. Phys. Chem. C*, vol. 119, no. 6, pp. 2969–2974, 2015.
- [205] M. S. Prévot *et al.*, “Evaluating Charge Carrier Transport and Surface States in CuFeO<sub>2</sub> Photocathodes,” *Chem. Mater.*, vol. 29, no. 11, pp. 4952–4962, 2017.
- [206] M. P. Dare-Edwards, J. B. Goodenough, A. Hamnett, and P. R. Trevellick, “Electrochemistry and Photoelectrochemistry of Iron(III) Oxide,” *J. Chem. Soc. Trans. I*, vol. 79, no. 1, pp. 2027–2041, 1983.
- [207] R. P. Antony *et al.*, “Electrospun Mo-BiVO<sub>4</sub> for Efficient Photoelectrochemical Water Oxidation: Direct Evidence of Improved Hole Diffusion Length and Charge separation,” *Electrochim. Acta*, vol. 211, pp. 173–182, 2016.



## Bibliography

---

- [208] F. F. Abdi, T. J. Savenije, M. M. May, B. Dam, and R. Van De Krol, “The Origin of Slow Carrier Transport in BiVO<sub>4</sub> Thin Film Photoanodes: A Time-Resolved Microwave Conductivity Study,” *J. Phys. Chem. Lett.*, vol. 4, pp. 2752–2757, 2013.
- [209] A. J. E. Rettie *et al.*, “Combined charge carrier transport and photoelectrochemical characterization of BiVO<sub>4</sub> single crystals: Intrinsic behavior of a complex metal oxide,” *J. Am. Chem. Soc.*, vol. 135, no. 30, pp. 11389–11396, 2013.
- [210] S. Chhajed, M. F. Schubert, J. K. Kim, and E. F. Schubert, “Nanostructured multilayer graded-index antireflection coating for Si solar cells with broadband and omnidirectional characteristics,” *Appl. Phys. Lett.*, vol. 93, no. 25, pp. 1–4, 2008.
- [211] H. S. Stein, E. Soedarmadji, P. F. Newhouse, Dan Guevarra, and J. M. Gregoire, “Synthesis, optical imaging, and absorption spectroscopy data for 179072 metal oxides,” *Sci. data*, vol. 6, no. 1, p. 9, 2019.
- [212] S. Haussener, “Computational tools,” 2019. [Online]. Available: <https://lrese.epfl.ch/research/page-134145-en-html/>. [Accessed: 09-Jul-2019].
- [213] Y. K. Gaudy, “POPe v.1. - Performance Optimization of Photoelectrode.” EPFL, 2019.
- [214] P. Aseev *et al.*, “Near-infrared emitting In-rich InGa<sub>N</sub> layers grown directly on Si: Towards the whole composition range,” *Appl. Phys. Lett.*, vol. 106, pp. 072102 1–4, 2015.
- [215] P. Aseev *et al.*, “Uniform low-to-high in composition InGa<sub>N</sub> layers grown on Si,” *Appl. Phys. Express*, vol. 6, pp. 115503 1–4, 2013.
- [216] S. Haussener, S. Hu, C. Xiang, A. Z. Weber, and N. S. Lewis, “ESI - Simulations of the irradiation and temperature dependence of the efficiency of tandem photoelectrochemical water-splitting systems,” *Energy Environ. Sci.*, vol. 6, no. 12, p. 3605, 2013.
- [217] J. Juodkazytė *et al.*, “In<sub>x</sub>Ga<sub>1-x</sub>N performance as a band-gap-tunable photoelectrode in acidic and basic solutions,” *Sol. Energy Mater. Sol. Cells*, vol. 130, pp. 36–41, Nov. 2014.

- 
- [218] G. F. Brown, J. W. Ager, W. Walukiewicz, and J. Wu, "Finite element simulations of compositionally graded InGaN solar cells," *Sol. Energy Mater. Sol. Cells*, vol. 94, no. 3, pp. 478–483, 2010.
- [219] L. Hsu and W. Walukiewicz, "Modeling of InGaN/Si tandem solar cells," *J. Appl. Phys.*, vol. 104, no. 2, 2008.
- [220] H. Dotan *et al.*, "Resonant light trapping in ultrathin films for water splitting," *Nat. Mater.*, vol. 12, no. 11, pp. 158–64, 2013.
- [221] H. Dotan *et al.*, "Resonant light trapping in ultrathin films for water splitting," *Nat. Mater.*, vol. 12, no. 11, pp. 158–64, 2013.
- [222] A. Hazari *et al.*, "Optical constant of  $\text{In}_x\text{Ga}_{1-x}\text{N}$  ( $0 \leq x \leq 0.73$ ) in the visible and near-infrared wavelength regimes," *Opt. Lett.*, vol. 40, no. 14, pp. 3304–3307, 2015.
- [223] D. F. Edwards, "Silicon (Si)\*," in *Handbook of Optical Constants of Solids*, Volume I, E. D. Palik, Ed. Academic Press, 1985, pp. 547–569.
- [224] X. Li *et al.*, "Photoelectrochemical hydrogen evolution of tapered silicon nanowires," *Phys. Chem. Chem. Phys.*, vol. 17, no. 2, pp. 800–804, 2015.
- [225] F. Urbain, V. Smirnov, J. P. Becker, and F. Finger, "Impact of Light-Induced Degradation on the Performance of Multijunction Thin-Film Silicon-Based Photoelectrochemical Water-Splitting Devices," *ACS Omega*, vol. 1, no. 5, pp. 832–836, 2016.
- [226] C. Xiang, A. C. Meng, and N. S. Lewis, "Evaluation and optimization of mass transport of redox species in silicon microwire-array photoelectrodes," 2012.
- [227] A. Goossens, E. M. Kelder, R. J. M. Beeren, C. J. G. Bartels, and J. Schoonman, "Structural, Optical, and Electronic Properties of Silicon/Boron Phosphide Heterojunction Photoelectrodes," *Ber. Bunsenges. Phys. Chem.*, vol. 95, pp. 503–510, 1991.
- [228] S. Lehner, M. Ciobanu, K. Savage, and D. E. Cliffel, "Electrochemical Impedance Spectroscopy of Synthetic Pyrite Doped with As, Co, and Ni," *J. Electrochem. Soc.*, vol. 155, no. 5, pp. 61–70, 2008.
- [229] B. S. Yadav, P. Mohanta, R. S. Srinivasa, and S. S. Major, "Electrical and optical properties of transparent conducting  $\text{In}_x\text{Ga}_{1-x}\text{N}$  alloy films deposited

## Bibliography

---

- by reactive co-sputtering of GaAs and indium,” *Thin Solid Films*, vol. 555, pp. 179–184, 2014.
- [230] A. Cuevas, P. A. Basore, G. Giroult-Matlakowski, and C. Dubois, “Surface recombination velocity of highly doped n-type silicon,” *J. Appl. Phys.*, vol. 80, no. 6, pp. 3370–3375, 1996.
- [231] H. Kumano *et al.*, “Effect of indium doping on the transient optical properties of GaN films,” *Appl. Phys. Lett.*, vol. 75, no. 19, pp. 2879–2881, 1999.
- [232] C. C. Hu, *Modern Semiconductor Devices for Integrated Circuits*, Pearson Ed. 2010.
- [233] X. Qi *et al.*, “High-performance n-Si/ $\alpha$ -Fe<sub>2</sub>O<sub>3</sub> core/shell nanowire array photoanode towards photoelectrochemical water splitting,” *Nanoscale*, vol. 6, no. 6, pp. 3182–9, Mar. 2014.
- [234] A. J. Bard, L. R. Faulkner, E. Swain, and C. Robey, *Fundamentals and Applications*. .
- [235] P. E. Ciddor, “Refractive index of air: new equations for the visible and near infrared,” *Appl. Opt.*, vol. 35, no. 9, pp. 1566–1573, 1996.
- [236] Ioffe Physico-Technical Institute, *NSM Archive - Physical Properties of Semiconductors*. 2001.
- [237] J. Robertson, “Band offsets of wide-band-gap oxides and implications for future electronic devices,” *J. Vac. Sci. Technol. B Microelectron. Nanom. Struct.*, vol. 18, no. 3, pp. 1785–1791, 2000.
- [238] J. Robertson, “Force measurements in positive unipolar wire-to-plane corona discharges in air,” *Eur. Phys. J. Appl. Phys.*, vol. 28, pp. 265–291, 2004.
- [239] R. Brenot, R. Vanderhaghen, B. Drevillon, I. French, and P. Roca i Cabarrocas, “Time resolved microwave conductivity measurements for the characterization of transport properties in thin film micro-crystalline silicon,” *Thin Solid Films*, vol. 296, no. 1–2, pp. 94–97, 1997.
- [240] J. P. Perdew *et al.*, “Restoring the Density-Gradient Expansion for Exchange in Solids and Surfaces,” *Phys. Rev. Lett.*, vol. 100, pp. 1–4, 2008.
- [241] G. Kresse and J. Hafner, “Ab initio molecular dynamics for liquid metals,” *Phys. Rev. B*, vol. 47, no. 1, pp. 558–561, 1993.

- [242] G. Kresse and J. Hafner, “Ab initio molecular-dynamics simulation of the liquid-metal-amorphous-semiconductor transition in germanium,” *Phys. Rev. B*, vol. 49, no. 20, pp. 14251–14269, 1994.
- [243] G. Kresse and J. Furthmüller, “Efficiency of ab-initio total energy calculations for metals and semiconductors using a plane-wave basis set,” *Comput. Mater. Sci.*, vol. 6, pp. 15–50, 1996.
- [244] G. Kresse and J. Furthmüller, “Efficient iterative schemes for ab initio total-energy calculations using a plane-wave basis set,” *Phys. Rev. B*, vol. 54, no. 16, pp. 11169–11186, 1996.
- [245] P. E. Blöchl, “Projector augmented-wave method,” *Phys. Rev.*, vol. 50, no. 24, pp. 17953–17979, 1994.
- [246] G. Kresse and D. Joubert, “From ultrasoft pseudopotentials to the projector augmented-wave method,” *Phys. Rev. B*, vol. 59, no. 3, pp. 1758–1775, 1999.

# Curriculum Vitae

**Yannick Kenneth Gaudy**

Mobile: +41 (0)76 615 38 48

Email: [yannick\\_gaudy@hotmail.com](mailto:yannick_gaudy@hotmail.com)

Address: Route des Tattes-d'Oie 4, 1260 Nyon, Switzerland

**PhD in Energy  
Engineer in Mechanics**

---

<b>Education</b>	<b>2015-2019</b>	<b>École Polytechnique Fédérale de Lausanne, Switzerland</b> PhD in energy
	<b>2012-2013</b>	Master in mechanical engineering
	<b>2007-2010</b>	Bachelor in mechanical engineering
		<b>Technical University of Denmark (DTU), Lyngby, Denmark</b>
	<b>2011-2012</b>	First year of master in mechanical engineering (Erasmus program)
<b>Book chapter</b>	<b>2018</b>	S. Haussener, <b>Y. Gaudy</b> , and S. Tembhurne, "Modelling-derived Design Guidelines for Photo- electrochemical Devices," in <i>Advances in Photoelectrochemical Water Splitting: Theory, Experiment and Systems Analysis</i> , S. D. Tilley, S. Lany, and R. van de Krol, Eds. RSC, 2018
<b>Publications</b>	<b>2019</b>	<b>Y. K. Gaudy</b> and S. Haussener, <i>Theoretical maximum efficiency and performance characterization of <math>\text{In}_x\text{Ga}_{1-x}\text{N}/\text{Si}</math> tandem water-splitting photoelectrodes</i> , 2019, in preparation.
	<b>2019</b>	<b>Y. K. Gaudy</b> , S. Dilger, S. Pokrant, and S. Haussener, Majority charge carrier transport in particle-based photoelectrodes, 2019, in review
	<b>2019</b>	<b>Y. K. Gaudy</b> and S. Haussener, Rapid performance optimization method for photoelectrodes, <i>Journal of Physical Chemistry C</i> , 2019, in press
	<b>2018 Front cover</b>	<b>Y. K. Gaudy</b> , S. Dilger, S. Landsmann, U. Aschauer, S. Pokrant, and S. Haussener, "Determination and optimization of material parameters of particle-based $\text{LaTiO}_2\text{N}$ photoelectrodes," <i>J. Mater. Chem. A</i> , vol. 6, no. 36, pp. 17337-17352, 2018
	<b>2018</b>	S. Suter; M. Cantoni; <b>Y. K. Gaudy</b> ; S. Pokrant; S. Haussener, "Linking Morphology and Multi-Physical Transport in Structured Photoelectrodes", <i>Sustainable Energy and Fuels</i> , vol. 2, no. 12, pp. 2662-2673, 2018

	2016	<b><u>Y. K. Gaudy</u></b> and S. Haussener, “Utilizing modeling, experiments, and statistics for the analysis of water-splitting photoelectrodes,” <i>J. Mater. Chem. A</i> , vol. 4, no. 8, pp. 3100–3114, 2016
Conferences	2018	<b><u>Y. Gaudy</u></b> , <b><u>S. Haussener</u></b> , Determination and optimization of material parameters of particle-based LaTiO <sub>2</sub> N photoelectrodes, Gerischer Electrochemistry Today 2018 – A Symposium, August 2018, Colorado, USA (poster presentation)
	2018	<b><u>Y. Gaudy</u></b> , P. Aseev, <b><u>S. Haussener</u></b> , Numerical and experimental study of In <sub>x</sub> Ga <sub>1-x</sub> N water-splitting photoelectrodes, MRS, April 2018, Phoenix, USA (poster presentation)
	2017	<b><u>Y. Gaudy</u></b> , S. Landsmann, S. Dilger, U. Aschauer, S. Pokrant, S. Haussener, Coupled Experimental-Numerical Analysis of LaTiO <sub>2</sub> N Particle-Based Water-Splitting Photoelectrodes, ISF-2, July 2017, San Diego, USA (oral presentation)
	2017	<b><u>Y. Gaudy</u></b> , S. Landsmann, S. Dilger, U. Aschauer, S. Pokrant, S. Haussener, Coupled Experimental-Numerical Analysis of LaTiO <sub>2</sub> N Particle-Based Water-Splitting Photoelectrodes, NanoGE, September 2017, Barcelona, Spain (poster presentation)
	2016	<b><u>Y. Gaudy</u></b> , S. Landsmann, S. Dilger, S. Pokrant, S. Haussener, Coupled experimental-numerical analysis of particle-based water-splitting photoelectrodes, NanoGE, September 2016, Berlin, Germany (poster presentation)
	2016	<b><u>P. Aseev</u></b> , Z. Gačević, E. Calleja, B. Seger, P. Vesborg, I. Chorkendorff, <b><u>Y. Gaudy</u></b> , S. Haussener, Photoelectrochemical properties of full composition In <sub>x</sub> Ga <sub>1-x</sub> N/Si photoanodes, 21st International Conference on Photochemical Conversion and Storage of Solar Energy 2016, July 2016, St. Petersburg, Russia (poster presentation)
	2016	<b><u>Y. Gaudy</u></b> , <b><u>S. Haussener</u></b> , Utilizing modeling, experiments, and statistics for the analysis of water-splitting photoelectrodes, 229 <sup>th</sup> ECS meeting, May-June 2016, San Diego, USA (oral presentation)
	2015	<b><u>Y. Gaudy</u></b> , S. Haussener, Modeling and numerical design of experiment of the semiconductor-electrolyte interface, ISF-1, April-May 2015, Uppsala, Sweden
Key academic projects	Feb.-Jul. 2013	<b>Modeling of Z-scheme Photoelectrochemical Water Splitting Devices: Ohmic Wired Porous Electrodes and Particulate Semiconductors with Redox Mediators – Master’s thesis, Laboratory of Renewable Energy and Engineering (LRESE), EPFL, Prof. S. Haussener</b>

	Sep. 2012- Jan. 2013	<b>Microalgae culture and conditioning – Technology Review –</b> <i>Laboratory for Industrial Energy Systems (LENI), EPFL, Prof. F. Maréchal, Asst. A. Mian</i>
	Jun. 2012	<b>Simulation of a water drop on a liquid surface –</b> <i>Mechanical Engineering Department, DTU, Prof. J. H. Walther</i>
	Jan. 2012	<b>Planning and development of wind farms in Hidalgo, Mexico –</b> <i>Laboratory of Sustainable Energy, Risø DTU, Prof. N. G. Mortensen and N.- E. Clausen</i>
	Feb.-Jul. 2010	<b>Development of a bicycle frame and simulation of the mechanical constraints –</b> <i>Bachelor's thesis, EPFL, Prof. Gianola</i>
Work experience	2014-2015	<b>Research assistant in the laboratory of Material for Energy Conversion, EMPA, Dübendorf, Switzerland</b> 1D and 2D modeling and photoelectrochemical properties' determination of particle-based photoanodes.
	2013-2014	<b>Research assistant at LRESE, EPFL, Lausanne, Switzerland</b> Modelling, numerical design of experiment and experiment on semiconductor-liquid interface to determine key parameters for photoelectrochemical water splitting devices.
	Apr.-Jun. 2011	<b>Substitute teacher at the DIP of mathematics and physics in high schools and professional schools, Geneva, Switzerland</b>
	Oct. 2010- Mar. 2011	<b>Internship at Sunwat Bio Energy SA, Geneva, Switzerland</b> Structural study and installation of photovoltaic panels (58kWp) on the airport of Geneva. Energy study for three houses in Geneva to obtain the “Minergie” label.
Prizes	2013	<b>“État de Vaud” prize</b> awarded by the state of Vaud in Switzerland rewards an excellent master thesis with an original solution promoting rational use of energy
	2013	<b>“Prix concours RIE” prize</b> awarded by the association “For Research and Innovation in Energy” in Switzerland rewards an innovative master project in energy technology
Technical skills		<b>EDA and CAD tools:</b> Comsol Multiphysics, Solidworks, Autodesk Inventor, Matlab, WAsP, StarCD, Abaqus, Excel, and Origin <b>Operating systems:</b> Windows, Apple, and Linux <b>Languages:</b> Labview and Latex <b>Graphic design:</b> Inkscape, Gimp, and Adobe Photoshop

## Extra-professional activities

2018	2018	<b>Artwork</b>
		Front cover of the Journal of Material Chemistry A (issue 36)
2018	2018	Design and artwork of the music album from the band “The One Klaps”
2015-now	2015-now	<b>Music</b>
		Producer, composer, guitarist and lead singer of the band “The One Klaps” <a href="http://theoneklaps.bandcamp.com/">theoneklaps.bandcamp.com/</a>
2014-2017	2014-2017	Co-producer, composer, and musician of the band “Resources” ( <a href="http://resources17.bandcamp.com">resources17.bandcamp.com</a> )
2004-2014	2004-2014	Composer and musician of the band “Jetlakes”, 3 albums, numerous video clips, TV and radio broadcasts, and hundreds of lives ( <a href="http://mx3.ch/jetlakes">mx3.ch/jetlakes</a> )
2008	2008	<b>Voluntary project</b>
		Water supply project in Uganda with “Nouvelle Planète”

## References

**Sophia Haussener**, *Prof. and head of the Laboratory of Renewable Energy Science and Engineering (LRESE) at EPFL*, [sophia.haussener@epfl.ch](mailto:sophia.haussener@epfl.ch)  
**Simone Pokrant**, *Prof. of chemistry at the University of Applied Sciences, HTW Saar*, [simone.pokrant@htw-saar.de](mailto:simone.pokrant@htw-saar.de)





